Development of a semi-empirical three-dimensional model for predicting the peak cutting forces in rock cutting

Experimentally-based research

M.H. (Maarten) de Jonge

Delft University of Technology

TU Delft Delft University of Technology

Challenge the future

DEVELOPMENT OF A SEMI-EMPIRICAL THREE-DIMENSIONAL MODEL FOR PREDICTING THE PEAK CUTTING FORCES IN ROCK CUTTING

EXPERIMENTALLY-BASED RESEARCH

by

M.H. (Maarten) de Jonge

in partial fulfillment of the requirements for the degree of

Master of Science
in Offshore & Dredging Engineering

at the Delft University of Technology,
to be defended on Monday February 10, 2020 at 09:00 AM.

Chairman:	Dr. ir. S.A. Miedema	Delft University of Technology
Thesis committee:	Ir. X. Chen	Delft University of Technology
	Dr. G. Liu	CCCC NERCD
	Dr. Ir. P.N.W. Verhoef	Delft University of Technology

This thesis is confidential and cannot be made public

TU Delft Delft University of Technology

中交疏浚技术装备国家工程研究中心有限公司
CCCC National Engineering Research Center of Dredging Technology and Equipment Co.,Ltd

ABSTRACT

On a global scale, the present-day demand of coastal protections, port expansions and construction of artificial islands, rises. To be able to accommodate for all these environmental changes, complex dredging operations have to be performed. Depending on the type of soil and in-situ conditions, a suitable excavation and transportation method has to be chosen. From an economic point of view it is desired to make this process as efficient as possible. The only way in doing this, is to understand the physics of the rock cutting process and be able to predict the behaviour of the rock formation during cutting.

This research focusses on the physics that come paired with the excavation of rock deposits under atmospheric conditions. The removal of rock results from the interaction between the cutting tool and intact rock, destructing the internal structure of the rock formation. A rock may either fail in a brittle tensile, brittle shear or ductile manner. Over the past decades various calculation models have been developed to predict the cutting forces in rock cutting. Most known prediction models assume one failure mechanism to be dominant, using a specific cutting tool geometry. For the sake of this research a sharp pickpoint is used. The elaborated, existing calculation models within this research using a sharp pickpoint as a cutting tool, all consider the rock cutting process to be a two-dimensional problem. To investigate if this hypothesis about the rock cutting process is correct, experimental research is conducted. A distinction is made between two different rock types, both varying in strength (e.g. sandstone and artificial rock).

Experimental research revealed that the measured forces greatly underestimate the results of the existing prediction models. The author states that this inaccuracy partially arises from the fact that, in practice, the excavation of rock is actually a three-dimensional problem, since visual observations clearly showed that chips broke out sideways. Based on the experimental measurements, two new calculation models were set up, incorporating this three-dimensional effect. The first model implemented fracture mechanics theory, focussing on the required local crack tip stresses to initiate a tensile crack. Due to several unknown empirical parameters, the tensile-dominated fracture model gave unsatisfactory results, underestimating the measured cutting forces. The second model was set up by focussing on the actual physics that were observed during cutting. Based on visual observations and individual chip investigation, three different failure mechanisms can be substantiated that occur during cutting: crushing, major shear failure and tensile failure.

By elaborating on the developed prediction model, it appears that the forces due to crushing dominate the total force spectrum. For a crushed zone to develop, penetration into the material is required. The author discovered that rock's resistance to obtain a certain penetration, needs to be accounted for when calculating the stresses within the crushed zone. By achieving the desired penetration, a large vertical force arises, indicating that frictional effects also need to be considered. This means that forces due to crushing are dependent on the hardness of the rock and frictional resistance between the cutting tool and rock's top interface. Based on production measurements and cutting groove analysis, the crushed zone dimensions were able to be determined, whereupon an expression for the pickpoint's indentation area was found. A surprising discovery was made during the analysing phase of the force data. Regardless of the pre-set cutting configuration, a basic force level was observed during cutting, which is quite well-approximated by the crush force component, including frictional effects. Despite the formation of a crushed zone, chips failed in a cataclysmic manner. Individual chip investigation revealed that a certain fraction of shear and tensile failure is present along the failure plane. It appeared that the contribution due to tensile failure becomes more significant as the penetration depth of the pickpoint increases. This can be explained by the fact that a tensile crack has the ability to grow and propagate to the rock's top interface. The results of this research show that predictability of the forces increased significantly, compared to the existing two-dimensional calculation models.

PREFACE

First of all, I would like to express my gratitude to *Dr. Ir. Sape Miedema* and *Ir. Xiuhan Chen* for the great support they have given me throughout my graduation period. They provided me with the right knowledge, by sharing their years of experience and creative view on the topic. This kept me on the right track and led to the work that you will be reading throughout this report.

Secondly, I would like to thank the CCCC National Engineering Research Center of Dredging for making use of their impressive research facility and the support they have given me in the four months that I spent at their company. A special thanks goes out to *Dr. Liu*, *Mr. Shao* and *Mr. Liwei* for the great collaboration within the lab, sharing their knowledge and arranging all necessities outside working hours. Because of their great caring and advice, I really enjoyed my stay in Shanghai.

Finally, my deepest gratitude goes out to my family and friends, who supported me through some tough and turbulent times during my academic career. Their mental support, encouragement and belief contributed a lot to my personal development and made me the person that I am today.

M.H. (Maarten) de Jonge
Delft, January 2020

CONTENTS

1

INTRODUCTION

1.1. BACKGROUND

Rapidly changing economies, speculations about sea level rise, developments within the offshore wind and mining industry and so on, show that dredging operations are indispensable in today's society. The term 'dredging' can be defined as the excavation of sediments and debris from various water bodies to reshape, improve and/or stimulate the environment. These dredging operations are mainly executed by two types of marine dredging vessels, depending on the soil conditions. For the removal of loose, soft soils such as sand, silt, gravel or clay, a Trailing Suction Hopper Dredger (TSHD) is being used. The excavation process is executed by two suction tubes, both equipped with a drag head. This drag head basically functions as a large vacuum cleaner that removes the soil due to the vessel's trailing movement. When excavating more stiff soil deposits like rock and (hard) clay, a Cutter Suction Dredger (CSD) is being deployed. This vessel is equipped with a rotating cutter head that excavates stiff chemically bonded particles due to the mutual interaction between the interchangeable attached teeth and in-situ soil. The shape of the teeth and design of the cutter head depend on the soil characteristics. One can imagine that the interaction between the cutting teeth and tight-grained soil deposit may lead to significantly high cutting forces and various types of wear development. In dredging processes one of the most important system deliverables is the production. By knowing or predicting the production of your dredging vessel, calculations for the feasibility of tender projects or instantaneous soil transportation of your pump system can be made. Before these production calculations can be completed, the underlying physics of the tool-rock interaction needs to be known. In general, a rock structure fails if the internal yield strength of the material is exceeded, leading to the arise of fractures in the rock mass. This happens due to the interaction of the intact rock and mechanical movement of the cutting tool at a certain cutting velocity. The fragmentation of rock can be considered as the process of destructing the rock under indentation of a cutting tool into the surface of the material, whereas the fracturing describes the propagation of cracks formed by *shear* and *tensile* stresses. In literature these two different failure mechanisms are considered to be dominant within the cutting process. It must be noted that, depending on the rock type, its internal properties and the environmental conditions the rock is in, a distinction is to be made between brittle, brittle-ductile and ductile failure. These failure modes depend on the shear-tensile capacity ratio of the in-situ rock mass. Multiple linear force prediction models have been developed over the years to determine the resulting cutting forces in two-dimensional space. The term 'linear' relates to the way the cutting force is developing by increasing the cutting depth. The model that is most frequently been mentioned in literature, is the model of Evans [1]. Evans assumed that the breakage of a brittle material happens in a purely tensile manner. By saying this, only the tensile strength properties of the rock are being used within the calculation. Another well-known prediction model is the model of Nishimatsu [2], which uses only brittle shear failure as its dominant failure mechanism. Due to the fact that most existing prediction models only use one dominant failure mechanism, and approach the rock cutting process in 2D, the problem gets significantly simplified. In practice, the cutting of rock is a three-dimensional problem, as chips breakout when penetrating the material along its cutting trajectory.

1.2. RESEARCH OBJECTIVES

This study attempts compose and validate a self-constructed force prediction model by performing full-scale rock cutting experiments. To achieve this, a broad range of data is required, where the desired input parameters, such as the cutting angle and depth of the mechanically driven cutting tool (pickpoint), are varied. The research is conducted in corporation with a sub-group of the China Communication Construction Company (CCCC) Ltd.: the CCCC National Engineering Research Center of Dredging Technology and Equipment Co.,Ltd. This state of the art dredging lab is based in the Pudong New Area, Shanghai. During the experiments a distinction is to be made between two different types of rock, namely: artificial rock (e.g. concrete) and sandstone. Both rock compositions have different strength parameters, making it possible to study the physical differences of the cutting process. This can be related to the type of failure, amount of produced material, resulting cutting forces and potential wear on the pickpoint. By performing multiple cutting experiments with different input parameters on both the sandstone and concrete, the following research question arises:

"Is it possible to develop a three-dimensional model approach to predict the cutting forces for the application of various types of rock?"

Based on this research question, multiple sub-questions can be investigated to support the outcome of the main research objective.

- *"Is the assumption of the proportional increasing relationship between the cutting forces and cutting depth a correct hypothesis, named in literature"?*
- *"What is the effect on the cutting forces by varying the cutting angle and cutting depth?"*
- *"How does the specific energy behave when increasing the cutting depth of the pickpoint?"*

1.3. OUTLINE

This thesis consists out of seven (7) chapters. Within this section a brief introduction of each subject per chapter is given.
Chapter 2 contains a study on required theoretical and experimental background information. This preliminary research discusses the physics that come paired during rock cutting, elaborates on existing force prediction models and test approaches for the preliminary data acquisition.
Chapter 3 explains the complete experimental configuration that has been used during testing in the NERCD lab. All components that have been used during test are explained on their specific function.
Chapter 4 focusses on the preliminary data acquisition of the various rock types. The experiments that have been executed to characterize the (artificial) rock are critically analyzed and explained on the basis of their data sets. Furthermore, an introduction is given to the experimental sequence and used input parameters for the actual rock cutting tests.
Chapter 5 elaborates on the complete data analysis of the rock cutting experiments. The force data, specific energy distribution, production of the sandstone and concrete experiments have been substantiated on basis of the visual observations during testing.
Chapter 6 is focussed on the analytical derivation of two different force prediction model approaches. Both models have been explained extensively and compared to the measured cutting forces.
Chapter 7 contains the conclusions and recommendations that have been drawn from the complete process.

2

PRELIMINARY RESEARCH

This chapter outlines the background theory from a theoretical and experimental point of view. The basic principle of a linear cutting process was analyzed where the various failure modes of the rock are investigated. Furthermore, multiple theories have been studied how the cutting depth, friction between the rock and cutting tool and propagation of the wear flat affect the cutting process.

2.1. THEORETICAL BACKGROUND

To fully understand the physics that lie behind the rock cutting process, an extensive literature study is performed. In dredging most rock cutting operations are executed underwater, meaning that hydrostatic pressures need to be taken into account when analyzing the cutting process. These confining pressures that act on the rock mass, influence the type of failure mode of the rock. This study mainly focusses on the condition of zero confining pressures on the rock specimen (e.g. atmospheric conditions). The fact that no hydrostatic pressure is present, also has influence on the failure process of the rock. When cutting dry, intact rock, due to the mechanical movement of a cutting tool, multiple physical phenomena occur. These phenomena can be categorized in the fragmentation and fracturing of rock. The fragmentation of rock can be seen as the process of destructing the rock under indentation of a cutting tool into the surface of the material, whereas the fracturing describes the propagation of cracks formed by shear and tensile stresses. During the cutting process, the rock failure mechanism depends on many factors. The most significant factors for failure are the type of in-situ rock and its characteristics, specific design of the cutting tool, environmental conditions and the operational parameters of the cutting process itself such as cutting speed and cutting depth. Depending on the type of rock, rock properties and the conditions the rock is in, a distinction can be made between brittle, brittle ductile and ductile failure, where brittle can be brittle shear failure, brittle tensile failure or a combination of both. The upcoming section will pay more attention to the physics of the rock failure process.

2.2. ROCK FAILURE MODES

When considering rock mechanics tests, rock failure may occur under several failure mechanisms, depending on the rock properties, temperature and applied stresses on the rock piece. The following failure mechanisms can be distinguished: *Tensile failure*, *Shear failure* and *Compressive failure*. The actual failure of the specimen may either fail in a brittle, brittle-ductile or ductile manner. To determine which failure mechanism is dominant in a rock, often the brittleness (or ductility number) is used and defined as

$$B = \frac{\sigma_{ucs}}{\sigma_{bts}} \tag{2.1}$$

where σ_{ucs} is defined as the Uniaxial Compressive Strength and σ_{bts} as the Brazilian Tensile Strength. Categorizing a rock in the type of failure that will occur is described by Gehring [3]. He stated that below a ratio of 9 ductile failure will occur, while above a ratio of 15 brittle failure will occur. In between theses limits there is a transition between ductile and brittle failure, which is also in accordance with the findings of Fairhurst [4].

Depending on the confining stresses that are applied to the rock specimen, various macro-scale failure modes may occur. Figure 2.1 represents an overview of failure modes under axial-symmetric conditions, where the radial stresses on the cylindrical rock sample are equal. The actual mode of failure is determined by the isotropic skeleton stresses.

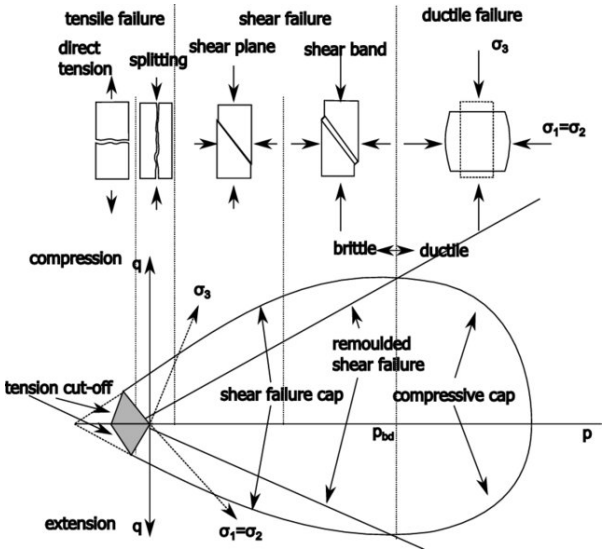

Figure 2.1: Rock failure modes according to van Kesteren [5]

The separation of interconnected grains of a rock can considered to be failing in a shear or tensile manner. When applying normal, negative axial stresses to the rock, elongation and eventually failure of the specimen is the result. Tensile failure may also occur when positive, low confining stresses are being applied in uniaxial compressive tests and triaxial compressive tests. This is called axial splitting and is mostly common for rocks with a high strength ratio. When increasing the confining stresses the failure mode will change from tensile failure to shear failure. The shear failure mode can be divided into shear plane failure and shear band failure. As figure **??** shows, the mode of brittle shear failure highly depends on the applied confining stress. When moving in the ductile failure regime, the confining stresses need to be increased even more. The rock sample will eventually fail in a compressive ductile way. Summarizing the above modes of failure; brittle failure is always destructive, meaning that the structure of the rock changes during failure in an irreversible way. Ductile failure, on the other hand, fails plastically, meaning it is reversible. Although in rock ductile failure is usually cataclysmic: the microstructures are destroyed, making it an irreversible process.

2.3. FRICTIONAL AND WEAR EFFECTS

When considering two bodies in motion, interacting with each other, material loss of both components is the most probable result. This concerns the wear on the cutting tool and destruction of the examined rock. The material loss accumulation of the pickpoint may trigger other physical phenomena in terms of required energy input. The energy distribution that is put in the rock cutting process is divided into the deformation, either elastically or plastically, of the bodies and the transformation into heat during frictional contact. The interaction due to these phenomena cause energy and material dissipates and is therefore of influence on the specific energy of the cutting system. Wear is a common result of two or more bodies in motion having contact where friction is involved. Both friction and wear are not intrinsic material properties, but characteristics of the system. Friction is the resistance that one surface or object encounters when moving over another. When considering the wear on a cutting tool, is it of great importance to be aware of the mutual interaction effects of the rock and material of the tool. As the cutting process evolves over time, the wear on the pickpoint may accumulate, followed by energy dissipation due to friction. The contact area of the wear flat depends on geometry of the tool and its initial cutting angle. In the next section more attention is paid to the explanation of the wear flat.

2.4. WEAR FLAT

In rock cutting, wear is a result of to the continuous mutual contact of the cutting tool with the intact rock during the removal of material. It is considered to be the removal of tool material from the cutting edge of the bit. In the past, many research has been done on the wear of cutting tools Verhoef [6], Dagrain and Richard [7], where the focus mainly was on the *abrasive* wear of the tool. Practical experiences of various researches reveals that the use of sharp cutting tools is merely limited to a relatively short cutting time, before the tool becomes blunt. As the tool becomes blunt, the cutting forces increase, as the resistance to remove material becomes higher. A potentially important part of the resulting cutting forces is the frictional resistance of the wear flat with the rock sample. These frictional forces are mainly described by the contact area of the cutting tool and resulting normal force to the specimen.

2.5. INFLUENCE OF CUTTING ANGLE

The cutting angle, or rake angle, in rock cutting mechanics describes the angle of the cutting face and the plane normal to the rock its horizontal cutting interface. A distinction can be made between positive and negative rake angles (figure 2.2). Both of these configurations are being used in different industries. In drilling operations generally a negative rake angle is being used on the rotating cutting tool, combined with very shallow cutting depths. The combination of these two cutting parameters results into fine crushing of the rock material, meaning that the failure mechanism is mainly in the ductile regime (e.g plastic failure). In dredging and mining operations, and therefore relevant for the sake of this research, the rake angle of the cutting blade is kept positive. Figure 2.2 shows that a positive rake angle slopes anti-clockwise from the fictional, orthogonal line to the rock interface. The rake angle increases as it slopes away. Within the dredging industry cutting angles of 40°-60° are most widely used. The rake angle has great influence on the cutting forces and thus specific energy of the process. By moving the tool to a more horizontal orientation, vertical forces will decrease. Note that the vertical force will, theoretically, be equal to zero if the cutting face of the tool is symmetrical with regard to the vertical plane, meaning the rake angle is 0° and only the horizontal force component is present. Frictional effects between the cutting tool and rock interface will also increase, as the positive cutting angle is enlarged. This can be explained by the fact that the vertical cutting forces become more dominant when increasing the rake angle, meaning that more vertical pressure is applied to the cutting tool. By assuming a constant feed, one can imagine that friction also causes an increase in heat development on the blade, leading to an increase in wear (Deketh [8]).

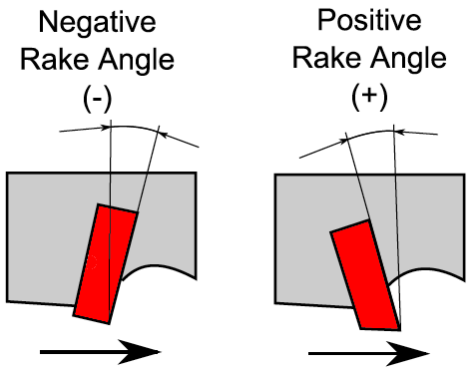

Figure 2.2: Orientation of positive and negative rake angle (Helmons [9])

Depending on having a negative or positive rake angle, abrasive wear of the cutting tool can turn out to be beneficial or disadvantageous for the cutting process. In drilling operations the rock cutting tools are designed in such a way that it is self-sharpening while wearing. In most cases, when dredging, wear on the tool makes it blunt, leading to an increase in cutting forces. Deketh [8] investigated the abrasive wear on cutting tools, but it is still unclear if the wear on the tool is accumulating when increasing the positive rake angle.

2.6. INFLUENCE OF CUTTING DEPTH

The depth of a cut within the cutting process is of great influence on the resulting cutting forces and specific energy that is put in the in-situ rock. The cutting process itself can be characterized by a ductile or brittle failure mode, depending on the cutting depth and confining pressure. When applying shallow cuts, rock fails in a ductile manner, where crushed material flows to the surface along the rake plane. This crushed zone is developing near the cutting tool and is a zone of highly fractured and inelastically deformed rock, mainly driven by compressive failure. This zone has an important effect on the chipping process and energy utilization in cutting. As the tool moves further into the rock, no crushed material is able to flow to the surface, which means that the stresses in the crushed zone will increase strongly. The transition from the ductile regime to the brittle regime is defined as the critical cutting depth. Beyond this point there is an increase in volumetric expansion and tensile stress, leading to propagation of tensile cracks to the rock's top interface. Richard *et al.* [10] says that the depth of the cut, characterizing the transition of the ductile and brittle regime, scales by the rock intrinsic length scale $(\frac{K_{Ic}}{\sigma_c})^2$. Where K_{Ic} is the critical stress intensity factor of the rock, which is applied in fracture mechanics to predict the stress state near a crack due to tensile failure. According to this formula the critical depth of the cutting tool can be determined, which defines this transition regime (figure 2.3).

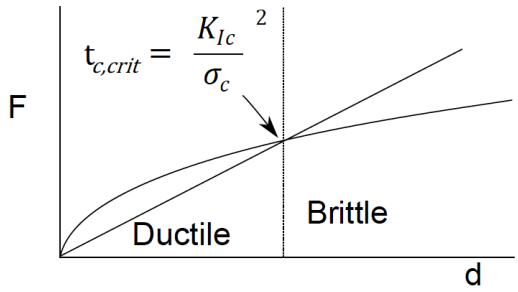

Figure 2.3: Transition from ductile to brittle regime Richard *et al.* [10]

As mentioned before, the cutting forces increase when applying deeper cuts. Force measurements in the ductile regime looks like high frequency response signal that fluctuates around a constant value. This is typical for plastically deforming rocky materials. When moving into the brittle regime, the fluctuation in terms of force amplitudes become much larger. The force signal consists out of many peaks and valleys corresponding to the formation of rock chips (Verhoef [6]). The brittle nature of this cutting regime, and increasing fluctuations, means a higher output in terms of cutting forces. This can be related to application deeper cuts. Figure 2.4 represents a general cutting force signal for shallow 2.4a and deep 2.4b cuts.

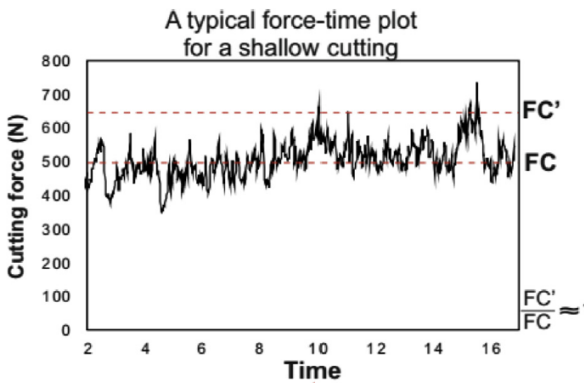

(a) Typical force-time plot for a shallow cutting

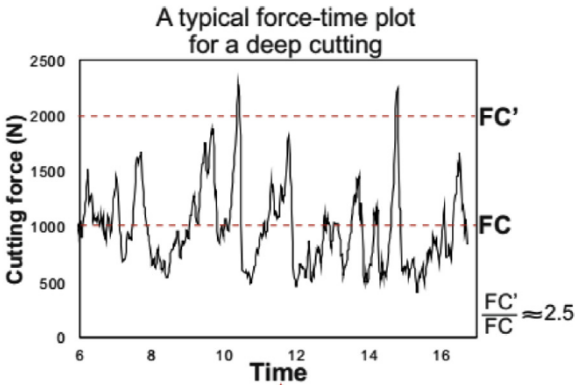

(b) Typical force-time plot for a deep cutting

Figure 2.4: Typical Force-Time plots of two cutting depth regimes

2.7. INFLUENCE OF CUTTING VELOCITY

In existing atmospheric-based linear rock and coal cutting models, the cutting velocity is not a variable that is incorporated in the theory for determining the cutting forces. The velocity mainly influences two different outcomes of the rock cutting process: cutting forces and development of wear. When considering the cutting process itself, the point of impact, which is the first mutual contact between the cutting tool and rock specimen, experiences a high peak in the cutting force (T.Rutten [11]). The author noticed that the peak forces at impact became even higher when the cutting velocity was increased.

When having significantly high contact stresses and an increase in cutting velocity, internal temperatures within the cutting tool will rise, softening the material and causing wear. In literature this is referred to as *adhesive wear*. The point where the steel alloy appears to weaken is called the critical temperature. This critical temperature is reached at the critical velocity (V_{crit}). Figure 2.5 shows the transition point of abrasive wear to adhesive wear, as the cutting velocity increases (Deketh [8]). Adhesive wear has negative effect on the lifetime of the cutting tool, meaning that frequent replacement of these modular pieces is most apparent. One can imagine that, in some project, it is desired that the cutting velocity is kept below this critical value to avoid undesired wear development. Though, it must be noted that the critical velocity is affected by several factors such as rock properties, tool material and geometry of the tool.

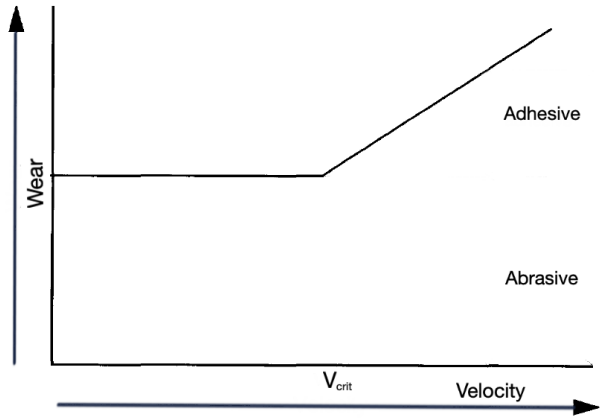

Figure 2.5: Adhesive/abrasive wear development by increasing the critical velocity (Deketh [8])

2.8. LINEAR ROCK CUTTING MODELS

Over the years various cutting models have been developed to substantiate the physics that come paired with the rock cutting process. The existing models can be subdivided into semi-empirical and analytical models, all having different assumptions and parameters. The assumptions made mainly focus on the dominating failure mode that occurs during the cutting process, as shown in figure 2.1. These discontinuous cutting processes can either be tensile or shear dominated. The analytical rock cutting models that have been developed over the years, are often limited to a certain dominant failure mechanism. A very important aspect of these prediction models is that the cutting process is considered in two-dimensional space. This means that the cutting force output will be in vertical direction and horizontal direction along the cutting trajectory of the blade. Each model assumes an effective cutting area that is calculated by the depth of the cut h_i and width of the cutting tool w. In practice this is not the case. Many rock cutting researches have shown that, when a heterogeneous rock is being cut, discontinuities arise in the observed cutting area. This means that not only forces result in vertical direction and in the direction of the cutting trajectory, but also sideways. This relatively unknown phenomena is called sideways outbreaking, making it the linear rock cutting theory a three-dimensional problem, which is not incorporated in the theory by the existing models.

The analytical and semi-empirical existing rock cutting models that have been developed over the past decades all used a specific failure mechanism. This report focusses on three different failure mechanisms that, according to the writer, are most applicable for this research. A distinction can be made between: *brittle tensile*, *brittle shear* or *ductile* failure. All these mechanisms have been incorporated in different analytical and semi-empirical existing rock cutting models that have been developed over the past decades. To obtain a broad understanding of the rock cutting process, researchers varied with shapes and geometries of the cutting tools. For this research a pick point is being used. For eventually developing a self-made prediction model, all decisions, assumptions and mathematical approaches researches made, were studied. This includes the variation in tool shapes. As the rock cutting experiments are executed under atmospheric conditions, ductile failure will most likely only be concentrated within the crushed zone, because the rock is being subjected to high compressive stresses of the cutting tool. In practice, ductile failure occurs when having a low ductility number or having high confining pressure and deviatoric stress. High confining pressures usually occur at great water depths where the hydrostatic pressure acts on the in-situ saturated rock formation.

2.8.1. EVANS

Evans [1] assumed in his brittle rock cutting theory that tensile failure was the dominating failure mechanism of the rock, during the cutting process. He developed this theory to estimate the peak cutting forces for symmetrical point-attack picks, derived from the dimensions of the blade and tensile strength of the rock (σ_{bts}) and cutting depth. Evans his cutting theory is the most widely accepted in literature. Several researchers expanded this theory or used the assumptions he made. The assumptions made for Evans's analytical model for determining the required force of a blunt wedge to cut through coal have been described by Miedema [12]. All assumptions are being explained on basis of the schematic representation of Evans [1] theoretical model, given in figure 2.6.

The cutting process is assumed to be strictly two-dimensional and moving with a constant velocity in horizontal direction. However, the effect of velocity in this theory is neglected. The force R acts near the tip and on both sides of the symmetrical point-attack pick. The vector stands at an angle δ, normal to the surface **A-C**. Along the line **C-D** tensile stresses act. It is assumed that a resultant force T acts at the center of **C-D**. The line **C-D** is defined as the length of the shear plane and depends on the shear angle β. The shear angle β is defined as the angle between the intact rock and shear plane, which has failed due to the exceedance of the peak frictional strength of the rock. It is determined using the minimum energy principle. When the cutting energy is at a minimum it is assumed that failure will occur at shear angle β Helmons [9].

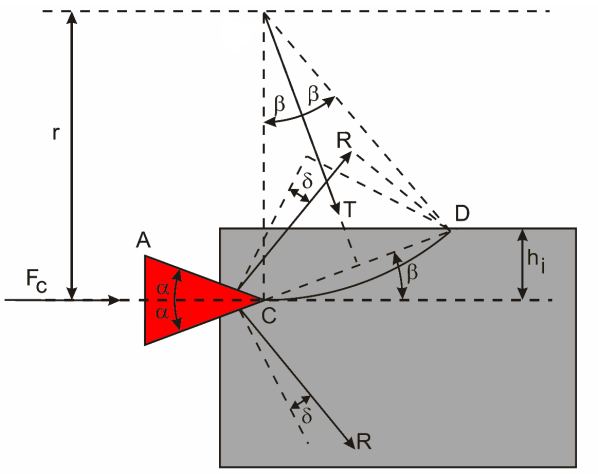

Figure 2.6: Schematic representation of Evans [1]

$$T = \sigma_T \cdot r \cdot w \cdot \int_{-\beta}^{\beta} cos(\omega) \cdot d\omega = 2 \cdot \sigma_T \cdot r \cdot w \cdot sin(\beta) \tag{2.2}$$

By assuming that the penetration of cutting tool is relatively small, compared to the cutting depth h_i, it can be said that the penetration of the blade its edge can be neglected.

$$\frac{R \cdot h_i}{sin(\beta)} \cdot cos(\alpha + \beta + \delta) = 2 \cdot \sigma_T \cdot w \cdot r^2 \cdot sin^2(\beta) = 2 \cdot \sigma_T \cdot w \cdot \frac{h_i^2}{4 \cdot sin^2(\beta)} \tag{2.3}$$

After applying some geometric relations and simplifying the equation, the force R acting near the tip of the blade will become

$$R = \frac{\sigma_T \cdot w \cdot h_i}{2 \cdot sin(\beta) \cdot cos(\alpha + \beta + \delta)} \tag{2.4}$$

The forces acting on the cutting tool can be derived from R by subdividing this force into a horizontal and vertical component. Figure 2.6 shows that the blade angle α and angle of external friction angle δ determine the magnitude of these forces. Both forces can be written as

$$F_{h,Evans} = \frac{\sigma_T \cdot h_i \cdot w}{2 \cdot sin(\beta) \cdot cos(\alpha + \beta + \delta)} \cdot sin(\alpha + \delta) \tag{2.5}$$

$$F_{v,Evans} = \frac{\sigma_T \cdot h_i \cdot w}{2 \cdot sin(\beta) \cdot cos(\alpha + \beta + \delta)} \cdot cos(\alpha + \delta) \tag{2.6}$$

Because the cutting process is modelled by the assumption of having two deformation areas, the energy that is needed to deform these areas can be written as a function of the shear angle β and cutting force F_c on the cutting tool. To calculate the shear angle β the minimum energy principle can be used. This numerical solution is solved by equating the derivative of the cutting force F_c with respect to the shear angle β to zero.

$$\frac{dF_{c,Evans}}{d\beta} = 0 \tag{2.7}$$

$$\beta = \frac{\pi}{4} - \frac{\alpha + \delta}{2} \tag{2.8}$$

By using the expression for the shear angle, derived from the principle of minimum energy theorem, the horizontal cutting force and vertical(normal) force on each side of the wedge can be written as

$$F_{h,Evans} = \frac{\sigma_T \cdot h_i \cdot w}{1 - sin(\alpha + \delta)} \cdot 2 \cdot sin(\alpha + \delta) \tag{2.9}$$

$$F_{v,Evans} = \frac{\sigma_T \cdot h_i \cdot w}{1 - sin(\alpha + \delta)} \cdot cos(\alpha + \delta) \tag{2.10}$$

2.8.2. MIEDEMA - TEAR TYPE AND CHIP MODEL

During the rock cutting process, bonded grains are being destroyed due to the impact of the cutting tool. Miedema [12] stated that a distinction can be made between different failure mechanisms by looking at the $\frac{\sigma_{ucs}}{\sigma_{bts}}$ ratio of the rock. Table 2.1 shows three different types of failure mechanisms that are able to occur during the cutting process. As for this research large cutting depths are being applied, it is most likely that only shear failure (e.g. *Shear Type*) will not occur. The two failure mechanisms that are being considered in this cutting model are the *Tear Type* and *Chip type*.

Failure mechanism	$\frac{\sigma_{ucs}}{\sigma_{bts}}$	Type of failure
Tear Type	Large	Tensile failure
Chip Type	Medium	Shear failure, Tensile failure
Shear type	Small	Shear failure

Table 2.1

Chip Type

Depending on the $\frac{\sigma_{ucs}}{\sigma_{bts}}$ ratio and cutting tool angle, a combination of two failure modes may occur; shear failure and tensile failure. Near the tip of the blade plastic failure is present in the form of a crushed zone. When the layer cut is sufficiently thick, the crushed zone will exist, but will not reach the free surface of the rock. Within the crushed zone a shear plane is created, which leads to a tensile crack up to the free surface.

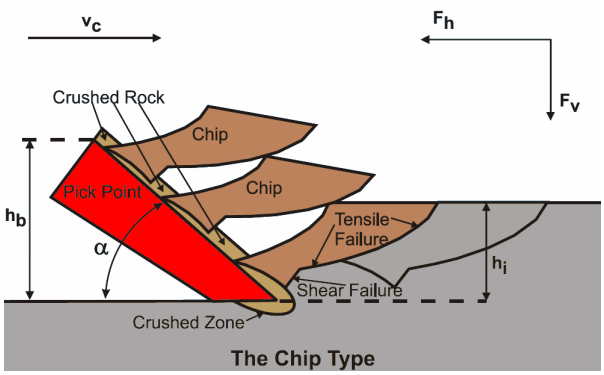

Figure 2.7: Schematic representation of Chip Type model (Miedema [12])

Tear Type

The Tear Type cutting mechanism is based on 100 percent tensile failure as its failure mechanism. This discontinuous mechanism has a large $\frac{\sigma_{ucs}}{\sigma_{bts}}$ ratio.

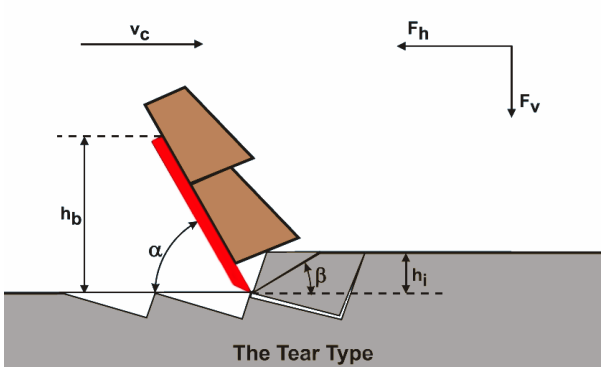

Figure 2.8: Schematic representation of Tear Type model (Miedema [12])

As mentioned before, compressive and tensile strength are typical parameters for a rock. These parameters depend on the composition of the chemically bonded grains. Rock also has the property to resist itself to shear,

meaning that the rock will have a internal and external friction angle. When the compressive stresses within the rock are equal to zero, the remaining shear strength is called the cohesion c. The cohesion can be determined by using the Mohr-Coulomb theory and depends on the internal friction angle ϕ of the soil. The internal friction angle is a physical property of the rock itself. Bonded particles deliver an internal resistance force due to the tended shearing motion of the rock's microstructure. The point of failure due to shearing is when the uniaxial compressive strength σ_{ucs} of the rock is exceeded. The cohesion can be calculated by

$$c = \frac{\sigma_{ucs}}{2} \cdot (\frac{1 - sin(\phi)}{cos(\phi)}) \tag{2.11}$$

Using the Mohr-Coulomb failure criterion, the shear stress τ_s on the chip's shear plane can be calculated by

$$\tau_s = c + \sigma_n \cdot tan(\phi) \tag{2.12}$$

Where σ_n is the normal stress acting on the shear plane and ϕ the internal friction angle of the material. Figure 2.9 illustrates the Mohr circle for the Tear Type. The Mohr circle is a tool to calculate the principal stresses on the soil. The principal stresses can be divided into the major and minor principal stress, which is defined as the plane on which the normal stress attains its maximum or minimum value. This is at the point where the shear stress on principal plane is zero.

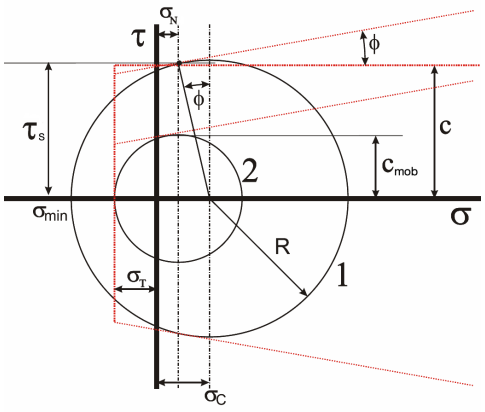

Figure 2.9: Mohr circle of Tear Type model (Miedema [12])

For calculating the actual resulting cutting forces, a mobilized cohesive shear strength c_{mob} needs to be defined by using the tensile strength σ_{bts} of the rock. By using this, it is not required that the tensile stress is to be equal to the tensile strength along the complete failure plane. This gives the ability to predict the cutting forces at the point of tensile failure. Figure 2.9 shows the second Mohr circle that is constructed due to the mobilized cohesive shear strength.

$$c_{mob} = \frac{\sigma_{bts}}{(\frac{sin(\frac{\alpha+\delta-\phi}{2})}{cos(\frac{\alpha+\delta-\phi}{2})} - 1) \cdot (\frac{1-sin(\phi)}{cos(\phi)})} \tag{2.13}$$

According to Miedema the cutting forces in horizontal and vertical direction are

$$F_{h,Miedema} = 2 \cdot c_{mob} \cdot h_i \cdot w \cdot \frac{cos(\phi) \cdot sin(\alpha + \delta)}{1 + cos(\alpha + \delta + \phi)} \tag{2.14}$$

$$F_{v,Miedema} = 2 \cdot c_{mob} \cdot h_i \cdot w \cdot \frac{cos(\phi) \cdot cos(\alpha + \delta)}{1 + cos(\alpha + \delta + \phi)} \tag{2.15}$$

2.8.3. GOKTAN AND GUNES

Goktan and Gunes [13] developed a semi-empirical model for asymmetrical point-attack picks, by extending the theory of Evans [1]. The theory of Evans was limited to the assumption of symmetrical cutting picks that act along the line of advance. The author stated that, in practice, cutting picks do not act symmetrically on cutter heads or mechanical excavators. Full-scale experimental data showed that Evans his theory and its recent modification underestimated the peak cutting forces within the linear rock cutting process. To account for rock breakage under asymmetrical attack, Goktan and Gunes [13] conducted full-scale rock cutting experiments, using a broad range of brittle rock materials, all having a different $\frac{\sigma_{ucs}}{\sigma_{bts}}$ ratio (Goktan and Gunes [13]). A distinction was made between *sandstone*, *siltstone*, *limestone*, *chromite*, *harzburgite*, *sepantine* and *trona*. Figure 2.10 shows the schematic test setup for the cutting experiments by using a asymmetrical point-attack pick.

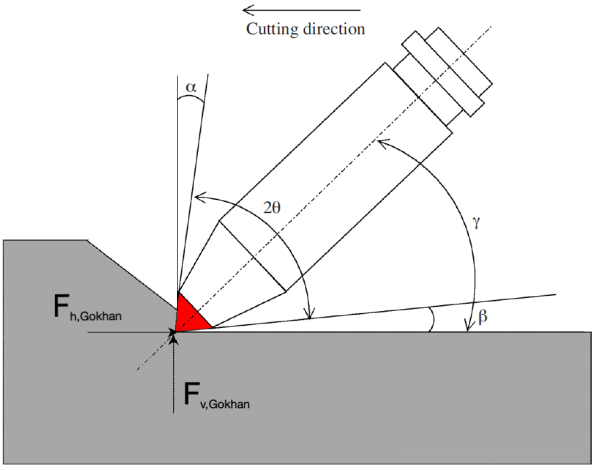

Figure 2.10: Schematic representation of the asymmetrical point-attack pick configuration of Goktan and Gunes [13]

By analyzing the raw cutting data and combining the theoretical model of Goktan [14], a semi-empirical technique arose for constructing a formula for predicting the cutting force of point-attack picks under asymmetrical attack. The total peak cutting force can be calculated according to

$$F_{Goktan-Gunes} = \frac{12 \cdot \pi \cdot \sigma_{bts} \cdot h_i^2 \cdot sin^2(\frac{90-\alpha}{2} + \psi)}{cos(\frac{90-\alpha}{2} + \psi)} \tag{2.16}$$

Where α is the rake angle of the point-attack and ψ the external friction angle between the tool and the rock. When looking into operational purposes in dredging projects, it is important to know what power requirements and delivered cutter head torque a machine can deliver. For calculating these system properties, the mean cutting force F' is a significant parameter. Goktan and Gunes [13]found a strongly correlated relationship between the peak cutting force F and the mean cutting force F' by analyzing the full-scale cutting data. The total mean cutting force can be written as

$$F'_{Goktan-Gunes} \simeq \frac{F_{Goktan-Gunes}}{3} \simeq \frac{4 \cdot \pi \cdot \sigma_{bts} \cdot h_i^2 \cdot sin^2(\frac{90-\alpha}{2} + \psi)}{cos(\frac{90-\alpha}{2} + \psi)} \tag{2.17}$$

2.8.4. NISHIMATSU

Nishimatsu [2] developed a model for shear failure in the brittle regime. Nishimatsu assumed that the stress distribution for orthogonal rock cutting along the failure plane **A-B** is proportional to $n^t h$ power of the distance λ from point **A** to point **B** (figure 2.11), where n is a constant that indicates the state of stress in the rock-cutting process (e.g. stress distribution factor). The stress distribution on plane **A-B** is to be divided into a normal and shear component. As the cutting process is assumed to be brittle, ductile failure due to crushing of the rock is to be neglected. This only holds for a sharp chisel. Furthermore, Nishimatsu calculated the brittle shear failure of the rock according to a linear Mohr envelope, which is determined from the σ_{ucs} and σ_{bts}. The last assumption he made was that the cutting velocity has no effect on the cutting process itself.

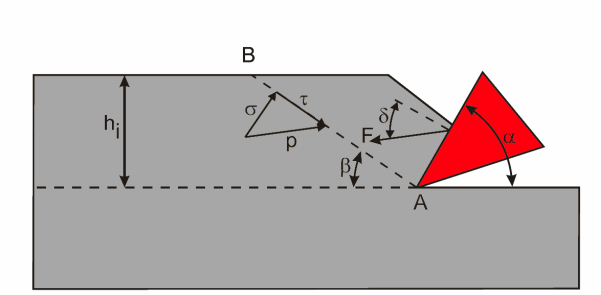

Figure 2.11: Schematic representation model of Nishimatsu [2]

From figure 2.11 it can be seen that β is the shear angle, which can be defined as the angle at which the rock is failing due to shearing. For the rock to fail, the shear strength capacity of the rock needs to be exceeded. The shear stress that acts along the plane **A-B** is indicated as τ. Furthermore, the cutting angle is labelled as α and the external friction angle as δ.

As a first simplification, let us assume that the magnitude of the resultant stress p acting on the unit length of the line **A-B** is given by

$$p = p_0(\frac{h_i}{sin\beta} - \lambda)^n \tag{2.18}$$

Where n is called the stress distribution factor. Nishimatsu also assumed that the direction of the resultant stress p is constant along the line **A-B**.

$$F_c = p_0 \cdot w \cdot \int_0^{\frac{h_i}{sin(\beta)}} (\frac{h_i}{sin(\beta)} - \lambda)^n \cdot d\lambda \tag{2.19}$$

The constant p_0, which is determined from the equilibrium of forces, can be obtained by integrating equation 2.19.

$$p_0 = (n+1) \cdot (\frac{h_i}{sin(\beta)})^{-(n+1)} \cdot \frac{F_c}{w_c} \tag{2.20}$$

Where w_c is the width of the cut and F_c the resulting total cutting force. By now having an expression for p_0, equation 2.20 can be substituted into equation 2.18.

$$p = (n+1) \cdot (\frac{h_i}{sin(\beta)})^{(n+1)} \cdot \frac{F_c}{w_c} \cdot (\frac{h_i}{sin(\beta)} - \lambda)^n \tag{2.21}$$

The resultant stress p can be separated into a tangential (τ_t) and normal (σ_n) component.

$$\tau_t = (n+1) \cdot (\frac{h_i}{sin(\beta)})^{-(n+1)} \cdot \frac{F_c}{w_c} \cdot (\frac{h_i}{sin(\beta)} - \lambda)^n \cdot sin(\alpha + \beta + \delta) \tag{2.22}$$

$$\sigma_n = (n+1) \cdot (\frac{h_i}{sin(\beta)})^{-(n+1)} \cdot \frac{F_c}{w_c} \cdot (\frac{h_i}{sin(\beta)} - \lambda)^n \cdot cos(\alpha + \beta + \delta) \tag{2.23}$$

Nishimatsu [2] analyzed the peak stresses that occurred during the cutting process. The maximum normal and tangential stress occurs near the tip of the chisel. This means that the distance from point **A** to **B** in figure 2.11 is zero (λ=0).

$$\tau_{t,0} = (n+1)\cdot(\frac{h_i}{sin(\beta)})^{-1}\cdot\frac{F_c}{w_c}\cdot sin(\alpha+\beta+\delta) \tag{2.24}$$

$$\sigma_{n,0} = (n+1)\cdot(\frac{h_i}{sin(\beta)})^{-1}\cdot\frac{F_c}{w_c}\cdot cos(\alpha+\beta+\delta) \tag{2.25}$$

To describe the actual response of the brittle material, the expressions for the stress in tangential (τ_t) and normal (σ_n) direction can be implemented into the Coulomb-Mohr failure criterion

$$\tau_{t,0} = c + \sigma_{n,0}\cdot tan(\phi) \tag{2.26}$$

After substitution of the stresses and simplification of failure criterion, the resulting force $F_{Nishimatsu}$ can be written as

$$F_{Nishimatsu} = \frac{c\cdot w_c\cdot h_i}{n+1}\cdot\frac{cos(\phi)}{sin(\beta)\cdot sin(\alpha+\beta+\delta+\phi)} \tag{2.27}$$

$$F_{h,Nishimatsu} = \frac{c\cdot w_c\cdot h_i}{n+1}\cdot\frac{cos(\phi)\cdot sin(\alpha+\delta)}{sin(\beta)\cdot sin(\alpha+\beta+\delta+\phi)} \tag{2.28}$$

$$F_{v,Nishimatsu} = \frac{c\cdot w_c\cdot h_i}{n+1}\cdot\frac{cos(\phi)\cdot cos(\alpha+\delta)}{sin(\beta)\cdot sin(\alpha+\beta+\delta+\phi)} \tag{2.29}$$

2.8.5. LI

Li *et al.* [15] developed an analytical approach for estimating the peak cutting force on conical picks, by using fracture mechanics. Figure 2.12a shows a schematic overview of the conical pick the author considered. Li used full-scale rock cutting configuration to verify his results. The angle of attack of the conical pick was fixed to 55° to make a clear comparison between different models, which is indicated as ϕ_{Li} in figure 2.12a.

Li assumed that during the rock cutting process cracks would propagate to the rock's free surface, only by tensile fracturing. He assumed a linear stress distribution over the complete contact face of the conical pick with the intact rock. The initiation of the cracks occurs at the tip of the blade, because the concentrated stresses at this point are highest due to compression. The compressive stresses acting on section **A-A** at an arbitrary height act as displayed in figure 2.12b. It is observed that due to these compressive stresses, a crushed zone develops in front of the pick. It must be noted that the author did not clearly account for the shear stresses within this crushed zone. He concluded that the cutting force reaches its peak when a tensile crack is initiated at the tip of the conical pick and therefore assumed that tensile failure dominates the total cutting forces, despite the fact that there is a crushed zone present.

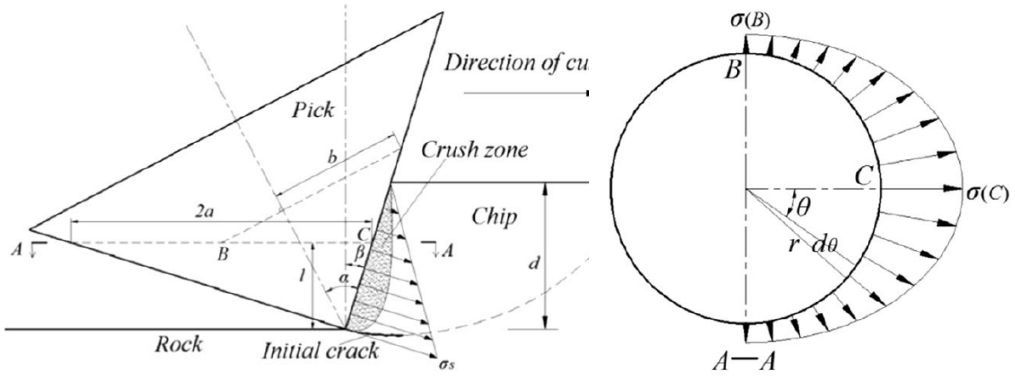

(a) Stress distribution on conical pick over cutting depth

(b) Compressive stress distribution on section A-A

Figure 2.12: Schematic overview of stress distribution on conical pick (Li *et al.* [15])

For determining the total peak cutting forces due to tensile fracturing of the conical pick, several geometric calculations have to be performed, which will not be incorporated within this report. One important assumption that Li made was that the shape of **A-A** in figure 2.12b is a perfect circle with radius r. In practice this projected surface would be considered to be a ellipse. On the basis of figure 2.12, and applying the geometric calculations, the stress distribution on the conical surface can be expressed as

$$\sigma_{Li} = \left[\frac{2}{\pi}\left(\frac{sin(\alpha)}{\cos(\beta)} - 1\right)\cdot\theta + 1\right]\cdot\frac{d - l_a}{d}\cdot\sigma_s \tag{2.30}$$

Where α is the semi-tip angle of the conical pick, β the rake angle, θ the central angle between the tip point and cutting direction. Furthermore, l_a is an arbitrary height of section **A-A** and σ_s is the critical stress at which a crack is initiated.

Griffith [16], the critical stress of crack initiation for a brittle rock is calculated by equation 2.31. Griffith's theory describes a method to analytically calculate the driving force of a crack that is initiated by a peak stress. Griffith considered three modes of fractures to occur

- Mode I: tensile or opening mode;
- Mode II: in-plane shear or sliding mode;
- Mode III: anti-plane shear or tearing mode.

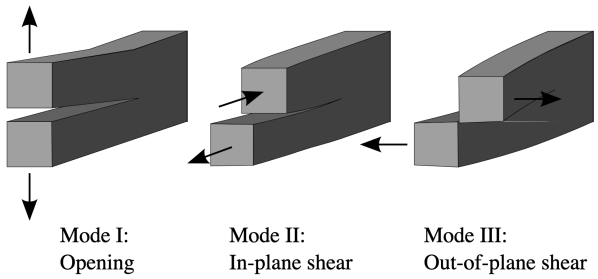

Figure 2.13: Various modes of fracturing according to Griffith [16]

$$\sigma_{crit} = \sqrt{\frac{2\cdot E\cdot\gamma}{\pi\cdot r_c}} \tag{2.31}$$

Where r_c is to be the size of the crack and γ the rock surface energy density, defined as the energy consumed in generating a unit of surface. Because Li used tensile failure as the failure criterion, only the mode I fracture toughness of the rock is applied in the derivation. K_{Ic} is also used for calculating the surface energy density of the rock.

$$\gamma = \frac{K_{Ic}^2}{2\cdot E} \tag{2.32}$$

By combining equation (2.30), (2.31) and (2.32) the stress distribution on the surface of the conical pick can be expressed as

$$\sigma_{Li} = \left[\frac{2}{\pi}\left(\frac{sin(\alpha)}{\cos(\beta)} - 1\right)\cdot\theta + 1\right]\cdot\frac{(d - l_a)\cdot K_{Ic}}{d\sqrt{\pi\cdot\delta}}\cdot\sigma_{crit} \tag{2.33}$$

As the compressive stresses act over the cutting depth and rake surface of the cone with rock, the following integration boundaries have been taking into account to calculate the peak cutting force

$$F_{peak,Li} = \int_0^d\int_{-\frac{\pi}{2}}^{\frac{\pi}{2}}\sigma_{Li}\cdot cos(\theta)\cdot r_c\cdot d\theta dl_a \tag{2.34}$$

By applying all intermediate steps and combining several equations, the peak cutting force of a conical pick, according to Li's theory is

$$F_{peak,Li} = \frac{\lambda^{\frac{5}{6}} K_{Ic} d^{\frac{5}{3}}}{3 \cdot \sqrt[6]{\frac{\pi^2}{12 \cdot cos(\beta)} \left[\frac{1}{3} \left(\frac{sin(\alpha)}{cos(\beta)} - 1 \right)^2 + 1 \right]}} \tag{2.35}$$

Where λ is a geometrically determined value due to the orientation of the conical pick. This expression can be found in Li *et al.* [15].

2.8.6. DISCUSSION ABOUT THE LIMITATIONS OF THE PREDICTION MODELS

This paragraph introduced multiple theoretical and (semi-)empirical rock cutting models that were developed over the years. All used different assumptions and mathematical approaches for predicting the cutting forces. A distinction was made between a chisel type (Evans [1], Nishimatsu [2]), point-attack (Goktan and Gunes [13]) and conical pick (Li *et al.* [15]) for evaluating the considerations various researchers took for developing their prediction model. In practice, the applicability of these models may be very limited due to their simplifications. Some of the above mentioned models are all based on two-dimensional modelling effects, while the actual rock cutting process is a three-dimensional mechanism. This means that the sideways outbreaking of the rock, during cutting, is neglected in the simplified prediction models, potentially underestimating the cutting forces. Furthermore, most models use only one failure mechanism (e.g. shear or tensile failure), where the assumption of brittle failure is assumed. In practice a combination of these types of failure may occur when a sufficient cutting depth is achieved. This can be explained by the fact that first crushing occurs near the tip of the pickpoint, forming a plastic region of fine material. At the end of this crushed zone, shear cracks start to develop, where after tensile cracks start to propagate to the rock's surface.

When going more into depth into the developed models, certain calculation methods and decisions stand out. Li *et al.* [15] applied rock fracture mechanics theory into their theoretical model, assuming a mode I loading condition. By critically looking at the derivation, it is noticed that the units do not match with the proposed output, which should be in kiloNewtons [kN] (equation 2.35). Since the the stress intensity factor K_{Ic} has units $[MPa \cdot \sqrt{m}]$, it is not possible to obtain a pure force output by multiplying it with $d^{\frac{5}{3}}$. Furthermore, the assumption that the application of Griffith's theory is valid for the used cutting configuration is also not correct. This theory is applicable for a bilateral-loaded crack, applied at the boundaries of an infinite plate. This is not the case in the problem that Li sketched. The application of Evans [1] also brings some complications. When cutting a rock having a large relatively large external friction angle δ, under a steep cutting angle of, let's say, 70°, it appears that the angle of the failure plane β, as in equation 2.8, converges to zero or even become negative. From a physical point of view this is incorrect, because a crack will always propagate into the direction of least resistance, which is to the rock's top interface.

The reason why a variety of models have been studied is to gain knowledge about their methods, way of thinking and reasons for certain assumptions. Because the writer thinks that the failure process of cutting rock is a combination of crushing, shearing and tensile failure, it can be said that this study about the physics of each existing force prediction model, can be seen as valuable and potentially applicable for the development of a self-made model.

2.9. EXPERIMENTAL BACKGROUND ON ROCK PROPERTIES

Material properties of a rock specimen that is being used during the linear rock cutting tests are highly important. By knowing the failure boundaries of the rock under multiple loading conditions, a classification of the strength parameters can be obtained. In practical rock mechanics tests, a distinction can be made between several failure mechanisms: uni-axial compression, tri-axial compression and Brazilian splitting test. Procedures for rock testing have been recommended by the International Society of Rock Mechanics (ISRM) (Bieniawski and Bernede [17]) and the American Society for Testing and Materials (ASTM). In rock engineering the most widely used parameter is the Uniaxial Compressive Strength, which provides the capacity of the material to withstand loads tending to deform in a compressive manner. The standard UCS tests provide satisfactory results under conditions where the sample is free from planes of weakness, discontinuities and micro-cracks. (Opposite to compressive failure, is tensile failure. The Brazilian Tensile Strength (BTS) of a rock specimen can be defined as the maximum resistance capacity a rock or rock mass can withstand before the tensile crack propagation is at its limit, and thus fails. A very common way of testing is by doing a Brazilian splitting test. It is determined by an indirect suggested testing method, standardized by the ISRM Bieniawski and Hawkes [18]. The UCS and BTS of the rock can be calculated from the Indentation Hardness Index (IHI), if strong predictive correlations are established. The IHI indicates the hardness of the rock. This coefficient is derived from the bit penetration into the rock due to a vertically applied load that acts perpendicular the rock's surface. To understand the methods of the above mentioned rock property tests, the UCS, BTS and IHI tests will be elaborated according to the ISRM standards.

2.9.1. UNIAXIAL COMPRESSIVE STRENGTH TEST

The main goal of this test method is to measure the uniaxial compressive strength of sample, generally having a cylindrical shape. Uniaxial basically means that a force is applied from one direction, and one direction only. In this case a vertical force, parallel to the rock sample its longitudinal axis (e.g. axial). This force needs to be applied by a hydraulically driven machine, which consists of a load frame that applies an axial load, force sensing device, force display or readout, grips or fixtures, displacement sensor that measures the compression of the specimen. The accuracy of the load results have to be within a specific range of allowable variation. The accuracy of such testing machine has to be calibrated and verified by using standard weights, elastic calibration devices and equal-arm balances. The press capacity of the machine should be sufficiently large and be able to apply a load at a rate conform the ISRM standard Suggested Methods for Determining the Uniaxial Compressive Strength and Deformability of Rock Materials (Bieniawski and Bernede [17]). Figure 2.14a represents a simplified, schematic representation of such a testing machine. The rock specimen is placed between two steel platens, where at least one has a spherical seat, because it is important that the two loading faces on each side of the rock sample are parallel to each other. The sample, spherical seat and platens shall be axially centred w.r.t. the to hydraulically controlled loader and consecutive parts below.

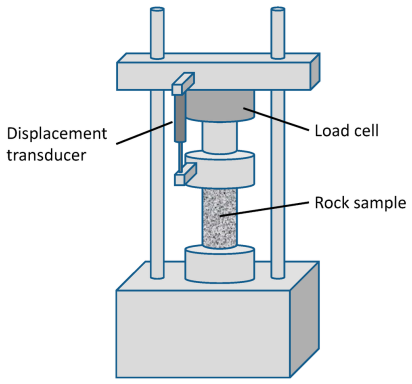

(a) Schematic overview of UCS setup Mwanga *et al.* [19]

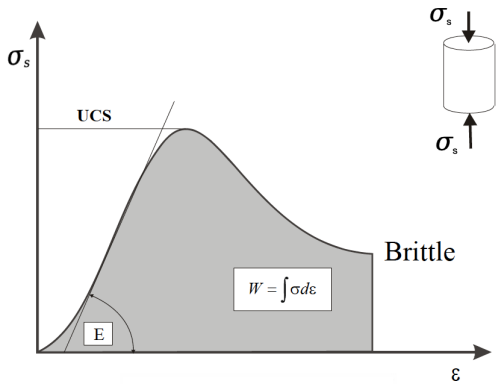

(b) Typical stress-strain curve of a UCS test

Figure 2.14: Schematic and graphical representation of UCS test

Focussing on the physical part of the test, it is known that the UCS value is equal to the maximum allowable stress that is applied to the specimen, having a certain compressive strain ϵ. Figure 2.14 represents a typical stress-strain curve of a brittle rock sample where the peak stress at a certain strain is indeed the UCS value. The stress applied, needed to let the rock fail in a certain failure mechanism can be calculated according to

$$\sigma_s = \sigma_{ucs} = \frac{F_u}{A_s} \tag{2.36}$$

Where σ_s is equal to the UCS value of the rock composition, F_u the axially applied force in vertical direction and A_s the cross-sectional area of the cylindrical rock specimen.

2.9.2. BRAZILIAN SPLITTING TEST

This test method makes it possible to measure the uniaxial tensile strength (e.g. Brazilian Tensile Strength) of a cylindrical rock sample, which is stressed under a linear compressive load. The cylindrical specimen is loaded radially by applying compressive forces between by two curved plates. By inducing this compressive force an indirect tensile stress is measured having a deformation in orthogonal direction. The uniaxial tensile strength of a rock sample is determined by the maximum load applied at the point of failure

$$\sigma_t = \sigma_{bts} = \frac{2 \cdot F_b}{\pi \cdot D_s \cdot t_s} \tag{2.37}$$

Where F_b is the applied load at failure, D_s the rock sample's diameter and t_s the thickness or length of the sample. Failure of the cylindrical specimen is visually observed by vertical fractures over the radial axis, splitting the rock in half. The International Society for Rock Mechanics developed a suggested method for determining the indirect tensile strength of a rock material by executing the Brazilian Split Test. Figure 2.15a shows a basic test setup for doing such experiments. The setup consists of a hydraulic cylinder, mounted to a load cell, which applies pressure to the rock its outer surface. Normally bi-axial strain gauges are being used to measure the strain of the material in two directions. As a result of the load being applied, a compressive strain in vertical direction and tensile strain in horizontal direction, perpendicular to the longitudinal axis, will occur. According to the ISRM (Bieniawski and Hawkes [18]) it is stated these kind of tests are based on the experimental fact that most rocks, in biaxial stress fields, fail in tension at their BTS value. This occurs when one principal stress is tensile and the other principal stress is compressive. The ISRM indicates that the magnitude of the compressive principal stress may not exceed three times the tensile principal stress.

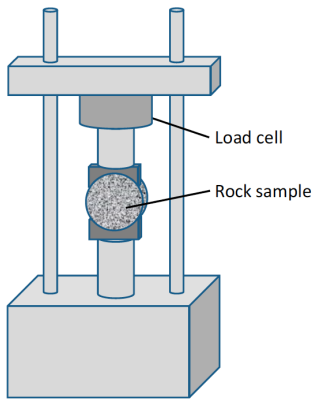

(a) Schematic overview of BTS setup Mwanga *et al.* [19]

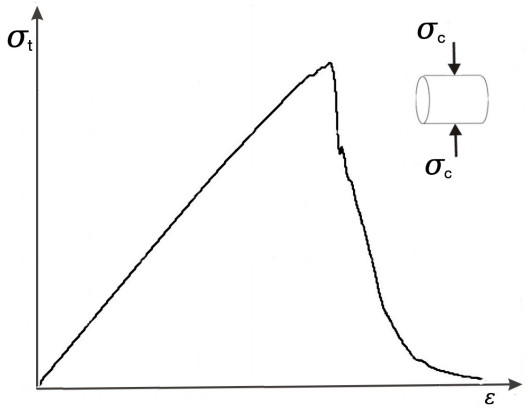

(b) Typical stress-strain curve of a BTS test

Figure 2.15: Schematic and graphical representation of BTS test

2.9.3. ROCK INDENTATION HARDNESS TEST

Rock indentation experiments are mainly done to classify and characterize rock samples in terms of hardness. In practice this characterization could be very useful to predict the cuttability or drillability of rock formations. The rock area that is available for indentation has to be horizontally flat, so the indenter will penetrate the rock specimen perpendicularly. During testing, a conical indenter penetrates the rock sample under an applied load, creating a crater in the surface. Conform the ISRM Suggested Method for Determining the Indentation Hardness Index of Rock Materials (Szwedzicki [20]), a loading device has to be used that can measure the failure load to an accuracy of approximately 1%, independently of the material that has been used. Furthermore, the apparatus has to consist out of two platens; a lower one, which is considered as the horizontally flat base platen and an upper platen which should be a conical indenter having a 60° cone and 5mm radius spherical tip. A proposed test procedure can be found in the ISRM standard Szwedzicki [20]. This procedure describes the standard loading rate for the hydraulic press, type of cementing agent, which is the plaster in figure 2.16, requirements for molding the cored rock sample in a fixed position, limitation criteria for termination of the test and a sequence of logging various data sets.

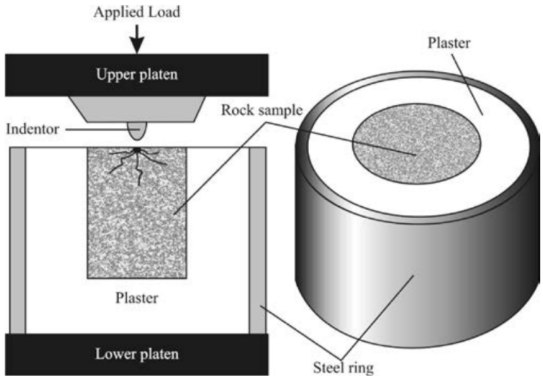

Figure 2.16: Schematic setup of an indentation apparatus (Yagiz *et al.* [21])

To gain more insight in the physical process during these indentation tests, a distinction can be made between three consecutive phases. The identification of these phases is visualized by a load-penetration curve, showing the applied load with corresponding penetration of the indenter. In *Phase 1* the applied load is proportional to penetration in the rock sample. The rock shows elastic deformation and very fine crushing of the rock surface. *Phase 2* can be seen as the transition zone where the elastic behaviour of the rock transforms to an irreversible deformation state (e.g. plastic). From a physical perspective this plastic deformation can be seen as crushing of the rock fabric. Within *Phase 3* cracks propagate to the rock surface, leading to chipping. For determining the Indentation Hardness Index (IHI) only the linear elastic region is being considered, where the maximum applied load $[p_i]$ and its corresponding penetration depth $[h_p]$ is used.

$$IHI = \frac{p_i}{h_p} \tag{2.38}$$

A classification of rock hardness on indentation tests was proposed by Szwedzicki [20]. He executed multiple indentation tests, using a wide range of rock types. Table 2.2 shows various rock sample classifications having a certain IHI range.

Rock sample classification	Indentation Hardness Index $[\frac{N}{mm}]$
Extremely hard	>50
Very hard	40-50
Hard	30-40
Moderately hard	20-30
Moderately soft	20-25
Soft	15-20
Very soft	8-15
Extremely soft	<8

Table 2.2: Rock hardness classification based on indentation testing (Szwedzicki [20])

3

EXPERIMENTAL CONFIGURATION

The linear rock cutting experiments are conducted in the research lab of the National Engineering Research Center of Dredging, based in Shanghai. The lab is equipped with a 118x9x4m [LxWxH] water flume that consists out of three main sections: *the grab test area*, *drag suction test area* and a *trailing suction test area*, as seen in figure 3.1. This last area is used for the linear rock cutting experiments. The test setup consists a movable platform that manages all the controls and can set the parameters of each cutting experiment. This control platform is driven by a set of winches, moving on a 3 meter high positioned rail track. This unidirectional movement is used to account for the cutting direction at a certain desired velocity. The platform is equipped with a hydraulically controlled rod, which is connected to the cutting tool. This rod can be set to a desired cutting depth and cutting angle, all controlled by an operator in the control room of the platform. The cutting forces, due to these preset conditions, are all measured and logged by pressure sensors. By accurately measuring these forces, existing linear cutting models can be analyzed, compared, expanded or even give insights into other modelling methods for predicting these forces.

The experiments focus on two types of rock; sandstone and artificial rock (e.g. concrete). Both rock types have different strength properties, making it possible to analyze both cutting processes, separately. All tests are being carried out under atmospheric conditions, meaning that the rock samples will not be saturated. Performing tests in saturated conditions is only interesting when cavitation can occur. This can only be achieved when having very high cutting velocities or hyperbaric conditions. Cavitation can therefore have major impact on the cutting process, making it a much more complicated problem.

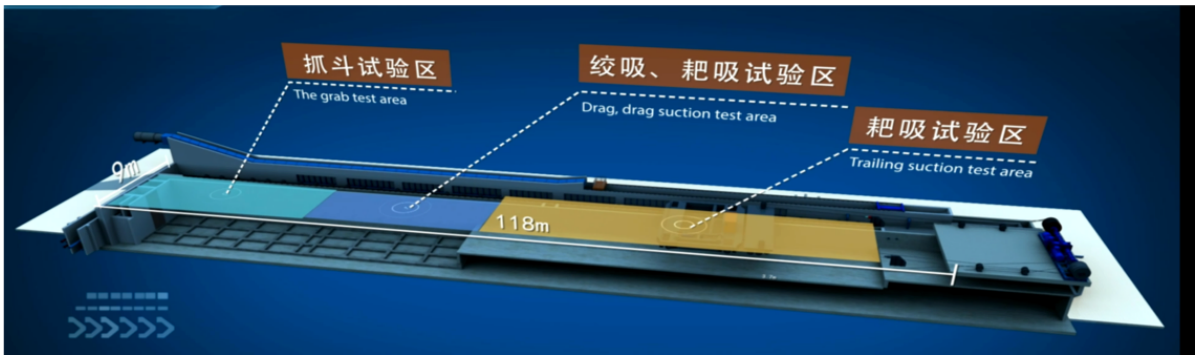

Figure 3.1: Overview water flume

3.1. CUTTING TOOL CONFIGURATION

The aim of this research is to obtain cutting force data by setting certain test parameters. To get a physical insight on how the cutting forces behave under different conditions, a broad collection of data sets should be obtained, analyzed and compared. To do this, the preset test parameters should be varied before each test. For this research the cutting angle α_c and cutting depth h_c are the main parameters that are being varied. Figure 3.2a shows the cutting tool configuration that is being used for the linear rock cutting experiments, which consists out of four main components. The pick-point (1) is a modular mountable tooth that can be changed at any time. It is installed on a steel mount (2) that supports the pick-point under an angle of $\gamma_p = 35°$. To measure the force data, two load sensors (3) are installed on the steel mount. As one of the objectives is to analyze the behaviour of the cutting forces and specific energy at deeper cutting depths, the force capacity should be sufficiently large. It is expected that the cutting forces become significantly large when increasing the cutting depth. This is the reason why two sensors are being used, instead of one. Both load sensors have a different loading capacity and mounted in such a way that the sensor with the highest capacity is closest to the pick-point. Figure 3.2b shows the load sensor configuration and corresponding free body diagram, due to the resulting cutting forces. It must be noted that the horizontal cutting forces will be a function of the axial measured forces of both sensors (e.g. Z^+/Z^-). The output of the resulting vertical cutting forces will be given by the measurements in X^+/X^--direction. The direction of the lateral cutting forces F_{cy} coincide with the Y-direction.

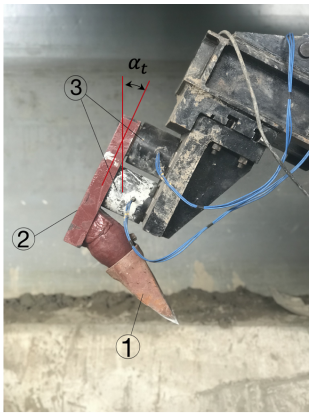

(a) Numbered components of cutting tool configuration

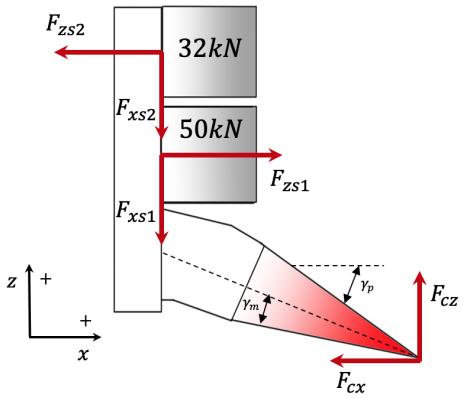

(b) Force balance cutting tool

Figure 3.2: Overview of cutting tool configuration

A force balance can be constructed to calculate the resulting cutting forces in X-,Y- and Z-direction. It must be noted that the force balance in both directions has been constructed according to the output signals of the sensors. To clarify this, for example, F_{zs2} has a positive force output, whereas F_{zs1} gives a negative output. To determine the resultant force in this direction, both forces simply need to be added to each other. The same holds for the measured forces in different directions. The pickpoint (1) itself has a fixed angle γ_p of 35°, relative to the steel mount (2), as in figure 3.2a. By incorporating both fixed angles, the measured forces can be calculated and converted to the desired cutting angle. The top angle α_t, which determines at which angle the force is acting on the sensors, is calculated according to: $\alpha_t = \alpha_c$ - γ_p.

$$\Sigma F_x = 0 \tag{3.1}$$

$$-F_{cx} - cos(\alpha_c - \gamma_p) \cdot (F_{zs1} + F_{zs2}) + sin(\alpha_c - \gamma_p) \cdot (F_{xs1} + F_{xs2}) = 0 \tag{3.2}$$

$$F_{cx} = -cos(\alpha_c - \gamma_p) \cdot (F_{zs1} + F_{zs2}) + sin(\alpha_c - \gamma_p) \cdot (F_{xs1} + F_{xs2}) \tag{3.3}$$

$$\Sigma F_z = 0 \tag{3.4}$$

$$-F_{cz} - sin(\alpha_c - \gamma_p) \cdot (F_{zs1} F_{zs2}) - cos(\alpha_c - \gamma_p) \cdot (F_{xs1} + F_{xs2}) = 0 \tag{3.5}$$

$$F_{cz} = -sin(\alpha_c - \gamma_p) \cdot (F_{zs1} + F_{zs2}) - cos(\alpha_c - \gamma_p) \cdot (F_{xs1} + F_{xs2}) \tag{3.6}$$

3.2. LOAD SENSOR

To measure the forces due to the interaction of the cutting tool with the rock, two three-component load sensors are used. This means that the forces are being measured in X-,Y- and Z-direction. Table 3.2 shows the loading capacity of the sensors in all directions. The load sensors both use a strain gauge which is deformed by the applied load. This deformation of the strain gauge is measured in $X^{+/-}$-,$Y^{+/-}$- and $Z^{+/-}$-direction as its electrical resistance changes. The output is given in microVolt(uV), using a measuring frequency of 200Hz. All measuring directions (X,Y and Z) are separately connected to a digital dynamic strain meter and a laptop. By using a Waveform display software (WF-7630) the electrical output from the load sensor can be visualized in a time-microVolt plot. The conversion of microVolt [μV] to force [N] can be calculated according to equation 3.7

$$F_{applied} = \frac{F_{capacity}}{K_{sensitivity} \cdot E_{total}} \cdot E_{measured} \tag{3.7}$$

Where $F_{applied}$ is the applied load [N], $F_{capacity}$ the capacity of the sensor [N], E_{total} total voltage of the sensor, $E_{measured}$ measured voltage [uV] and $K_{sensitivity}$ the sensitivity factor per direction [-]. The sensitivity factors differ per direction (K_{X_s}, K_{Y_s} and K_{Z_s}) and must be entered in formula 3.7 separately per direction (Table 3.1).

$F_{capacity}$	K_{X_s}	K_{Y_s}	K_{Z_s}	E_{total}
50 kN	0.55	0.305	0.68	2V
32 kN	0.8	0.46	0.44	2V

Table 3.1: Sensor load capacity, sensitivity coefficients in X-,Y- and Z-direction and total voltage

The capacity of the load sensors are identical for all directions of loading, as seen in table 3.2. Figure 3.3 shows a top view of the 50kN load sensor with its axis orientation. Table 3.2 shows the measuring capacity of both load sensors, as in figure 3.2. Whereby the sensor with the highest load capacity (**KD43050K**) is mounted in the lower position. Sensor **KD43032K** is placed in the upper position of the cutting tool configuration.

Sensor Type	F_x	F_y	F_z	M_x	M_y	M_z
KD43050K	± 50 kN	± 50 kN	± 50 kN	± 25 kNm	± 25 kNm	± 25 kNm
KD43032K	± 32 kN	± 32 kN	± 32 kN	± 16 kNm	± 16 kNm	± 16 kNm

Table 3.2: Capacity of both sensors in all measuring directions

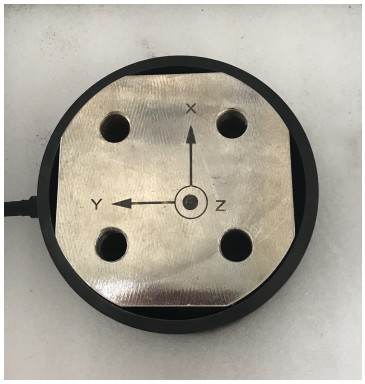

Figure 3.3: Load sensor type: KD43050K

3.3. PICKPOINT

The modular tooth that is cutting the rock specimens is called the pick-point. The pick-point is made of hard carbon steel to keep any damage or formation of wear at a low level. If any visible damage or wear that might influence the cutting process is developing on the tooth, the unit can be replaced or repaired. The tooth is fitted on the steel structure, after which it is secured by a steel pin to avoid any undesired movements during cutting. Before testing a check will be done to make sure that there is no tolerance between the tooth and structure. Figure 3.4a and 3.4b show a side and front view of the pick-point, respectively.

Most existing theoretical force prediction models are based on a pick-point that has a perfectly sharp tip. To compare these theoretical models with the experimental results, it was decided to grind the tip of the pick-point as sharp as possible. This parameter will contribute to the validation and/or modification of existing models or development of a new theory. Table 3.3 shows the dimensions of the pick-point after grinding took place.

Symbol	Description	Value	Unit
w	Tip width	17	mm
$\gamma_{m,2}$	Pickpoint angle	32	°
l_t	Tip length	70	mm

Table 3.3: Dimensions of pick-point

(a) Side view pick-point

(b) Front view pick-point

(c) Grinded pick-point tip

Figure 3.4: Overview of cutting tool configuration

3.4. CONCRETE TEST PIT

Within the water flume a concrete pit is dug where all rock cutting experiments are executed. Figure 3.5 shows the test setup and location of this concrete pit. All concrete and sandstone samples were placed on a level, steel transition piece, which is molded in the concrete pit. To avoid any undesired movements during testing, all (artificial) rock samples were secured by multiple clamps on the outside of each block (figure 3.5b).

(a) Concrete sample in place on transition piece

(b) Sandstone sample in place and clamped (T.Rutten [11])

Figure 3.5: Overview of concrete pit, including place (artificial) rock samples

4

EXPERIMENTAL PHASE

4.1. PRELIMINARY DATA ACQUISITION

Before going into the experimental phase of the actual linear rock cutting tests, the properties of two rock compositions have to be obtained, namely: sandstone and artificial rock. For both rock formations multiple UCS, BTS, Indentation and friction tests have to be executed. A distinction is to be made between the two, because the behavior of a high strength rock (sandstone) and relatively low strength composed material (artificial rock) will be significantly different during the rock cutting tests. The sandstone rock samples have been cut by the Yunnan Shihui Stone Co., Ltd obtained from a quarry in the Yunnan province of China. Nine rock pieces were cut into plates and transported to the Yunnan Institute of Product Quality Supervision & Inspection to test whether the rock meets its required property values. These requirements were predetermined by the Yunnan Institute. It is assumed that the rock pieces are homogeneous, meaning that it is uniform in composition. The requirements and outcomes of the general rock property tests are given in table 4.1. As the strength parameters of the rock samples are not exactly the same, the properties of each plate will differ from one another. To obtain accurate measurements during the rock cutting tests, each sample is to be tested separately. T.Rutten [11] partially tested the available rock samples, leaving four samples for this research. Each rock plate has an approximate size of 210x53x12cm (LxWxH). Due to dimensional limitations of the concrete pit, where each rock sample is to be fixed in place, all plates will be cut in half over length to make it suitable for the cutting experiments. The approximate size of the rock plates used for the experiments is 105x53x12cm (LxWxH).

Tested criteria	Required	Tested value	Unit
Density	≥ 2.00	2.34	$\frac{g}{cm^3}$
Water content	≤ 8.00	2.80	%
Compressive strength (dry)	≥ 12.60	36.00	MPa
Compressive strength (saturated)	≥ 12.60	49.00	MPa
Bending resistance (dry)	≥ 2.40	5.40	$N \cdot mm$
Bending resistance (saturated)	≥ 2.40	3.90	$N \cdot mm$
Water resistance	≥ 2.00	10.00	$\frac{1}{cm^3}$
Radionuclide limit	-	0.31	
Radionuclide limit	-	1.07	

Table 4.1: Tested rock properties delivered by Yunnan Institute of Product Quality Supervision & Inspection

To gain more insight in the physics of rock cutting it was decided to also conduct experiments on rock that has a strength <10MPa. In practice it is hard to sample low strength rock from a quarry without any irregularities in the microstructure. To mimic low strength sandstone rock, several concrete blocks in multiple batches were fabricated by CCCC itself. The concrete is composed out of three basic components: cement, small particle-sized gravel and water. Whereby cement works as a binding agent when it is mixed with the other two components. All compounds are combined in a mixer, where after it is poured in a 100x52x21cm (LxWxH) mold. When being poured, the mixed material is in a fully saturated condition. After pouring, the moulds are vibrated to remove trapped air bubbles. If the dried cement contains a lot of air bubbles, a significant strength degradation or

non-uniform strength profile over the complete volume of the block, may be a consequence. To obtain a more or less constant stress level in the concrete blocks, all specimens had to dry for at least thirty (30) days in a low-level humidity chamber. As mentioned before, the strength properties of the two different rock formations have to be determined by performing UCS, BTS and indentation tests. All tests have been executed at the Geotechnical Engineering depart of the Tongji University, Shanghai. In total 89 UCS, 88 BTS and 92 indentation tests were performed for the concrete samples. In total 4 UCS, 4 BTS and 2 indentation samples were taken from 24 blocks, divided over four different batches. Each concrete batch is named after its production date. The UCS and BTS experiments for the sandstone samples have already been executed by T.Rutten [11].

4.1.1. UNIAXIAL COMPRESSIVE STRENGTH TEST RESULTS

For the UCS tests three cylindrical samples have been cored from the sandstone specimens and five core samples have been taken from the artificial rock blocks. Because the artificial rock has been made by human expertise, the doubt exists that the desired UCS value will deviate too much from the experimental results. By testing more samples, the convergence of the final UCS value of an arbitrary block will determine if it is usable or not. Conform the ISRM standard Bieniawski and Bernede [22], the test specimens are straight cylinders, having a length to diameter ratio of 2.0. The surface of the cylinder its circumference and loading area is free from irregularities. Each cylindrical rock specimen is axially loaded until failure. During the process the applied force and corresponding deformation is measured. To visualize this behavior in a graphical sense, a stress-strain curve can be plotted.

ARTIFICIAL ROCK

Figure 4.1a shows the UCS test result of concrete sample *B3.2*, obtained from batch *7-11*. The batch indication of *7-11* stands for the production date of the concrete blocks. Seen from the yellow dashed line, one major failure plane is clearly visible. Furthermore, the cylindrical specimen also shows a minor tensile failure plane, which is not dominant in the failure process, as the crack does not propagate completely to the outer ends of the cylinder. In total 89 cored concrete samples have been tested, which were obtained from 24 blocks. As the desired Uniaxial Compressive Strength of the material is <10MPa, not all blocks were suitable for use. Some samples, cored from the same block, showed a strength that deviated too much to obtain reliable results during the rock cutting tests. A strength deviation of $\pm 10-15\%$ was set to be allowed between the cored samples of a specific block. Figure 4.1b displays the stress-strain diagram of three different UCS samples, cored from the same block. The UCS values of the consecutive tests are: $UCS_{B3.2}$ = 6.51 MPa, $UCS_{B3.3}$ = 7.54 MPa, $UCS_{B3.4}$ = 7.22 MPa. During the analytical phase of the rock cutting data, a representative UCS value of each block should be used. To do that, the mean value of the combined tests per block has to be taken. For $7-11-B3$ this is: UCS_{B3}=7.09 MPa. A selective procedure is to be carried out for the usability of certain blocks during the rock cutting experiments. The experiments that show significant strength deviations between samples of the same block, are not being further used.

During this test phase, two failure patterns were clearly dominating the results: axial splitting and single plane shearing. These types of failure are most common for rock formations that show brittle behavior. During axial splitting, micro cracks propagate parallel to the direction of maximum far field compression. Single plane shearing happens non-parallel to the loading direction. For both failure modes holds that crack initiation occurs by the amount energy that is put in the rock by the system. As the crack propagates, energy dissipates and will converge to zero when the crack fully extends to the rock its surface.

Sample property	Symbol	Value	Unit
Diameter	D_{csu}	0.055	m
Length	L_{csu}	0.11	m
Area	A_{csu}	0.0024	m^2
Unit weight	ρ_{csu}	2025	$\frac{kg}{m^3}$

Table 4.2: Dimensions of the cylindrical concrete samples used for UCS tests

Where D_{csu} is the diameter of the concrete sample that was used during the UCS test and L_{csu} the length of the cylindrical specimen. The corresponding cross-sectional area of the concrete sample is referred to as A_{csu}.

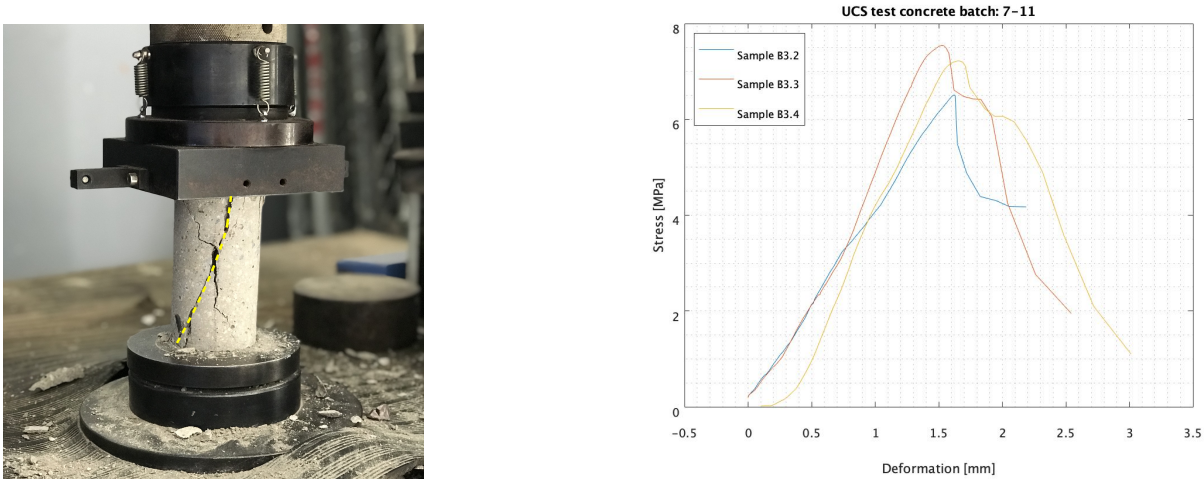

(a) Visible single shear plane failure of concrete sample

(b) Outcomes UCS test 7-11-B3 (sample 2,3,4)

Figure 4.1: Failure path and UCS results of batch 7-11-B3

SANDSTONE

In total twelve samples, cored from four blocks, have been loaded until failure. Figure 4.2a shows the axial splitting failure path of a cored sample of block 4, meaning that the rock specimen exceeded its yield strength due to the axially applied load. The mode of failure can be explained by the fact that under low or zero confining pressure rock usually fails along a single shear plane or due to axial splitting. As for the sake of the cutting experiments only the atmospheric pressure is considered, so the confining pressure on the specimen can be neglected. All other tests showed similar failure behavior; either failing along a single shear plane or split axially.

Sample property	Symbol	Value	Unit
Diameter	D_{rsu}	0.055	m
Length	L_{rsu}	0.11	m
Area	A_{rsu}	0.0024	m^2
Unit weight	ρ_{rsu}	2276	$\frac{kg}{m^3}$

Table 4.3: Dimensions of the cylindrical rock samples used for UCS tests

Where D_{csu} is the diameter of the rock sample that was used during the UCS test and L_{csu} the length of the cylindrical specimen. The corresponding cross-sectional area of the rock sample is referred to as A_{csu}.

Figure 4.2b shows the combined stress-strain curve of three cored sandstone cylinders of sample 4. The maximum force that a cylindrical specimen can resist before plastic shear failure is visible, is called the UCS value. In a graphical sense this is the point of zero change in stress. The outcomes of the Sandstone sample 1 test are as follows: $UCS_{4.1}$=13.05 MPa, $UCS_{4.2}$=19.64 MPa and $UCS_{4.3}$=12.75 MPa. To use a representative UCS value for the rock cutting tests, the mean value of the cored samples is taken of each rock sample; UCS_4= 15.15 MPa.

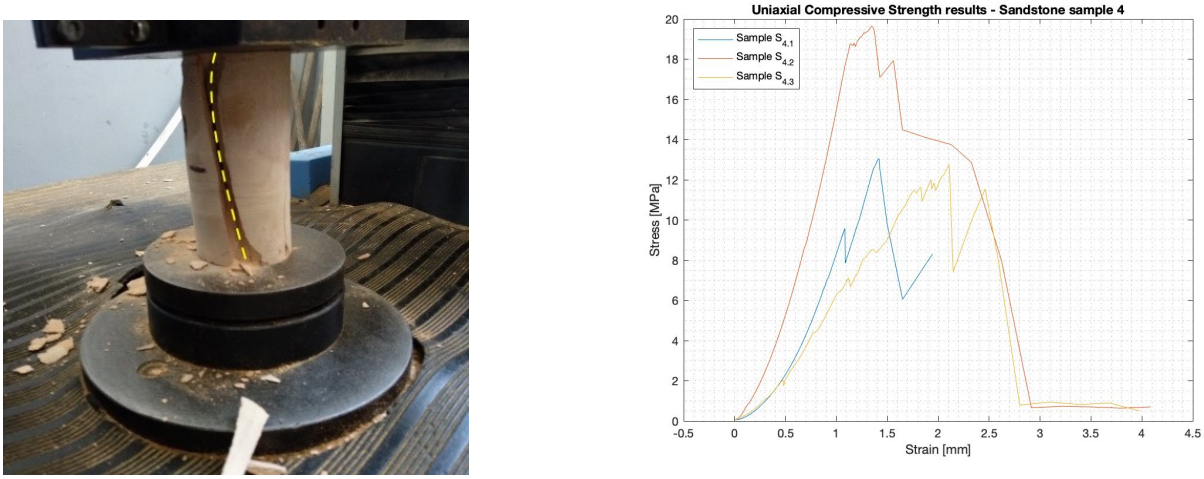

(a) Visible shear failure of the cylindrical rock sample Sample 4.3

(b) Stress-strain curve UCS test Sandstone sample 4

Figure 4.2: UCS test of sandstone rock samples at Tongji University

4.1.2. BRAZILIAN TENSILE STRENGTH TEST RESULTS

Similar to the cored samples for the UCS tests, three cylindrical test specimens have been cored from the sandstone samples and concrete blocks. The length to diameter ratio of the cylindrical sample used in the BTS test differs from the ones used in the UCS test. Conform the Bieniawski and Bernede [17] standard, the $\frac{L}{D}$ ratio is one (1). The surface of the cylinder its circumference, which is its the loading face, is free from irregularities. The drilled cores are loaded radially with compressive forces between two curved clamps, which give an indirect tensile stress and corresponding deformation in orthogonal direction. Both forces and strain data are logged and to be plotted in a stress-strain curve. Prior to the experiments, a strength deviation range of 20-25% was set between the BTS values each cylindrical sample of the same block. If strength difference of the highest and lowest value falls outside this range, the block in question is not used for further experiments.

ARTIFICIAL ROCK

By assuming that the structure of the concrete samples is isotropic and continuous, the BTS value of each specimen can be determined by equation 2.37, which uses the theory of elasticity. The theory of elasticity uses the fact that a solid material is able to regain its original shape, after it is loaded. This is until the point of failure. Figure 4.3a shows a typical failure path of a BTS test, which was observed every single experiment. For maintaining consistency in the analysis of the concrete properties, sample *B3.2*, obtained from batch *7-11*, is used again. As seen from figure 4.3b the stress-strain relationship of the rock is linear until the point of failure, which means that the elasticity theory is applicable. The BTS values of the consecutive tests are: $BTS_{B3.1}$ = 1.14 MPa, $BTS_{B3.2}$ = 1.29 MPa, $BTS_{B3.3}$ = 1.13 MPa. It is seen that sample $B_{3.1}$ and $B_{3.3}$ have a slightly lower strength capacity than sample $B_{3.2}$, but all experiments show similar behavior. The BTS value of sample $B_{3.2}$, can be explained by the production process of the concrete batches. During fabrication process air bubbles arise when molding the each individual batch. Because it is quite challenging to remove all the air entrapments out of the liquid composition, an uneven stress distribution over the complete volume of the material will be the result. This also explains why a strength deviation range was set, before doing the experiments.

Sample property	Symbol	Value	Unit
Diameter	D_{csb}	0.055	m
Length	L_{csb}	0.055	m
Area	A_{csb}	0.0024	m^2
Unit weight	ρ_{csb}	2025	$\frac{kg}{m^3}$

Table 4.4: Dimensions of the cylindrical concrete samples used for UCS tests

Where D_{csu} is the diameter of the concrete sample that was used during the BTS test and L_{csu} the length of the cylindrical specimen. The corresponding cross-sectional area of the concrete sample is referred to as A_{csu}.

(a) Visible central splitting of sample $7-11-B3$ due to tensile stresses

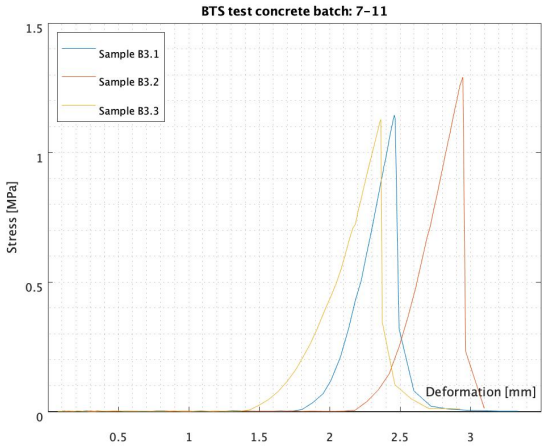

(b) Stress-strain curve of BTS test $7-11-B3$

Figure 4.3: BTS test of concrete samples at Tongji University

SANDSTONE

The compression that is induced on the rock sample shown in figure 4.4a generated a central extensional fracture path over its diametral plane. Although the failure path of the sandstone sample looks the same as the concrete BTS test, it acts differently when it cracks. During the BTS test of the sandstone, crack propagation over time was too fast. The crack immediately splitted the rock when the maximum allowable stress was reached. From figure 4.4b it can graphically be seen that the fracture toughness of the sandstone samples are significantly higher than the concrete samples (4.3a). This can be derived from the evolving deformation due to the applied loading rate. The BTS values of the consecutive tests are: $BTS_{4.1}$ = 2.52 MPa, $BTS_{4.2}$ = 1.26 MPa, $BTS_{4.3}$ = 1.43 MPa.

Sample property	Symbol	Value	Unit
Diameter	D_{rsb}	0.055	m
Length	L_{rsb}	0.055	m
Area	A_{rsb}	0.0024	m^2
Unit weight	ρ_{rsb}	2276	$\frac{kg}{m^3}$

Table 4.5: Dimensions of the cylindrical rock samples used for BTS tests

(a) Visible central splitting of sample 4 due to tensile stresses

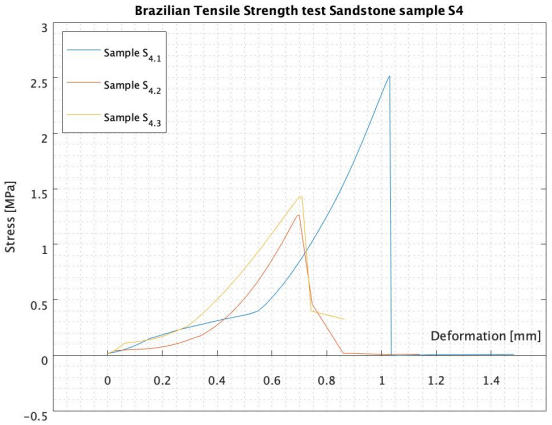

(b) Stress-strain curve of BTS test sandstone sample 4

Figure 4.4: BTS test of sandstone rock samples at Tongji University

4.1.3. INDENTATION HARDNESS TEST RESULTS

To characterize the hardness of the concrete and sandstone, indentation tests are performed. The test procedure is in line with the ISRM Suggested Method for Determining the Indentation Hardness Index of Rock Materials Szwedzicki [20], which is explained in 2.9.3. The main purpose of these tests is to investigate if it is possible to approximate the stress level in the crushed zone. The Indentation Hardness Index is determined by equation 2.38, where p_i is the maximum applied force by the conical indenter within the linear elastic region of the rock. Conform the recommended standard, the test is performed until a distinct crater of 1mm is formed, by applying a loading rate of 0.15 kN/s (Szwedzicki [20]). To make sure the end of the linear elastic region is within measurement bounds, force data is logged until a penetration depth of approximately 1.5mm is reached.

ARTIFICIAL ROCK

Figure 4.5a shows the test configuration used for the indentation tests. Each concrete sample is moulded into a steel frame, by using a high grade plaster. The casin ensures a confining stress on the circumferential surface of the cylinder, preventing potential axial splitting of the sample. Figure 4.5b displays the indentation test results of sample $B3$ of the $7-11$ batch. From the graph it is observed that the load-penetration curve is still within the linear-elastic regime. This means that the transition from crushing to chipping is not visible in a graphical sense. Due to this unsatisfactory result, it might be quite difficult to determine the stress level within the crushed zone. Though, the Indentation Hardness Index can be determined by calculating the gradient of the linear-elastic regime.

(a) Configuration concrete indentation test

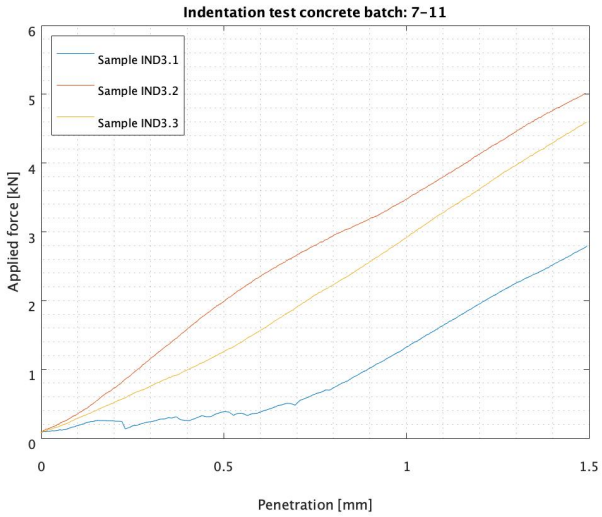

(b) Force-penetration curve of $7-11-B3.2$

Figure 4.5: Test setup and results of concrete indentation tests

Sample	IHI_{mean}	Unit
$7-11-B_3$	2.31	$\frac{kN}{mm}$
$7-11-B_2$	2.86	$\frac{kN}{mm}$
$7-11-B_5$	2.07	$\frac{kN}{mm}$
$7-11-B_4$	2.81	$\frac{kN}{mm}$
$7-11-B_6$	2.84	$\frac{kN}{mm}$

Table 4.6: Results Indentation Hardness Index experiments - artificial rock

SANDSTONE

Figure 4.6 shows the sandstone sample S_4 indentation results, where five individual samples were tested. It is clearly seen that sample $IND_{4.5}$ exceeded the linear-elastic capacity of the rock, meaning that fine crushing transitioned to chipping. It must be noted that not all of the samples reached this stress state. Despite the suggested method by Szwedzicki [20], which has been kept as reference, the penetration depth of the cone was still insufficient.

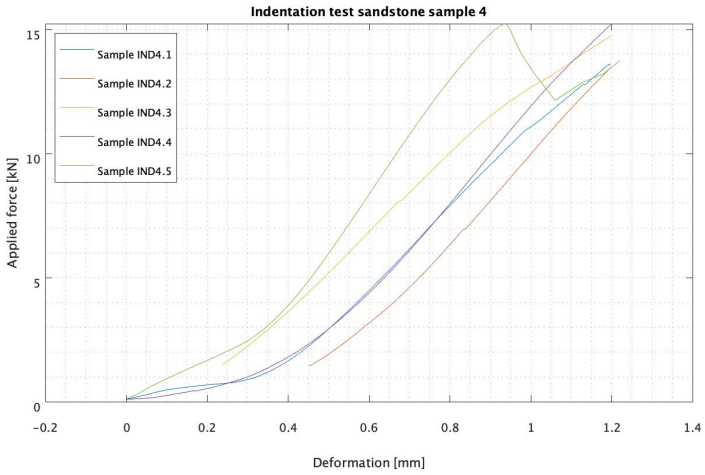

Figure 4.6: Indentation results sandstone sample 4

Sample	IHI_{mean}	Unit
S_1	15.22	$\frac{kN}{mm}$
S_2	15.22	$\frac{kN}{mm}$
S_3	12.76	$\frac{kN}{mm}$
S_4	11.33	$\frac{kN}{mm}$

Table 4.7: Results Indentation Hardness Index experiments - sandstone

4.1.4. TEST RESULTS ROCK PROPERTIES

In total ten concrete and four sandstone blocks will be used for the rock cutting experiments. Before entering this experimental phase, all blocks have been tested separately conform the above mentioned test methods. To complete the desired collection of rock properties, three additional parameters have to be determined, namely the cohesion c, internal friction angle ϕ' and external friction angle δ'. These parameters can be calculated by applying the Hoek-Brown failure criterion Hoek and Brown [23]. This theory was derived from the research into brittle failure of intact rock by Hoek [24]. The generalized Hoek-Brown criterion is expressed as

$$\sigma_1' = \sigma_{ci} \cdot \left(m_b \cdot \frac{\sigma_3'}{\sigma_{ci}} + s \right)^a \tag{4.1}$$

Where σ_1' and σ_3' are the major and minor effective principal stresses at failure, respectively. Since the UCS and BTS experiments were conducted under atmospheric conditions, it is assumed that there is zero confining pressure applied on the rock specimen. This means that the minor effective stress σ_3' will be disregarded. Within equation 4.1 m_b and m_i are both material constants, where m_b is a reduced value of m_i. The constant m_i is an already known parameter, namely the brittleness of the material.

$$m_b = m_i \cdot e^{\frac{GSI-100}{28-14D_s}} \tag{4.2}$$

In equation 4.2 GSI is called the Geology Strength Index and is based on the discontinuities in the microstructure of a rock. For an intact rock formation GSI=100. D_s is the diameter of the cylindrical sample. The two other

material constants s and a from equation 4.1 are both empirically determined variables, where s=1 for intact rock formations.

$$s = e^{\frac{GSI-100}{9-3D}} \tag{4.3}$$

$$a = \frac{1}{2} + \frac{1}{6} \cdot \left(e^{\frac{-GSI}{15}} - e^{\frac{-20}{3}} \right) \tag{4.4}$$

When all stresses and material constant have been calculated, the effective internal friction angle ϕ' and the effective cohesion c' can be determined. Because the experiments are conducted under atmospheric conditions, the confining stress term σ'_3 can be neglected. By disregarding this term, the internal friction angle ϕ and cohesion c can be determined.

$$\phi' = sin^{-}1 \left[\frac{6 \cdot m_b \cdot (s + m_b \cdot \sigma_{3n})^{a-1}}{2 \cdot (1+a) \cdot (2+a) + 6 \cdot a \cdot m_b \cdot (s + m_b \cdot \sigma'_3 n)^{a-1}} \right] \tag{4.5}$$

$$c' = \frac{\sigma_{ci} \cdot [(1+2a) \cdot s + (1-a) \cdot m_b \cdot \sigma_{3n}] \cdot (s + m_b \cdot \sigma_{3n})^{a-1}}{(1+a) \cdot (2+a) \sqrt{\frac{1+(6 \cdot a \cdot m_b \cdot (s+m_b \cdot \sigma_{3n})^{a-1})}{(1+a) \cdot (2+a)}}} \tag{4.6}$$

To complete the desired collection of rock parameters, the external friction angle δ can be calculated according to

$$\delta = \frac{2}{3}\phi' \tag{4.7}$$

For accurately determining the to be used rock mass strength parameters, the software 'RocLab' is used. All equations related to the generalized Hoek-Brown failure criterion are implemented into this program, making it also an efficient tool to gather the data of the high number of tests. Though, it must be noted that, when looking very critical to the Hoek-Brown failure criterion, the actual internal friction angle may deviate from the calculated value. Hoek and Brown [23] indicates that the friction angle is determined by the UCS value of your rock specimen. The failure envelope is being drawn due to this single strength parameter. In reality this method will not give the exact value of your specimen's basic friction angle. The basic friction angle is defined as the angle that the rock resists itself due to shear failure. For the sake of simplicity, this theory and its outcomes will be applied for further use in this report. All properties of the various sandstone and concrete samples are found in table 4.8 and 4.9, respectively.

When applying the Hoek-Brown criterion with confining pressures, a more accurate value for the basic friction angle can be found. Because the experiments are conducted under atmospheric conditions, no confining pressures are present, meaning that the friction angle only depends on the UCS and BTS value of the rock specimen. This often results in a quite large friction angle. To partially account for this expected large friction angle, Barton and Choubey [25] applied a correction factor for the basic friction angle. Furthermore, from personal communication with X. Chen it is learned that the application of a correction of 20° to the internal friction angle is common when only the UCS and BTS values are known.

$$\phi_c = \phi - 20^\circ \tag{4.8}$$

4.1.5. YOUNG'S MODULUS

To measure the stiffness of a rock, the Young's modulus has to be determined. This mechanical property defines the relationship between the applied stress and corresponding deformation of the internal structure of the material within the linear elastic regime. The linear-elastic regime can be defined as the proportional relationship between the stress and strain. Equation 4.9 determines the Young's Modulus E.

$$E = \frac{F_A / A_s}{\Delta L / L_s} \tag{4.9}$$

Where F_A is the tensional force applied to the cylindrical specimen in axial direction, A_s the cross-sectional area of the sample, ΔL the amount at which the length of the cylindrical sample is changing and L_s its original length, which is kept as reference.

SANDSTONE

Sample number	UCS [MPa]	BTS [MPa]	IHI [kN/mm]	B [-]	c [MPa]	ϕ_c °	δ °	ρ_{cs} $\frac{kg}{m^3}$
$S_{1.1}$	32.17	1.81	15.10	17.76	4.40	41	27	2277.19
$S_{1.2}$	44.21	2.19	15.66	20.18	5.69	43	29	2263.55
$S_{1.3}$	20.18	1.82	14.79	11.08	2.84	40	27	2270.37
$S_{1,mean}$	35.59	2.06	15.22	17.24	4.44	44	29	2270.37
$S_{2.1}$	32.17	1.81	15.10	17.76	4.40	41	27	2277.19
$S_{2.2}$	44.21	2.19	15.66	20.18	5.69	43	29	2263.55
$S_{2.3}$	20.18	1.82	14.79	11.08	2.84	40	27	2270.37
$S_{2,mean}$	35.59	2.06	15.22	17.24	4.44	44	29	2270.37
$S_{3.1}$	25.61	1.54	13.75	16.60	3.62	40	27	2263.55
$S_{3.2}$	27.58	1.49	11.76	18.53	3.70	42	28	2270.37
$S_{3.3}$	25.73	2.63	12.69	9.77	4.62	33	22	2263.55
$S_{3,mean}$	26.27	1.89	12.76	13.91	4.02	38	25	2265.82
$S_{4.1}$	13.05	2.52	11.40	5.18	3.07	22	15	2331.73
$S_{4.2}$	19.64	1.26	11.11	15.57	2.86	40	26	2331.73
$S_{4.3}$	12.76	1.43	11.48	8.92	2.39	31	21	2311.28
$S_{4,mean}$	15.15	1.74	11.33	8.72	2.86	31	21	2324.91

Table 4.8: Tested strength parameters - Sandstone

ARTIFICIAL ROCK

Sample number	UCS [MPa]	BTS [MPa]	IHI [kN/mm]	B [-]	c [MPa]	ϕ_c °	δ °	ρ_{cs} $\frac{kg}{m^3}$
$7-11-B_{2.1}$	8.29	1.02	2.54	8.16	1.61	29	19	2025.76
$7-11-B_{2.2}$	8.65	0.90	2.56	9.62	1.56	32	21	2025.76
$7-11-B_{2.3}$	7.80	1.06	2.33	7.35	1.59	28	19	2025.76
$7-11-B_{2,mean}$	8.25	0.99	2.45	8.31	1.59	30	20	2025.76
$7-11-B_{2.1}$	6.51	1.14	2.49	5.69	1.47	24	16	2025.76
$7-11-B_{2.1}$	7.54	1.29	2.26	5.84	1.69	24	16	2025.76
$7-11-B_{2.1}$	7.22	1.13	2.17	6.41	1.56	26	17	2025.76
$7-11-B_{2,mean}$	7.09	1.19	2.31	5.97	1.57	25	16	2025.76
$7-11-B_{2.1}$	8.56	1.67	2.54	5.14	2.02	22	15	2025.76
$7-11-B_{2.1}$	9.08	1.10	2.68	8.28	1.76	30	20	2025.76
$7-11-B_{2.1}$	8.10	1.15	2.41	7.02	1.68	27	18	2025.76
$7-11-B_{2,mean}$	8.58	1.31	2.55	6.57	1.82	26	18	2025.76
$7-11-B_{2.1}$	7.40	0.95	2.22	7.80	1.47	29	19	2025.76
$7-11-B_{2.1}$	6.94	1.20	2.10	5.80	1.56	24	16	2025.76
$7-11-B_{2.1}$	6.94	1.45	2.09	4.79	1.68	21	14	2025.76
$7-11-B_{2,mean}$	7.09	1.20	2.14	5.92	1.57	25	16	2025.76
$7-11-B_{2.1}$	8.03	1.18	2.39	6.82	1.68	27	18	2025.76
$7-11-B_{2.1}$	7.22	1.59	2.17	4.54	1.80	20	13	2025.76
$7-11-B_{2.1}$	6.68	1.04	2.02	6.43	1.44	26	17	2025.76
$7-11-B_{2.1}$	7.55	0.91	2.26	8.33	1.45	30	20	2025.76
$7-11-B_{2,mean}$	7.37	1.18	2.21	6.25	1.59	26	17	2025.76
$7-11-B_{2.1}$	5.39	1.02	1.66	5.31	1.25	23	15	2025.76
$7-11-B_{2.1}$	4.80	0.90	1.49	5.34	1.11	23	15	2025.76
$7-11-B_{2.1}$	6.48	1.06	1.97	6.10	1.42	25	17	2025.76
$7-11-B_{2,mean}$	5.56	0.99	1.71	5.60	1.26	24	16	2025.76
$7-15-B_{2.1}$	7.19	1.05	2.16	6.85	1.51	27	18	2025.76
$7-15-B_{2.1}$	7.91	0.76	2.36	10.42	1.38	33	22	2025.76
$7-15-B_{2.1}$	7.98	1.03	2.38	7.74	1.59	29	19	2025.76
$7-15-B_{2,mean}$	7.70	0.95	2.30	8.13	1.49	30	20	2025.76
$7-17-B_{2.1}$	6.04	0.80	1.84	7.57	1.20	28	19	2025.76
$7-17-B_{2.1}$	5.97	0.94	1.82	6.34	1.30	25	17	2025.76
$7-17-B_{2.1}$	5.84	0.76	1.79	7.69	1.16	29	19	2025.76
$7-17-B_{2,mean}$	5.95	0.83	1.82	7.14	1.22	27	18	2025.76
$7-17-B_{3.1}$	5.28	0.96	1.63	5.52	1.21	23	15	2025.76
$7-17-B_{3.1}$	3.91	0.96	1.24	4.09	1.00	18	12	2025.76
$7-17-B_{3.1}$	3.82	0.88	1.21	4.32	0.96	19	13	2025.76
$7-17-B_{3.1}$	4.11	0.91	1.29	4.51	1.02	20	13	2025.76
$7-17-B_{3,mean}$	4.28	0.93	1.34	4.62	1.05	20	13	2025.76
$7-17-B_{5.1}$	8.03	0.74	2.39	10.88	1.37	34	23	2025.76
$7-17-B_{5.1}$	7.54	1.17	2.26	6.43	1.62	26	17	2025.76
$7-17-B_{5.1}$	7.01	0.84	2.11	8.31	1.35	30	20	2025.76
$7-17-B_{5.1}$	6.91	1.14	2.09	6.06	1.52	25	17	2025.76
$7-17-B_{5,mean}$	7.37	0.92	2.21	8.03	1.47	29	19	2025.76

Table 4.9: Tested strength parameters - Artificial rock

4.1.6. FRICTION TEST RESULTS

Friction between the cutting tool and rock may be of great influence on the cutting forces. To track down how many percent of the cutting power used is due to the frictional interaction between the tool and the rock, an accurate value of the dynamic friction coefficient is required. The aim is to obtain a convergent value for the dynamic friction coefficient between the rock and and hard alloyed steel of the pickpoint. This is done by doing scraping tests on each sandstone/concrete sample, using the cutting tool mounted on the actual linear rock cutting test setup. The scraping tests can be repeated as many times as desired, because no significant damage is caused on the microstructure by this contact. For obtaining a reliable friction coefficient of the tool-rock interface, a precut trench was made as in figure 4.7.

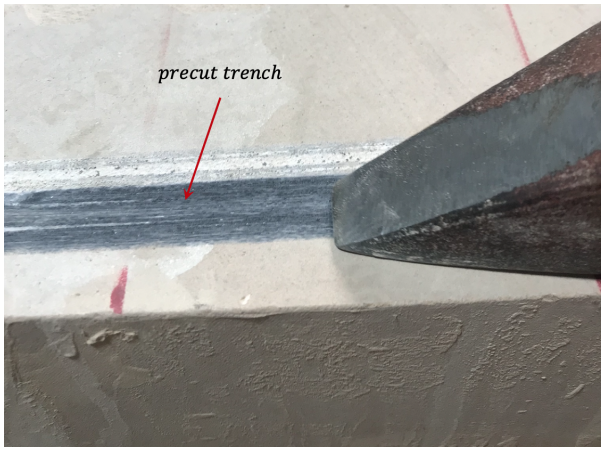

Figure 4.7: Visible precut sandstone trench used for friction tests

The available force measuring equipment is able to measure the forces in three directions. For these tests only, the normal force (F_N) and friction force, that is in line with its scraping trajectory (F_k), are to be considered. By knowing these two forces, the dynamic friction coefficient can be calculated according to

$$\mu_k = \frac{F_k}{F_N} \tag{4.10}$$

Where F_k is the horizontal frictional force, F_N vertically applied force to the rock's top interface and μ_d the dynamic friction coefficient.

For both the sandstone and concrete, five individual friction experiments were performed. Due to the fact that a large amount of concrete samples were made, it is assumed that the friction coefficient is more or less the same for all. This assumption also holds for the sandstone samples.

	μ_{k1}	μ_{k2}	μ_{k3}	μ_{k4}	μ_{k5}	$\mu_{k,mean}$
Sandstone	0.3713	0.346	0.3681	0.3777	0.349	**0.362**
Artificial rock	0.491	0.506	0.483	0.497	0.507	**0.497**

Table 4.10: Dynamic friction test results Sandstone and Artificial rock

The calculated dynamic friction coefficient of the sandstone seems to be a fairly well-approximated value. According to the Defence Nuclear Agency (Gaffney [26]) a common value for the dynamic friction coefficient between sandstone and steel is about μ_d=**0.39**. From measurements, the dynamic friction coefficient for concrete is slightly higher than for sandstone. Though, it must be noted that for the concrete it was difficult to only scrape the top interface, due to the fact that concrete has a lower strength than the sandstone. A small crushed zone formed in front of the blade and small chips were breaking out, leading to an undesired, excessive force in both X-, and Z-direction.

4.2. SENSOR CALIBRATION

Force measurements, resulting from the cutting process, is the most important data set to be obtained. To strive for high-accuracy measurements, it is crucial that the sensor is to be calibrated properly in all three directions (e.g. X,Y and Z). For each force direction, the goal is to align the applied force exactly with its axis, in positive and negative direction. To do this, a steel calibration frame was designed to obtain these pure loading conditions. The frame is designed in such a way that the X^+-, X^--, Y^+-, Y^-- and Z^--direction are able to be calibrated. Figure 4.8 shows the setup for testing the loading conditions in positive X-direction (X^+). A shackle interconnects the hook and the eye of the steel frame. The loading direction is exactly aligned with the coordinate system of the sensor and therefore obtaining pure loading in the desired direction. Four (4)loading directions can be tested with this configuration by axially rotating the sensor with 90°. Figure 4.9 display the side- and front view of loading the sensor in negative Z-direction (Z^-). The sensor is axially aligned with the loading direction.

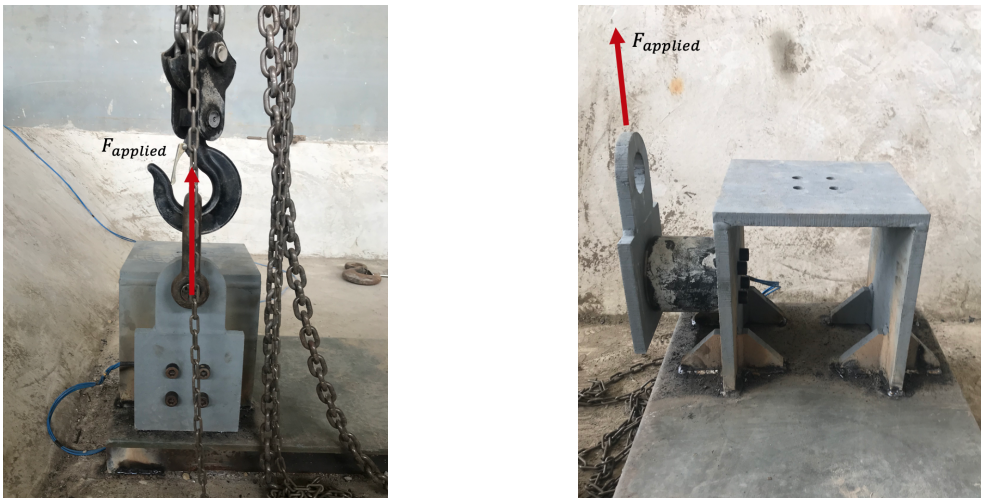

(a) *Sideview* **(b)** *Frontview*

Figure 4.8: Setup for sensor calibration in positive X-direction (X^+)

(a) *Sideview* **(b)** *Frontview*

Figure 4.9: Setup for sensor calibration in negative Z-direction (Z^-)

The load sensor is equipped with a strain gauge, which measures the strain within the sensor when it is loaded in positive or negative direction. The strain gauge uses a geometry dependent conductor that is stretched within its elasticity limits by using the physical property of electrical conductance. This means that the load sensor's output is in microvolts(uV), using a frequency of 200 Hz. To read out this voltage output during the calibration,

a digital dynamic strain meter is used. To log the sensor its behavior due to the applied load, a time-microvoltage graph is constructed.

The five directions were calibrated by increasing the applied load $F_{applied}$ in steps of 200kg to a limit of approximately 3000kg. This weight limit was chosen to exclude the failure risk of the concrete floor. As it is expected that the Force-Voltage relationship is linear, data can be extrapolated from 3000kg to its loading capacity. To compare the measured output voltage from the tests with the calibration requirements of the supplier, equation 3.7 is used again. By using the total voltage E_{total}, sensor capacity $F_{capacity}$, measured voltage $E_{measured}$ and sensitivity factors X_s,Y_s and Z_s from table 3.1, the to be examined sensor can be calibrated in the direction of interest. Figure 4.10 shows a linear relationship between the applied force $F_{applied}$ and the measured voltage $E_{measured}$ of two arbitrary calibration directions of the 50kN load sensor. Both figures show good correlation between the measured and calculated values. This proves that there is a linear relationship between the applied load and voltage output. This calibration method has been applied for both sensors in positive and negative X-,Y- or Z-direction.

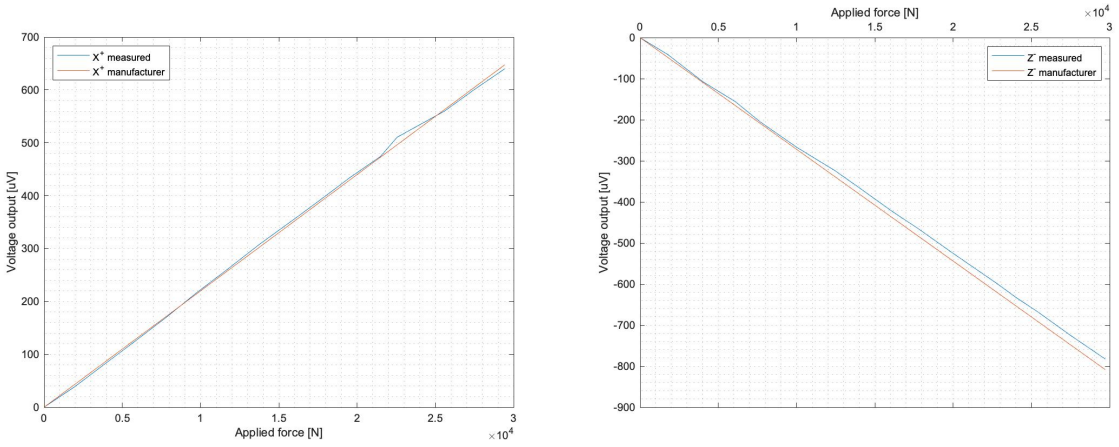

(a) Calibration in X^+-direction

(b) Calibration in Z^--direction

Figure 4.10: Calibration of 50kN

4.3. EXPERIMENTAL SEQUENCE

The experimental design of the test procedure has been visualized in a flow chart diagram, figure 4.11. This flow chart shows the experimental sequence of the tasks that have to be executed to successfully conduct the rock cutting experiments. All peripheral experiments, for obtaining the material properties of the (artificial) rock, have not been taken into account in this diagram, because these tests were not in line with the actual rock cutting experiments. For each experiment multiple input parameters had to be set, to comply with the desired cutting configuration. The duration of each experimental sequence, as in figure 4.11, was about 10 minutes, not incorporating the (artificial) rock block replacement. Normally, on both flat cutting interfaces on either side of the block, three cutting experiments were able to be conducted, depending on the preset cutting depth.

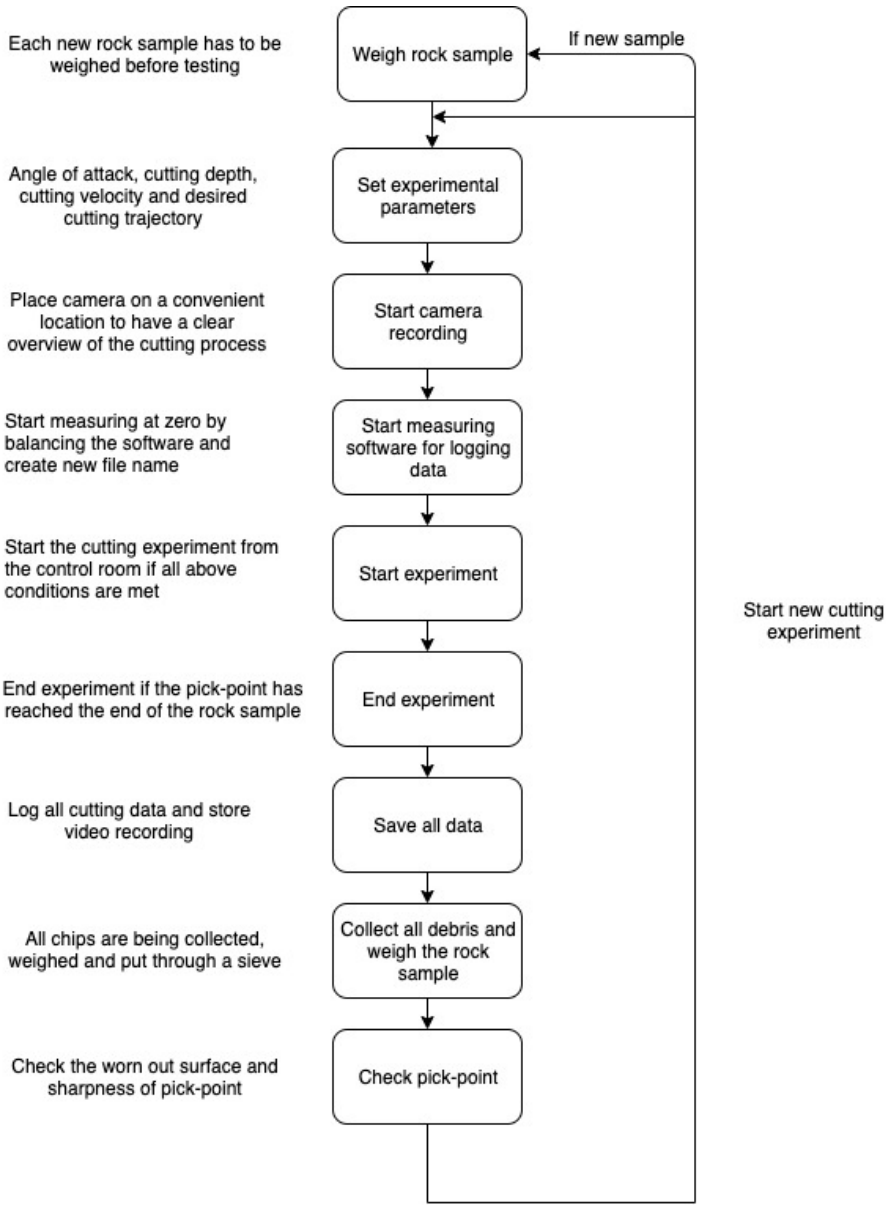

Figure 4.11: Flow chart of experimental sequence

4.4. EXPERIMENTAL PARAMETERS

One of the objectives is to examine the development of the cutting forces and specific energy by alternating the cutting depth h_c and angle α_c. To obtain a broad range of data, these input parameters were varied during every cutting experiment. Table 4.11 and 4.12 shows the preset alternating and fixed parameters of the concrete and sandstone cutting experiments, respectively. A distinction is made between experiments using a sharp and blunt pickpoint tip. Concerning the alternating parameters, it must be noted that different increments are being used. For the cutting angle an increment of 5° is applied. For the first step of the cutting depth an increment of 5mm is used, whereafter, for the continuation of the test procedure, an increment of 10mm. The cutting velocity v_c is being kept constant at 0.05m/s during every test. Table 4.11 and 4.12 show the parameter combinations that have been chosen to execute all cutting experiments. Appendix C.1 and C.2 elaborated more concisely on the various cutting depth and cutting angle increments of all experiments.

#	Alternating parameter	Range	Unit		Fixed parameter	Value	Unit	Tip
1	Cutting depth	5-40	mm	+	Cutting angle	40	°	Sharp
2	Cutting depth	5-40	mm	+	Cutting angle	45	°	Sharp
3	Cutting depth	5-40	mm	+	Cutting angle	50	°	Sharp
4	Cutting depth	5-40	mm	+	Cutting angle	55	°	Sharp
5	Cutting depth	5-40	mm	+	Cutting angle	60	°	Sharp
6	Cutting angle	40-60	°	+	Cutting depth	10	mm	Sharp
7	Cutting angle	40-60	°	+	Cutting depth	15	mm	Sharp
8	Cutting angle	40-60	°	+	Cutting depth	15	mm	Blunt

Table 4.11: Parameter combinations of various tests - concrete

#	Alternating parameter	Range	Unit		Fixed parameter	Value	Unit	Tip
9	Cutting depth	5-15	mm	+	Cutting angle	45	°	Sharp
10	Cutting depth	5-25	mm	+	Cutting angle	50	°	Sharp
11	Cutting depth	5-25	mm	+	Cutting angle	55	°	Sharp
12	Cutting depth	5-25	mm	+	Cutting angle	60	°	Sharp
13	Cutting angle	40-60	°	+	Cutting depth	15	mm	Blunt

Table 4.12: Parameter combinations of various tests - sandstone

For making a good physical comparison between the two rock compositions, it decided to focus on the cutting experiments where a sharp tool was used and the cutting depth range was varied when using a fixed cutting angle. This means that the data sets of number 1-5 in table 4.11 and 1-4 in table 4.12 are being used for further analysis throughout the complete report.

5

DATA ANALYSIS

This chapter first describes the concrete and sandstone cutting results, in terms of forces, specific energy and production. All cutting data is analyzed and physically explained on its behavior. Secondly, all force data is compared with the existing force prediction models.

5.1. CUTTING DATA

Within the experimental phase, all cutting data is measured and logged in three-dimensional space. All forces that result from the unidirectional movement of the pick-point, and variation of input parameters, is to be analyzed and compared in a scientific way. Because, initially, the output of the sensor data is in microVolt (μV), conversion formula 3.7 is applied to obtain a force output. Within the rock cutting process, the peak and mean forces on the pick-point are most important. Being able to predict the total peak cutting forces, when having certain input parameters, the operating boundaries of the cutting system can be determined. The composition of the total peak forces can be derived from the forces in longitudinal (X), lateral (Y) and vertical (Z) direction. The mean cutting forces are more of interest when computing the cutterhead torque and power requirements of the system. To show the development of these forces during the cutting process, all force outputs are being plotted against time t. Figure 5.1 shows a schematic representation of the cutting process, showing an arbitrary output of the total forces which develops over time t.

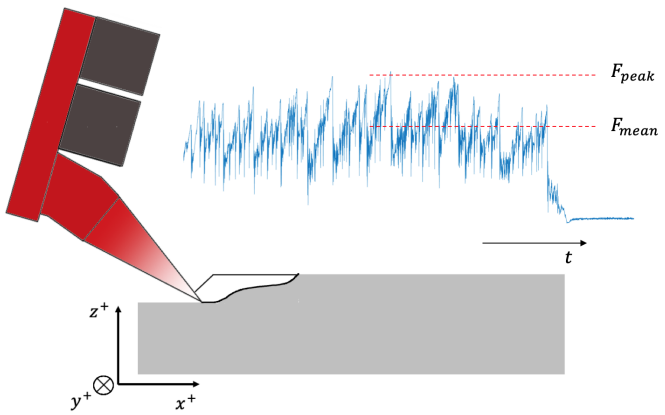

Figure 5.1: Development of total force over time within the rock cutting process

Most existing theoretical rock cutting models are derived for determining the total peak forces. In the upcoming force analyzing process, the peak force in X,Y and Z-direction, which corresponds to the cutting depth and width at that point in time, is shown. The total peak cutting force is determined using equation 5.1.

$$F_{ct,peak} = \sqrt{F^2_{cx,peak} + F^2_{cy,peak} + F^2_{cz,peak}} \tag{5.1}$$

5.2. CUTTING DATA ARTIFICIAL ROCK

In total 42 artificial rock cutting experiments were conducted on 8 different samples. For the sake of consistency, the cutting process of concrete sample $7-11-B3$ will be analyzed within this section. The complete block was used for five different experiments, varying in cutting depth h_c. Table 5.1 shows the parameter settings of each test and resulting cutting depths and widths. All measurements were logged over a 90cm long cutting trajectory in longitudinal direction. For determining the mean cutting depth h_{mean}, the local cutting depths were measured at Δx=10cm over the complete length, after which the average was taken. The peak cutting depth corresponds with the point where the peak cutting force, in X,Y and Z-direction, was measured. All Force-Time plots of the $7-11-B3$ sample will be explained and supported by the noted visual observations during the experiments. The remaining Force-Time plots and noted experimental observations of the concrete cutting tests, according to the various parameter combinations of table 4.11, can be found in appendix C.3 and A, respectively.

Experiment	α_c °	h_c [mm]	h_{mean} [mm]	h_{peak} [mm]	w_{mean} [mm]	w_{peak} [mm]
$7-11-B_{3.1}$	40°	5	3.3	4.0	26.4	33.0
$7-11-B_{3.2}$	40°	10	9.3	10.0	53.9	55.0
$7-11-B_{3.3}$	40°	20	16.6	17.0	117.6	150.0
$7-11-B_{3.4}$	40°	30	21.1	22.7	94.9	140.5
$7-11-B_{3.5}$	40°	40	28.3	30.7	139.5	184.0

Table 5.1: Desired input parameters and results due to cutting

Experiment $7-11-B_{3.1}$ (40° - 5mm)

From figure 5.2 it can be seen that the data logging of the cutting forces started at approximately 40 seconds. From visual observations and video recordings, it was seen that the desired cutting depth h_c was not reached. Due to this insufficient cutting depth, the tool was mostly scraping the rock its interface, resulting in very fine crushed material in front of the pickpoint, as production. This plastic zone is dominated by shear failure of the microstructure. This desired cutting depth lead to very few and small-sized outbreaking chips. The Force-Time plot shows that the variation of forces in all measuring directions. The horizontal cutting forces F_{cx} are slightly lower than the vertical cutting forces F_{cz}. This can be explained by the fact that more vertical forces are expected when the cutting angle is shallower. This makes it harder for the pickpoint to reach the desired cutting depth. It can be seen from figure 5.2 that for both horizontal as vertical forces, there is some kind of basic force level. It is expected that this basic force level arises from the combination of forces due to crushing and dynamic friction. Furthermore, it appears from figure 5.2 that some global peaks and troughs are visible. This gradual change in cutting force is a result of an uneven cutting interface. The increase in forces basically means an increase in cutting depth. Table 5.2 displays the peak forces in X-,Y- and Z-direction, including the total peak force of all directions combined. These peak forces are measured at the corresponding depth h_{peak} as in table 5.2.

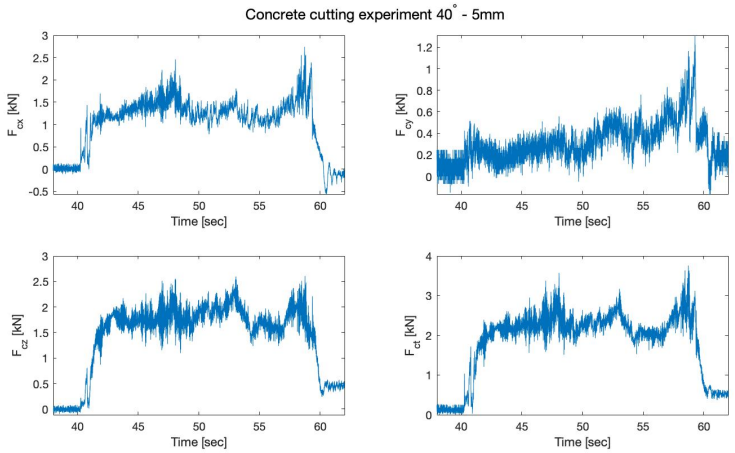

Figure 5.2: Development of total force over time within the rock cutting process

Experiment	$F_{cx,peak}$ [kN]	$F_{cx,mean}$ [kN]	$F_{cy,peak}$ [kN]	$F_{cy,mean}$ [kN]	$F_{cz,peak}$ [kN]	$F_{cz,mean}$ [kN]	$F_{ct,peak}$ [kN]	$F_{ct,mean}$ [kN]
$7-11-B_{3.1}$	2.74	1.32	1.31	0.35	2.61	1.73	4.00	2.21

Table 5.2: Peak forces experiment $7-11-B_{3.1}$

Experiment $7-11-B_{3.2}$ (40° - 10mm)

By increasing the cutting depth to 10mm, the force response in X- and Z-directions already becomes different, compared to $7-11-B_{3.1}$. From figure 5.3 it can be seen that the force amplitudes became larger, meaning that not only crushing exists, but also chip forming. The various intermediate peaks in the output signal represent the forces that are needed to break the rock's internal structure. These peak forces depend on the local cutting depth and width of the cutting profile. As seen, these peaks vary over the complete cutting trajectory, meaning that chip forming is an irregular process. It must be noted that the chips were accumulating on the cutting face of the pick-point. This shows that the post failure process appears to be ductile. The test results of the preliminary data acquisition for concrete batch $7-11-B3$, in section 4.1.4, points out that the brittleness index B is equal to 3.43. According to Miedema [12] a material with a brittleness index, or ductility number, below 9 can be considered as ductile.

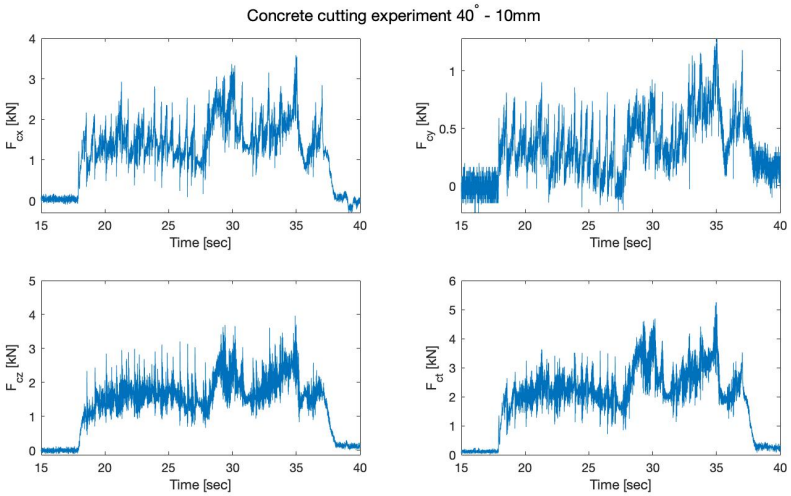

Figure 5.3: Development of total force over time within the rock cutting process

Experiment	$F_{cx,peak}$ [kN]	$F_{cx,mean}$ [kN]	$F_{cy,peak}$ [kN]	$F_{cy,mean}$ [kN]	$F_{cz,peak}$ [kN]	$F_{cz,mean}$ [kN]	$F_{ct,peak}$ [kN]	$F_{ct,mean}$ [kN]
$7-11-B_{3.2}$	3.58	1.56	1.28	0.40	3.96	1.72	5.49	2.39

Table 5.3: Peak forces experiment $7-11-B_{3.2}$

Experiment $7-11-B_{3.3}$ (40° - 20mm)

Figure 5.4 shows that the cutting forces approximately increased with a factor 2 in all measuring directions. Compared to experiment $7-11-B_{3.2}$, magnitude of the output signal shows more severe local peaks and troughs. This large force fluctuation means that larger chips are being formed over the cutting process. Video analysis shows that the chip size and overall production, compared to the previous experiment, progressively increased. It is clearly seen that the horizontal cutting force still dominates the total force output. Table 5.4 shows the results of the peak and mean cutting forces during this experiment.

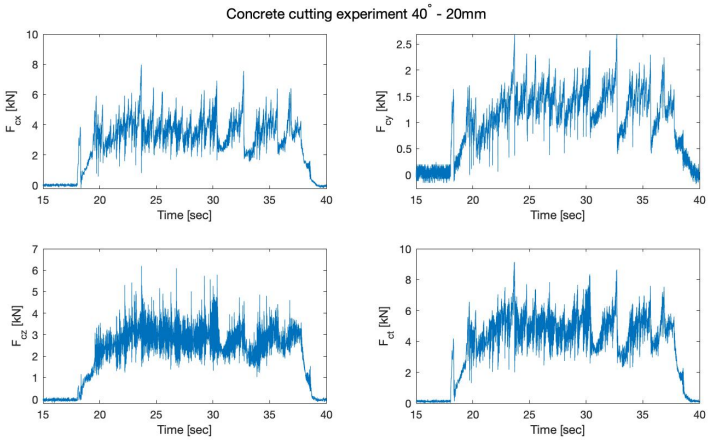

Figure 5.4: Development of total force over time within the rock cutting process

Experiment	$F_{cx,peak}$ [kN]	$F_{cx,mean}$ [kN]	$F_{cy,peak}$ [kN]	$F_{cy,mean}$ [kN]	$F_{cz,peak}$ [kN]	$F_{cz,mean}$ [kN]	$F_{ct,peak}$ [kN]	$F_{ct,mean}$ [kN]
$7-11-B_{3.3}$	7.97	3.41	2.69	1.24	6.20	2.61	10.19	4.51

Table 5.4: Peak forces experiment $7-11-B_{3.3}$

Experiment $7-11-B_{3.4}$ (40° - 30mm)

For the rock cutting process to be linear, the peak cutting force should proportional to the increase in cutting depth h_c. Comparing experiment $7-11-B_{3.3}$ to the results in figure 5.5, it can be seen that the measured peak force approximately increased with a factor 2, whereas the increase in peak cutting depth h_{peak} is less than a factor 1.5. This indicates that the peak force development is not exactly linear. Observations during the experiment showed that the chip size, compared to $7-11-B_{3.3}$, were not necessarily larger, but the failure process acted more cataclysmic. This means that the chip forming happened in a more violently destructive way.

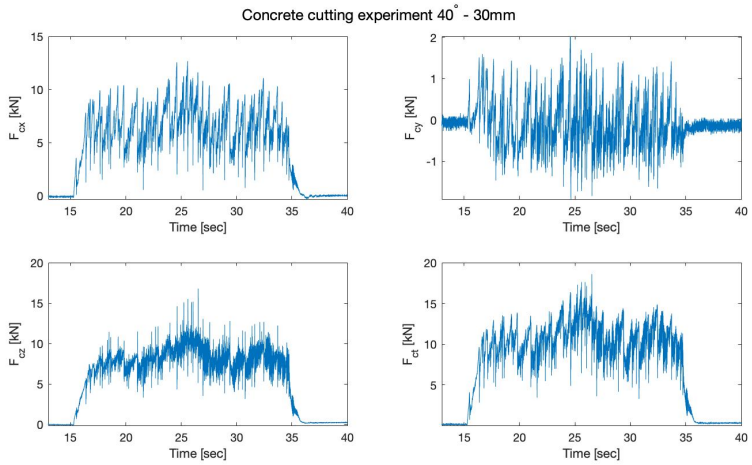

Figure 5.5: Development of total force over time within the rock cutting process

Experiment	$F_{cx,peak}$ [kN]	$F_{cx,mean}$ [kN]	$F_{cy,peak}$ [kN]	$F_{cy,mean}$ [kN]	$F_{cz,peak}$ [kN]	$F_{cz,mean}$ [kN]	$F_{ct,peak}$ [kN]	$F_{ct,mean}$ [kN]
$7-11-B_{3.4}$	12.68	6.48	2.03	-0.07	16.80	7.66	20.82	10.11

Table 5.5: Peak forces experiment $7-11-B_{3.4}$

Experiment $7-11-B_{3.5}$ (40° - 40mm)

During this research a cutting depth h_c of 40mm was set as a maximum for the concrete experiments. Though, as for all the other tests, this desired cutting depth is not completely reached. Force analysis points out that changes in the total peak forces, compared to $7-11-B_{3.4}$, are minor. Since the increase in h_{peak} is approximately 5mm and the difference in measured peak force, compared to $7-11-B_{3.4}$, is small, this could indicate that with an aimed cutting depth of 40mm, using a 40° cutting angle, is more efficient in terms of production. Following on this force analysis, visual observations pointed out that the chip dimensions and amount of crushed material increased, compared to the previous experiment.

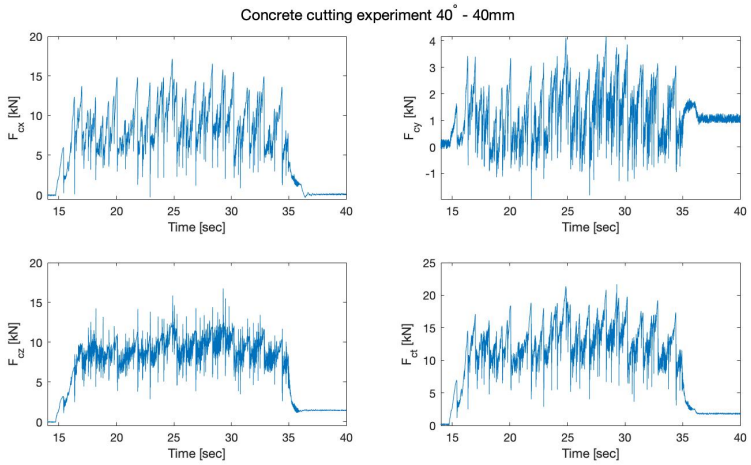

Figure 5.6: Development of total force over time within the rock cutting process

Experiment	$F_{cx,peak}$ [kN]	$F_{cx,mean}$ [kN]	$F_{cy,peak}$ [kN]	$F_{cy,mean}$ [kN]	$F_{cz,peak}$ [kN]	$F_{cz,mean}$ [kN]	$F_{ct,peak}$ [kN]	$F_{ct,mean}$ [kN]
$7-11-B_{3.5}$	17.14	8.64	4.17	1.23	16.76	8.57	23.89	12.34

Table 5.6: Peak forces experiment $7-11-B_{3.5}$

To visualize the development of the total peak force $F_{ct,peak}$ over the depth at which this force occurs h_{peak}, figure 5.7 is constructed. By applying the preset parameters in table 5.1, it is seen that the total forces approximately increase linearly. The measured data points fluctuate around the linear-plotted trendline. Section 5.2.1 investigates if the total force development over the cutting depth has a linear relationship for the remaining concrete cutting experiments.

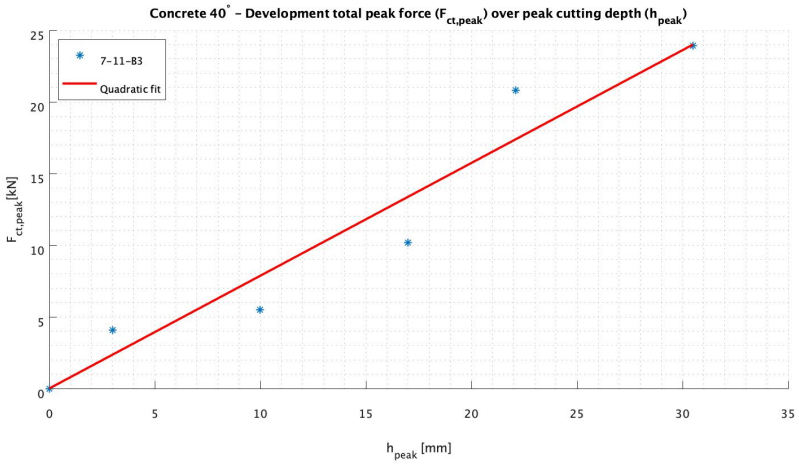

Figure 5.7: Development of total force over time within the rock cutting process

Discussion - 7 – 11 – $B3$

By comparing all the measured vertical and horizontal force components, it is noticed that the both peak forces do not differ a lot from each other in terms of magnitude. Though, it must be noted that the peaks and troughs of the horizontal component fluctuate more significantly. The vertical force component seems to have some kind of basic stress level for all experiments, having discontinuous, sharp, intermediate peaks. Fundamentally seen, this can be explained by the fact that the vertical component needs to deliver a certain amount of force to reach the required cutting depth. When critically looking at the existing force prediction models, it is noticed that the vertical force component is almost always lower than its horizontal component. This is because these models assume that the cutting configuration always reaches its desired cutting depth, without encountering the resistance of the rock.

Another factor that may have influenced the vertical forces is the insufficient stiffness of the structure. The cutting tool configuration was elastically deforming, meaning that an undesired vertical force was measured by the load sensors. The magnitude of this force is hard to determine, but to partially account for this excess force a correction factor $\frac{h_{mean}}{h_c}$ is given to the measured vertical forces. This ratio is defined as the mean cutting depth that is measured along the complete cutting trajectory, divided by the desired, preset cutting depth. So, the assumption is made that, partially, due to the lack of stiffness of the structure, the desired cutting depth was not reached, and is accounted for by this multiplication factor for the measured vertical cutting force.

Concerning the lateral force response, it is expected that, in an ideal situation, the net contribution is zero. When chips are formed, the breakage path left and right of the cutting groove is approximately equal. Compared to the forces in longitudinal and vertical direction, the lateral forces are rather small, meaning that the contribution due to outbreaking in Y-direction is minor. From the experimental observations (appendix A) it is clearly seen that there is an outbreaking path when a chip is formed. So, it is thought that the force contribution due to this breakage is measured in X- and Z-direction. Further video analysis also showed that the block slightly rotated around its Z-axis, because of insufficient clamping. When relating this to the lateral force data, it is expected that the force would be measured in Y^- or Y^+ direction, depending on the block's rotation. One can simply see this in some of the Force-Time plots.

5.2.1. PEAK FORCE ANALYSIS

To visualize the behavior of the peak cutting forces for different cutting angles, the same test sequence, in terms of cutting depth increments, has been followed for the various concrete blocks. Within this section parameter combinations 1-5, as in table 4.11, are being compared in terms of horizontal and vertical peak forces. The same analyzing approach as in section 5.2 has been used for all experiments and is more concisely elaborated within appendix C.

Figure 5.8 shows the horizontal peak force trend of five test sequences, measured at the peak cutting depth h_{peak} of the experiment in question. Figure 5.8 shows that the measured data points of the horizontal force component approximately increases linearly with the cutting depth for each cutting configuration. In contrary to the existing theories, it surprises that the magnitude of horizontal forces is higher for the shallow cutting angles than the steeper cutting angles. A possible explanation for this could be that the dynamic friction between the rock and cutting tool plays a role. The application of a shallow cutting angle means that the contact area of the pickpoint will be larger, meaning that the vertical force, pointing upwards, will be larger. This directly influences the horizontal component in terms of additional frictional forces. To make this force distribution more clear, reference is made to Evans [1] where the pickpoint's angle of attack is zero, which means that only vertical forces will be considered. When the cutting angle is increased, the contribution of vertical forces becomes larger.

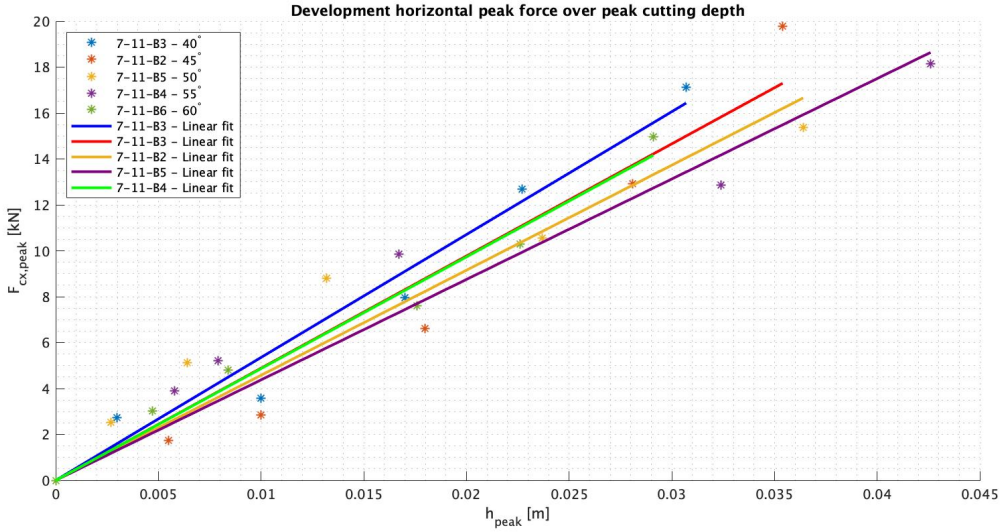

Figure 5.8: Horizontal peak force comparison of concrete tests

Figure 5.9 shows the evolution of vertical peak forces $F_{cz,peak}$ over the peak cutting depth h_{peak}. It can be seen that the dispersion within the shallow cutting regime (h_{peak}<0.01m) is quite large. Though, it must be noted that the vertical force of the shallow cutting angles are highest. When relating this to the results in figure 5.8, it partially proves that frictional forces do contribute to the total forces.

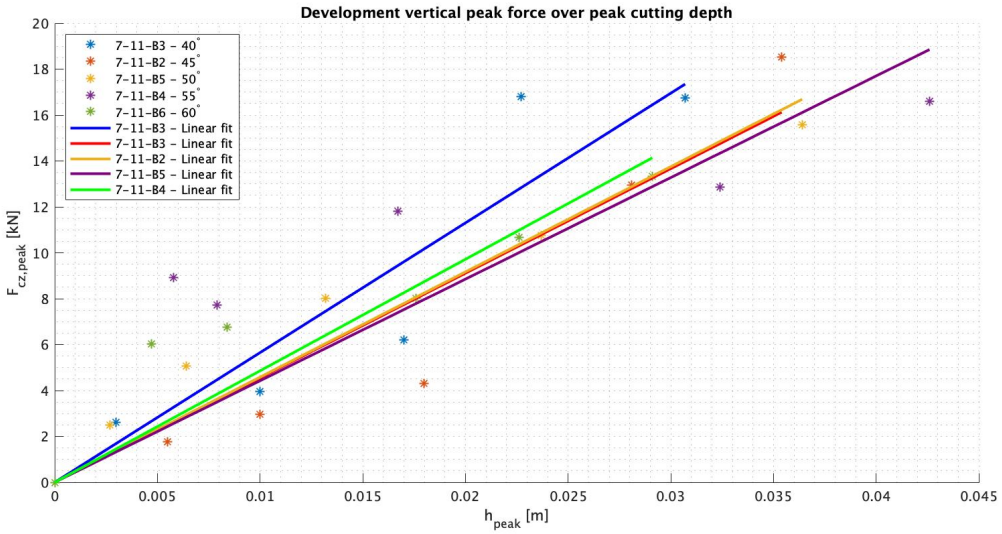

Figure 5.9: Vertical peak force comparison of concrete tests

5.2.2. PRODUCTION DATA

During the rock cutting process various-sized chips and crushed material is removed from the intact rock due to the tool-rock interaction. The total amount of removed material that is cut, is called the production. Primarily, the production of intact rock depends on the compressive and tensile strength of the rock and its deformation properties. Secondarily, the production is influenced by the cutting angle α_c and cutting depth h_c. When the rock properties are known, one can imagine that the cutting depth is the most significant parameter for the amount of production.

After each cutting experiment all chips and fine debris is collected and weighed. To gain more insight into the chipping process after cutting, a particle distribution analysis can be executed. To do this, the gathered production of every individual experiment is placed into a sieve. The sieve consists out of six stacked layers of variable diametral opening. The process of chip distribution happens due to vibration of the sieve. When chips or fine material are smaller than the diametral opening of the concerned layer, it falls down until it settles in a more narrow layer. The particle size distribution can indicate the type of failure that has occurred during the cutting process. The lowest layer, which only allows very fine material to enter, contains the amount of crushed material that is produces. By knowing the length of the cut block, one can make an educated guess on the size of the crushed zone.

Table 5.7 shows the production data and the distribution of chips in the consecutive sieve layers for concrete block $7-11-B3$. It can be seen that the production progressively increases by an increase in cutting depth. When specifically looking at the <1mm layer, which corresponds to the amount of crushed material, it is observed that the crushed zone is developing over the cutting depth. More fine material is being produced, meaning that this also may influence the cutting forces. By analyzing the larger chips within the top layer in table 5.7 (>20mm), it can be seen that there is a quite large transition between the h_c=5mm and h_c=10mm in terms of production. By combining the visual observations and production data it can be concluded that tensile failure is starting to play a role from h_c=10mm and up.

Sample	α_c	h_c	h_{mean}	Production	Chip size distribution/g					
	[°]	[mm]	[mm]	[g]	<1mm	1-2mm	2-5mm	5-10mm	10-20mm	>20mm
7-11-$B_{3.1}$	40	5	3.3	96.79	12.51	4.69	13.48	15.88	32.66	17.57
7-11-$B_{3.2}$	40	10	9.3	689.11	39.12	12.29	19.81	24.33	44.67	548.89
7-11-$B_{3.3}$	40	20	16.6	2004.14	110.90	37.41	44.72	59.64	101.45	1650.02
7-11-$B_{3.4}$	40	30	21.1	2237.52	242.84	79.24	79.94	76.53	147.97	1611.00
7-11-$B_{3.5}$	40	40	28.3	4117.63	311.76	109.33	84.18	107.88	216.48	3288.00

Table 5.7: Production data concrete sample $7-11-B3$

Figure 5.10 displays the production of the $7-11-B3$ concrete experiments, distributed over the various particle size diameters. This so called Particle Size Distribution shows the contribution, in terms of production, of each particle size to the total production of the cutting experiment in question. To continue to look critically to the production data, not the aimed cutting depth h_c has been used, but the mean cutting depth h_{mean} over the complete cutting trajectory has been applied. This value is obtained by measuring the in-situ cutting depth at Δx=10cm.

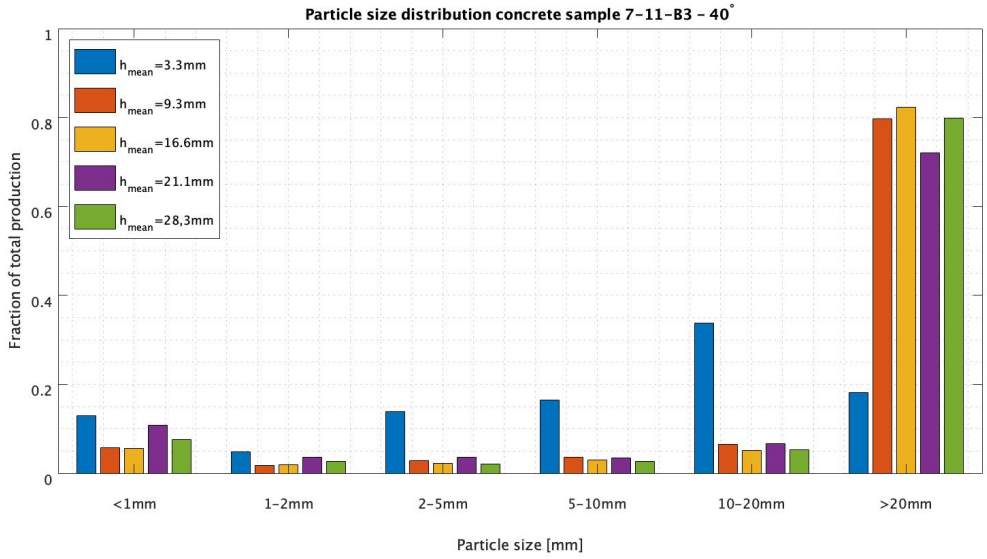

Figure 5.10: Particle Size Distribution of sandstone sample $7-11-B3$

When analyzing the production data of the collection of concrete blocks with different input parameters, it is hard to conclude which configuration is most efficient in terms of production and cutting forces. This is due to the fact that the desired cutting depth was not always reached during each experiment, meaning that the forces and production per test fluctuated significantly. Table C.25 in appendix C.5 shows that experiment $7-11-B_{4.5}$ has the highest production of all. Though, it must be noted that this test reached the deepest, in terms of cutting depth. From a physical point of few, the most amount of crushed material (e.g. <1mm) should be produced by the steepest cutting angle h_c=60°. By applying a steeper cutting angle, the pickpoint's cutting face is subjected to more horizontal forces, as the frontal area is increasing. This increase in contact area can also be considered as the indentation area of the pickpoint. A larger indentation area, correlates to more crushed material. To get an indication of the amount of produced material for each cutting configuration used, reference is made to appendix C.5 where all concrete production data is shown.

5.3. CUTTING DATA SANDSTONE

In total 22 sandstone cutting experiments have been performed on four different blocks. To be consistent with the analyzing process of the report, Sample S_4 is being considered. This section will discuss the force data and visual observations of sample S_4 for each cutting depth. Table 5.8 shows the desired parameter settings (α_c, h_c) and resulting values after cutting (h_{mean}, h_{peak}, w_{mean}, w_{peak}) for sample S_4. As for the concrete experiments, the sandstone peak cutting forces, measured in X-, Y- and Z-direction, are being collected at the peak cutting depth h_{peak} and corresponding chip outbreaking width w_{peak}. To be consistent with the concrete tests, the resulting forces are logged over the same cutting distance; 90cm. By critically looking at the UCS, BTS and indentation data in section 4.1, it can be concluded that the bonds of the sandstone's microstructure are stronger than the artificial rock. This can be explained by the fact that the yield stress due to shear and tensile failure is significantly higher. Furthermore, the sandstone has a larger indentation resistance capacity, compared to the concrete. From a physical point of view, it is logical that a material with a lower strength needs more penetration by the indenter to reach the outer boundary of its linear-elastic region. Beyond this point, chipping occurs. It can thus be said that sandstone will fail in a more brittle and cataclysmic way than concrete.

Experiment	α_c °	h_c [mm]	h_{mean} [mm]	h_{peak} [mm]	w_{mean} [mm]	w_{peak} [mm]
$S_{4.1}$	60°	5	2.1	2.4	17.1	19.3
$S_{4.2}$	60°	10	3.4	3.8	22.5	33.1
$S_{4.3}$	60°	15	10.8	11.2	67.0	80.7
$S_{4.4}$	60°	20	10.9	12.3	56.2	86.6
$S_{4.5}$	60°	25	14.3	15.3	72.2	97.8

Table 5.8: Desired input parameters and results due to cutting sandstone

Experiment $S_{4.1}$ (60° - 5mm)

Figure 5.11 shows the Force-Time plot of experiment $S_{4.1}$. When looking at the shape of the output signal in X- and Z-direction, it appears that the force is slowly increasing over the length of the cutting trajectory. This may be explained by two dependent factors; in-situ cutting depth and a crushed zone. It was observed that during the cutting process, only crushed material formed in front of the pickpoint. The forming of chips was, due to the shallow cutting depth, irrelevant for the force output. Cutting depth measurements at Δx=10cm over the length of the block showed that the cutting depth was slowly increasing. Despite the increase in cutting depth, the process was still within the crushing regime. This regime can be fed back by the small force fluctuations in the output signal. When chipping occurs, more severe peaks and troughs will appear. It must be noted that the desired cutting depth h_c was not reached due to insufficient stiffness of the construction. To partially account for this stiffness, the output signal of the forces in vertical direction have been multiplied by $\frac{h_{mean}}{h_c}$, as correction factor. This factor will be applied for all sandstone cutting tests.

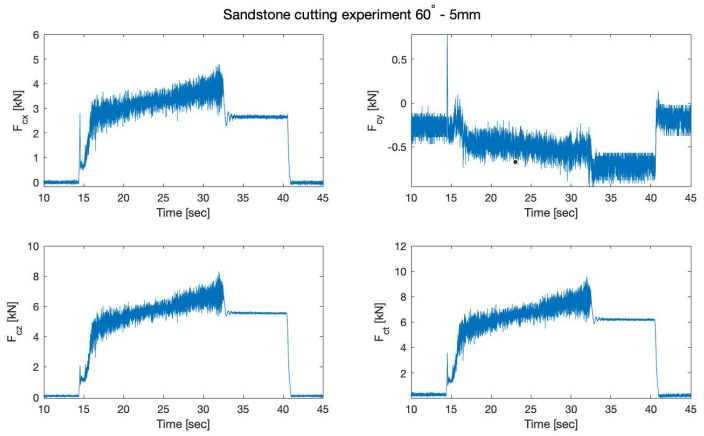

Figure 5.11: Development of total force over time within the rock cutting process

Experiment	$F_{cx,peak}$ [kN]	$F_{cx,mean}$ [kN]	$F_{cy,peak}$ [kN]	$F_{cy,mean}$ [kN]	$F_{cz,peak}$ [kN]	$F_{cz,mean}$ [kN]	$F_{ct,peak}$ [kN]	$F_{ct,mean}$ [kN]
$S_{4.1}$	4.77	3.12	0.78	-0.47	8.31	5.43	9.61	6.29

Table 5.9: Peak forces experiment $S_{4.2}$

Experiment $S_{4.2}$ (60° - 10mm)

Figure 5.12 shows a similar shape as experiment $S_{4.1}$. In terms of the Force-Time plot, the main difference between $S_{4.1}$ and $S_{4.2}$ is the amplitude of the intermediate peaks. The increase in peak values indicates the development of small chips. Video analysis shows that the build-up of crushed material is still dominating the cutting forces at this cutting depth. By comparing the cutting depth with the previous experiment, it is noticed that the increase in mean cutting depth h_{mean} is only 1mm. This, again, is a consequence of the lack in stiffness of the cutting tool construction. As the desired cutting depth was set to 10mm, the correction factor for the vertical forces will be of greater influence.

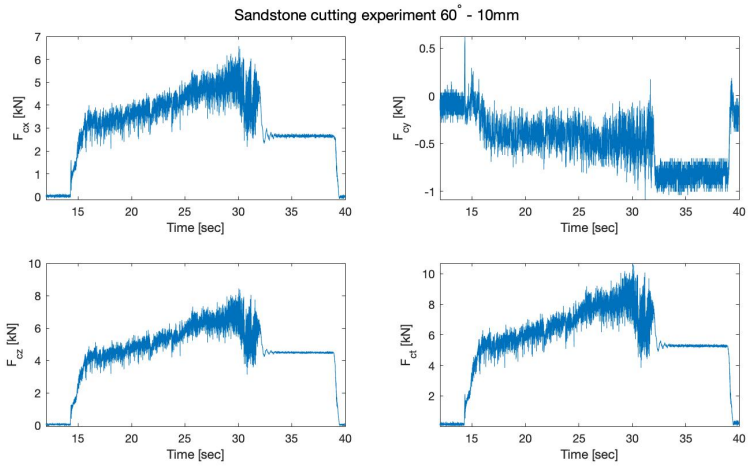

Figure 5.12: Development of total force over time within the rock cutting process

Experiment	$F_{cx,peak}$ [kN]	$F_{cx,mean}$ [kN]	$F_{cy,peak}$ [kN]	$F_{cy,mean}$ [kN]	$F_{cz,peak}$ [kN]	$F_{cz,mean}$ [kN]	$F_{ct,peak}$ [kN]	$F_{ct,mean}$ [kN]
$S_{4.2}$	6.58	3.91	0.62	-0.40	8.44	5.19	10.72	6.51

Table 5.10: Peak forces experiment $S_{4.2}$

Experiment $S_{4.3}$ (60° - 15mm)

By setting h_c to 15mm, the output signal of cutting forces drastically changed, compared to the previous tests. Table 5.8 shows that a mean cutting depth h_{mean} of 10.8mm was achieved, leading to a more violent failure process. Figure 5.13 displays the evolution of peak forces. Video analysis showed that the size and amount of outbreaking chips accumulated over the cutting trajectory. Furthermore, the production of very fine material, due to the indentation of the tool with the rock, also increased significantly. In theory, the horizontal forces should dominate the spectrum, because of the 60° cutting angle α_c. When increasing the cutting angle, the length of the rock's theoretical shear plane also increases. This means that the tool needs to deliver a higher impact force to overcome the internal resistance of the rock's internal structure, than when using a small cutting angle. In addition to these forces, indentation resistance also plays a large role due to the preset cutting angle. As α_c=60° is the steepest cutting angle used, it is expected that the forces due to crushing in front of the pickpoint, are largest. This is due to the increase in indentation area, implying that the pickpoint acts more blunt when cutting.

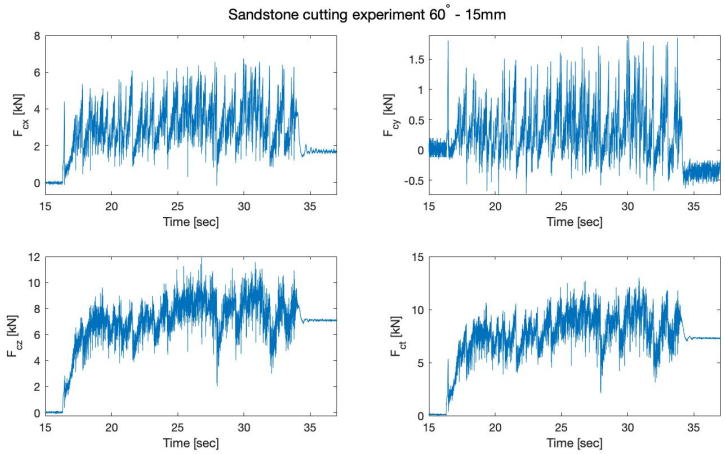

Figure 5.13: Development of total force over time within the rock cutting process

Experiment	$F_{cx,peak}$ [kN]	$F_{cx,mean}$ [kN]	$F_{cy,peak}$ [kN]	$F_{cy,mean}$ [kN]	$F_{cz,peak}$ [kN]	$F_{cz,mean}$ [kN]	$F_{ct,peak}$ [kN]	$F_{ct,mean}$ [kN]
$S_{4.3}$	6.74	3.22	1.89	0.36	12.05	7.10	13.94	7.85

Table 5.11: Peak forces experiment $S_{4.3}$

Experiment $S_{4.4}$ (60° - 20mm)

The Force-Time plot of experiment $S_{4.4}$ shows similar behaviour as for $S_{4.3}$. This can be derived from the fact that the mean cutting depth h_{mean} for both experiments is, unexpectedly, almost the same (table 5.8). The correction factor $\frac{h_{mean}}{h_c}$, to partially account for the stiffness of the construction, will be larger than experiment $S_{4.3}$, as the desired cutting depth was set to 20mm. It must be noted that video analysis showed that the failure process of the current experiment, acted differently than $S_{4.3}$. The formation of chips was clearly more present, which agrees with the large peak values in the force output.

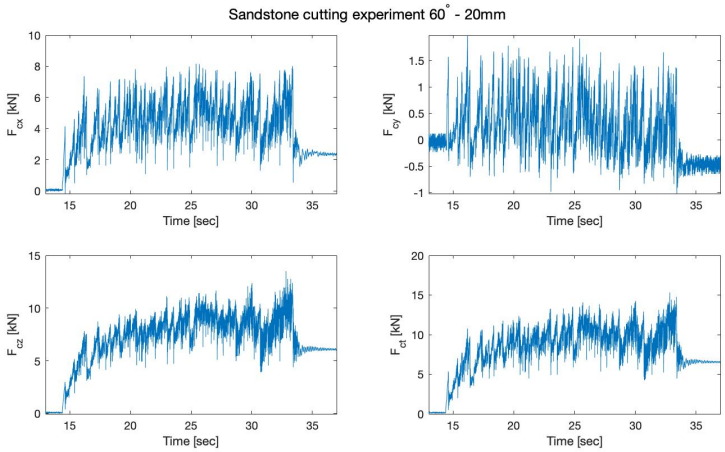

Figure 5.14: Development of total force over time within the rock cutting process

Experiment	$F_{cx,peak}$ [kN]	$F_{cx,mean}$ [kN]	$F_{cy,peak}$ [kN]	$F_{cy,mean}$ [kN]	$F_{cz,peak}$ [kN]	$F_{cz,mean}$ [kN]	$F_{ct,peak}$ [kN]	$F_{ct,mean}$ [kN]
$S_{4.4}$	8.16	4.52	1.98	0.33	13.51	7.62	15.91	8.90

Table 5.12: Peak forces experiment $S_{4.4}$

Experiment $S_{4.5}$ (60° - 25mm)

Figure 5.15 clearly shows the highest force output of the 60° cutting sequence. The fluctuation in magnitude of forces is even more severe than the previously executed experiments. The large peaks and troughs indicate the formation of coarse chips. Video analysis clearly showed that the outbreaking pattern increased, meaning that the overall production will be more.

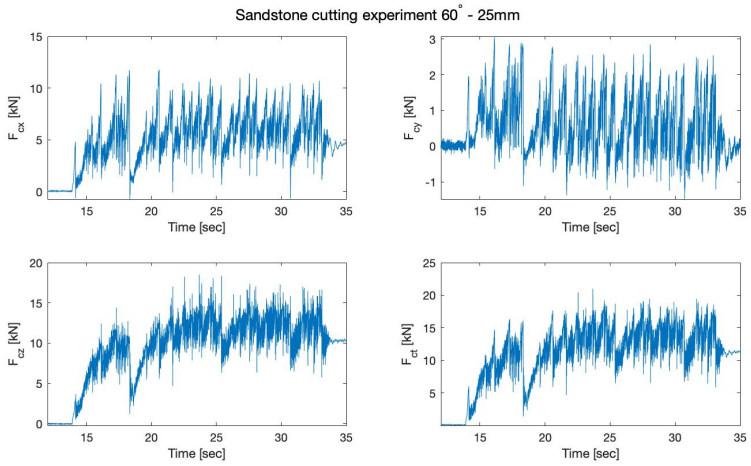

Figure 5.15: Development of total force over time within the rock cutting process

Experiment	$F_{cx,peak}$ [kN]	$F_{cx,mean}$ [kN]	$F_{cy,peak}$ [kN]	$F_{cy,mean}$ [kN]	$F_{cz,peak}$ [kN]	$F_{cz,mean}$ [kN]	$F_{ct,peak}$ [kN]	$F_{ct,mean}$ [kN]
$S_{4.4}$	11.79	5.66	3.08	0.69	18.52	10.26	22.17	11.82

Table 5.13: Peak forces experiment $S_{4.5}$

The development of the peak cutting forces $F_{ct,peak}$ over the peak cutting depth h_{peak} can now be constructed for sample S_4. Figure 5.16 shows a linear fitted line though the measured data points. The data shows that the forces within the shallow cutting regime are relatively high and do therefore not comply with fitting of the linear trend line. A physical explanation for this might be that the combination of friction between the pickpoint and rock interface and the crushing of material significantly contributes to the cutting forces.

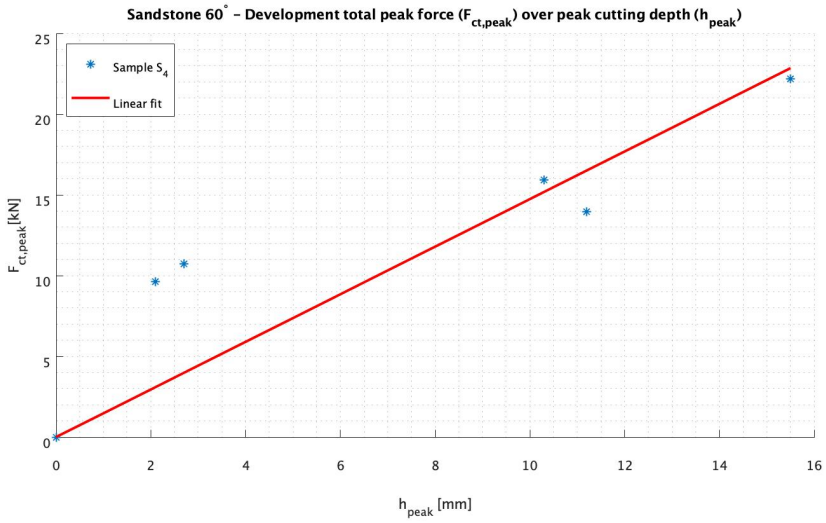

Figure 5.16: Development of total peak force over time within the rock cutting process

5.3.1. PEAK FORCE ANALYSIS

To give an impression about the force development of the horizontal and vertical peak forces for the various sandstone experiments, figure 5.17 and 5.18 are constructed. Each data point represents the maximum vertical or horizontal cutting force that occurred at its corresponding peak cutting depth h_{peak} (e.g. $F_{cx,peak}$,$F_{cz,peak}$, respectively). The peak cutting depth was obtained by looking at the exact moment in time that F_{cx} and F_{cz} occurred in the Force-Time plot and then tracing it back to its location along the cutting trajectory.
Within the shallow cutting regime in figure 5.17 (e.g. $h_{peak} < 5$mm), it is observed that the resulting horizontal cutting forces are relatively large. Within this region the material was mostly crushing and scraping the rock's interface, meaning that the cutting forces are mainly dominated by the stresses within the crushed zone and frictional effects. From a physical point of view it is expected that the small-angle cutting tests experienced more dynamic friction effects than the steep-angle experiments. This is due to the increase in contact surface of the pickpoint with the rock. This can be partially validated by the fact the 45° trend has a larger force-depth gradient than the other experiments. During the experiments it was observed that bending of the structure appeared to be more by using small cutting angles. This means that more vertical pressure by the pickpoint is being applied to the rock's top interface to achieve the desired cutting depth, leading to large horizontal frictional forces. Furthermore, it is expected that the horizontal forces for the steep-angle experiments are more dominated by crushing and less by friction. When increasing the cutting angle α_c, the frontal surface of the blade will have a larger contact area to indent the sandstone. This will lead to higher compression and thus larger shear forces.

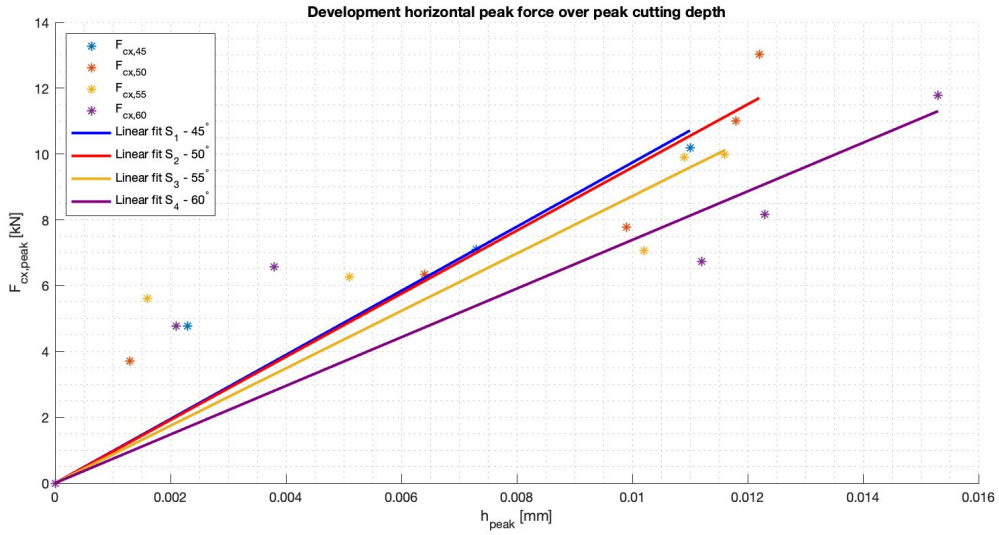

Figure 5.17: Development of horizontal peak forces for sandstone samples S_1,S_2,S_3,S_4

Figure 5.18 shows that the vertical force-depth gradient is larger for small cutting angles than the measured horizontal cutting forces, which is contrary to the described existing theories in section 2.8. It can be seen that the vertical peak force gradient of the 45° experiments is largest. Keeping figure 5.17 as reference, it is most likely that the dynamic friction of the mutual contact between the pickpoint and sandstone, plays a dominant role within this region. When looking to the existing theories, it is observed that, when decreasing the cutting angle, the horizontal forces will contribute less to the total forces than the vertical component. From a physical point of view, it is now understood that the application of a shallow cutting angle requires a large vertical force to reach the desired cutting depth. As mentioned before, this has to do with the hardness or resistance of the rock composition. When using a lower-strength rock, like concrete, the vertical force has to deliver a smaller force to reach the desired cutting depth. That is why the vertical and horizontal component of the concrete experiments deviate less from each other than the sandstone experiments.

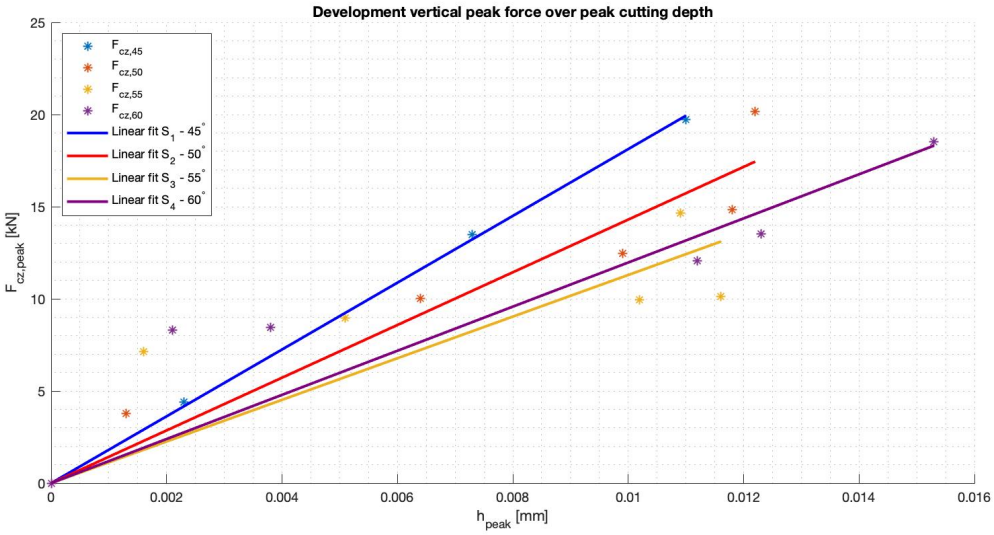

Figure 5.18: Development of vertical peak forces for sandstone samples S_1,S_2,S_3,S_4

5.3.2. PRODUCTION DATA

Table 5.14 shows the complete production data and particle distribution of sandstone sample S_4. The behavior of forces can be partially validated by the production data. When looking back at force data of experiment in figure 5.11 and 5.12, a low-amplitude white noise is being produced by the output of the load sensors. This indicates that no significantly large chips are being produced. Instead, the pickpoint is just scraping the material, mostly producing only very fine crushed material (<1mm). Feeding this back to the production data, it is observed that, indeed, crushing is dominating the cutting process. By critically analyzing the data of the deeper cutting depths, the amplitude of the peaks and troughs become larger, indicating that more significant-sized chips will develop. The production data shows that the particles >20mm start to dominate the total production. From the combined production data in table 5.14, the hypothesis about the increase of crushed material by applying a steeper cutting angle, can be partially proven. The data shows a gradual increase in the production of very fine material (<1mm and 1-2mm).

Sample	α_c	h_c	h_{mean}	Production	Chip size distribution/g					
	[°]	[mm]	[mm]	[g]	<1mm	1-2mm	2-5mm	5-10mm	10-20mm	>20mm
$S_{4.1}$	60	5	2.4	32.16	12.53	2.19	3.27	1.31	1.95	10.91
$S_{4.2}$	60	10	3.4	75.08	19.19	3.26	14.01	14.43	7.71	16.48
$S_{4.3}$	60	15	10.8	712.52	51.55	10.08	28.94	41.89	59.27	520.79
$S_{4.4}$	60	20	10.9	692.04	45.47	9.85	32.68	37.28	81.40	485.36
$S_{4.5}$	60	25	14.3	1246.05	56.40	10.90	38.22	51.75	58.09	1020.83

Table 5.14: Production data sandstone sample S_4

To give more clear representation of the sample S_4 production data, a Particle Size Distribution is constructed in the form of a histogram. Figure 5.19 implemented the production of the various particle diameters from table 5.14. It shows how many percentage a certain particle diameter contributes to the total production of the cutting process.

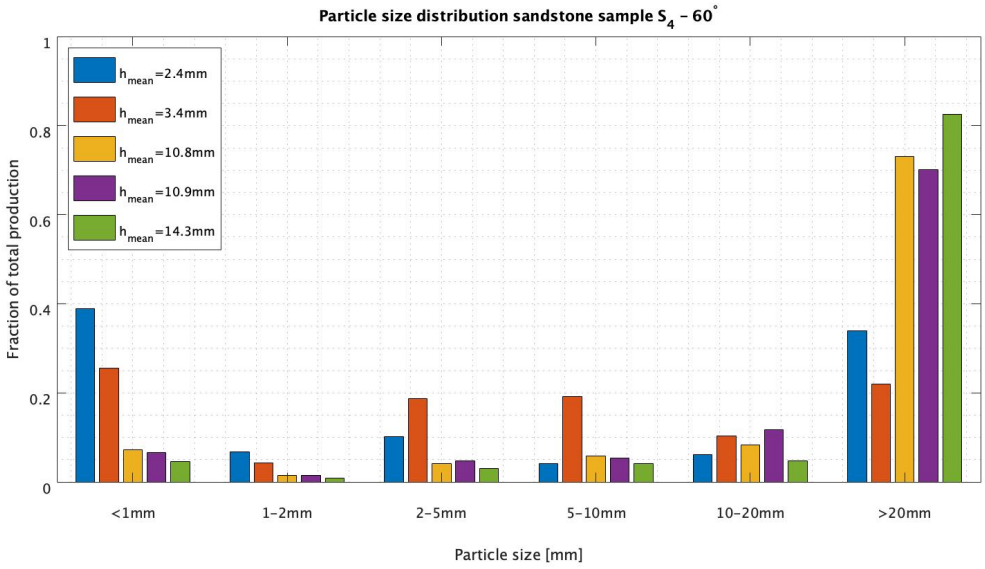

Figure 5.19: Particle Size Distribution of sandstone sample S_4

5.4. SPECIFIC ENERGY

From the cutting force and production data it is hard to determine which preset parameter combination is most efficient during the cutting process. The efficiency of a cutting process, and wear rate of the cutting tool, is influenced by the cutting velocity, shape of cutting surface, design of the cutting tool and rock properties. The excavation of rock requires energy to obtain a certain production. The efficiency of this process is at an optimum, when the lowest amount of work is done to excavate the rock. A quantity to describe efficiency, is the specific energy. This term is defined as 'the quantity of energy that is required to cut unit volume of rock' within an excavation process. In general the specific energy E_{sp} can be written as

$$E_{sp} = \frac{\sum_{i=1}^{n} E_i}{V} \tag{5.2}$$

Where $\sum_{i=1}^{n} E_i$ refers to the total amount of energy used and dissipated during the cutting process to remove a volume V of rock. The total amount of required energy to cut a specific volume of rock is equal to the required power to cut this specific volume. The power per unit width of the cutting tool is a function of the mean horizontal cutting force $F_{h,mean}$ and the velocity of the cutting tool v_c and expressed as $P_c = F_{h,mean} \cdot v_c$. As mentioned in section 5.1, the mean cutting forces are used to calculate the power requirements of the system. This naturally means that $F_{h,mean}$ says something about the efficiency of the cutting process. By maintaining this dependency, the specific energy can be expressed as

$$E_{sp} = \frac{P_c}{V} = \frac{F_{h,mean} \cdot v_c \cdot t}{h_{mean} \cdot w_{mean} \cdot l_b} \approx \frac{F_{h,mean} \cdot v_c \cdot t}{m_{prod}/\rho_{s,c}} \approx \frac{F_{h,mean} \cdot v_c \cdot t}{V_{tot}} \tag{5.3}$$

Where w_{mean} is the mean width of the cutting profile, h_{mean} is the mean cutting depth along the complete cutting trajectory, l_b the length of the block and t the duration of cutting. In existing theories about the specific energy, the tip width of the pickpoint is being used to account for the groove width. In reality chips also breakout, laterally, meaning that this total cut volume V_{tot} also needs to be taken into account. The amount of cut volume can be obtained from the gathered production data. To gain more information about the development of the specific energy by a changing cutting angle α_c and cutting depth h_c, a graphical analysis needs be performed for both rock specimens to visualize the behavior of the specific energy.

5.4.1. ARTIFICIAL ROCK ANALYSIS

Figure 5.20 shows the specific energy distribution over the mean cutting depth. It is clearly seen that by increasing the cutting depth, the specific energy seems to converge to a, more or less, constant value. From a physical point of view, this basically means that the efficiency of the amount of required energy to remove a volume of rock, will increase by increasing the cutting depth. In other words; the removed volume of rock increases more drastically than the horizontal cutting forces, by increasing the cutting depth.

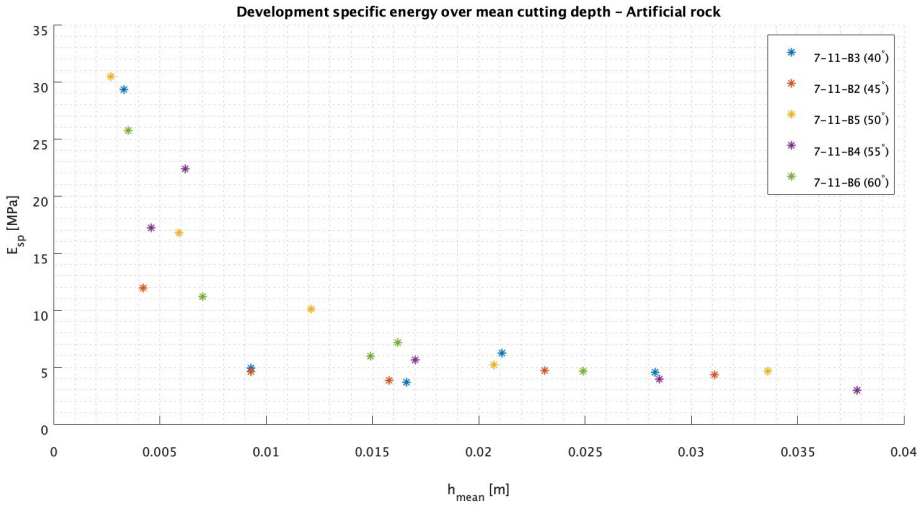

Figure 5.20: Specific energy distribution of artificial rock experiments

5.4.2. SANDSTONE ANALYSIS

Figure 5.21 displays the development of the specific energy by an increase in cutting depth. This graphical representation shows that the specific energy distribution of the sandstone is significantly higher than for the concrete. This is due to the fact that the force-production ratio of the sandstone is higher. In other words; a sandstone cutting experiment delivers a lower production in combination with high cutting forces, compared to a concrete experiment, having the same input parameters. This is due to the fact that the artificial rock has a lower strength, meaning that it is easier for the pickpoint to obtain a high production with lower cutting forces. Conclusively, this implies that the amount of required energy input is higher for sandstone than for concrete.

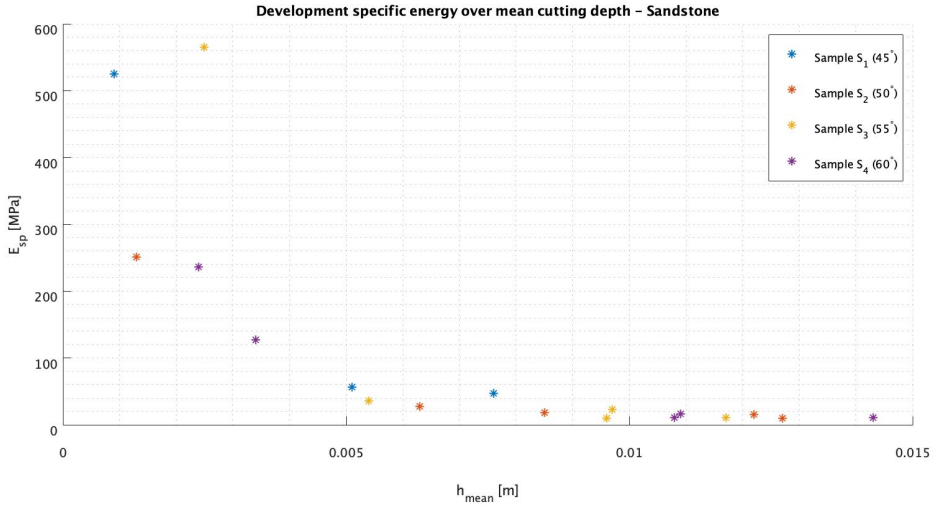

Figure 5.21: Specific energy distribution of concrete experiments

5.5. DATA COMPARISON WITH EXISTING MODELS

Within section 2.8 multiple force prediction models were discussed. To obtain a reliable comparison between the measured cutting forces and the ones that result from the prediction models, one should strive for a comparable cutting configuration (e.g. the use of a pickpoint). The existing theories using a sharp cutting tool, and thus comparable to the cutting configuration used during the experiments within this report, are:

- Evans [1] → Brittle tensile failure
- Nishimatsu [2] → Brittle shear failure
- Miedema [12] Tear Type → Brittle tensile failure

All the preliminary obtained rock property data will be implemented in each of the above mentioned models. Each model contains a horizontal and a vertical force component which will be separately plotted, where a clear distinction between the concrete and sandstone data will be made. It must be noted that the basic friction angle ϕ used, is calculated by Hoek and Brown [23].

5.5.1. EVANS

From figure 5.22 and 5.23 show the results of the implemented rock properties into the Evans model (linear lines) and the measured cutting forces during the experiments in horizontal and vertical direction for both rock compositions. It is clearly seen that for the sandstone, that Evans overestimates the measured horizontal cutting forces and underestimates the measured vertical cutting forces. A serious limitation of Evans is the applicability of large cutting angles. By analyzing the model, it appeared that the predicted cutting forces, for cutting angles larger than 55°, diverge to very large values. This means that the applicability of this model is limited.

SANDSTONE

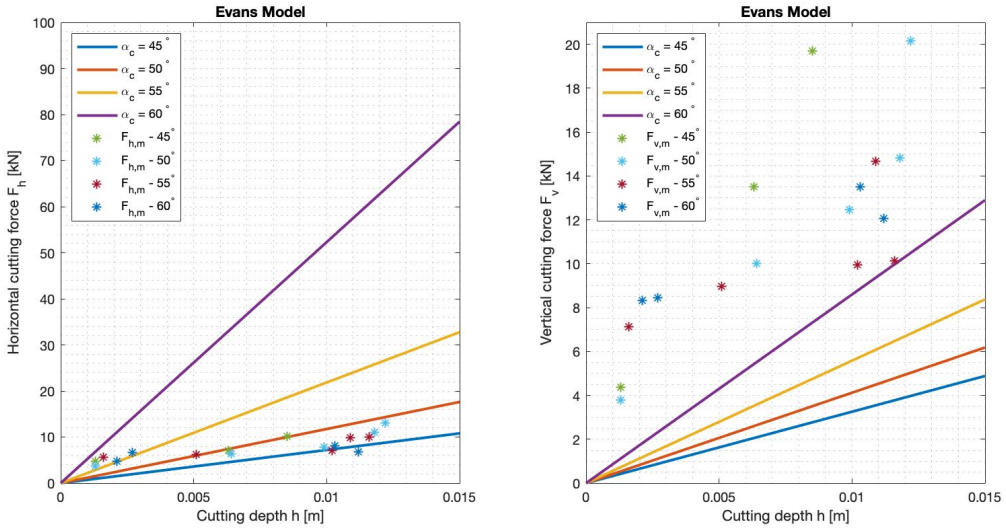

Figure 5.22: Outcomes Evans model - Sandstone

ARTIFICIAL ROCK

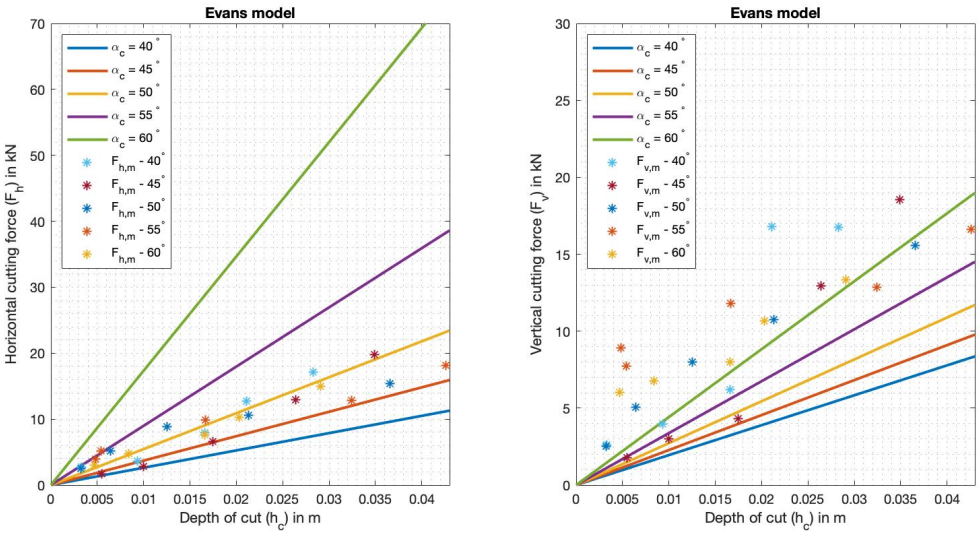

Figure 5.23: Outcomes Evans model - Concrete

5.5.2. NISHIMATSU

Nishimatsu's cutting theory mainly focuses on the application of relatively shallow cutting depths, having brittle shear failure as its dominant failure mechanism. Figure 5.24 and 5.25 show that the horizontal and vertical component of Nishimatsu's prediction model greatly underestimate the measured values for both rock compositions. The measured values in both figures are indicated as dots. The fact that only shear failure is encountered as a dominant failure mechanism, and underestimating the measured forces, indicates that it is most probable that another failure mechanism is missing within the model. Furthermore, Nishimatsu assumed that the desired cutting depth is reached at all times, without encountering the hardness of the rock. This means that the rock's internal resistance to reach a certain cutting depth is not implemented within the model, which would lead to a larger vertical force.

SANDSTONE

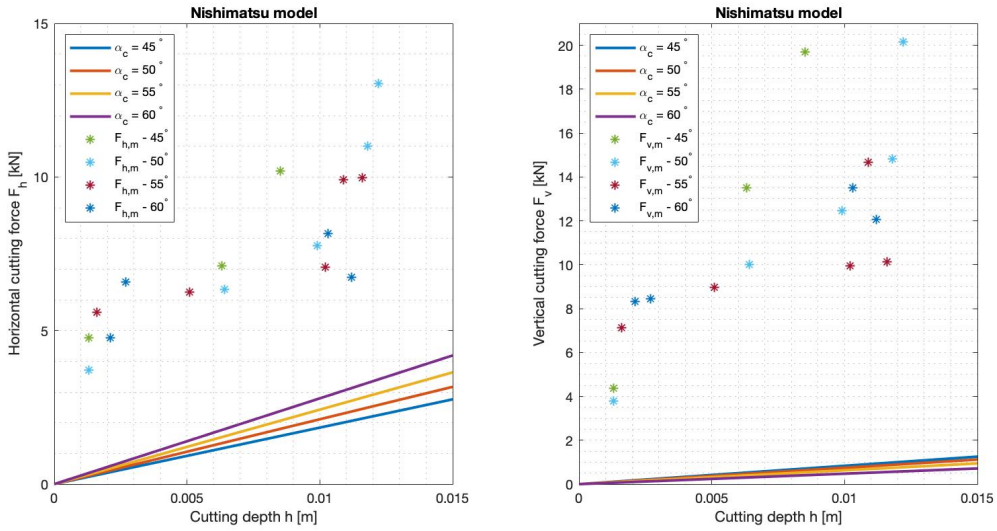

Figure 5.24: Outcomes Nishimatsu model - Sandstone

ARTIFICIAL ROCK

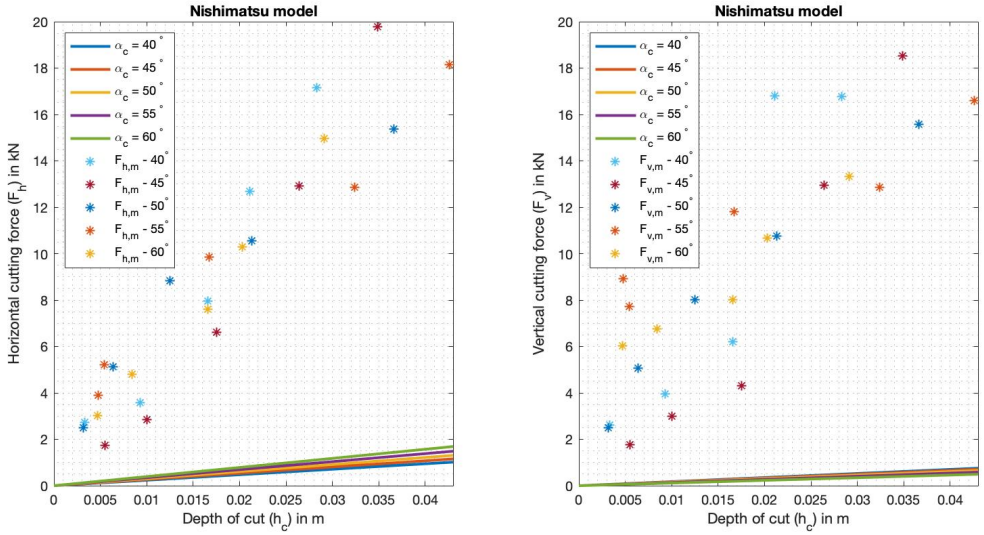

Figure 5.25: Outcomes Nishimatsu model - Concrete

5.5.3. MIEDEMA - TEAR TYPE

Miedema's Tear Type model rests on the assumption of only brittle tensile failure. When looking at the implemented sandstone properties into Tear Type prediction model, as in figure 5.26, there is a large deviation between horizontal component of the sandstone 60° results and the shallower cutting angles. The fact that the horizontal force starts to deviate significantly when $\alpha_c = 60°$ from the other cutting angles, is because the shear angle β becomes very small. A decreasing shear angle, indicates a larger failure plane. This means that more material has to be removed, consequently increasing the cutting forces. The vertical component remains relatively the same and is significantly lower than the horizontal force. For both rock compositions it clearly shows that Miedema's model is underestimating the measured horizontal and vertical forces. As for this model, the rock's resistance to reach the desired cutting depth, is not incorporated. It is therefore assumed that the cutting depth is instantly reached and constant over the cutting trajectory.

SANDSTONE

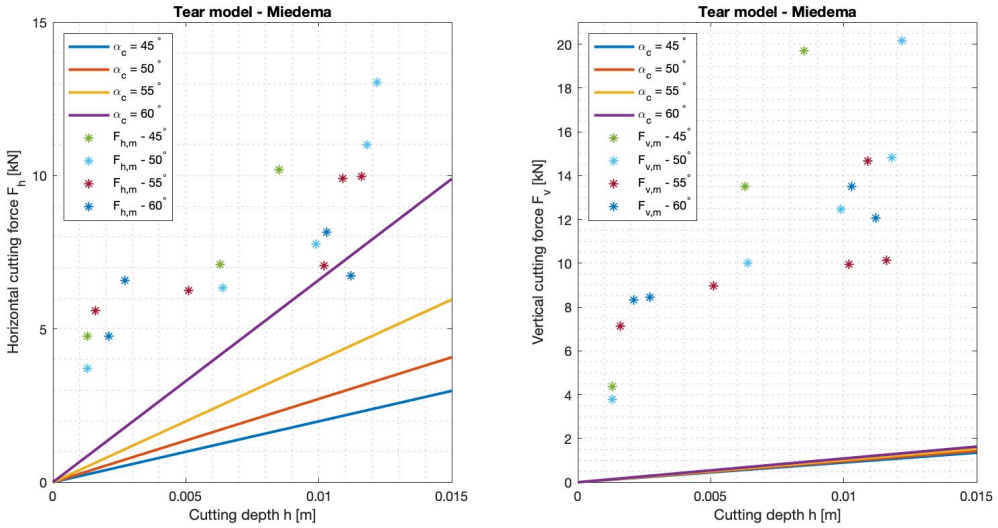

Figure 5.26: Outcomes Tear model Miedema - Sandstone

ARTIFICIAL ROCK

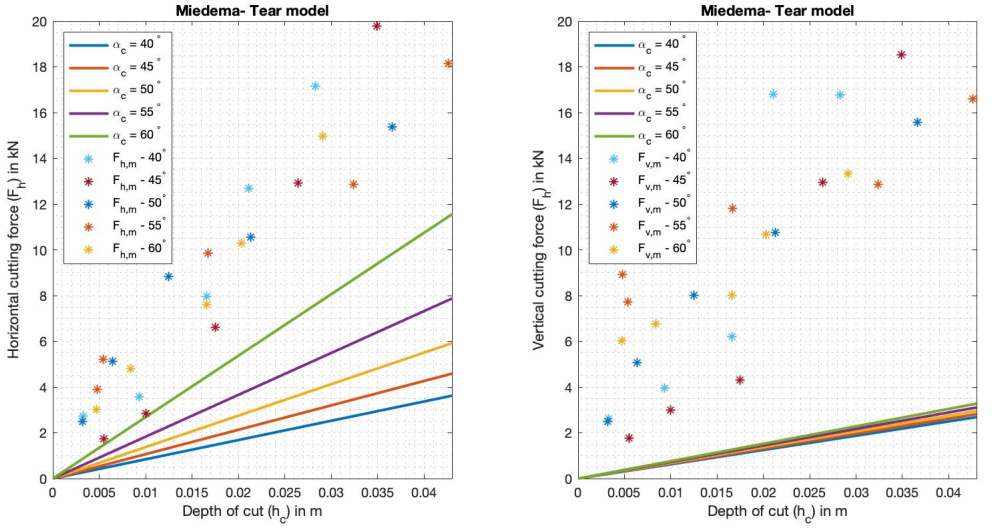

Figure 5.27: Outcomes Tear model Miedema - Concrete

6

NUMERICAL MODELLING

This chapter considers and explains two different model approaches for predicting the peak cutting forces of the rock cutting process. The most suitable model approach will be chosen and compared to the experimental measurements.

6.1. COMBINED FORCE BALANCE MODEL

In literature, most force prediction models are derived in terms of a force balance for one specific failure mechanism. When looking critically to the cutting process, and thus the present failure mechanisms, it is observed that three different physical phenomena are responsible for the total force output, namely *crushing*, *shear failure* and *tensile failure*. Verhoef [6] also observed a combination of failure types during the rock cutting process. Near the tip of the pickpoint an accumulation of crushed material forms a plastic zone of high compressive stresses. What basically happens is that the rock's internal structure fails continuously due to shearing of the small granular particles. The accumulation of these fine-grained particles is called the plastic deformation zone, or crushed zone. Since there is a localized pressure build up within the crushed zone, one can imagine that the stresses within this plastic region contribute significantly to the total cutting forces. The existing prediction models in literature describe the cutting process in two-dimensional space. The performed cutting experiments show that the process needs to be considered in three-dimensional space, as chips are also breaking out. This means that the initiated cracks do not only propagate in the XZ-plane, but also in the YZ-plane.

The existing model comparison in section 5.5 shows that for the Nishimatsu [2] model, where shear failure is the dominant failure mechanism, the horizontal (F_h) and vertical (F_v) forces are underestimating measured forces. The model of Evans [1], which assumed only tensile failure, overestimated the cutting forces drastically, especially with the application of a large cutting angle. The tear model by Miedema [12], which also assumes only tensile failure, underestimates the cutting forces for cutting angles $\leq 55°$, but overestimates them for larger cutting angles. Based on the results of these prediction models, the author states that the the cutting process is most probably a combination of both failure mechanisms. Critical experimental analysis of the cutting process, individual chips, force-time data and production measurements show that, indeed, three different failure mechanisms are present in cutting rock by using the assigned pickpoint. The only question is what the total force distribution may be due to the combination of shear failure, tensile failure and compressive stresses within the crushed zone by changing the input parameters of the cutting experiments. Video analysis shows that the development of crushed material is always present during cutting, independent of the cutting depth h_c. The presence of shear and tensile failure do depend on the cutting depth, meaning that one, or both, of these mechanisms will not always be apparent. When considering an ideal situation where only fine material is being produced, it indicates that shear and tensile cracks were not able to develop throughout the material, meaning that no chips were formed. The presence of chips depends on several factors, such as the brittleness B of the rock, cutting depth h_c and cutting angle α_c. When having a very ductile material (e.g. low brittleness number), it is most likely that ductile failure is dominant within the cutting process, leading to plastic failure. This means that less chips are being formed and the amount of crushed material will be dominant. Furthermore, the development of chips are being retained by applying a shallow cutting depth an steep cutting angle. When h_c is too shallow, the distance for crack to propagate to the rock's horizontal interface is too small.

The principle for the development of this force prediction model rests on the combination of the three mentioned failure mechanisms (e.g. crushing, shearing and tensile failure). Figure 6.1 shows a schematic representation of the force prediction model. The assumption is made that first a crushed zone is developing in front tip of the pickpoint, resulting in high compressive stresses. The stress level within this crushed zone can be determined from the performed indentation experiments, found in section 4.1.3. Due to the accumulation of crushed material, the size of the crushed zone increases over the cutting trajectory, to a certain extend. After a period of time during the cutting process, the crushed zone can be considered as fully developed, meaning that its size will not further increase. Though, it must be noted that the size of the crushed zone may fluctuate, as the breakage of chips may happen in a cataclysmic manner. This means that the crushed zone needs to periodically redevelop in size when a chip bursts out. It is assumed that the stresses within this plastic region decrease when moving to its outer boundary. At its perimeter the stress decays to the cohesion, which the shear strength property of the rock formation. This implies that, partly, chip formation is due to shear failure, failing along the shear plane under an angle β_s. Shear failure is mostly dominant when shallow cuts are being applied on the rock specimen. When increasing the cutting depth, failure due to the exceedance of the tensile strength will become more apparent. It is assumed that this happens at the point where the cohesive strength of the rock has decayed to the tensile strength. The tensile crack will then propagate in the direction of β_t. The approach for determining cutting forces due to the combination of these three failure mechanisms will be explained in the upcoming sections, where the crushed zone stresses and the fraction of shear and tensile stresses will be elaborated, separately.

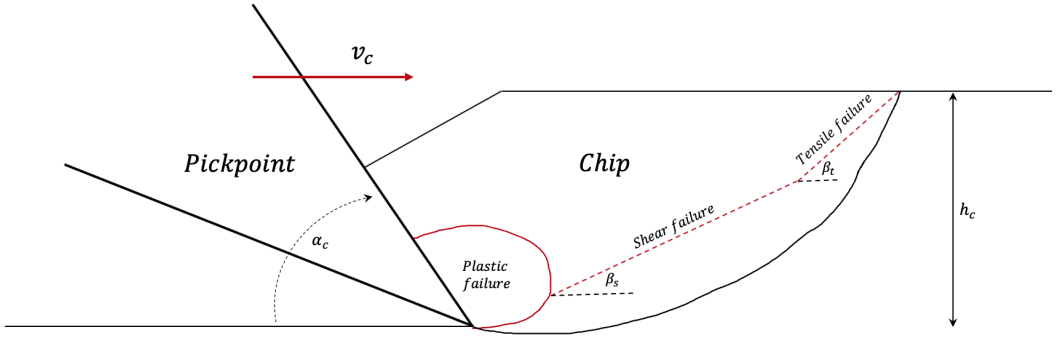

Figure 6.1: Schematic overview of all assumed present failure mechanisms during cutting

6.2. CRUSHED ZONE STRESSES

The stress level within the crushed zone can be determined according to the indentation data that has been gathered within the preliminary data acquisition. During the indentation tests for both sandstone and concrete, the aim was to determine the Indentation Hardness Index (IHI), which is a measure for the toughness of the material. A suggested method by Szwedzicki [20] was used to accurately determine these values. It must be noted that the indentation results for the concrete samples were not satisfactory, since the limit of the linear-elastic region was not reached. This due to an insufficient penetration depth of the cone. Based on the sandstone results, and comparing the UCS and BTS values, an educated guess has been conducted to estimate the peak force and corresponding penetration depth at the end of the linear-elastic region for the concrete samples. T.Rutten [11] assumed that the stress within the crushed zone is equal to $3{\cdot}\sigma_{ucs}$ for all tested samples. In practice, this coefficient is different for every rock composition.

The forces due to crushing of the intact rock near the tip of the pickpoint changes by varying the cutting depth h_c and cutting angle α_c. When increasing the h_c or α_c the indentation area A_{ind} of the pickpoint increases, meaning that the crush forces must be a function of this indentation area. Equation 6.1 shows the constructed formula for determining the total cutting force due to crushing. This shows that the multiplication of the indentation coefficient K_{ind} with the UCS value of the rock determines the stress level within the crushed zone. Since the shear strength of both rock compositions are already known, the two variables left to calculate are K_{ind} and A_{ind}.

$$F_{crush} = K_{ind} \cdot \sigma_{ucs} \cdot A_{ind} \tag{6.1}$$

6.2.1. INDENTATION COEFFICIENT

To determine the indentation coefficient K_{ind} for both the sandstone and concrete samples, the force-penetration graphs need to be analyzed, separately. The indentation force and corresponding cone penetration at the end of the linear-elastic region indicates the hardness of the material. By knowing the applied load with the resulting vertical indentation, the indentation area of the cone can be determined. Figure 6.2 shows a schematic overview of the cone penetration test, where the red hatched area represents the indentation distance of the cone into the material. By knowing the indentation depth h_{ind}, the indentation area, known as the spherical cap of the cone, can be calculated as

$$A_{cap} = 2 \cdot \pi \cdot R_{tip} \cdot h_{ind} \tag{6.2}$$

Where R_{tip} is the radius of the cone tip, which is a constant value. A_{cap} is the indentation area of the cone tip. This area can be seen as the footprint of the cone tip into the rock due to vertical compression. By knowing the indentation area of the cone A_{cap} and its corresponding indentation force F_{ind}, an estimate can be made of the stresses within the crushed zone σ_{crush}.

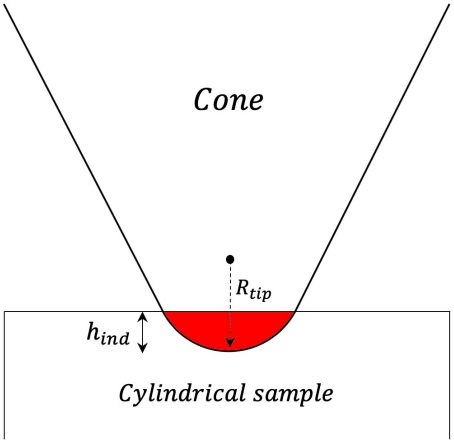

Figure 6.2: Front view of conical indenter to determine the indentation area

As known, the point at which fine crushing transitions to crack initiation and propagation within the internal structure of the cylindrical specimen, is to be used. Appendix B shows the results of the sandstone and concrete indentation tests that are used for the comparison analysis. It must be noted that, for the concrete, the indentation depth was insufficient to visualize the limit of the linear-elastic region. Though, the Indentation Hardness Coefficient was able to be determined by calculating the gradient of the force-penetration curve. This means that ratio of indentation force F_{ind} and corresponding indentation depth h_{ind} is approximately the same along within this linear-elastic region. Based on these numbers, the stresses within the crushed zone can be calculated by

$$\sigma_{crush} = \frac{F_{ind}}{A_{cap}} \tag{6.3}$$

Based on equation 6.3, the indentation coefficient K_{ind} can be determined. To express the the crushing forces in terms of the rock's UCS value, K_{ind} needs to be expressed as a multiplication factor. This variable can be obtained by the σ_{crush}-to-σ_{ucs} ratio.

$$K_{ind} = \frac{\sigma_{crush}}{\sigma_{ucs}} \tag{6.4}$$

Because the hardness of each individual (artificial) rock sample is different, it is obvious that the indentation coefficients also differ from each other. Table 6.1 shows the results that arose from the indentation tests and explained calculation methods. All separate values for K_{ind} will be applied within equation 6.1 to, eventually, determine the cutting forces due to crushing.

Sample	IHI [kN/mm]	F_{ind} [kN]	h_{ind} [mm]	A_{cap} [mm^2]	σ_{crush} [N/mm^2]	σ_{ucs} [N/mm^2]	K_{ind} [-]
S_1	15.24	13.27	0.875	27.49	482.74	35.59	13.56
S_2	15.24	13.27	0.875	27.49	482.74	35.59	13.56
S_3	12.61	12.36	0.98	30.79	401.46	26.27	15.31
S_4	12.18	14.68	1.21	37.88	387.66	15.15	25.59
$7-11-B_3$	2.30	6.44	2.80	87.96	73.21	7.09	10.33
$7-11-B_2$	2.86	6.29	2.20	69.12	91.04	8.49	10.72
$7-11-B_5$	2.07	4.97	2.40	75.40	65.89	7.09	9.29
$7-11-B_4$	2.80	6.16	2.20	69.12	89.13	8.58	10.39
$7-11-B_6$	2.80	6.46	2.30	72.26	89.13	7.37	12.10

Table 6.1: Indentation test results for the determination of the indentation coefficient K_{ind}

6.2.2. SIZE OF THE CRUSHED ZONE

The size determination of the crushed zone is in literature, still, a very complex phenomena. In previous research Verhoef [6] stated that approximately 90% of the cutting energy is due to the high compressive stresses within the crushed zone, near the tip of the pickpoint. As the indentation coefficient K_{ind} has already been determined in 6.2.1 for both rock compositions, the only unknown variable to determine the cutting forces due to crushing of fine material, is the indentation area of the pickpoint A_{ind}. For calculating this indentation area, first the size of the crushed zone needs to be determined.

By critically analyzing the cutting trajectories after the execution of all sandstone and concrete tests, a striking discovery was made. As known, the input parameters (α_c, h_c) were varied each test, which resulted in different magnitudes for the cutting forces and production measurements. At the bottom of the cutting groove a smooth path was observed that appeared to have the same shape as the pickpoint. The height of this trapezoid-shaped path varied as the cutting depth increased. Figure 6.3 clearly shows a smooth path approximately following the shape of the pickpoint. Hypothetically, the writer states that this trapezoid-shaped area is caused by the development of the crushed zone, meaning that the force transmission due to particle-to-particle interaction is localized within this region. To determine the height of this crushed zone, the production of all sandstone and concrete cutting experiments is to be studied, again. As known, crushed material only consists out of very fine particles. It is thus of interest to know how the total volume of fine particles (<1mm, 1-2mm) is distributed over the complete cutting trajectory, when varying the input parameters.

Figure 6.3: Visible smooth cutting path at bottom of the groove

Appendix C.7 and C.5 shows the collection of production data, where the mass of fine particles, obtained from the sandstone and concrete cutting tests, is found. Only the collection of particles smaller than 2mm are used to account for the crushed zone volume. Figure 6.5 shows a cross-sectional area of an arbitrary block that already has been cut. This schematic representation displays a typical chip and bottom groove shape that has been observed during testing. On the basis of these visual observations, an elaboration can be made for the size of the crushed zone. As known, the crushed zone needs some time to develop in size over the length of the cutting trajectory. This means that the volume of the crushed zone will fluctuate over the length of the block. Experimental observations have shown that, when a chip cataclysmically breaks out, crushed material mostly follows, destructing the formation of the crushed zone. This means that the crushed zone is constantly fluctuating in size. To be able to determine the height of this plastic region, an equivalent length L_{eq} is to be assumed. This equivalent length accounts for the fluctuations in crushed volume, meaning that a constant cross-sectional area can be assumed over this length. This makes it possible to calculate the height of the crushed zone. The equivalent length is assumed to be 0.7· length of the block, written as: $L_{eq} = K_{eq} \cdot l_b = 0.7 \cdot l_b$. It is said that within the first 10% of cutting, the crushed zone is developing until a certain size. Within section 2 another 10%

is lost due to the constant fluctuation of the crushed zone size. Within the last sector, it was observed that most of the time a large rock piece broke out at the end of the block, meaning that no accumulation of the crushed material was apparent. Figure 6.4 shows a schematic overview of the assumed percentage lost in each section due to size development and fluctuations of the crushed zone. These losses have been implemented to account for a constant crushed zone height.

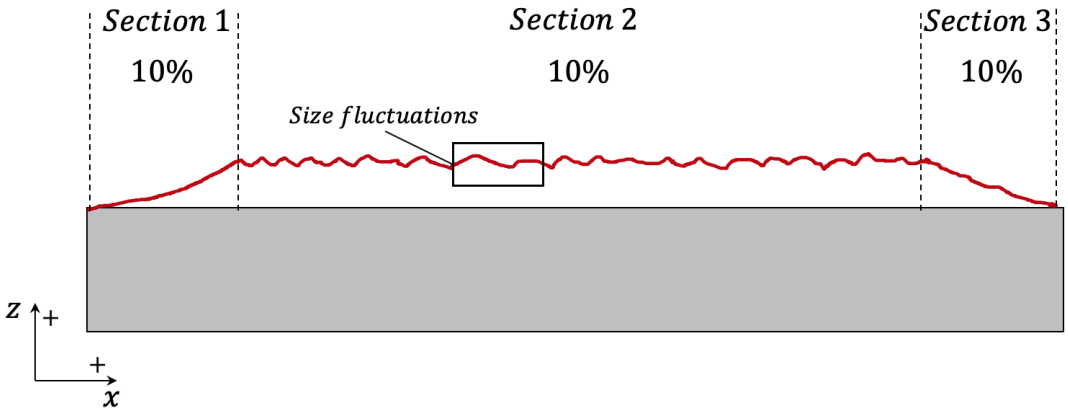

Figure 6.4: Crushed zone size development and fluctuations

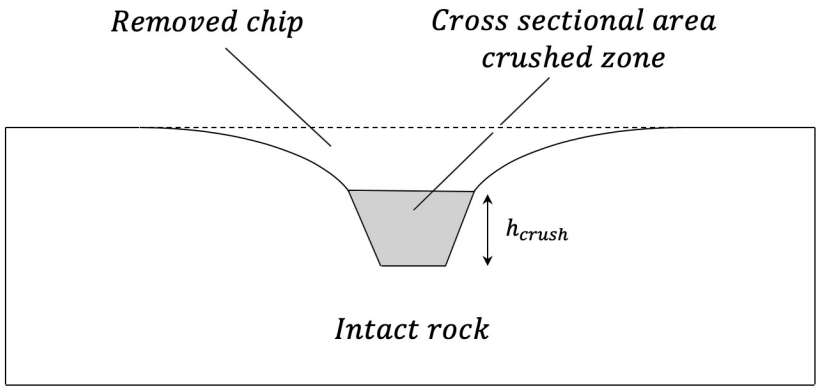

Figure 6.5: Cross sectional view of cutted rock sample

By changing the cutting angle α_c and cutting depth h_c, the volume of crushed material also changes. This means that each cutting experiment will have a different crushed zone height h_{crush}. A volume balance can be set up to calculate the unknown crushed zone height. Equation 6.6 shows a second order degree polynomial function, which can be numerically solved for the crushed zone height $h_{\alpha_c,i}$ (h_{crush} in figure 6.5), depending on the preset cutting angle α_c. Where $i\{1,2...5\}$ is the number of the consecutive tests for the same cutting angle, but different cutting depths. To determine the crushed zone height correctly, the projected area A_{pr} of the pickpoint is used, multiplied with the equivalent length of the crushed zone ($K_{eq} \cdot l_b$) and set equal to the crushed zone volume $V_{\alpha_{c,i}}$ of the experiment in question.

$$\left[tan(\eta) \cdot \frac{h_{\alpha_{c,i}}^2}{sin^2(\alpha_{c,i})} + \frac{h_{\alpha_{c,i}}}{sin(\alpha_{c,i})} \cdot w\right] \cdot K_{eq} \cdot l_b \cdot cos(90° - \alpha_{c,i}) = \frac{m_{\alpha_{c,i}}}{\rho_{s,c}} = V_{\alpha_{c,i}} \tag{6.5}$$

Where l_b is the total length of block, $m_{\alpha_{c,i}}$ the total mass of the crushed material, depending on the cutting depth and cutting angle and $\rho_{s,c}$ the density of the sandstone or concrete. The sandstone and concrete production data, found in appendix C.7 and C.5, respectively, shows that the dispersion in the production of fine crushed material (e.g. <1mm, 1-2mm) is relatively small, when changing the cutting angle and increasing the cutting depth. For predicting the amount of crushed volume at an arbitrary cutting depth for concrete and sandstone, figure C.34 and C.35, in appendix C.6 and C.8, respectively, can be used.

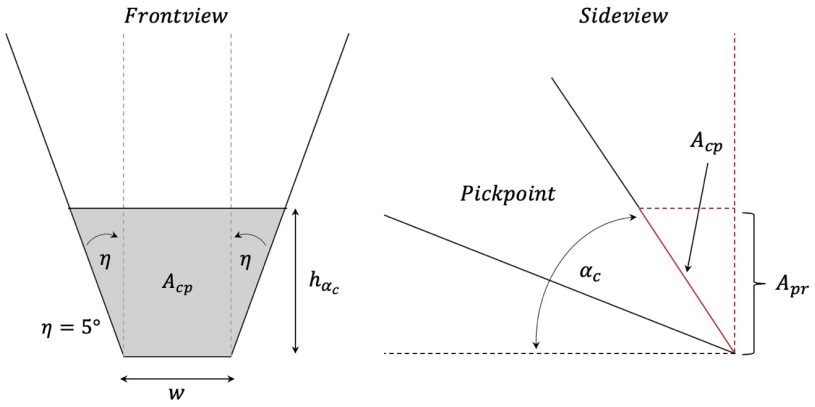

Figure 6.6: Front and side view of pickpoint to define the indentation area A_{cp}

Where η defines the shape of the pickpoint, which is a constant value. To partly validate if the self-made assumptions for the crushed zone theory are correct, the calculated crushed zone height can be compared with the experimental height measurements of the smooth cutting groove. Figure 6.7 compares the calculated data with the measured data of the sandstone and concrete samples.

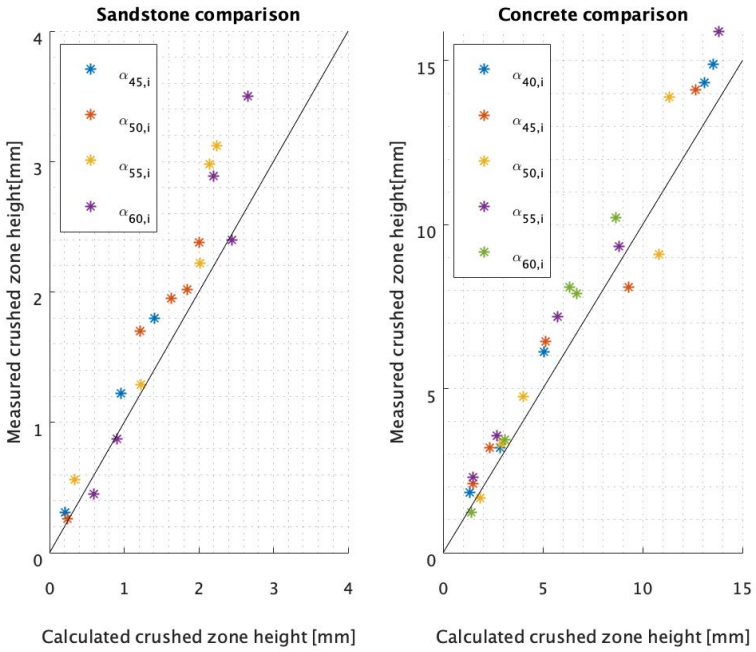

Figure 6.7: Crushed zone height comparison between measured and calculated values

By comparing both figures, it is clearly seen that the crushed zone height of concrete is significantly higher than the sandstone cutting experiments. This can be explained by the fact that the shear capacity of the artificial rock is lower than the sandstone. Consequently, the accumulating isotropic compression near the tip of the pickpoint creates a larger-sized compression zone. This means that the concrete acts more ductile than the sandstone. Furthermore, the resulting cutting depth of each experiment also influences the amount of crushed material. The cutting groove data in appendix C.2 and C.1 shows that the desired cutting depth of the concrete experiments was better reached, meaning that amount of crushed material must be more than the sandstone. The obtained cutting depth can be fed back by the resistance material gives due vertical compression. This is correlated to the hardness of the material (section 4.1.3). By keeping this is in mind, the remaining variable A_{ind} of equation 6.1 can be determined. It has been assumed that the contacting area between the pickpoint and fully developed crushed zone is equal to the projected interface A_{pr} of the pickpoint under an arbitrary cutting angle α_c. The crushed zone height $h_{\alpha_{c,i}}$, calculated in equation 6.5, is to be implemented in equation 6.6 to determine the indentation area A_{ind} of the pickpoint.

$$A_{ind} = \left[tan(\eta) \cdot \frac{h^2_{\alpha_{c,i}}}{sin^2(\alpha_{c,i})} + \frac{h_{\alpha_{c,i}}}{sin(\alpha_{c,i})} \cdot w \right] \cdot cos(90° - \alpha_{c,i}) \tag{6.6}$$

6.2.3. FORCES DUE TO CRUSHING

Data analysis of the rock cutting experiments showed that, for sandstone, the vertical forces appeared to be larger than the horizontal forces. When looking at the concrete experiments, the horizontal and vertical force component appeared to be approximately the same. By critically analyzing all the force diagrams, the writer discovered a certain pattern concerning the shape of the output signal. Figure 6.8 shows the output signal of an arbitrary cutting experiment. The discovery was made that a certain basic stress level was present during all the force outputs for both sandstone and concrete. This basic stress level can be defined as a boundary where the cutting force do not go below. The writer states that this basic stress level is composed out of the dynamic friction between the rock and pickpoint and the stresses within the crushed zone. This hypothesis can be supported by the fact that the vertical forces due to friction, in this case, is higher than the horizontal component, because the friction coefficient is below 1. Within the existing cutting theories, the vertical forces are, most frequently, higher than the horizontal forces. This is due to the fact that a constant cutting depth is assumed and always reached. In practice this is a wrong assumption. Depending on the hardness of the rock, the vertical component really needs to deliver a high amount of force to achieve the desired cutting depth.

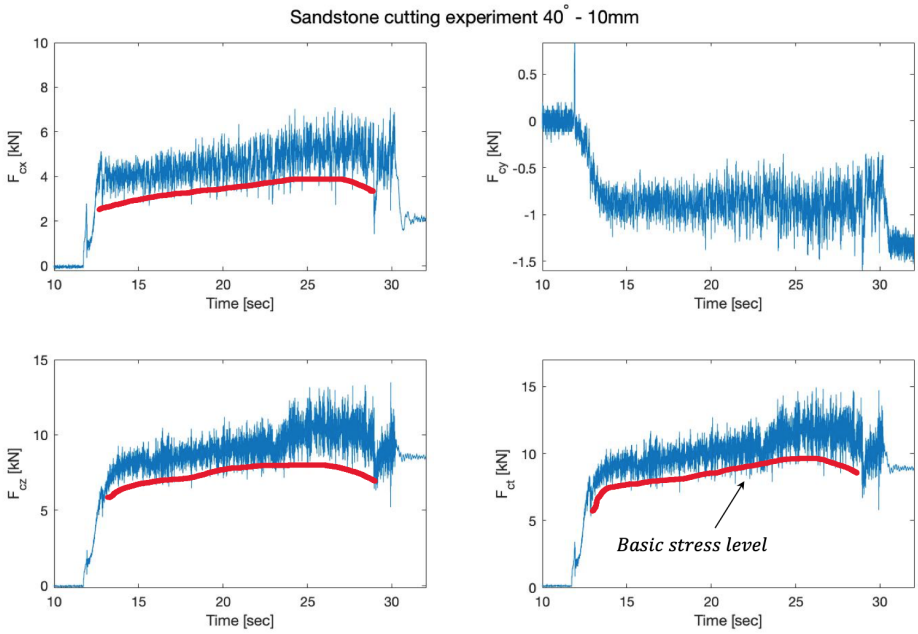

Figure 6.8: Indication of the basic stress level that is present during cutting

Since the writer states that this basic stress level is composed out of the dynamic friction and crushed zone stresses, an expression needs to be found for the horizontal and vertical force component. For determining the forces due to these combined physical processes, it is assumed that the lower boundary of total forces F_b, designated as the basic stress level, is equal to the total crushed zone forces F_{crush}. The following expressions can be written for the horizontal and vertical force component, by implementing equation 4.10 in the total crushed zone force for both rock compositions.

$$F_b = F_{crush} = \sqrt{\left(\frac{F_{h,crush}}{\mu_d}\right)^2 + F_{h,crush}^2} \tag{6.7}$$

$$F_b = F_{crush} = \sqrt{\left(\mu_d \cdot F_{v,crush}\right)^2 + F_{v,crush}^2} \tag{6.8}$$

Section 4.1.6 contains the obtained dynamic friction coefficients between sandstone-steel and concrete-steel. By knowing this property, the horizontal and vertical component can be expressed in terms of F_{crush}. Both expressions for the sandstone and concrete will be given, separately. By incorporating the friction coefficient and solving equation 6.7 and 6.8 for sandstone, this leads to

$$F_{h,crush,s} = 0.36 \cdot F_{crush} \tag{6.9}$$

$$F_{v,crush,s} = 0.93 \cdot F_{crush} \tag{6.10}$$

Applying the same solving method by implementing the dynamic friction coefficient for concrete, gives the following relation between the horizontal and vertical forces

$$F_{h,crush,c} = 0.45 \cdot F_{crush} \tag{6.11}$$

$$F_{v,crush,c} = 0.89 \cdot F_{crush} \tag{6.12}$$

Because the indentation area A_{ind} has been determined in section 6.2.2, it is now possible determine the magnitude of forces in horizontal and vertical direction due to crushing. Figure 6.9 shows the force balance between the pickpoint and crushed zone that has been assumed for this situation.

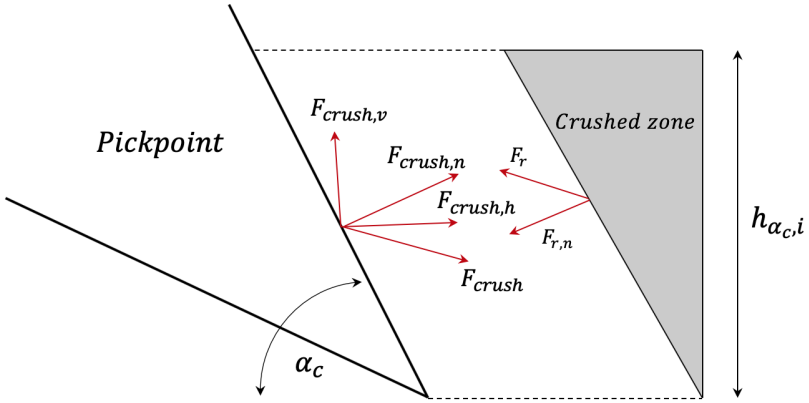

Figure 6.9: Free Body Diagram crushed zone forces

SANDSTONE

$$F_{h,crush,s} = 0.36 \cdot K_{ind} \cdot \sigma_{ucs} \cdot \left[tan(\eta) \cdot \frac{h^2_{\alpha_{c,i}}}{sin^2(\alpha_{c,i})} + \frac{h_{\alpha_{c,i}}}{sin(\alpha_{c,i})} \cdot w \right] \cdot cos(90^\circ - \alpha_{c,i}) \tag{6.13}$$

$$F_{v,crush,s} = 0.93 \cdot K_{ind} \cdot \sigma_{ucs} \cdot \left[tan(\eta) \cdot \frac{h^2_{\alpha_{c,i}}}{sin^2(\alpha_{c,i})} + \frac{h_{\alpha_{c,i}}}{sin(\alpha_{c,i})} \cdot w \right] \cdot cos(90^\circ - \alpha_{c,i}) \tag{6.14}$$

ARTIFICIAL ROCK

$$F_{h,crush,c} = 0.45 \cdot K_{ind} \cdot \sigma_{ucs} \cdot \left[tan(\eta) \cdot \frac{h^2_{\alpha_{c,i}}}{sin^2(\alpha_{c,i})} + \frac{h_{\alpha_{c,i}}}{sin(\alpha_{c,i})} \cdot w \right] \cdot cos(90^\circ - \alpha_{c,i}) \tag{6.15}$$

$$F_{v,crush,c} = 0.89 \cdot K_{ind} \cdot \sigma_{ucs} \cdot \left[tan(\eta) \cdot \frac{h^2_{\alpha_{c,i}}}{sin^2(\alpha_{c,i})} + \frac{h_{\alpha_{c,i}}}{sin(\alpha_{c,i})} \cdot w \right] \cdot cos(90^\circ - \alpha_{c,i}) \tag{6.16}$$

It must be mentioned that some empirical parameters, in determining the forces due to crushing, may deviate from the actual value, potentially causing an error in the force prediction model. The horizontal and vertical crush component differ from each other based on the frictional contact between the pickpoint and rock interface. Based on the friction experiments performed in section 4.1.6, a certain friction coefficient was determined. The accuracy of this parameter may, in practice, deviate from the actual value and fluctuate along the complete cutting trajectory. This means that the force distribution in horizontal and vertical direction is sensitive to this friction coefficient. The reader must be aware that these values may slightly be different in practice.

Furthermore, another parameter that could differ from its actual value is the calculated crushed zone height. The crushed zone height $h_{\alpha_{c,i}}$ affects the indentation area A_{ind} of the pickpoint and is calculated according to the production data. Subsequent to this is the equivalent L_{eq} has been assumed where the crushed zone height is considered to be a constant value. This equivalent length incorporates the periodically fluctuations in crushed zone size. Because it is very difficult to see what the actual behaviour of the crushed zone size is along the cutting trajectory, a factor of $0.7 \cdot l_b$ is assumed to account for these fluctuations. The author is aware that this factor may diverge in practice.

Another parameter that is sensitive to the outcome of the prediction model, is the indentation coefficient. If the indentation coefficient is not correctly determined, the expression for the stresses within the crushed zone may change significantly.

6.3. COMBINED SHEAR AND TENSILE COMPONENT

Section 6.1 briefly pointed out that three different failure mechanisms take place during the cutting of rock (e.g. plastic, shear and tensile failure). In principle, the plastic deformation zone is also failing due to shearing, but is considered as a separate failure mechanism. By keeping figure 6.1 as reference, it is assumed that a major shear failure is initiated at the boundary of the crushed zone, since this is the transition point of the decay in crushed zone stresses to the cohesive shear strength property of the rock. The crushed zone is assumed to act as fully developed stress zone, having a spherical shape. Figure 6.10 shows a schematic representation of the shear-tensile failure part. For the sake of having a clear overview of the direction of forces and stresses, the crushed zone is not incorporated within this figure. It is expected that shear and tensile failure happens approximately simultaneously, but at a different fraction length. Figure 6.10 shows the length of the failure plane $l_{failure}$ under a shear angle β_s when tensile failure is not apparent. Because the assumption is made that both failure mechanisms take place, the variable K_s is introduced. This parameter is called the '*shear crack factor*' and indicates the fraction that is subjected to shear failure along the failure plane $l_{failure}$. The remaining fraction of the failure plane is then subjected to only tensile failure. In literature it is often mentioned that the angle of the tensile failure plane is smaller than the shear angle β_s. To partly verify this, a broad range of collected chips were analyzed and studied on its shape and failure behaviour. It was observed that, for various h_c and α_c, the failure plane deflected under a small angle starting at the end of the shear plane, propagating to the rock's top interface. This may indicate that tensile failure takes at a certain fraction of $l_{failure}$.

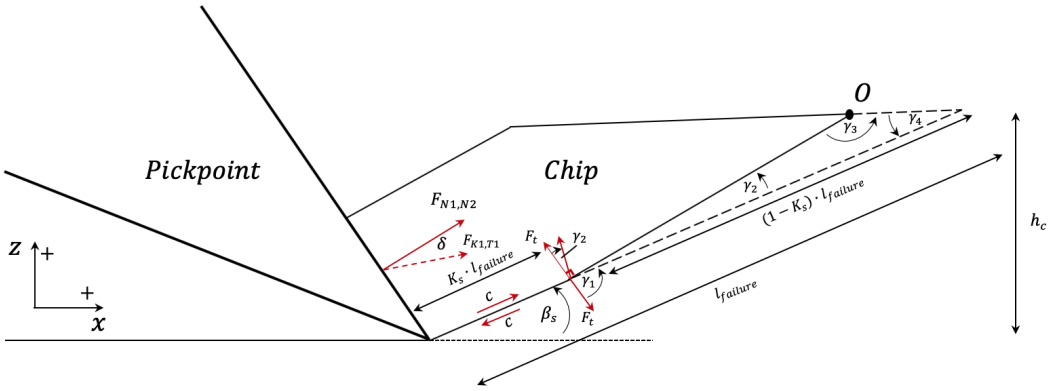

Figure 6.10: Schematic representation of shear and tensile failure component

To predict the peak forces of the cutting process in three-dimensional space, it is of great importance to know what the total failure area is within the rock's internal structure that is subjected to both shear and tensile stresses. Visual observations and video analysis showed that a frequently returning particular chip shape appeared during the rock cutting experiments. Figure 6.11 shows a schematic and real life representation of this typical chip shape that was apparent for both sandstone and concrete. This shape is kept as reference to determine the failure area of the of the chip. The failure area of the chip is considered to be the bottom surface of the inclined failure plane.

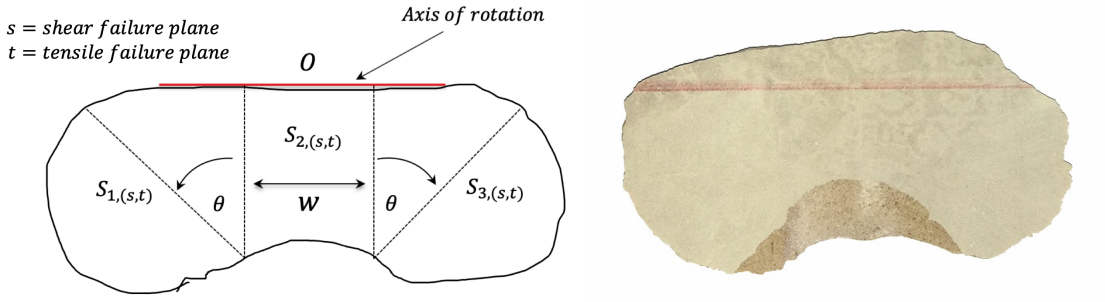

(a) Schematic representation of typical chip shape

(b) Typical chip shape that was observed during testing

Figure 6.11: Typical chip shape as a result of experimental research

Because the assumption is made that two failure mechanisms take place at the same time, also two different failure areas have to be calculated that correspond to the fraction length of the total failure plane. Each failure area can be subdivided into three sections $S_{1,(s,t)}$, $S_{2,(s,t)}$ and $S_{3,(s,t)}$. A critical chip shape study revealed that $S_{1,(s,t)}$ and $S_{3,(s,t)}$, approximately, have a radius that is equal to the length of the failure plane $l_{failure}$. This means that the failure area can be approximated by integrating the length of each failure plane over θ (figure 6.11a). The total failure plane area can be expressed as

$$S_{failure} = \sum_{n=1}^{3} S_{n,s} + \sum_{n=1}^{3} S_{n,t} \tag{6.17}$$

$S_{n,s}$ and $S_{n,t}$ represent the area of the total shear and tensile failure plane, respectively.

6.3.1. SHEAR FORCE COMPONENT

The shear force component is dominated by the resistance of the rock due to shearing. For a shear plane to be developed, the cohesive shear strength of its internal structure needs to be exceeded. This stress parameter acts along the complete shear failure plane of the chip. An important coefficient for determining the magnitude of the shear area is the shear coefficient K_s. This experimentally-based parameter describes the fraction of the total failure plane that is only subjected to shear failure. Section 6.1 already pointed out that the crushed zone, that is developing in front of the cutting tool, is assumed to have a spherical shape. As stress within this plastic region is decaying from the tip of the blade to its outer boundary, a basic height needs to be taken into account at which the shear crack starts to develop. Figure 6.12 shows a schematic representation of the assumed crushed zone shape and direction of the shear plane. To determine the length of the shear plane, first the height where the shear crack is initiated h_s needs to be calculated. Since the transition point of σ_{crush} to c lies at the boundary of the crushed zone, its radius can be used to determine h_s.

$$h_s = sin(\beta_s) \cdot h_{\alpha_{c,i}} \tag{6.18}$$

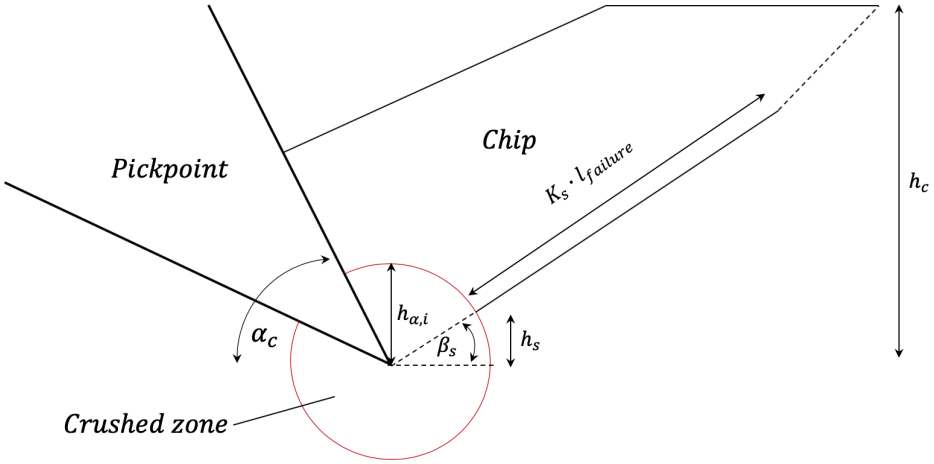

Figure 6.12: Schematic representation of length of the shear failure plane, incorporating the crushed zone shape

Now the height at which the major shear plane initiated is known, an expression for the shear plane length can calculated as $K_s \cdot (\frac{h_c - h_s}{sin(\beta_s)})$. Keeping the typical chip shape of figure 6.11a as reference, the failure area, where only the cohesion acts, can be calculated according to

$$S_s = \sum_{n=1}^{3} S_{n,s} = \int_{-\frac{\pi}{2}}^{\frac{\pi}{2}} \int_{0}^{K_s \cdot \left(\frac{h_c - h_s}{sin(\beta_s)}\right)} r_s \; dr_s d\theta + \int_{0}^{K_s \cdot \left(\frac{h_c - h_s}{sin(\beta_s)}\right)} w \; dr_s = \frac{\pi}{2} \cdot \left(K_s \cdot (\frac{h_c - h_s}{sin(\beta_s)})\right)^2 + w \cdot K_s \cdot (\frac{h_c - h_s}{sin(\beta_s)}) \tag{6.19}$$

Where r_s is the length of the shear plane. By making use of the shear strength property c of the rock and calculated shear area of the shear plane, a force balance in X- and Z-direction can be constructed to determine the resultant forces on the rake face of the pickpoint. To visualize the direction of forces, a free body diagram is drawn as in figure 6.13.

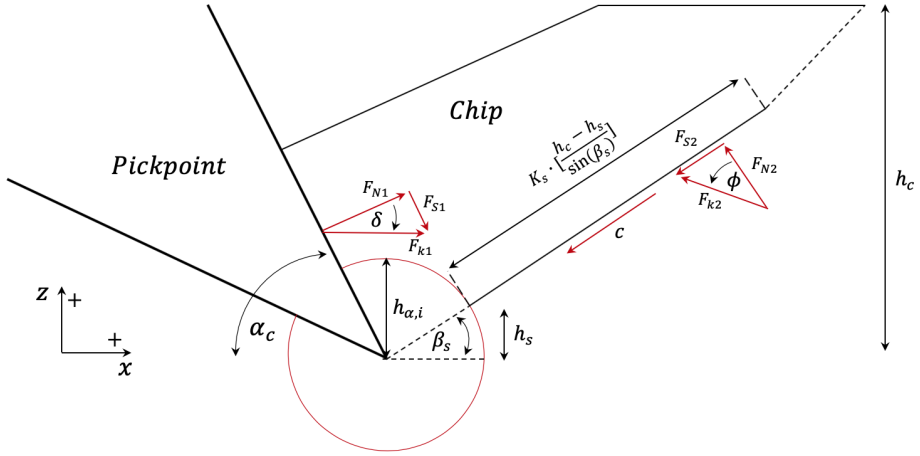

Figure 6.13: Free Body Diagram shear part of forces

The following force balance in X- and Z-direction follows from the free body diagram. It must be noted that the cohesive forces play a dominant role, meaning that gravity and inertia effects can be neglected.

$$\Sigma F_{s,x} = 0 \tag{6.20}$$

$$F_{k1} \cdot sin(\alpha_c + \delta) - F_{k2} \cdot sin(\beta_s + \phi) - c \cdot cos(\beta_s) \cdot \sum_{n=1}^{3} S_{n,s} = 0 \tag{6.21}$$

$$\Sigma F_{s,z} = 0 \tag{6.22}$$

$$F_{k1} \cdot cos(\alpha_c + \delta) + F_{k2} \cdot sin(\beta_s + \phi) - c \cdot sin(\beta_s) \cdot \sum_{n=1}^{3} S_{n,s} = 0 \tag{6.23}$$

It is of interest to determine the magnitude of the reaction force on the rake face of the pickpoint F_{k1}. The constructed force balance equations in X- and Z-direction both contain two unknown parameters F_{k1} and F_{k2}. By substituting equation 6.21 into equation 6.23, an expression for reaction force F_{k1} can be given. By multiplying equation 6.21 with $cos(\beta_s + \phi)$ and equation 6.23 with $sin(\beta_s + \phi)$ the denominators, in rearranging the fused equations, can be set equal. The application of several goniometric rules and further simplification, leads to the following expression for F_{k1}

$$F_{k1} = \frac{c \cdot [S_{1,s} + S_{2,s} + S_{3,s}] \cdot cos(\phi)}{sin(\alpha_c + \phi + \beta_s + \delta)} \tag{6.24}$$

The total force component F_{k1} can be decomposed into X- and Z-direction to determine the horizontal and vertical cutting forces due to shear failure.

$$F_{h,k1} = \frac{c \cdot [S_{1,s} + S_{2,s} + S_{3,s}] \cdot cos(\phi)}{sin(\alpha_c + \phi + \beta_s + \delta)} \cdot sin(\alpha_c + \delta) \tag{6.25}$$

$$F_{v,k1} = \frac{c \cdot [S_{1,s} + S_{2,s} + S_{3,s}] \cdot cos(\phi)}{sin(\alpha_c + \phi + \beta_s + \delta)} \cdot cos(\alpha_c + \delta) \tag{6.26}$$

The complete derivation for determining the force components due to shearing, can be found in Appendix D.1. The angle of the shear plane β_s can be determined in terms of the principle of minimum energy (e.g the point where the cutting energy is minimal). This is due to the fact that a shear crack propagates in the direction of least resistance. The minimum energy principle can be written as

$$\frac{dF_{h,k1}}{d\beta_s} = 0 \tag{6.27}$$

Solving equation 6.27, the following expression arises, according to Kerkvliet [27].

$$\beta_s = \frac{\pi}{2} - \frac{\alpha_c + \phi + \delta}{2} \tag{6.28}$$

6.3.2. TENSILE FORCE COMPONENT

To complete the combined force prediction model, it is assumed that a certain fraction of the total forces is due to the initiation of tensile cracking. The magnitude of this fraction highly depends on the cutting depth h_c and angle α_c. One can imagine that a sufficient cutting depth is required for a tensile crack to develop and, subsequently, be able to propagate to the rock's top interface. A tensile crack is initiated when local tensile stress exceeds the tensile strength capacity of the rock. Tensile stresses always act perpendicular to the direction of crack propagation. For the development of this model, it is assumed that the tensile stress on the rock formation acts perpendicular and linear decaying along the tensile plane. This means that the tensile strength along the tensile plane is not constant and will be zero at the rock's top interface. From a physical point of view this can be explained by the fact that the energy that is needed to develop a crack is at the point of initiation. Meaning that the energy distribution along the tensile plane should decay. Figure 6.14 shows the free body diagram for the tensile part of forces. It can be seen that a moment is exerting around point O due to the tensile force F_{T2}, which acts $\frac{2}{3}\cdot t_c$ from point O. By critically studying the failure paths of a collection of sandstone and concrete chips, it appeared that tensile cracks propagate in the direction of least resistance γ_2 to the rock's top interface. Many chips appeared to have this significant deflection of γ_2 , indicating that this part is most probably subjected to tensile failure. This angular parameter is assumed to be calculated according to equation 6.29 (Miedema [12]). Miedema used this angle of failure as a correction to the Tear Type, indicating that an optimum angle of failure is present, far away from the transition point from the Flow Type to the Tear Type.

$$\gamma_2 = \frac{\pi}{2} - \frac{\frac{\pi}{4} + \alpha_c + \delta + \phi}{2} \tag{6.29}$$

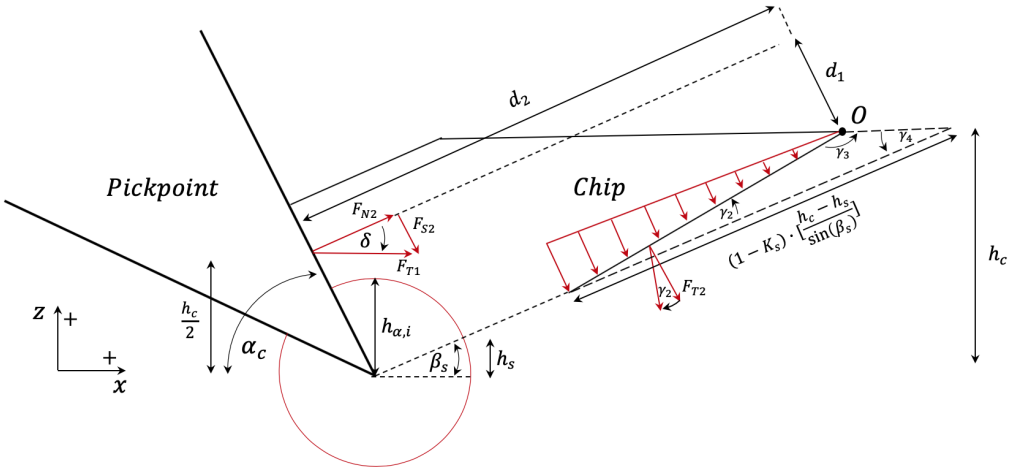

Figure 6.14: Free Body Diagram tensile part of forces

It is of interest to determine the reaction force on the rake face of the cutting tool. To do this, a moment equilibrium equation can be constructed. This moment equilibrium consists out of two force components, acting at a certain distance from rotation point O. As it is assumed that the mutual contact of the pickpoint and in-situ rock is at half of the cutting depth $\frac{1}{2}h_c$, at all times, it is said that reaction force F_{T1} will act in the middle of this plane. Since there is an interface friction present between the cutting face and (artificial) rock, F_{T1} acts under an angle δ, with respect to the normal force F_{N1} on the blade. For a moment to be created an arm needs to be present. Because F_{T1} does not act perpendicular to the rake face of the cutting tool, two arms (d_1,d_2) need to be calculated. Furthermore, an expression for the length of the tensile plane needs to be found, as F_{T2} acts along this failure plane. To do this, a collection of trigonometric functions need to be solved on the basis of the gray-shaded triangles in figure 6.15. It must be noted that the crushed zone is disregarded from the figure for the sake of keeping a clear overview. The radius of the crushed zone is incorporated within the calculations. Because both triangles have unequal angles and sides, the trigonometry law of sines needs to be applied.

$$\underbrace{\frac{sin(\gamma_2)}{t_a} = \frac{sin(\gamma_3)}{t_{b,2}} = \frac{sin(\gamma_4)}{t_c}}_{\text{Top triangle}} \quad and \quad \underbrace{\frac{sin(\gamma_2)}{b_2} = \frac{sin(\epsilon_3)}{t_s} = \frac{sin(\epsilon_2)}{t_{b,1}}}_{\text{Bottom triangle}} \tag{6.30}$$

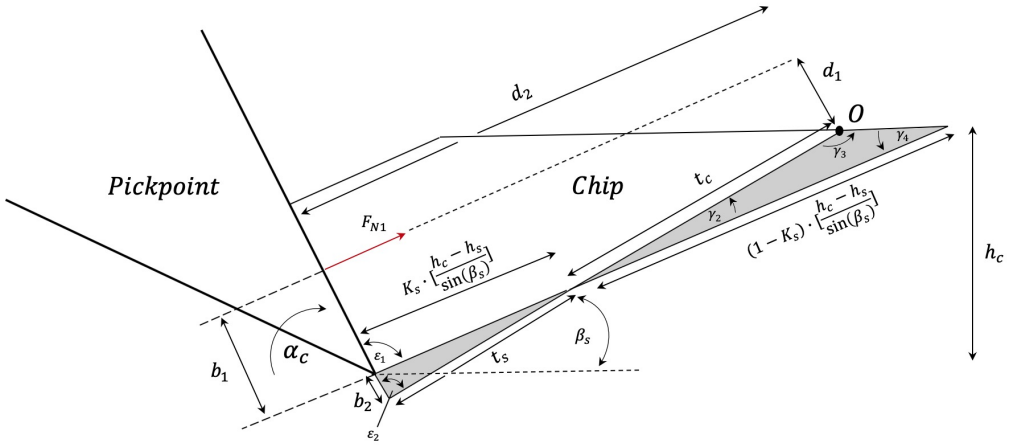

Figure 6.15: Dimensional calculations of shaded triangles

For convenience, both gray-shaded triangles will be considered, separately. Figure 6.16 displays the triangle that contains the deflection angle of the tensile crack γ_2. To determine the arm t_c of the critical tensile force around point O, the sine rule needs to be applied. Before doing this, a few angle expressions can be constructed to clarify the calculation.

$$\gamma_4 = \beta_s \tag{6.31}$$

$$\gamma_3 = 180^\circ - \gamma_2 - \gamma_4 \tag{6.32}$$

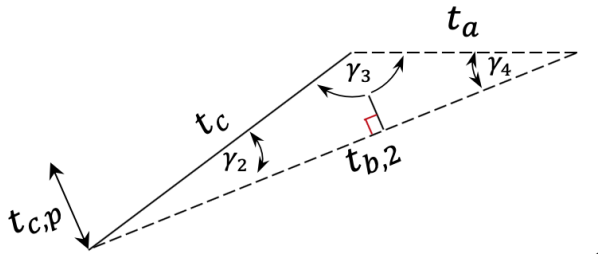

Figure 6.16: Variable top triangle for tensile part of forces

The length of the tensile plane t_c can be calculated by using the top triangle sine rule in equation 6.30. From here it follows that

$$t_c = \frac{t_{b,2} \cdot sin(\gamma_4)}{sin(\gamma_3)} = (1 - K_s) \cdot [\frac{h_c - h_s}{sin(\beta_s)}] \cdot \frac{sin(\gamma_4)}{\sin(\gamma_3)} \tag{6.33}$$

Where $t_{b,2} = (1 - K_s) \cdot [\frac{h_c - h_s}{sind(\beta_s)}]$. Now the arm of F_{T2} is known around point O, an expression for the two remaining parameters d_1 and d_2 has to be found. It is said that $d_1 = b_1 - t_{c,p}$, where b_1 acts in the middle of the $\frac{1}{2}h_c$ plane.

$$d_1 = \frac{h_c}{2 \cdot sin(\alpha_c)} - sin(\gamma_2) \cdot t_c \tag{6.34}$$

The perpendicular arm d_2 to the cutting face of the blade can be calculated by, partially, using the bottom triangle as in figure 6.17. For the sake of having a complete overview of all the goniometric expressions within the cutting configuration, an expression for ϵ_2 and ϵ_3 can be found

$$\epsilon_3 = 180^\circ - \underbrace{(180^\circ - \alpha_c - \beta_s)}_{\epsilon_1} \tag{6.35}$$

Now ϵ_2 can be expressed as

$$\epsilon_2 = 180^\circ - \epsilon_3 - \gamma_2 \tag{6.36}$$

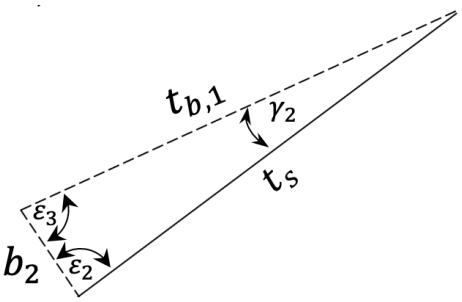

Figure 6.17: Variable bottom triangle for tensile part of forces

Keeping figure 6.15 as reference, it follows that

$$d_2 \approx t_{b,1} + cos(\gamma_2) \cdot t_c = K_s \cdot \left[\frac{h_c - h_s}{sin(\beta_s)}\right] + cos(\gamma_2) \cdot t_c \tag{6.37}$$

To complete the desired parameters for constructing the moment balance, the failure area, where σ_{bts} is acting, needs to be determined. The typical chip shape as in figure 6.11 is, again, kept as reference. An important variable to use within this calculation is the length of the tensile plane t_c. The total area of this tensile plane can, again, be separated into three sections $S_{1,t}$,$S_{2,t}$ and $S_{3,t}$. Where $S_{1,t}$ and $S_{3,t}$ use the length of the tensile plane as its radius, rotating over θ (figure 6.11a). $S_{2,t}$ is determined by using the constant blade width w property and length of the tensile plane. Combining this textual description into numerical form for the total area of the tensile failure plane can be expressed as

$$S_t = \sum_{n=1}^{3} S_{n,t} = \int_{-\frac{\pi}{2}}^{\frac{\pi}{2}} \int_{t_s}^{t_s+t_c} r_t \ \ dr_t d\theta + \int_0^{t_c} w \ \ dr_t \tag{6.38}$$

The first term in equation 6.38 is considered to be the outbreaking term, which is calculated as a circle segment, by keeping figure 6.11a as reference. The variable r_t is the radius of the tilted tensile plane. The unknown parameter t_s can be calculated from the bottom triangle sine rule in equation 6.30.

$$t_s = \frac{sin(\epsilon_3)}{\epsilon_2} \cdot t_{b,1} = \frac{sin(\epsilon_3)}{\epsilon_2} \cdot K_s \cdot \left[\frac{h_c - h_s}{sin(\beta_s)}\right] \tag{6.39}$$

Elaborating on the integral form of equation 6.38, gives the following expression arises for the total tensile failure area

$$S_t = \frac{\pi}{2} \cdot [t_c^2 + 2 \cdot t_s \cdot t_c] + w \cdot t_c \tag{6.40}$$

Keeping figure 6.14 as reference, the moment balance around the rotation axis O can be constructed. It is assumed that F_{T2} acts perpendicular to this axis of rotation at all times.

$$\Sigma M_O = 0 \tag{6.41}$$

$$\underbrace{\sigma_{bts} \cdot S_t}_{F_{T2}} \cdot \left[\frac{2}{3} \cdot \underbrace{\frac{t_{b,2} \cdot sin(\gamma_4)}{sin(\gamma_3)}}_{t_c}\right] - \underbrace{F_{T1} \cdot cos(\delta)}_{F_{N2}} \cdot d_1 + \underbrace{F_{T1} \cdot sin(\delta)}_{F_{S2}} \cdot d_2 = 0 \tag{6.42}$$

To determine what fraction of the total forces are due to tensile failure, equation 6.42 needs to be rewritten to the reaction force F_{T1}, acting on the rake face of the pickpoint.

$$F_{T1} = \frac{\sigma_{bts} \cdot S_t}{cos(\delta) \cdot d_1 - sin(\delta) \cdot d_2} \cdot \left[\frac{2}{3} \cdot \frac{t_{b,2} \cdot sin(\gamma_4)}{sin(\gamma_3)}\right] \tag{6.43}$$

Decomposing this resultant force into horizontal and vertical direction gives

$$F_{T1,h} = \frac{\sigma_{bts} \cdot S_t}{cos(\delta) \cdot d_1 - sin(\delta) \cdot d_2} \cdot [\frac{2}{3} \cdot \frac{t_{b,2} \cdot sin(\gamma_4)}{sin(\gamma_3)}] \cdot sin(\alpha_c + \delta) \tag{6.44}$$

$$F_{T1,v} = \frac{\sigma_{bts} \cdot S_t}{cos(\delta) \cdot d_1 - sin(\delta) \cdot d_2} \cdot [\frac{2}{3} \cdot \frac{t_{b,2} \cdot sin(\gamma_4)}{sin(\gamma_3)}] \cdot cos(\alpha_c + \delta) \tag{6.45}$$

6.4. FRACTURE MECHANICS

Most cutting force prediction models nowadays are setup by applying a force balance and determining a dominant failure mechanism (e.g. shear failure or tensile failure). Very few researchers investigated the potential of applying fracture mechanics theory into the rock cutting theory. Fracture mechanics is based on the initiation and propagation of a crack within a linear-elastic material. A crack is initiated by a concentrated high stress, impacting the material. Griffith [16] developed a brittle fracture theory that is considered a reliable method to predict the fracture initiation stress. He explained by the first law of thermodynamics that the propagation of a crack depends on the amount of mechanical energy that is put in to a material. three modes of brittle deformation may occur due to an energy input. Mode I *Opening mode* is initiated by an input of tensile strain energy. A tensile stress acts normal to the plane of the crack, which opens the fracture surface. Mode II *in-plane shearing* (or sliding) is initiated by shear strain energy. The shear stresses act parallel to the fracture surface and in direction of crack propagation. Mode III *anti-plane shearing* (or tearing) is also initiated by shear stain energy and acts parallel to the fracture surface. Contrary to mode II, crack propagation happens perpendicular to the direction of the fracture (Z-direction). In-plane and anti-plane shear is a certain state of strain in a rigid body. The in-plane strain in a body is only nonzero in the plane of crack propagation, thus parallel to the fracture surface. The displacements in the body of an anti-plane strain condition are zero in the plane of interest, but nonzero in the direction perpendicular to the plane.

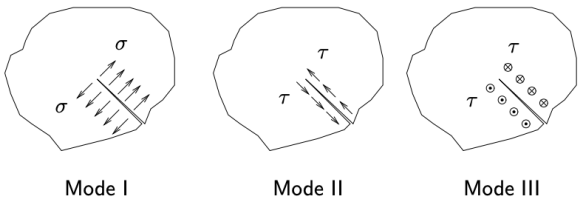

Figure 6.18: Schematic representation of the various fracture modes Dr.ir. P.J.G. Schreurs [28]

The initiation and propagation of crack growth depends on multiple factors, such as material properties, body geometry, crack geometry, loading distribution, loading rate, load magnitude, environmental conditions, time effects and microstructure Broberg, K Bertram [29]. For determining or predicting the crack forces that occur during the fracturing process, two main concepts arise: *crack extension force approach* and *stress intensity analysis*. These two concepts differ in the fact that the stress intensity analysis focusses on the local crack tip stresses and the crack extension force approach uses thermodynamic energy relationships to examine the energy loss per unit of new crack separation area, formed during an increment of crack extension Atkinson, B.K. [30]. The writer has chosen to only elaborate on the stress intensity analysis, which is concentrated near the tip of the pickpoint.

6.4.1. STRESS INTENSITY ANALYSIS

When using the stress intensity analysis, the stress components at the crack tip are being used. Depending on the Mode of loading, the stress intensity factors can be determined, where after the stress levels at the crack tip. In practice it is not common for a crack to propagate in the direction parallel to its failure plane. To account for fracturing non-parallel to the failure plane, multiple failure modes can be combined. This is called mixed-mode crack loading. In practical situations, a crack is mostly subjected to a combined Mode I and Mode II loading. The resulting crack tip stresses due to the combination of these failure modes, can be determined by the superposition of the separate stress components. Figure 6.19 represents the transformation of a material volume, due to the application of Mode I and Mode II loading, where θ is the crack angle w.r.t. the horizontal direction vector $\vec{e}_1$.

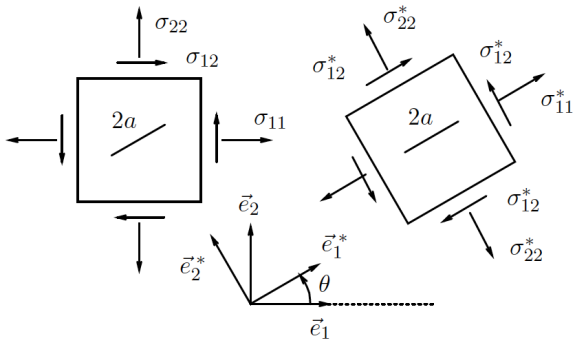

Figure 6.19: Transformation of a material volume element due to mixed-loading conditions Dr.ir. P.J.G. Schreurs [28]

To determine the stress components at the tip of the blade, one must take the critical crack angle θ_c into account. All stress components acting on the control volume, as displayed in figure 6.19 act in two-dimensional space in the direction of $\vec{e}_1^*$ and $\vec{e}_2^*$. To express the crack tip stresses in the rotated coordinate system, the transformation matrix $\bar{T}$ can be used

$$\bar{\sigma^*} = \bar{T}^T \bar{\sigma} \bar{T} \tag{6.46}$$

$$\begin{bmatrix} \sigma_{11}^* & \sigma_{12}^* \\ \sigma_{21}^* & \sigma_{22}^* \end{bmatrix} = \begin{bmatrix} cos(\theta_c) & sin(\theta_c) \\ -sin(\theta_c) & cos(\theta_c) \end{bmatrix} \begin{bmatrix} \sigma_{11} & \sigma_{12} \\ \sigma_{21} & \sigma_{22} \end{bmatrix} \begin{bmatrix} cos(\theta_c) & -sin(\theta_c) \\ sin(\theta_c) & cos(\theta_c) \end{bmatrix}$$

$$\begin{bmatrix} \sigma_{11}^* & \sigma_{12}^* \\ \sigma_{21}^* & \sigma_{22}^* \end{bmatrix} = \begin{bmatrix} cos^2(\theta_c)\sigma_{11} + 2cos(\theta_c)sin(\theta_c)\sigma_{12} + sin^2(\theta_c)\sigma_{22} \\ -cos(\theta_c)sin(\theta_c)\sigma_{11} + (cos^2\theta_c - sin^2(\theta_c))\sigma_{12} + cos(\theta_c)sin(\theta_c)\sigma_{22} \\ -cos(\theta_c)sin(\theta_c)\sigma_{11} + (cos^2\theta_c - sin^2(\theta_c))\sigma_{12} + cos(\theta_c)sin(\theta_c)\sigma_{22} \\ sin^2(\theta_c)\sigma_{11} + 2cos(\theta_c)sin(\theta_c)\sigma_{12} + cos^2(\theta_c)\sigma_{22} \end{bmatrix}$$

The crack tip stresses can thus be written in terms of two tensile components (e.g s_{11} and s_{22} and one shear component s_{12}. The crack tip stress s_{11} is considered to be a zero-stress component, because it is assumed that no tensile stresses will act parallel to the crack, meaning that σ_{11}^* is zero at all times. The tensile component that acts perpendicular to the direction of propagation (e.g. σ_{22}^*) is a nonzero stress component. At crack initiation the shear component σ_{12}^* will also be present, meaning that this stress is nonzero. The crack tip stresses in i and j direction $(i, j = 1, 2)$ can now be written as a mixed-mode loading condition

$$s_{ij} = \frac{K_I}{\sqrt{2 \cdot \pi \cdot r}} \cdot f_{I_{ij}}(\theta_c) + \frac{K_{II}}{\sqrt{2 \cdot \pi \cdot r}} \cdot f_{II_{ij}}(\theta_c) \tag{6.47}$$

Where the functions $f_{I_{22}}$ and $f_{I_{12}}$ for mode I fracturing can be written as

$$f_{I_{22}}(\theta_c) = cos\left(\frac{\theta_c}{2}\right) \cdot \{1 + sin\left(\frac{\theta_c}{2}\right) \cdot sin\left(\frac{3\theta_c}{2}\right)\} \tag{6.48}$$

$$f_{I_{12}}(\theta_c) = sin\left(\frac{\theta_c}{2}\right) \cdot cos\left(\frac{\theta_c}{2}\right) \cdot cos\left(\frac{3\theta_c}{2}\right) \tag{6.49}$$

For Mode II the fracturing functions $f_{II_{22}}$ and $f_{II_{12}}$ can be written as

$$f_{II_{22}}(\theta_c) = sin\left(\frac{\theta_c}{2}\right) \cdot cos\left(\frac{\theta_c}{2}\right) \cdot cos\left(\frac{3\theta_c}{2}\right) \tag{6.50}$$

$$f_{II_{12}}(\theta_c) = cos\left(\frac{\theta_c}{2}\right) \cdot \{1 - sin\left(\frac{\theta_c}{2}\right) \cdot sin\left(\frac{3\theta_c}{2}\right)\} \tag{6.51}$$

The stress intensity factor, or fracture toughness factor, K is a dimensionless quantity that determines the magnitude of the crack tip stress field within a homogeneous linear-elastic material. For each mode of fracture the stress intensity factor is different. Equation 6.52 and 6.53 represent the stress intensity factors for Mode I and Mode II fracturing, respectively. $\beta_{I,II}$ are dimensionless parameters dependent on the rock specimen and crack geometry.

$$K_I = \beta_I \cdot \sigma_{22}^* \cdot \sqrt{\pi a} \tag{6.52}$$

$$K_{II} = \beta_{II} \cdot \sigma_{12}^* \cdot \sqrt{\pi a} \tag{6.53}$$

The K-value is actually a complex parameter that highly depends on the type of loading for initiating a crack. In literature a broad range of existing crack loading configurations have been tested to construct an expression for the various crack intensity factors K_I, K_{II} and K_{III}. The initiation will occur when the stress intensity factor reaches its critical value, called the fracture toughness K_{nc} ($n = \{I, II, III\}$) of the material. The fracture toughness is a property of the material itself and can be obtained by executing various tests. So, the following condition must hold for a stable crack to be initiated and then propagate into the direction of least resistance.

$$K_n \geq K_{nc} \quad n = \{I, II, II\} \tag{6.54}$$

6.5. TENSILE-DOMINATED FRACTURE MODEL

In the previous chapter the assumption was made that a combined loading condition is most likely to be apparent at the tip of a cutting tool, the point at which the stresses are highest. Further research showed that, in developing an analytical mixed-mode prediction model based on fracture mechanics, the level of complexity is too high to accurately determine the crack tip stresses. So, for this model a mode I loading condition is assumed at the crack tip. This means that the initiation of the crack is dominated by tensile failure. Figure 6.20 shows the schematic basis of the tensile-dominated fracture model. It is assumed that the total contact surface of the pickpoint's rake face with the intact rock is needed to initiate a crack at the tip. A linear distribution profile is assumed to act on this cutting face, having its peak at σ_c and is zero at the top interface of the rock.

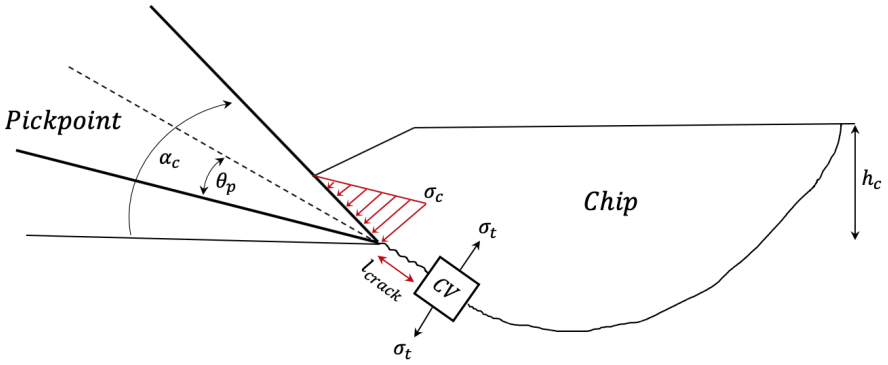

Figure 6.20: Crack loading distribution for tensile-dominated fracture model

As known, tensile cracks are initiated by tensile stresses that act perpendicular to the direction of crack propagation. The control volume CV in figure 6.20 is considered to be an element very close to the crack tip that is subjected to this stress tensor.

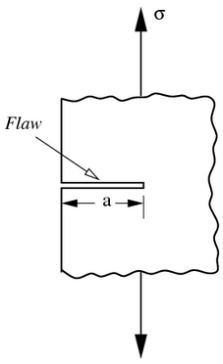

(a) Crack loading according to Griffith [16]

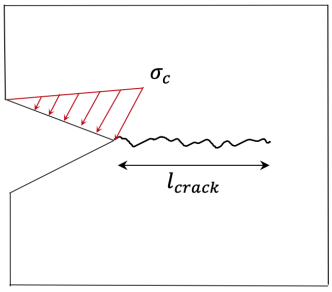

(b) Crack loading for tensile-dominated fracture model

Figure 6.21: Crack loading conditions

Figure 6.21b gives a closer look on the linear stress distribution and dimensional variables that are needed to develop a numerical expression for the peak cutting force due to tensile fracturing. The first thing to do is to write an expression for the crack stress component for a mode I fracture problem. The assumption is made to use the stress criterion of Griffith's linear-elastic brittle fracture theory. Griffith's theory states that crack propagation occurs when the reduction in potential energy, that originates from crack growth, is greater than or equal to the increase in surface energy γ_s due to the creation of new free surfaces Griffith [16]. More fundamentally seen, this release in potential energy arises from the fact that linear-elastic energy is stored until the elastic limit of the rock is reached. This limit can be seen as the allowable strain of a material, before a crack is initiated due to an external force. So, all the work done in stretching the material is Elastic Strain Energy. The applicability of Griffith's theory is only for linear-elastic materials, creating brittle fractures. Based on the (artificial) rock properties, obtained within the preliminary data acquisition, it was noticed that, in theory, the concrete is to be considered as a less-brittle material. Though, it must be mentioned that concrete acted as brittle during the cutting experiments. It is thus assumed that both rock compositions are to be considered as brittle. For a crack to be initiated, the stored elastic strain energy within the material should be sufficiently large to generate a new crack surface. According to Griffith [16] it is assumed that the available external energy U_e and internal energy U_i is transferred into surface energy U_a. The following energy balance can be constructed according to this assumption

$$\frac{dU_e}{dl_{crack}} - \frac{dU_i}{dl_{crack}} = \frac{dU_a}{dl_{crack}} \tag{6.55}$$

For simplification reasons it is assumed that the crack propagates in an infinite plate with a uniform thickness. Furthermore it is assumed that the applied stress by the pickpoint acts at a far distance from the crack. This means that the displacements at these boundaries will be minor, when small crack displacement increments occur. This means that, during crack propagation, no external work is done ($dU_e = 0$). So, for a crack to be able to grow, the energy release rate due to the internal, elastic stored potential, has to equal the surface energy that is required to initiate a new crack.

$$\frac{-dU_i}{dl_{crack}} = \frac{dU_a}{dl_{crack}} \tag{6.56}$$

Where the internal stored energy U_i and the required energy U_a, to create a new surface crack, is written as

$$U_i = -\frac{\pi \cdot l_{crack}^2 \cdot \sigma_c^2}{E} \tag{6.57}$$

$$U_a = 4 \cdot l_{crack} \cdot \gamma_s \tag{6.58}$$

Where γ_s is the surface energy in $\frac{J}{m^2}$. To write the energy balance in terms of the critical crack length, the derivative of the total energy $(U_a + U_i)$ should be set equal to zero.

$$\frac{d(U_a + U_i)}{dl_{crack}} = 0 \tag{6.59}$$

$$\frac{d}{dl_{crack}}\left(4 \cdot \gamma_s \cdot l_{crack} - \frac{\pi \cdot l_{crack}^2 \cdot \sigma_c^2}{E}\right) = 0 \tag{6.60}$$

By solving and rearranging equation 6.60, an expression for the Griffith stress σ_c given

$$\sigma_c = \sigma_{griffith} = \sqrt{\frac{2 \cdot E \cdot \gamma_s}{\pi \cdot l_{crack}}} \tag{6.61}$$

Where γ_s is the surface energy (Griffith [16]), based on the properties of the material and written as

$$\gamma_s = \frac{K_{Ic}^2}{2 \cdot E} \tag{6.62}$$

Now that an expression is given for the critical stress σ_c that is needed to create a crack due to a mode I loading condition, the stress distribution over the contact face of the pickpoint can be defined. Figure 6.22b shows the assumed loading condition of the crack due to the cutting configuration. The height parameter l_c in figure 6.22b is a variable height.

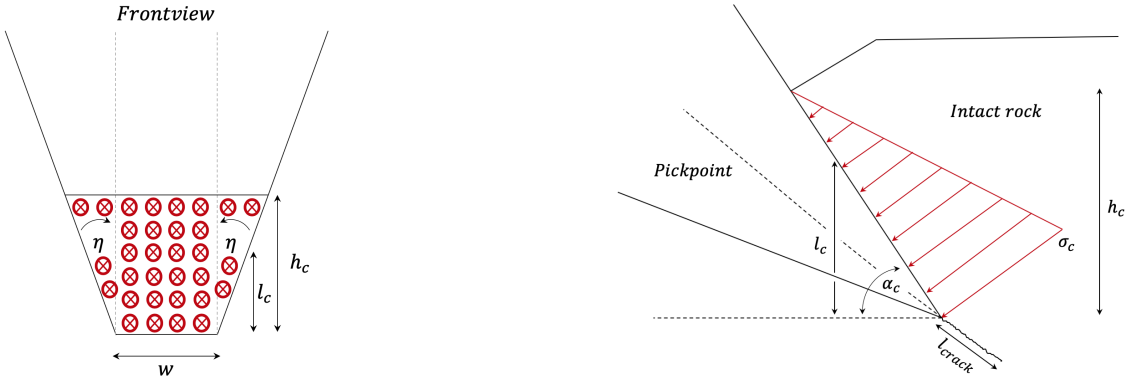

(a) Applied stress to rake face pickpoint - frontview

(b) Applied stress to rake face pickpoint - sideview

Figure 6.22: Applied stress to crack initiation by the pickpoint's rake face

The linear stress distribution can be expressed in terms of the cutting depth h_c, arbitrary height parameter l_c and rewritten function of σ_c, where γ_s is substituted in the determination of the total stress acting on the pickpoint's rake face $\sigma(P)$.

$$\sigma(P) = \frac{(h_c - l_c)}{h_c} \cdot \sigma_c = \frac{(h_c - l_c)}{h_c} \cdot \frac{K_{Ic}}{\sqrt{\pi \cdot l_{crack}}} \tag{6.63}$$

The fracture toughness due to tensile cracking K_{Ic} is a variable that depends on the specific strength properties of the rock. In practice, to determine an accurate value for K_{Ic}, various experiments have to be executed, all having different loading conditions. Because the writer was not able to perform any of these experiments, an empirical formula 6.64, proposed by Kahraman and Altindag [31], is found. The fracture toughness is written as a function of the UCS and BTS value of the (artificial) rock. Li *et al.* [15] showed that there is a good correlation between equation 6.64 and the outcomes of the experimental-based values for K_{Ic}.

$$K_{Ic} = 0.11 \cdot \left(\frac{\sigma_{ucs} \cdot \sigma_{bts}}{2}\right)^{0.43} \qquad [MPa \cdot \sqrt{m}] \tag{6.64}$$

One of the unknown parameters in equation 6.63 is the initiated crack length l_{crack}, which is formed due to the applied stresses on the crack itself. Due to the fact that no experimental work was done on determining the fracture toughness K_{Ic}, a reasonable assumption has to be made for l_{crack}. Guo *et al.* [32] developed a numerical model to predict the crack path of major chip formation by applying mode I failure mode for brittle rocks. For modelling the crack propagation, an initial crack length of $0.2 \cdot h_c$ was assumed (Guo *et al.* [32]). Furthermore, the assumption was made that the stress distribution acts at $0.5 \cdot h_c$ over the rake face of the pickpoint. This means that the full contact area of the pickpoint with the intact rock, is from $0.5 \cdot h_c$ downwards to the tip of the blade. Because the numerical results of Guo *et al.* [32] are in agreement with the experimental evidence and former developed models, it is fair to say that the assumptions made are reasonable enough to apply within this model. Before using these boundary values, a general force derivation has to be made, according to the situation sketch in figure 6.22.

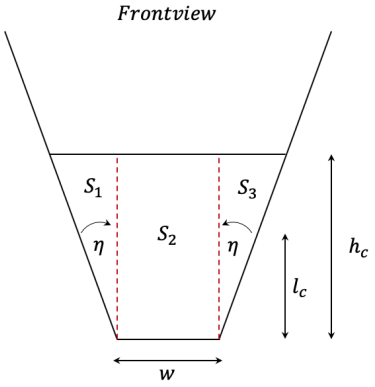

Figure 6.23: Divided area sections pickpoint - frontview

Because the linear stress distribution acts over the contact surface of the intact rock with the rake face of the pickpoint, an expression for the cutting forces can be constructed. A mathematical method can be applied where the linear stress distribution is integrated over the contact area of the pickpoint. This contact surface can be divided into three areas to clarify the calculation (figure 6.23). The boundaries of these surfaces have been implemented into the integration limits of the following force expressions due to tensile fracturing

$$F_{f,1} = \int_0^{\frac{h_c}{sin(\alpha_c)}} \int_0^{\eta} \frac{1}{sin(\alpha_c)} \cdot \frac{(h_c - l_c)}{h_c} \cdot \frac{K_{Ic}}{\sqrt{\pi \cdot l_{crack}}} \cdot l_c \cdot \eta' \; d\eta' \; dl_c \tag{6.65}$$

$$F_{f,3} = \int_0^{\frac{h_c}{sin(\alpha_c)}} \int_0^{\eta} \frac{1}{sin(\alpha_c)} \cdot \frac{(h_c - l_c)}{h_c} \cdot \frac{K_{Ic}}{\sqrt{\pi \cdot l_{crack}}} \cdot l_c \cdot \eta' \; d\eta' \; dl_c \tag{6.66}$$

$$F_{f,2} = \int_0^{\frac{h_c}{sin(\alpha_c)}} \frac{(h_c - l_c)}{h_c} \cdot \frac{K_{Ic}}{\sqrt{\pi \cdot l_{crack}}} \cdot w \; dl_c \tag{6.67}$$

By solving and combining the above integration functions (Appendix D.2), an expression for the total force can be written as

$$\sum_{n=1}^{3} F_{f,n} = F_f = \left[\frac{\eta^2}{2} \cdot \left(\frac{h_c^2}{sin^3(\alpha_c)} \right) - \frac{\eta^2}{3 \cdot h_c} \cdot \left(\frac{h_c^3}{sin^4(\alpha_c)} \right) + \left(\frac{h_c}{sin^2(\alpha_c)} - \frac{h_c}{2 \cdot sin^3(\alpha_c)} \right) \cdot w \right] \cdot \frac{K_{Ic}}{\sqrt{\pi \cdot l_{crack}}} \tag{6.68}$$

Decomposing the total force component in horizontal and vertical direction and substituting the assumptions made about the initial crack length (l_{crack}= 0.2·h_c) gives

$$F_{f,h} = \left[\frac{\eta^2}{2} \cdot \left(\frac{h_c^2}{sin^3(\alpha_c)} \right) - \frac{\eta^2}{3 \cdot h_c} \cdot \left(\frac{h_c^3}{sin^4(\alpha_c)} \right) + \left(\frac{h_c}{sin^2(\alpha_c)} - \frac{h_c}{2 \cdot sin^3(\alpha_c)} \right) \cdot w \right] \cdot \frac{K_{Ic}}{\sqrt{\pi \cdot 0.2 \cdot h_c}} \cdot cos(\alpha_c) \tag{6.69}$$

$$F_{f,v} = \left[\frac{\eta^2}{2} \cdot \left(\frac{h_c^2}{sin^3(\alpha_c)} \right) - \frac{\eta^2}{3 \cdot h_c} \cdot \left(\frac{h_c^3}{sin^4(\alpha_c)} \right) + \left(\frac{h_c}{sin^2(\alpha_c)} - \frac{h_c}{2 \cdot sin^3(\alpha_c)} \right) \cdot w \right] \cdot \frac{K_{Ic}}{\sqrt{\pi \cdot 0.2 \cdot h_c}} \cdot sin(\alpha_c) \tag{6.70}$$

6.5.1. DISCUSSION FRACTURE MODEL

The application of fracture mechanics within the rock cutting theory is very challenging and complex. The assumption was made that only one dominant failure mechanism was present within the cutting process. When looking at the executed experiments, it was clearly seen that multiple failure mechanism took place. In terms of the crack tip analysis, it is very complex to approach the crack initiation by a mixed-mode loading condition. To do this, a range of preliminary experiments have to be executed to obtain information about the stress intensity factor of the failure mode in question, critical crack length and direction of crack propagation.

When looking at the developed tensile-dominated fracture model, also a lot of information is missing, and therefore assumed, considering the fracture toughness, critical crack length, dominant failure mechanism and corresponding stress criterion. The stress criterion of Griffith [16] was assumed to act as a normal stress, perpendicular to the direction of crack propagation, at an infinite distance from the crack. When critically looking at the cutting configuration as in figure 6.22, it is clearly seen that the crack is differently loaded than Griffith's theory (figure 6.21a).

Furthermore, an empirical was found for determining the fracture toughness K_{Ic} for a mode I loading condition, which were assumed applicable for both rock compositions. For a crack to be initiated, this stress intensity factor K_I needs to be exceeded. A stress intensity factor highly depends on the type of crack loading and shape of the loaded object. Unfortunately, no existing solutions were found in literature for the cutting configuration used, based on the mode I loading condition. This means that no accurate comparison can be made for $K_I \geq K_{Ic}$, making outcomes of the tensile-dominated fracture model unreliable.

6.6. MODEL VALIDATION

Based on the experimental research that has been performed, two different approaches have been developed for predicting the peak cutting forces within the rock cutting process. The applicability and reliability of the tensile-dominated fracture model is most probably very limited. This made the writer decide to focus on the combined force prediction model, where the three individual failure components are implemented in. The results of the fracture mechanics model will still be presented to validate that the application of this theory is not possible without the required tested parameters. The validation of the combined force prediction model will be done by comparing the experimental cutting force measurements with the outcomes of the model. Furthermore, an analysis will be made of the force distribution due to the three failure components (e.g. *crushing*, *major shear failure* and *tensile failure*). The total force of these failure mechanisms combined is written as

$$F_{tot} = F_{crush} + F_{shear} + F_{tensile} \tag{6.71}$$

An important variable of the combined force prediction model, is the shear factor K_s. This factor determines the fraction of the amount of shear failure that takes place when a chip is formed. One can imagine, when increasing the cutting depth, tensile failure will become more apparent and may eventually dominate the total cutting forces. To determine this shear factor a wide variety of chips have been studied for both sandstone and concrete (Appendix C.9 and C.10). The analysis of these chips mainly focused on the transition point where an angle deflection of the crack was observed. This indicates that a tensile crack is forming at this transition point, propagating to the rock's top interface. Figure 6.24 shows the constructed shear factor graph, based on individual chip investigation, whereafter the trend is extrapolated and drawn in a form that is thought to be logical for the failure process. It can be seen that the K_s distribution is different for the range of cutting angles (40°- 60°).

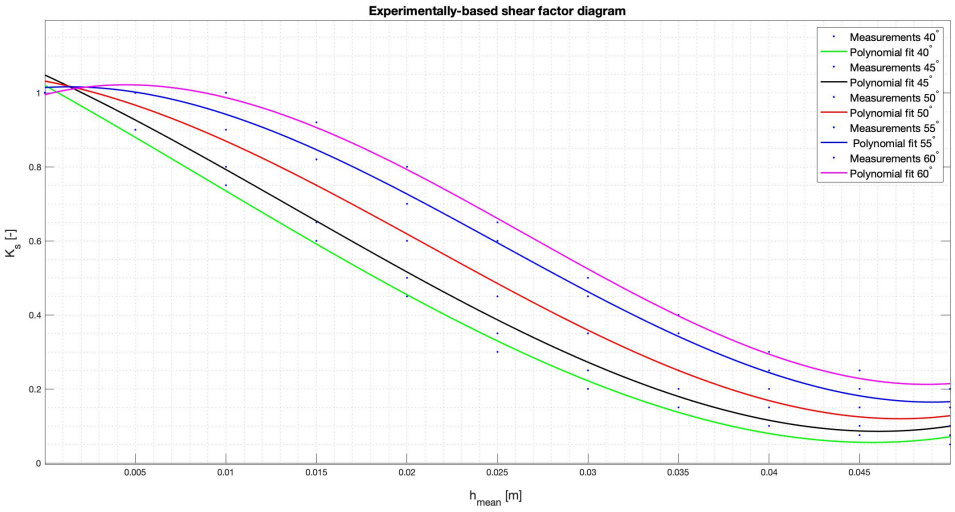

Figure 6.24: Shape of the experimentally-based shear factor diagram

One can imagine that a tensile crack is more likely to appear when applying a shallow cutting angle than a steep cutting angle. This can be explained by the fact that, when the pickpoint acts more horizontally to the intact rock, a tensile splitting situation becomes more apparent (Evans [1]). This also means that a steeper cutting angle is generally more shear dependent than the application of a shallow cutting angle. This is clearly observed in figure 6.24. The writer is aware that the difference in brittleness between the sandstone and concrete may influence the shape of the shear factor diagram. The individual chip investigation pointed out that the sandstone is mostly subjected to shear failure, because relatively shallow cuts were applied. This made the writer decide to use the same shear factor diagram shape for both rock compositions. It must be noted that the chip shear/tensile distribution and shape itself varied a lot, even from the same production series of the experiment in question. One can imagine that the shape of figure 6.24 may change in reality. The writer based the shape of this trend on individual chip measurements and what appeared to be logical from a scientific point of view. Table 6.2 shows the various shear factor values for both the sandstone and concrete experiments. Where $h_{c,i}$ is the peak cutting depth, corresponding to measured peak cutting force of the consecutive executed tests. As shown in section 6.3.2 the fraction of tensile failure can be calculated by $K_t = (1 - K_s)$.

	Sample	α_c [°]	$h_{c,1}$ [mm]	$K_{s,1}$ [-]	$h_{c,1}$ [mm]	$K_{s,2}$ [-]	$h_{c,3}$ [mm]	$K_{s,3}$ [-]	$h_{c,4}$ [mm]	$K_{s,4}$ [-]	$h_{c,5}$ [mm]	$K_{s,5}$ [-]
Sandstone	S_1	45°	2.3	1	7.3	0.87	11.0	0.8	-	-	-	-
Sandstone	S_2	50°	2.3	1	6.4	0.9	9.9	0.8	11.8	0.75	12.2	0.72
Sandstone	S_3	55°	1.6	1	5.1	0.95	10.2	0.9	11.6	0.85	10.9	0.9
Sandstone	S_4	60°	2.1	1	3.8	0.98	11.2	0.9	12.3	0.92	15.3	0.85
Concrete	$7-11-B_3$	40°	3.0	0.95	10.0	0.75	17.0	0.4	22.7	0.3	30.7	0.2
Concrete	$7-11-B_2$	45°	5.5	0.95	10.0	0.8	18.0	0.5	26.4	0.3	35.4	0.15
Concrete	$7-11-B_5$	50°	2.7	1	6.4	0.95	13.2	0.8	23.7	0.55	36.4	0.25
Concrete	$7-11-B_4$	55°	5.8	1	6.3	0.98	16.7	0.9	32.4	0.4	42.6	0.2
Concrete	$7-11-B_6$	60°	4.7	1	8.4	0.95	17.6	0.85	15.6	0.9	29.1	0.55

Table 6.2: Shear factor distribution

By knowing the fraction between K_s and K_t, the force distribution between these failure mechanisms can be determined. Before doing this, the crush component needs to be further elaborated on. As mentioned in section 6.2.2, the height of the crushed zone can be determined by analyzing the total amount of crushed volume. Figure 6.7 proves that the calculated crushed zone height for both sandstone and concrete is in good correlation with the measured height of the bottom groove. The calculated crushed zone heights can be individually substituted into equation 6.6 to determine the total indentation area of the experiment in question, where $h_{crush,i}$ is equal to $h_{\alpha_{c,i}}$. To determine the total cutting forces due to crushing, the shear strength property of the rock σ_{ucs} and indentation coefficient K_{ind} need to be implemented into equation 6.1. The indentation coefficient, that arose from the indentation experiments, and shear strength property of both rock compositions are collected in section 6.2.1, table 6.1.

Sample	α_c [°]	$h_{crush,1}$ [mm]	$h_{crush,2}$ [mm]	$h_{crush,3}$ [mm]	$h_{crush,4}$ [mm]	$h_{crush,5}$ [mm]
S_1	45°	0.21	0.96	1.41	-	-
S_2	50°	0.24	1.21	1.63	1.84	2.0
S_3	55°	0.34	1.22	2.02	2.14	2.24
S_4	60°	0.59	0.90	2.44	2.2	2.66
$7-11-B_3$	40°	1.34	2.87	5.02	13.52	13.11
$7-11-B_2$	45°	1.51	2.33	5.16	9.32	12.65
$7-11-B_5$	50°	1.87	2.94	4.01	10.83	11.33
$7-11-B_4$	55°	1.52	2.72	5.75	8.82	13.82
$7-11-B_6$	60°	1.41	3.10	6.71	6.34	8.54

Table 6.3: Calculated crushed zone height

Now all desired input parameters are known, the total force component, consisting out of the three failure mechanisms, can be constructed as

$$F_{tot} = \underbrace{K_{ind} \cdot \sigma_{ucs} \cdot \left[tan(\eta) \cdot \frac{h_{\alpha_{c,i}}^2}{sin^2(\alpha_{c,i})} + \frac{h_{\alpha_{c,i}}}{sin(\alpha_{c,i})} \cdot w \right]}_{\text{Crush component}} + \underbrace{\frac{c \cdot [S_{1,s} + S_{2,s} + S_{3,s}] \cdot cos(\phi)}{sin(\alpha_c + \phi + \beta_s + \delta)}}_{\text{Shear component}} + \underbrace{\frac{\sigma_{bts} \cdot S_t}{cos(\delta) \cdot d_1 - sin(\delta) \cdot d_2} \cdot \left[\frac{t_{b,2} \cdot sin(\gamma_4)}{sin(\gamma_3)} \right]}_{\text{Tensile component}} \quad (6.72)$$

For the validation of the combined force prediction model, the calculated total, horizontal and vertical forces will be compared to the measured values. A distinction will be made between both rock compositions.

SANDSTONE

The sandstone force can be decomposed into a horizontal and vertical component. The total horizontal force is determined by filling in equation 6.73 with the predetermined parameters. Table 6.4 shows the calculated horizontal forces, according to the combined force prediction model, compared to the measured horizontal forces. To visualize the measured forces with the calculated forces in a graphical sense, figure 6.25 is constructed. From table 6.4 it is clearly seen that the crush and shear forces dominate the total horizontal cutting forces. The magnitude of shear forces can be explained by the fact that, still, a relatively shallow cutting depth was applied, indicating that the development of a tensile crack is very small.

$$F_{h,tot,s} = 0.36 \cdot K_{ind} \cdot \sigma_{ucs} \cdot \left[tan(\eta) \cdot \frac{h_{\alpha_{c,i}}^2}{sin^2(\alpha_{c,i})} + \frac{h_{\alpha_{c,i}}}{sin(\alpha_{c,i})} \cdot w \right] + \left(\frac{c \cdot [S_{1,s} + S_{2,s} + S_{3,s}] \cdot cos(\phi)}{sin(\alpha_c + \phi + \beta_s + \delta)} + \frac{\sigma_{bts} \cdot S_t}{cos(\delta) \cdot d_1 - sin(\delta) \cdot d_2} \cdot \left[\frac{t_{b,2} \cdot sin(\gamma_4)}{sin(\gamma_3)} \right] \right) \cdot sin(\alpha_c + \delta) \quad (6.73)$$

Sample	$F_{h,crush}$ [kN]	$F_{h,shear}$ [kN]	$F_{h,tensile}$ [kN]	$F_{h,tot,s}$ [kN]	$F_{h,measured}$ [kN]
$S_{1.1}$	0.37	0.76	0.00	1.13	4.76
$S_{1.2}$	2.29	3.27	0.18	5.75	7.10
$S_{1.3}$	3.37	5.58	0.60	9.54	10.20
$S_{2.1}$	0.44	0.44	0.00	0.88	3.71
$S_{2.2}$	3.17	3.48	0.14	6.79	6.35
$S_{2.3}$	4.20	5.91	0.65	10.76	7.77
$S_{2.4}$	4.61	7.17	1.12	12.90	11.01
$S_{2.5}$	5.13	7.04	1.74	13.91	13.03
$S_{3.1}$	0.56	0.48	0.00	1.05	5.60
$S_{3.2}$	2.57	2.23	0.04	4.84	6.26
$S_{3.3}$	4.20	6.41	0.35	10.95	7.07
$S_{3.4}$	4.48	7.29	0.66	12.43	9.98
$S_{3.5}$	4.65	7.15	0.53	12.33	9.90
$S_{4.1}$	1.12	0.39	0.00	1.51	4.77
$S_{4.2}$	1.72	0.87	0.01	2.60	6.58
$S_{4.3}$	4.61	4.17	0.33	9.12	6.74
$S_{4.4}$	4.07	5.21	0.33	9.61	8.16
$S_{4.5}$	5.05	6.63	1.36	13.04	11.79

Table 6.4: Comparison between calculated and measured horizontal cutting forces - Sandstone

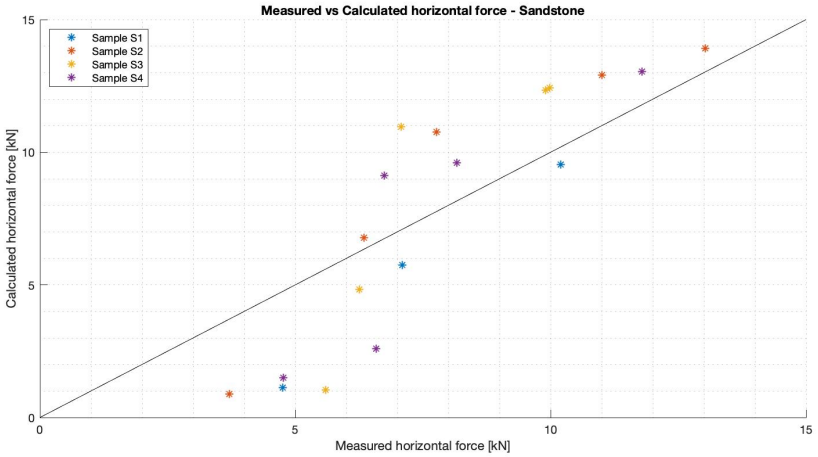

Figure 6.25: Calculated vs measured horizontal forces - Sandstone

Concerning the vertical component of the predicted forces, equation 6.74 can be applied. Table 6.5 shows the decomposed and total forces in vertical direction and compared to ones that were measured by the load sensor. When comparing the horizontal crush forces from table 6.4 to the vertical component, it is clearly seen that the vertical force contributes more significantly to the total cutting forces. This can be explained by the fact that the cutting tool is trying to reach the desired cutting depth, without success. This means that an excess vertical force arises, which can be traced back to the interface friction between the pickpoint and sandstone. That is why the crushed component is composed out of the actual crushing of material and friction between the two materials. In contemporary cutting theories it is assumed that the desired cutting depth is reached at all times, without encountering the resistance of the rock. In other words; depending on the hardness of the rock, a lot of energy required to reach the desired cutting depth. This explains the difference between the horizontal and vertical force component, as the sandstone is a relatively hard rock.

$$F_{v,tot,s} = 0.93 \cdot K_{ind} \cdot \sigma_{ucs} \cdot \left[tan(\eta) \cdot \frac{h^2_{\alpha_{c,i}}}{sin^2(\alpha_{c,i})} + \frac{h_{\alpha_{c,i}}}{sin(\alpha_{c,i})} \cdot w \right] + \left(\frac{c \cdot [S_{1,s} + S_{2,s} + S_{3,s}] \cdot cos(\phi)}{sin(\alpha_c + \phi + \beta_s + \delta)} + \frac{\sigma_{bts} \cdot S_t}{cos(\delta) \cdot d_1 - sin(\delta) \cdot d_2} \cdot \left[\frac{t_{b,2} \cdot sin(\gamma_4)}{sin(\gamma_3)} \right] \right) \cdot cos(\alpha_c + \delta) \quad (6.74)$$

Sample	$F_{v,crush}$ [kN]	$F_{v,shear}$ [kN]	$F_{v,tensile}$ [kN]	$F_{v,tot,s}$ [kN]	$F_{v,measured}$ [kN]
$S_{1.1}$	0.95	0.24	0.00	1.19	4.38
$S_{1.2}$	5.88	1.04	0.06	6.98	13.50
$S_{1.3}$	8.62	1.78	0.19	10.59	19.71
$S_{2.1}$	1.14	0.10	0.00	1.24	3.79
$S_{2.2}$	8.13	0.78	0.03	8.94	10.01
$S_{2.3}$	10.77	1.33	0.15	12.24	12.45
$S_{2.4}$	11.80	1.61	0.25	13.67	14.82
$S_{2.5}$	13.15	1.58	0.39	15.13	20.16
$S_{3.1}$	1.44	0.08	0.00	1.52	7.13
$S_{3.2}$	6.57	0.38	0.01	6.96	8.97
$S_{3.3}$	10.75	1.09	0.06	11.90	9.95
$S_{3.4}$	11.47	1.24	0.11	12.82	10.12
$S_{3.5}$	11.93	1.22	0.09	13.23	14.67
$S_{4.1}$	2.87	0.06	0.00	2.93	8.31
$S_{4.2}$	4.39	0.14	0.00	4.54	8.44
$S_{4.3}$	11.82	0.69	0.05	12.56	12.05
$S_{4.4}$	10.42	0.86	0.05	11.33	13.51
$S_{4.5}$	12.93	1.09	0.22	14.24	18.52

Table 6.5: Comparison between calculated and measured vertical cutting forces - Sandstone

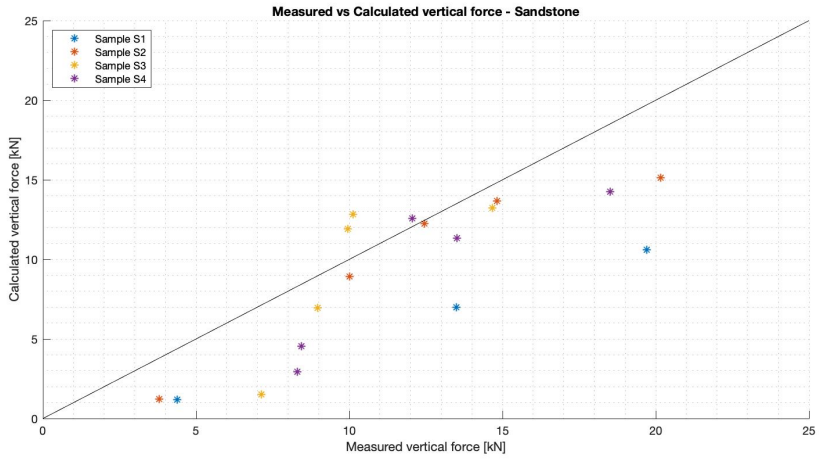

Figure 6.26: Calculated vs measured vertical forces - Sandstone

By applying equation 6.72, the total cutting forces can be calculated. Table 6.6 displays the comparison between the predicted and measured cutting forces.

Sample	$F_{t,crush}$ [kN]	$F_{t,shear}$ [kN]	$F_{t,tensile}$ [kN]	$F_{tot,s}$ [kN]	$F_{t,measured}$ [kN]
$S_{1.1}$	1.02	0.80	0.00	1.82	6.48
$S_{1.2}$	6.32	3.44	0.19	9.94	15.27
$S_{1.3}$	9.27	5.85	0.63	15.75	22.24
$S_{2.1}$	1.22	0.45	0.00	1.67	5.31
$S_{2.2}$	8.74	3.56	0.14	12.44	11.92
$S_{2.3}$	11.58	6.06	0.66	18.30	14.75
$S_{2.4}$	12.69	7.35	1.15	21.19	18.64
$S_{2.5}$	14.14	7.22	1.78	23.14	24.09
$S_{3.1}$	1.55	0.49	0.00	2.04	9.09
$S_{3.2}$	7.07	2.26	0.04	9.37	11.14
$S_{3.3}$	11.56	6.50	0.35	18.41	12.35
$S_{3.4}$	12.33	7.39	0.67	20.40	14.41
$S_{3.5}$	12.82	7.25	0.53	20.61	17.75
$S_{4.1}$	3.09	0.40	0.00	3.48	9.61
$S_{4.2}$	4.73	0.88	0.01	5.62	10.72
$S_{4.3}$	12.71	4.23	0.33	17.27	13.94
$S_{4.4}$	11.21	5.28	0.33	16.82	15.91
$S_{4.5}$	13.90	6.72	1.38	22.00	22.17

Table 6.6: Comparison between calculated and measured cutting forces - Sandstone

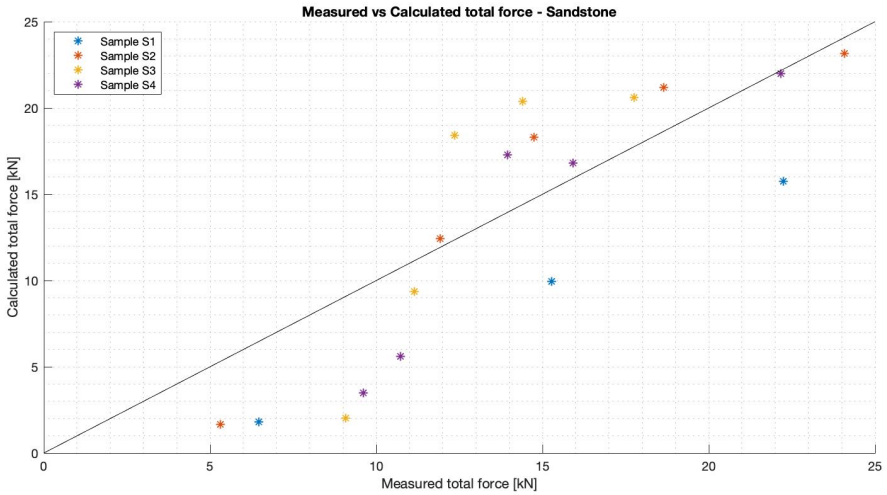

Figure 6.27: Calculated vs measured total forces - Sandstone

ARTIFICIAL ROCK

Experimental observations have shown that the concrete failed in a different way than the sandstone experiments. Due to the fact that the concrete is a less brittle material than the sandstone, it was already expected that the amount of crushed material would be significantly higher. By implementing the calculated parameters into equation 6.75, the total horizontal force component can be calculated. Table 6.7 shows that the forces due to the development of a crushed zone mostly dominate the total force spectrum in horizontal direction. When increasing the cutting depth, it appears that the force contribution due to tensile failure becomes more important. From a physical point of view this makes sense, because a tensile crack will have larger failure path to propagate over, meaning that the required energy to complete this crack will become higher.

$$F_{h,tot,c} = 0.45 \cdot K_{ind} \cdot \sigma_{ucs} \cdot \left[tan(\eta) \cdot \frac{h^2_{\alpha_{c,i}}}{sin^2(\alpha_{c,i})} + \frac{h_{\alpha_{c,i}}}{sin(\alpha_{c,i})} \cdot w \right] + \left(\frac{c \cdot [S_{1,s} + S_{2,s} + S_{3,s}] \cdot cos(\phi)}{sin(\alpha_c + \phi + \beta_s + \delta)} + \frac{\sigma_{bts} \cdot S_t}{cos(\delta) \cdot d_1 - sin(\delta) \cdot d_2} \cdot \left[\frac{t_{b,2} \cdot sin(\gamma_4)}{sin(\gamma_3)} \right] \right) \cdot sin(\alpha_c + \delta) \quad (6.75)$$

Sample	$F_{h,crush}$ [kN]	$F_{h,shear}$ [kN]	$F_{h,tensile}$ [kN]	$F_{h,tot,c}$ [kN]	$F_{h,measured}$ [kN]
$7-11-B_{3.1}$	0.73	0.08	0.00	0.81	2.74
$7-11-B_{3.2}$	1.58	0.48	0.01	2.07	3.58
$7-11-B_{3.3}$	2.88	0.83	0.25	3.97	7.97
$7-11-B_{3.4}$	7.86	0.39	2.27	10.52	12.68
$7-11-B_{3.5}$	7.94	0.45	5.81	14.20	17.14
$7-11-B_{2.1}$	1.05	0.37	0.00	1.42	1.73
$7-11-B_{2.2}$	1.61	0.88	0.00	2.50	2.84
$7-11-B_{2.3}$	3.65	1.33	0.32	5.29	6.62
$7-11-B_{2.4}$	6.83	1.57	2.35	10.75	12.93
$7-11-B_{2.5}$	9.46	1.12	7.27	17.84	19.77
$7-11-B_{5.1}$	0.94	0.04	0.00	0.98	2.51
$7-11-B_{5.2}$	1.46	0.28	0.00	1.74	5.11
$7-11-B_{5.3}$	2.03	1.06	0.29	3.39	8.82
$7-11-B_{5.4}$	5.72	1.31	3.30	10.33	10.55
$7-11-B_{5.5}$	6.01	1.98	11.18	19.17	15.37
$7-11-B_{4.1}$	1.02	0.56	0.00	1.57	3.89
$7-11-B_{4.2}$	1.84	0.73	0.00	2.57	5.20
$7-11-B_{4.3}$	3.96	2.33	0.48	6.77	9.86
$7-11-B_{4.4}$	6.22	4.61	2.88	13.72	12.85
$7-11-B_{4.5}$	10.03	5.21	8.36	23.60	18.14
$7-11-B_{6.1}$	0.96	0.37	0.00	1.32	3.03
$7-11-B_{6.2}$	2.14	0.72	0.00	2.85	4.80
$7-11-B_{6.3}$	4.71	2.14	0.32	7.17	7.61
$7-11-B_{6.4}$	4.42	4.63	1.51	10.56	10.29
$7-11-B_{6.5}$	6.03	4.34	4.66	15.03	14.96

Table 6.7: Comparison between horizontal calculated and measured cutting forces - Artificial rock

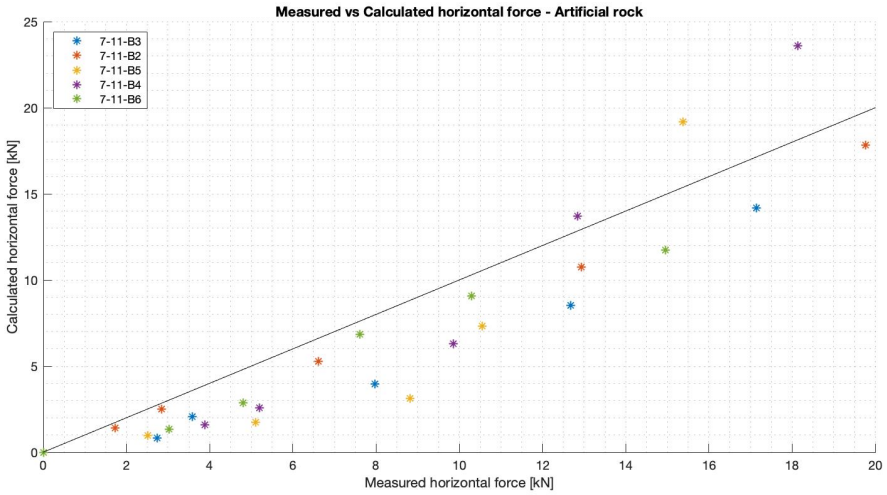

Figure 6.28: Calculated vs measured horizontal forces - Artificial rock

Table 6.8 shows the comparison between the calculated and measured forces in vertical direction. The calculated values show that the crush component still dominates the force spectrum. When critically looking at the vertical crush forces, the writer states that the applied dynamic friction coefficient between the pickpoint and concrete might differ from the actual value. This can be explained by the hypothesis that the author stated about the basic stress level in section 6.2.3. When looking at the concrete force-time plot in appendix C.3, it appears that the measured basic stress level for the large cutting depth regime (e.g. h_c >20mm for concrete) lies slightly lower than the calculated values. When looking at the shallow cutting regime (e.g. h_c <10mm), where mostly only crushing occurs, the vertical and horizontal force component are already better approximated. So, the author expects that the dynamic friction coefficient is responsible for the large force difference between the vertical and horizontal component due to crushing, when increasing the cutting depth. Figure 6.29 shows the comparison between the measured and calculated vertical forces in a graphical sense.

$$F_{v,tot,c} = 0.89 \cdot K_{ind} \cdot \sigma_{ucs} \cdot \left[tan(\eta) \cdot \frac{h_{\alpha_{c,i}}^2}{sin^2(\alpha_{c,i})} + \frac{h_{\alpha_{c,i}}}{sin(\alpha_{c,i})} \cdot w \right] + \left(\frac{c \cdot [S_{1,s} + S_{2,s} + S_{3,s}] \cdot cos(\phi)}{sin(\alpha_c + \phi + \beta_s + \delta)} + \frac{\sigma_{bts} \cdot S_t}{cos(\delta) \cdot d_1 - sin(\delta) \cdot d_2} \cdot \left[\frac{t_{b,2} \cdot sin(\gamma_4)}{sin(\gamma_3)} \right] \right) \cdot sin(\alpha_c + \delta) \quad (6.76)$$

Sample	$F_{v,crush}$ [kN]	$F_{v,shear}$ [kN]	$F_{v,tensile}$ [kN]	$F_{v,tot,c}$ [kN]	$F_{v,measured}$ [kN]
$7-11-B_{3.1}$	1.46	0.06	0.00	1.52	2.61
$7-11-B_{3.2}$	3.14	0.40	0.01	3.54	3.96
$7-11-B_{3.3}$	5.74	0.68	0.21	6.63	6.20
$7-11-B_{3.4}$	15.64	0.32	1.54	17.40	16.80
$7-11-B_{3.5}$	15.81	0.37	4.76	20.94	16.76
$7-11-B_{2.1}$	2.08	0.20	0.00	2.28	1.78
$7-11-B_{2.2}$	3.21	0.47	0.00	3.69	2.98
$7-11-B_{2.3}$	7.26	0.72	0.22	8.20	4.32
$7-11-B_{2.4}$	13.61	0.85	1.26	15.72	12.95
$7-11-B_{2.5}$	18.83	0.60	3.92	23.35	18.54
$7-11-B_{5.1}$	1.87	0.02	0.00	1.89	2.50
$7-11-B_{5.2}$	2.92	0.15	0.00	3.07	5.06
$7-11-B_{5.3}$	4.05	0.58	0.20	4.75	8.01
$7-11-B_{5.4}$	11.40	0.71	1.59	13.70	10.76
$7-11-B_{5.5}$	11.96	1.08	6.11	19.16	15.57
$7-11-B_{4.1}$	2.02	0.22	0.00	2.24	8.93
$7-11-B_{4.2}$	3.67	0.29	0.00	3.96	7.71
$7-11-B_{4.3}$	7.88	0.92	0.32	9.12	11.81
$7-11-B_{4.4}$	12.39	1.83	1.15	15.36	12.86
$7-11-B_{4.5}$	19.97	2.07	3.32	25.36	16.60
$7-11-B_{6.1}$	1.90	0.11	0.00	2.02	6.02
$7-11-B_{6.2}$	4.25	0.22	0.00	4.48	6.76
$7-11-B_{6.3}$	9.38	0.67	0.26	10.31	8.01
$7-11-B_{6.4}$	8.80	1.44	1.24	11.48	10.68
$7-11-B_{6.5}$	12.02	1.35	3.82	17.19	13.32

Table 6.8: Comparison between vertical calculated and measured cutting forces - Artificial rock

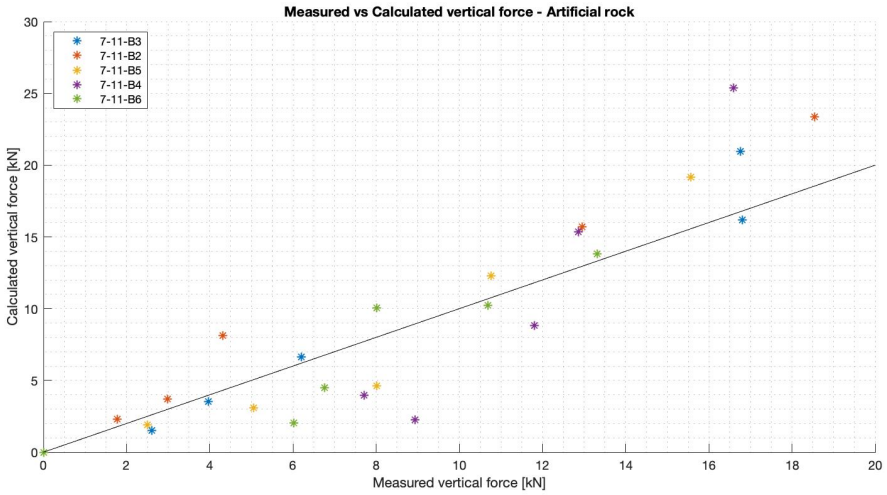

Figure 6.29: Calculated vs measured vertical forces - artificial rock

Table 6.9 shows the comparison between the measured and calculated total forces. It can be seen that the total forces are pretty well approximated according tot the combined force balance model. In partially agreement with the hypothesis of Verhoef [6], the numbers clearly show that the crush component dominates the total force spectrum. Figure 6.30 shows the data point spreading between the measured and calculated values.

Sample	$F_{t,crush}$ [kN]	$F_{t,shear}$ [kN]	$F_{t,tensile}$ [kN]	$F_{tot,c}$ [kN]	$F_{t,measured}$ [kN]
$7-11-B_{3.1}$	1.64	0.10	0.00	1.73	4.00
$7-11-B_{3.2}$	3.53	0.63	0.01	4.16	5.49
$7-11-B_{3.3}$	6.45	1.08	0.33	7.86	10.45
$7-11-B_{3.4}$	17.58	0.50	1.99	20.07	21.15
$7-11-B_{3.5}$	17.77	0.58	7.51	25.85	24.33
$7-11-B_{2.1}$	2.34	0.42	0.00	2.76	2.57
$7-11-B_{2.2}$	3.61	1.00	0.02	4.61	4.34
$7-11-B_{2.3}$	8.16	1.51	0.34	10.01	8.20
$7-11-B_{2.4}$	15.29	1.79	2.66	19.74	18.55
$7-11-B_{2.5}$	21.16	1.27	8.25	30.68	27.42
$7-11-B_{5.1}$	2.10	0.05	0.00	2.15	3.68
$7-11-B_{5.2}$	3.28	0.31	0.03	3.61	7.46
$7-11-B_{5.3}$	4.55	1.21	0.31	6.07	12.47
$7-11-B_{5.4}$	12.80	1.49	1.73	16.02	15.40
$7-11-B_{5.5}$	13.44	2.26	12.75	28.44	22.24
$7-11-B_{4.1}$	2.27	0.60	0.00	2.87	9.82
$7-11-B_{4.2}$	4.12	0.79	0.02	4.93	9.35
$7-11-B_{4.3}$	8.86	2.51	0.50	11.87	15.84
$7-11-B_{4.4}$	13.92	4.96	3.10	21.98	18.72
$7-11-B_{4.5}$	22.44	5.60	8.99	37.04	25.05
$7-11-B_{6.1}$	2.14	0.38	0.00	2.52	6.77
$7-11-B_{6.2}$	4.78	0.75	0.02	5.55	8.39
$7-11-B_{6.3}$	10.54	2.24	0.41	13.19	11.51
$7-11-B_{6.4}$	9.89	4.85	1.95	16.69	15.26
$7-11-B_{6.5}$	13.50	4.55	6.03	24.08	20.61

Table 6.9: Comparison between calculated and measured total cutting forces - Artificial rock

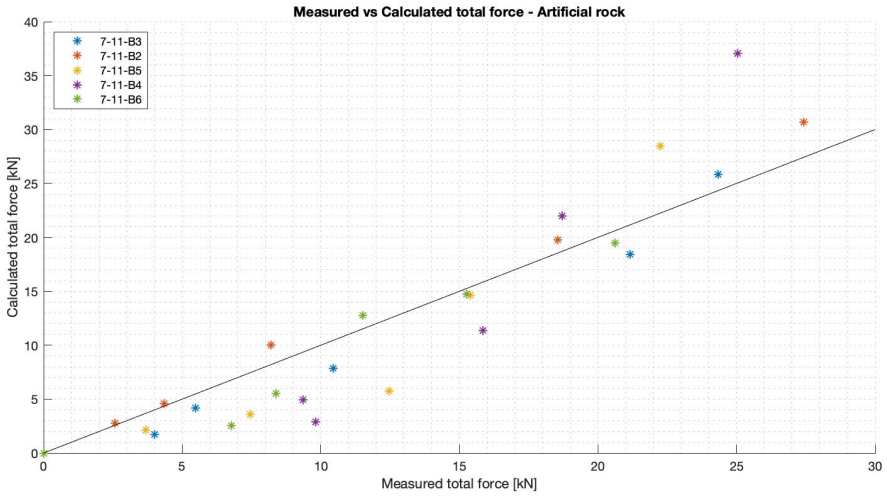

Figure 6.30: Calculated vs measured total forces - artificial rock

When decomposing the total cutting forces, it appears that the forces due to crushing are clearly dominating. Table 6.10 shows the contribution of $F_{crush,i}$ to the total forces, where $i = \{1,2..5\}$ is the number of consecutive experiments, by increasing the cutting depth. As expected, the contribution due to crushing is the highest within the shallow cutting depth regime. When increasing the cutting depth, shear and tensile failure will occur, meaning that the force distribution will become different. A surprising finding is the fact that the crush contribution for sandstone seems to converge to about 60% of the total forces, when increasing the cutting depth. The influence of the concrete crush component also seems to decrease when increasing the cutting depth. Since the concrete is more ductile than the sandstone, it can be proven by the numbers that the contribution of crushing to the total forces is smaller for a more brittle material, when increasing the cutting depth.

Sample	α_c [°]	$F_{crush,1}$ [%]	$F_{crush,2}$ [%]	$F_{crush,3}$ [%]	$F_{crush,4}$ [%]	$F_{crush,5}$ [%]
S_1	45	56.1	63.5	58.9	-	-
S_2	50	73.1	70.2	63.3	59.9	61.1
S_3	55	75.9	75.4	62.8	60.5	62.2
S_4	60	88.7	84.1	73.6	66.7	63.2
$7-11-B_3$	40	94.3	84.8	82.1	87.6	68.7
$7-11-B_2$	45	84.8	78.3	81.5	77.5	68.9
$7-11-B_5$	50	97.6	91.3	78.8	87.5	47.2
$7-11-B_4$	55	79.2	83.9	77.9	63.3	60.6
$7-11-B_6$	60	84.8	86.4	82.4	67.1	69.3

Table 6.10: Contribution crush forces to the total calculated forces

To clearly visualize the percentage distribution of the three failure mechanisms, by changing the input parameters for both rock compositions, a histogram is constructed. Figure 6.31 and 6.32 show the total force distribution due to crushing, major shear failure and tensile failure for the sandstone and concrete experiments, respectively. It can be seen that above each column the measured peak cutting depth h_{peak} for every single experiments is displayed. Because the Combined Force Balance model aims to predicts the peak cutting forces within the rock cutting process, it is of interest to implement h_{peak} into the model to make a good comparison with the measured forces.

By first analyzing the sandstone force distribution in figure 6.31, it is observed that the contribution due to tensile failure is minor to the total forces. This means, according to the model, that the cutting depth is too shallow for a major tensile crack to be able to propagate to the rock's top surface. Due to this hypothesis, it automatically means that the contribution due to shearing will dominate, as chips are being formed. From the figure, it is observed that the forces due to shearing slightly decrease as the cutting angle is increased. This can be fed back by the contribution due crushing. From a physical point of view, it makes sense that the contribution due to crushing increases when increasing the cutting angle. This can be explained by the fact that the indentation area of the pickpoint increases, meaning that it will act as a more blunt tool.

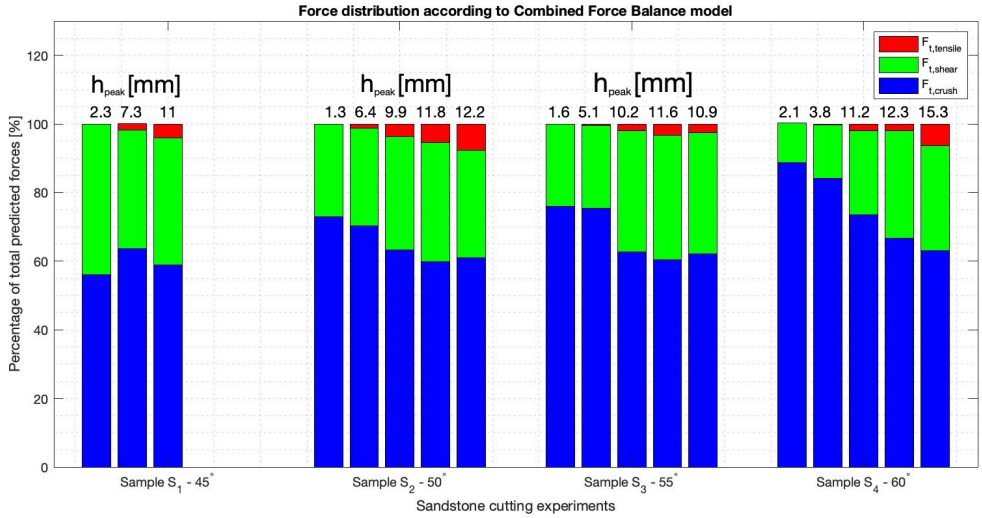

Figure 6.31: Force distribution due to crushing, shear and tensile failure - Sandstone

The concrete force distribution in figure 6.32 shows that the contribution due to tensile failure clearly becomes more important, as the cutting depth is increased. Because the concrete is a relatively low-strength material, and according to existing theories acts as ductile (Miedema [12]), it makes sense that the contribution due to crushing is highest. It is expected that at a certain cutting depth the crushed zone is fully developed in size, whereafter the other failure mechanisms will dominate the total force spectrum. The deeper the cutting depth, the higher the probability for a tensile crack to develop and be able to propagate to the rock's top interface.

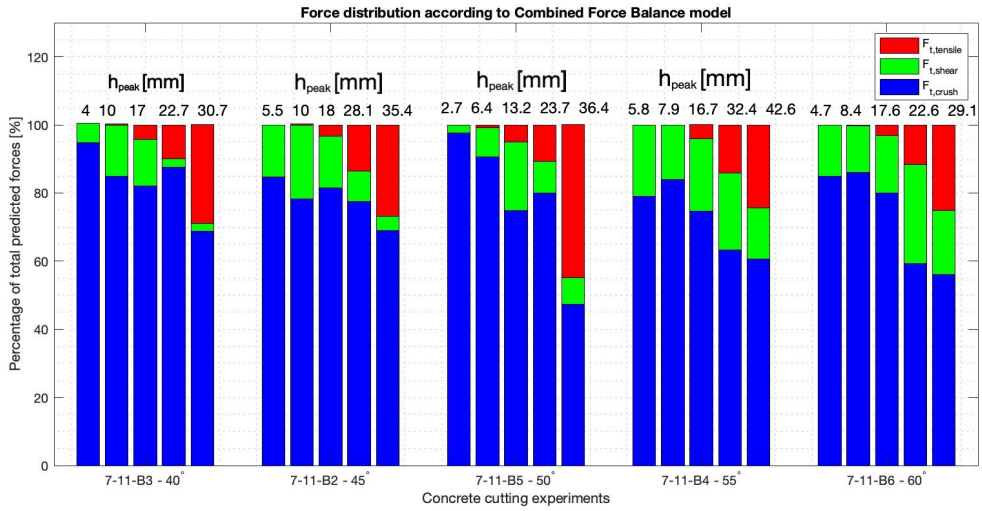

Figure 6.32: Force distribution due to crushing, shear and tensile failure - Concrete

Due to many uncertainties and assumptions made, the expectation arose that the application of the tensile-dominated fracture model would be very limited. For simplification reasons, only one dominant failure mechanism was applied in developing this model. In reality, a combination of multiple failure modes at the crack tip is most likely to be apparent. The way a crack is loaded highly depends on the geometry of your tool and type of loading distribution. For a crack to be initiated, it is important to know at which magnitude the stress intensity factor for the several loading conditions (K_I, K_{II} and K_{III}) is exceeding its critical value (equation 6.54). Because no existing solution was found for the crack loading conditions as in figure 6.20, using the mode I failure criterium. No reference value for K_I was found for this specific cutting configuration, meaning that the outcomes of the tensile-dominated fracture model are not reliable enough to apply. Table 6.11 and 6.12 show that the calculated force due to tensile fracturing are underestimating the measured forces by a large amount.

SANDSTONE

Sample	α_c [°]	$F_{h,fracture}$ [kN]	$F_{h,measured}$ [kN]	$F_{v,fracture}$ [kN]	$F_{v,measured}$ [kN]	$F_{t,fracture}$ [kN]	$F_{t,measured}$ [kN]
$S_{1.1}$	45	0.17	4.76	0.17	4.38	0.25	6.48
$S_{1.2}$	45	0.45	7.10	0.45	13.50	0.63	15.27
$S_{1.3}$	45	0.55	10.20	0.55	19.71	0.78	22.24
$S_{2.1}$	50	0.20	3.71	0.17	3.79	0.27	5.31
$S_{2.2}$	50	0.51	6.35	0.43	10.01	0.66	11.92
$S_{2.3}$	50	0.68	7.77	0.57	12.45	0.89	14.75
$S_{2.4}$	50	0.77	11.01	0.65	14.82	1.00	18.64
$S_{2.5}$	50	0.79	13.03	0.66	20.16	1.03	24.09
$S_{3.1}$	55	0.14	5.60	0.10	7.13	0.17	9.09
$S_{3.2}$	55	0.42	6.26	0.29	8.97	0.51	11.14
$S_{3.3}$	55	0.39	7.07	0.27	9.95	0.48	12.35
$S_{3.4}$	55	0.47	9.98	0.33	10.12	0.57	14.41
$S_{3.5}$	55	0.56	9.90	0.39	14.67	0.68	17.75
$S_{4.1}$	60	0.32	4.77	0.18	8.31	0.37	9.61
$S_{4.2}$	60	0.22	6.58	0.13	8.44	0.26	10.72
$S_{4.3}$	60	0.71	6.74	0.41	12.05	0.82	13.94
$S_{4.4}$	60	0.71	8.16	0.41	13.51	0.82	15.91
$S_{4.5}$	60	0.79	11.79	0.46	18.52	0.91	22.17

Table 6.11: Comparison between forces fracture model and measured values - Sandstone

ARTIFICIAL ROCK

Sample	α_c [°]	$F_{h,fracture}$ [kN]	$F_{h,measured}$ [kN]	$F_{v,fracture}$ [kN]	$F_{v,measured}$ [kN]	$F_{t,fracture}$ [kN]	$F_{t,measured}$ [kN]
$7-11-B_{3.1}$	40	0.11	2.74	0.13	2.61	0.17	4.00
$7-11-B_{3.2}$	40	0.26	3.58	0.32	3.96	0.41	5.49
$7-11-B_{3.3}$	40	0.43	7.97	0.51	6.20	0.67	10.45
$7-11-B_{3.4}$	40	0.58	12.68	0.69	16.80	0.90	21.15
$7-11-B_{3.5}$	40	0.81	17.14	0.96	16.76	1.26	24.33
$7-11-B_{2.1}$	45	0.19	1.73	0.19	1.78	0.26	2.57
$7-11-B_{2.2}$	45	0.29	2.84	0.29	2.98	0.40	4.34
$7-11-B_{2.3}$	45	0.46	6.62	0.46	4.32	0.65	8.20
$7-11-B_{2.4}$	45	0.70	12.93	0.70	12.95	1.00	18.55
$7-11-B_{2.5}$	45	0.89	19.77	0.89	18.54	1.26	27.42
$7-11-B_{5.1}$	50	0.15	2.51	0.12	2.50	0.19	3.68
$7-11-B_{5.2}$	50	0.24	5.11	0.20	5.06	0.32	7.46
$7-11-B_{5.3}$	50	0.40	8.82	0.34	8.01	0.53	12.47
$7-11-B_{5.4}$	50	0.65	10.55	0.54	10.76	0.84	15.40
$7-11-B_{5.5}$	50	0.96	15.37	0.81	15.57	1.25	22.24
$7-11-B_{4.1}$	55	0.27	3.89	0.19	8.93	0.33	9.82
$7-11-B_{4.2}$	55	0.33	5.20	0.23	7.71	0.40	9.35
$7-11-B_{4.3}$	55	0.55	9.86	0.38	11.81	0.67	15.84
$7-11-B_{4.4}$	55	0.94	12.85	0.66	12.86	1.15	18.72
$7-11-B_{4.5}$	55	1.21	18.14	0.85	16.60	1.48	25.05
$7-11-B_{3.1}$	60	0.23	3.03	0.13	6.02	0.27	6.77
$7-11-B_{3.2}$	60	0.33	4.80	0.19	6.76	0.38	8.39
$7-11-B_{3.3}$	60	0.53	7.61	0.31	8.01	0.62	11.51
$7-11-B_{3.4}$	60	0.64	10.29	0.37	10.68	0.74	15.26
$7-11-B_{3.5}$	60	0.79	14.96	0.45	13.32	0.91	20.61

Table 6.12: Comparison between forces fracture model and measured values - Artificial rock

7

CONCLUSIONS AND RECOMMENDATIONS

The conducted research revealed that the physical complexity, associated with the rock cutting process, is relatively high. This is due to the fact that the cutting of rock is a highly irregular and discontinuous process, leading to many uncertainties. The measured output, in terms of forces, appeared to be very sensitive to changes in the input parameters and material properties of the rock compositions. For simplification purposes, all rock formations were assumed to be homogeneous, indicating a uniform strength throughout the complete material. Because the predictability of the rock cutting process is relatively low, the author intended to think out of the box in developing a force prediction model. With the aim for diversity, a distinction was made between two (2) completely different model approaches; *Combined force prediction model* and the *Tensile-dominated fracture model*. For the development of the combined force prediction model, the author mainly focussed on the various failure processes that occurred during the experiments. By critically analyzing the post failure conditions and obtained data of both compositions, the author was able to substantiate the physics for the various failure mechanisms. This led to three composed force expressions, which were combined to predict the total force components.

7.1. CONCLUSIONS

Despite the magnitude of the theoretically-based ductility number for the sandstone and artificial rock samples, it was assumed that both rock compositions failed in a brittle manner, which was based on visual observations. The obtained experimental cutting data showed that the amount of crushed material increased when applying deeper cuts. The expectation arose that the crushed zone stresses would contribute most significantly to the total cutting forces. The physics behind the crushed zone were extensively studied, leading to an expression for the dimensions, stress level and force contribution of this plastic region. The indentation tests have shown that the assumed coefficient of T.Rutten [11] was not correct and cannot be applied for the each and the same rock composition. The indentation coefficients for each rock sample appeared to be significantly higher, indicating that the compressive stresses within the crushed zone are higher. The author found out that the horizontal and vertical force component due to the stresses within the crushed zone are friction dependent, since the tip of the pickpoint is in contact with the bottom of the trench. The reason why the shear and tensile component have not been assumed to be friction dependent is due to the fact that these failure modes occur outside the assumed crushed zone shape.

By critically analyzing the obtained Force-Time plots from the various experiments, the author noticed that there was a significant difference between the horizontal and vertical force component of the sandstone data. It appeared that the vertical force component was significantly higher than the horizontal component. This force difference arises from the resistance the rock gives to reach the desired, preset cutting depth. As expected, the internal resistance to penetrate the material is larger for sandstone than for the artificial rock, since the hardness of the sandstone compositions is higher. This indicates that the pickpoint needs to deliver a higher vertical force to reach the required cutting depth, leading to an increase in frictional forces. The author's hypothesis about the basic stress level, composed out of the forces that arise due to the formation of a crushed zone, including the

dynamic friction coefficient, is well-approximated for both rock compositions in horizontal and vertical direction within the shallow cutting regime (sandstone $h_c \leq 15$mm and artificial rock $h_c \leq 20$mm). When increasing the cutting depth, this basic stress level seems to diverge from the calculated crushed zone forces. This could be a result of an incorrectly calculated and assumed dynamic friction coefficient. According to the results of the combined force prediction model, the forces due to the stresses within the crushed zone seem to dominate the total force spectrum for most cutting configurations (figure 6.31 and 6.32). Depending on the preset cutting angle, it is expected that the forces due to crushing will converge to a, more or less, constant value when a certain cutting depth is reached. Furthermore, the forces due to tensile failure will become more dominant when increasing the cutting depth, because tensile cracks will get the ability to propagate to the rock's top interface.

As mentioned before, the two remaining failure mechanisms (e.g. shear and tensile failure) happen outside of the radius of the crushed zone. The fraction and the contribution to the total forces are based on experimentally-composed shear factor diagram (figure 6.24). This curved trend shows that the influence of shear failure becomes less when increasing the cutting depth. This is in agreement with the existing theories about rock fracturing. Especially for the concrete results, it is clearly seen that the tensile forces become more apparent when applying deeper cuts. The combined force prediction model shows, for the artificial rock, that when $h_c > 20$mm the forces due to tensile failure becomes important. The model results for the sandstone show that shear failure is dominating outside the crushed zone radius. This means that the preset cutting depth is insufficient for a tensile crack to properly develop and significantly contribute to the total forces. This indicates that all the sandstone experiments were performed within the shallow cutting depth regime, where only crushing and major shear failure occurs. It must be noted that, in theory, the shear factor diagram changes for each rock composition. Since the sandstone cutting experiment only consisted out of the application of shallow cutting depths, the same curve shape for both rock formations has been assumed. In reality, for determining the fraction of shear and tensile failure, actual the curve shape might change. It can be concluded that, with the assumptions made, that the calculated peak forces, according to the combined force prediction model, are pretty well predicted for both rock compositions.

The results of the tensile-dominated fracture model underestimated the measured cutting forces by a large amount, and thus not satisfactory for further use. The author concludes that the application of fracture mechanics for the current cutting configuration, is too complex to apply. In practice, it is expected that at the crack tip a combination of multiple failure modes is most likely to happen. Due to the fact that no existing solutions for stress intensity factors for this specific loading condition were available in literature. Furthermore, it is hard to determine if the assumptions made and parameters used are correct for the used cutting configuration. The author states that, in general, fracture mechanics is not a reliable theory to apply. This is because the expected large contribution of the forces due to crushing cannot be expressed in terms of fracture mechanics theory.

7.2. RECOMMENDATIONS

A first recommendation would be to strengthen the cutting tool configuration, to assure rigidity. This is to prevent any excessive bending of the structure. Based on the obtained measurements, it was observed that an undesired, excessive vertical force component was visible. To partially account for this, a factor $\frac{h_{mean}}{h_c}$ was applied. This factor represent a vertical force correction, based on the overall mean cutting depth over the desired, preset cutting depth. If the structure is rigid enough, this factor can be disregarded.

Secondly, the author advises to not proceed with the implementation of rock fracture mechanics within the rock cutting theory. There are too many uncertainties and assumptions that have to be made, making the outcomes unreliable and hard to validate.

During this research the author assumed, based on experimental observations and measurements, that a combination of crushing, shear failure and tensile failure happens as a combined failure mode for this specific cutting configuration, whereby a shear factor diagram was composed. To validate this shear factor diagram, a more critical numerical analysis can be done, creating a general formula that is applicable for multiple rock compositions, cutting angles and cutting depths.

Furthermore, it is recommended to execute a suggested method to determine the basic internal friction angles of the various rock samples. During this research the Hoek and Brown [23] method was assumed to be applicable for determining the friction angles, including a small correction.

The measurements for obtaining the dynamic friction coefficient were conducted on mechanically-driven cutting configuration. For accurate measurements, and therefore getting a converging value for the dynamic friction coefficient for both rock compositions, it is advised to used appropriate measuring equipment that is assigned to execute these kinds of tests.

Throughout the complete report, an unnecessary angle γ_m, in calculating the measured forces by the load sensors (section 3.1), has been used. It must be noted that the changes, by disregarding this angle, are minor. Though, it is advised, in revising the data, to leave γ_m out of the calculation.

It is advised to study the shear factor diagram (figure 6.24) more concisely for a broader range of material and chips to determine the correct shape. The author thinks that the shape might change by using rock with different strength properties.

Within the derivation phase of the Combined Force Balance model, the normal force due to the cohesive forces that act along the shear plane, have overlooked and not been incorporated. This force might play a minor role in calculating the moment around point O (figure 6.14). The author recommends to write one extensive expression for the total peak cutting force, including the mutual effects of the failure mechanisms.

A

EXPERIMENTAL OBSERVATIONS

A.1. EXPERIMENTS 13-08-2019

Concrete batch 7-11-B3 - **0.5cm - 40°**
Because of an uneven surface, the tool was mostly scraping the material. Very fine, but few crushing occurred.

A.2. EXPERIMENTS 14-08-2019

Concrete batch 7-11-B5 - **0.5cm - 50°**
Only very fine crushing occurred. The bottom surface of the cutting trench appeared to be very smooth.

Concrete batch 7-11-B5 - **1.0cm - 50°**
Very fine crushing and small chipping resulted from this test. The outbreaking path and chip size were relatively even.

Concrete batch 7-11-B5 - **1.5cm - 50°**
It seems like the amount of crushed material is accumulating over depth. The chips are getting a more irregular pattern, meaning that some chips are very large and some were quite small. The outbreaking chips are less big than using a shallower cutting angle.

General comment: it is observed that the preset cutting depth during the cutting process, is not reached. Only the first cut of the pick-point reaches its desired cutting depth. As the cutting process continues, approximately $0.6 \cdot h_c$ is reached. A possible cause might be a lack of stiffness of the structure. As the configuration is not rigid enough, bending will influence the cutting depth and most probably the cutting forces.

(a) 0.5cm-50° **(b)** 1.0cm-50° **(c)** 1.5cm-50°

Figure A.1: UCS test of sandstone rock samples at Tongji University

Concrete batch 7-11-B7 - **0.5cm - 55°**
The surface of this block was not even. Because levelness is crucial for obtaining the desired cutting depth and a reliable output of cutting forces, this block was not tested for further use. A test run was done with a cutting depth of 0.5cm and a cutting angle of 55°. The pre-observations were confirmed by the test run, as the pick-point was scraping the rock's interface and sometimes not even being in contact.

Figure A.2: Visible uneven surface of block

Concrete batch 7-11-B4 - **0.7cm - 55°**
More chipping was visible, compared to the 7-11-B5 $0.5cm$ - 50° test, though it was approximately 0.2cm deeper. Crushing was still dominant.

Concrete batch 7-11-B4 - **1.0cm - 55°**
The cutting process looked similar to the 0.7cm -55° test. The remarkable thing was that the production of the 0.7cm test seemed to be higher than the test in question. This could have been a result of an uneven surface or local strength difference of the rock.

Concrete batch 7-11-B4 - **1.0cm - 55°**
Very large chips occurred during the cutting process. Because the cutting depth was not constant along its cutting trajectory, it was clearly observed that the outbreaking chips became larger when the cutting depth increased.

(a) 0.7cm-55°

(b) 1.5cm-55°

(c) Overview 0.5-1.5cm-55°

Figure A.3: Concrete batch 7-11-B4, constant cutting angle

Concrete batch 7-11-B6 - **0.5cm - 60°**
Only fine crushing was observed, no chips were present. The pre-set cutting depth was not fully reached.

Concrete batch 7-11-B6 - **1.0cm - 60°**
Fine crushing and small chips were present.
Concrete batch 7-11-B6 - **2.0cm - 60°**
It was seen, compared to the $7-11-B4$ $2.0cm$ - 55° experiment, that the chips during this test were smaller. This

is contrary to the theory, because the shear angle of the 2.0cm - 60° test should be smaller, resulting in a bigger chip length.

(a) 0.5cm-60° **(b)** 1.0cm-60° **(c)** 2.0cm-60°

Figure A.4: Concrete batch 7-11-B6, constant cutting angle

A.3. EXPERIMENTS 15-08-2019

Concrete batch 7-11-B6 - **0.5cm - 60°**
Another test was done on 0.5cm. Very fine crushing was visible over the complete length of the concrete block. Between the 60-90cm line the cutting depth seemed to increase, because of an uneven surface. This also increased the crushed material at the end.

Figure A.5: Re-run 7-11-B6 **0.5cm - 60°**

Test specimen Sandstone - Tom Rutten - **1.0cm - 60°**
The desired cutting depth was not reached. Though, compared to the cutting experiment of Tom Rutten, it clearly visible that this cutting trench is a lot more smooth. This probably a consequence of the sharpness of the pick-point and the rigidity of the structure. Tom used a relatively blunt tool, compared to the one used during this experiment. The bottom of Tom's trench shows many bumps, which means that the force measurements probably contains a lot of peaks that partly consists of the momentum due to the resilience of the structure. The structure used for these experiments is a lot stiffer.

Test specimen Sandstone - Tom Rutten - **1.5cm - 60°**
Compared to the 1.0-60° experiment, a lot of chipping occurred and the amount of crushed material accumulated. The desired cutting depth was not reached.

(a) 1.0cm-60°

(b) 1.5cm-60°

(c) Cutting trench comparison 1.0cm-60°

Figure A.6: Sandstone experiments - test specimen of Tom Rutten

Concrete batch 7-11-B4 - **0.5cm - 55°**
Re-run of the 0.5cm - 55° test.

Figure A.7: Re-run 7-11-B4 **0.5cm - 55°**

For the following tests a constant cutting depth and a variation in cutting angles was applied.
Concrete batch 7-15-B1 - **1.5cm - 40°**
Appears that the chips are not breaking out, but continue to fail within the xz-plane. The explaination for this could be that the cutting angle is too shallow, so the vertical forces are dominant over the horizontal forces. It must be noted that the pre-set cutting depth was not entirely reached.

Concrete batch 7-15-B1 - **1.5cm - 45°**
Outbreaking path of the chips became more visible than the 1.5cm - 40° experiment. The amount of crushed material increased, so as the chip sizes.

Concrete batch 7-15-B1 - **1.5cm - 50°**
It was observed that the formed chips looked quite similar in size to the 1.5cm - 45° experiment. Also the amount of crushed material increased again, compared to the previous tests.

General comment: it must be noted for all tests that between 10-60cm line the cutting depth was relatively constant, but did not reach the desired value. When the 60cm line was passed, the cutting depth seemed to increase. This is probably due to uneveness of the concrete block.

(a) 1.5cm-40° **(b)** 1.5cm-45° **(c)** 1.5cm-50°

Figure A.8: Concrete batch 7-15-B1, constant cutting depth

Concrete batch 7-15-B1 - **1.5cm - 55°**
Chip forming and outbreaking path appears to be approximately the same as the 1.5cm - 45°/°. Crushing progressively increases.

Concrete batch 7-15-B1 - **1.5cm - 60°**
Again, chips and breaking path looks quite similar to 1.5cm - 45°/50°/55°. More crushed material than the tests before.

General comment: it can be concluded from the sequence of these tests that the amount of crushed material increases, as the cutting angle becomes larger. In a physical sense this can be interpreted by the fact that the horizontal force on the pick-point becomes larger, leading to an increase of the crushed zone.

(a) 1.5cm-55° **(b)** 1.5cm-60°

Figure A.9: Concrete batch 7-15-B1, constant cutting depth

The aim of the following experiments was to reach a cutting depth of 4cm. To see how the artificial rock behaves from 2cm to 4cm cutting depth, an intermediate step of h_d=3.0cm was added.
Concrete batch 7-11-B3 - **3.0cm - 40°**
As expected, the chips became larger than the 2.0cm - 40° test, done on **14-08-2019**. The amount of crushed material also increased drastically. It was observed that between the 50-70cm line, the outbreaking path, and thus chip size, increased.

Concrete batch 7-11-B3 - **4.0cm - 40°**
The production progressively became larger, compared to the 3.0cm - 40° experiment. Again, between the 50-70cm line, the chip size increased. The outbreaking path over the length of the block looks quite constant.

(a) 3.0cm-40° **(b)** 4.0cm-40° **(c)** Overview 3.0/4.0cm-40°

Figure A.10: Concrete batch 7-11-B3, constant cutting angle

A.4. EXPERIMENTS 16-08-2019

Concrete batch 7-11-B2 - **3.0cm - 45°**
Relatively even outbreaking path of the chips. Crushing appeared to increase during the cutting process.

Concrete batch 7-11-B2 - **4.0cm - 45°**
It is observed that the chips, compared to the 3.0cm - 45° experiment, are a lot larger. It is clearly seen that the production increased drastically.

General comment: The cutting profile of both experiments differ significantly. It might be that the transition point of a potential quadratically increase in cutting forces is between 3.0-4.0cm. It still has to be proven that the production and corresponding cutting forces at a depth larger than 4.0cm is efficient enough for practice. It must be noted that wear on the pick-point is not visible.

(a) 3.0cm-45° **(b)** 4.0cm-45° **(c)** Overview 3.0/4.0cm-45°

Figure A.11: Concrete batch 7-11-B2, constant cutting angle

Concrete batch 7-11-B5 - **3.0cm - 50°**
The outbreaking path of chips is to be very constant between 60-90cm. Desired cutting depth was not reached.

Concrete batch 7-11-B5 - **4.0cm - 50°**
On the eye the production seems to be less than the 4.0cm - 45° experiment. The chip size increased after approximately 40cm of cutting. Desired cutting depth was not reached.

(a) 3.0cm-50°

(b) 4.0cm-50°

(c) Overview 3.0/4.0cm-50°

Figure A.12: Concrete batch 7-11-B5, constant cutting angle

Concrete batch 7-11-B4 - **3.0cm - 55°**
The outbreaking path of the chips along the cutting trajectory looks relatively constant. Tough, the chip size accumulated over the length of the block. This increase in chip size has to do with breakage of the chips in the xz-plane. The production looks similar to the 3.0cm - 50° experiment.

Concrete batch 7-11-B4 - **4.0cm - 55°**
Chips during this experiment were very large. The production, as observed so far, is the largest from the 3.0-4.0cm experiments. The outbreaking path is again very constant along the path.

(a) 3.0cm-55°

(b) 4.0cm-55°

(c) Overview 3.0/4.0cm-55°

Figure A.13: Concrete batch 7-11-B4, constant cutting angle

Concrete batch 7-11-B6 - **3.0cm - 60°**
Chip forming appeared to be less than the 45°,50° and 55° - 3.0cm experiments. Also the production seems to be less. Outbreaking path a bit more irregular.

Concrete batch 7-11-B6 - **4.0cm - 60°**
Relatively large chips occurred, but less big than the 55° - 4.0cm experiment. The amount of crushed material also accumulated, compared to the 60° - 3.0cm test.

(a) 3.0cm-60°

(b) 4.0cm-60°

(c) Overview 3.0/4.0cm-60°

Figure A.14: Concrete batch 7-11-B6, constant cutting angle

Concrete batch 7-17-B2 - **1.0cm - 40°**
It was observed that the first 40cm of cutting, the obtained cutting depth was very shallow. Further into the cutting process, the cutting depth seemed to increase. A physical explanation for this could be that the rock's strength within the first 40cm is higher.

Concrete batch 7-17-B2 - **1.0cm - 45°**
A better, more constant cutting depth was achieved during this test. The production appears to be more than the 40° - 1.0cm experiment. Furthermore, the chips sizes seem to be larger than the previous test.

Concrete batch 7-17-B2 - **1.0cm - 50°**
It is clearly observed that the overall chip size accumulated, compared to the two previous experiments. Also the amount of crushed material increased. Partially indicating that, by increasing the cutting angle, the amount of crushed material increases. This can be fed back by the increase in indentation area of the pickpoint's cutting face.

(a) 1.0cm - 40°

(b) 1.0cm - 45°

(c) 1.0cm - 50°

Figure A.15: Concrete batch 7-17-B2, constant cutting depth

Concrete batch 7-17-B2 - **1.0cm - 55°**
Outbreaking of the chips appeared to be less than the 45° and 50° - 1.0 experiments.

Concrete batch 7-17-B2 - **1.0cm - 60°**
Overall, the cutting trench of the 60° experiment looks quite similar to the 55° test. This holds for the chip sizes and outbreaking profile.

(a) 1.0cm - 55° **(b)** 1.0cm - 60°

Figure A.16: Concrete batch 7-17-B2, constant cutting depth

A.5. EXPERIMENTS 19-08-2019

Sandstone - Sample 4 - **0.5cm - 45°**
Only crushing in front of the pickpoint happened. The preset cutting depth was not reached, probably because of the lack of stiffness of the construction and the hardness of the material. It was observed that the cutting depth became slightly more after 60cm into cutting.

Sandstone - Sample 4 - **1.0cm - 45°**
Again, a lot of crushing occurred, very few chips broke out. As for the previous experiment, the desired cutting depth was not reached.

Sandstone - Sample 4 - **1.5cm - 45°**
Small chips broke out and, again, crushing was dominant.

(a) 0.5cm - 45° **(b)** 1.0cm - 45° **(c)** 1.5cm - 45°

Figure A.17: Sandstone sample 4, constant cutting depth

A.6. EXPERIMENTS 21-08-2019

Sandstone - Sample 4 - **0.5cm - 60°**
As expected, a lot of crushed material resulted from the experiment. Desired cutting depth was not reached.

Sandstone - Sample 4 - **1.0cm - 60°**
Again, desired cutting depth was not reached very well. Mainly crushing occurred due to the shallow cut.

Sandstone - Sample 4 - **1.5cm - 60°**
Looked like the desired cutting depth is being approached better. A lot of chips broke out, having a smooth and even cutting profile.

(a) 0.5cm - 60° **(b)** 1.0cm - 60° **(c)** 1.5cm - 60°

Figure A.18: Sandstone sample 4, constant cutting angle

Sandstone - Sample 3 - **0.5cm - 55°**
Cutting depth not reached, mostly scraping of the rock's top interface. Very fine crushing.

Sandstone - Sample 3 - **1.0cm - 55°**
Approximately half of the desired cutting depth was reached. At some point along the cutting trajectory a deeper cutting depth was achieved, leading to chip forming.

(a) 0.5cm - 55° **(b)** 1.0cm - 55°

Figure A.19: Sandstone sample 3, constant cutting angle

Sandstone - Sample 3 - **1.5cm - 55°**
Compared to the 1.0cm - 55°, the chip size increased significantly. It appeared that the bottom of the cutting groove was a bit uneven, not as smooth as other experiments. The breakout pattern of the chips looked almost the same, on the other side of the groove.

Sandstone - Sample 3 - **2.0cm - 55°**
Chips are slightly bigger dan the 1.5cm - 55° experiment. Though, the desired cutting depth was not reached.

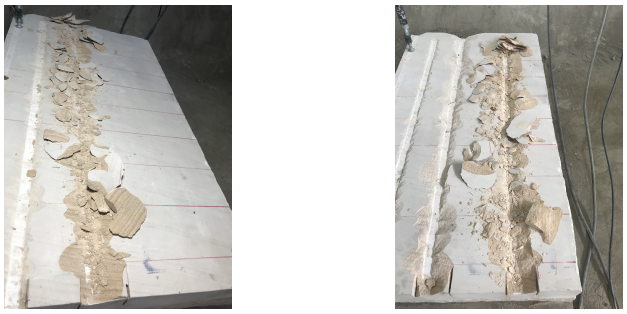

(a) 1.5cm - 55° **(b)** 2.0cm - 55°

Figure A.20: Sandstone sample 3, constant cutting angle

Sandstone - Sample 2 - **0.5cm - 50°**
Test was not usable. Pickpoint was just scraping the rock's top interface.

Sandstone - Sample 2 - **1.0cm - 50°**
Chips became larger over the length of the cutting trajectory. Desired cutting depth was not reached.

(a) 0.5cm - 50°

(b) 1.0cm - 50°

Figure A.21: Sandstone sample 2, constant cutting angle

Sandstone - Sample 2 - **1.5cm - 50°**
Chip forming became a lot more and bigger than the 1.0 cm - 50° experiment. Desired cutting depth not reached.

Sandstone - Sample 2 - **2.0cm - 50°**
Some very large chips broke out during cutting. Also excessive vibrations of the pickpoint itself were observed, followed by large chip formation.

(a) 1.5cm - 50°

(b) 2.0cm - 50°

Figure A.22: Sandstone sample 2, constant cutting angle

A.7. EXPERIMENTS 22-08-2019

Sandstone - Sample 4 - **2.0cm - 60°**
Approximately half of the cutting depth was reached. Along the complete length of the cutting groove, chip outbreaking happened. The pickpoint was vibrating along the complete cutting trajectory.

Sandstone - Sample 4 - **2.5cm - 60°**
Vibration increased. Very large chips broke out, causing the wide outbreaking profile. Also a lot of crushing occurred.

(a) 2.0cm - 60°

(b) 2.5cm - 60°

(c) Overview Sandstone 60°

Figure A.23: Sandstone sample 4, constant cutting angle

Sandstone - Sample 3 - **2.0cm - 55°**
Large chips broke out, also quite a lot of crushing occurred.

Sandstone - Sample 2 - **2.5cm - 50°**
It is clearly seen that the reached cutting depth is becoming more shallow, as the cutting angle becomes less. This is due to the comparisons made between other tests. For the pickpoint is is harder to reach the desired cutting depth when a small cutting angle is applied. Vertical force becomes higher. Even larger chips broke out than the previous experiments. Also the amount of crushed material increased.

B

INDENTATION TEST RESULTS

B.1. SANDSTONE

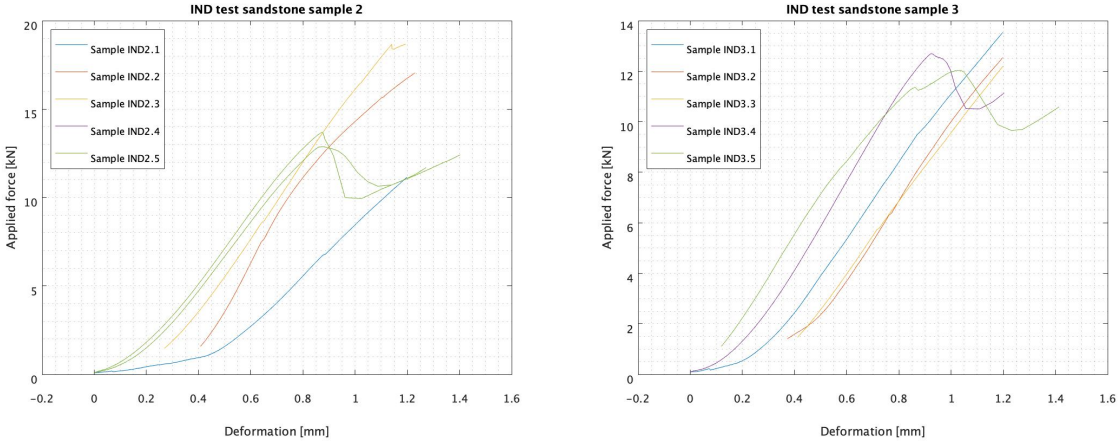

(a) Test results indendation test Sample S2

(b) Test results indendation test Sample S3

Figure B.1: Test results indendation test Sample S2 and S3

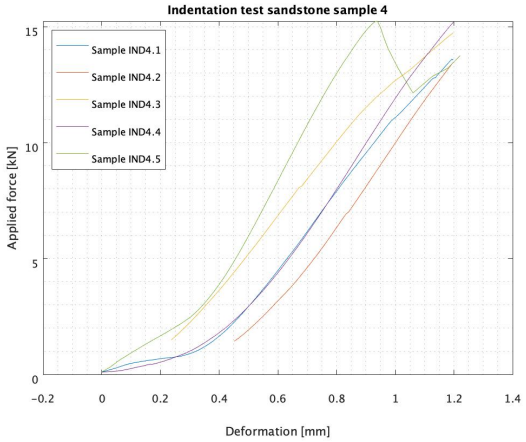

Figure B.2: Test results indendation test Sample S4

B.2. ARTIFICIAL ROCK

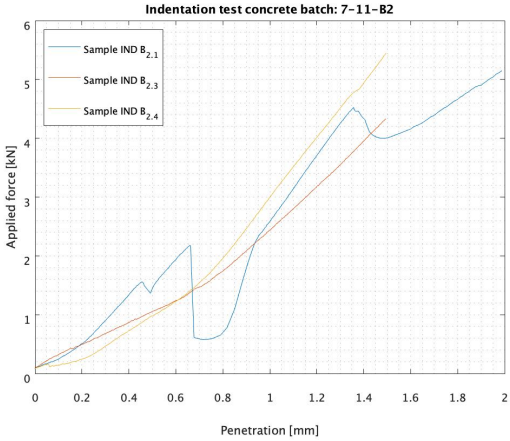

(a) Test results indendation test 7-11-B2

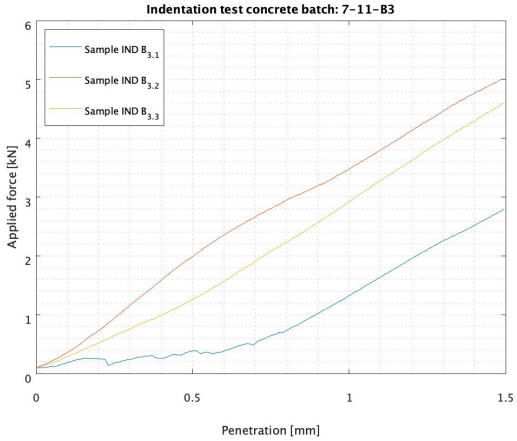

(b) Test results indendation test 7-11-B3

Figure B.3: Test results indendation test 7-11-B2 and 7-11-B3

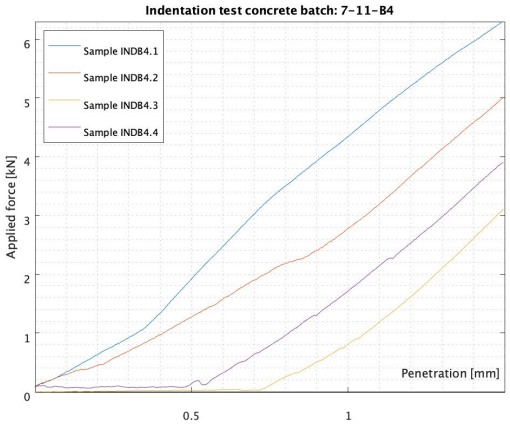

(a) Test results indendation test 7-11-B4

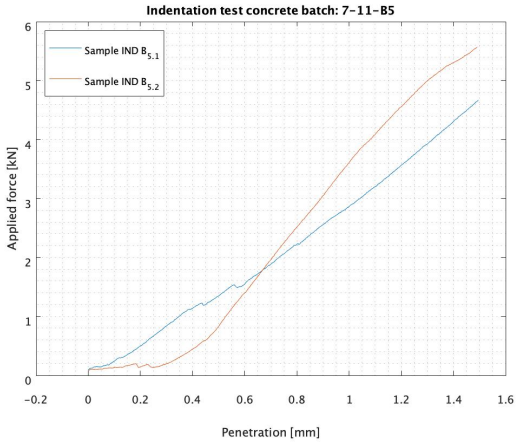

(b) Test results indendation test 7-11-B5

Figure B.4: Test results indendation test 7-11-B4 and 7-11-B5

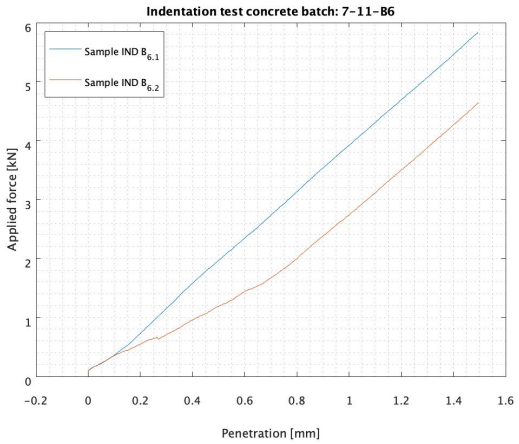

Figure B.5: Test results indendation test 7-11-B6

C

EXPERIMENTAL CUTTING DATA

C.1. CUTTING GROOVE DATA - ARTIFICIAL ROCK

#	Experiment	α_c ∘	h_c [mm]	h_{mean} [mm]	h_{peak} [mm]	w_{mean} [mm]	w_{peak} [mm]
1	$7-11-B_{3.1}$	40	5	3.3	4.0	26.40	27.12
	$7-11-B_{3.2}$	40	10	9.3	10.0	53.90	63.44
	$7-11-B_{3.3}$	40	20	16.6	17.0	117.60	150.32
	$7-11-B_{3.4}$	40	30	21.1	22.7	94.90	140.52
	$7-11-B_{3.5}$	40	40	28.3	30.7	139.50	184.78
2	$7-11-B_{2.1}$	45	5	4.2	5.5	29.00	37.44
	$7-11-B_{2.2}$	45	10	9.3	10.0	65.00	66.91
	$7-11-B_{2.3}$	45	20	14.8	18.0	106.00	135.11
	$7-11-B_{2.4}$	45	30	23.1	28.1	97.90	146.43
	$7-11-B_{2.5}$	45	40	31.1	35.4	147.00	189.34
3	$7-11-B_{5.1}$	50	5	2.7	2.77	20.40	20.4
	$7-11-B_{5.2}$	50	10	5.9	6.4	34.10	40.22
	$7-11-B_{5.3}$	50	20	12.1	13.2	68.80	82.16
	$7-11-B_{5.4}$	50	30	20.7	23.7	94.20	106.15
	$7-11-B_{5.5}$	50	40	33.6	36.4	123.90	138.05
4	$7-11-B_{4.1}$	55	5	4.6	5.8	30.80	32.56
	$7-11-B_{4.2}$	55	10	6.2	7.9	33.00	42.33
	$7-11-B_{4.3}$	55	20	17	16.7	87.70	113.87
	$7-11-B_{4.4}$	55	30	28.5	32.4	126.10	124.44
	$7-11-B_{4.5}$	55	40	37.8	42.6	163.00	195.12
5	$7-11-B_{6.1}$	60	5	3.5	4.7	22.50	26.55
	$7-11-B_{6.1}$	60	10	7	8.4	40.30	42.03
	$7-11-B_{6.1}$	60	20	14.9	17.6	67.00	90.19
	$7-11-B_{6.1}$	60	30	16.2	22.6	88.00	148.74
	$7-11-B_{6.1}$	60	40	24.9	29.1	146.80	200.22

Table C.1: Resulting cutting depth/width data - Artificial rock

C.2. CUTTING GROOVE DATA - SANDSTONE

#	Experiment	α_c °	h_c [mm]	h_{mean} [mm]	h_{peak} [mm]	w_{mean} [mm]	w_{peak} [mm]
9	Sample $S_{1.1}$	45	5	2.1	2.3	33.12	18.1
	Sample $S_{1.2}$	45	10	6.8	7.3	48.21	51.65
	Sample $S_{1.3}$	45	15	10.4	11	76.11	88.15
10	Sample $S_{2.1}$	50	5	1.2	1.3	16.9	17.1
	Sample $S_{2.2}$	50	10	6.34	6.4	36.31	38.22
	Sample $S_{2.3}$	50	15	8.46	9.9	57.41	77.56
	Sample $S_{2.4}$	50	20	12.68	11.8	74.06	69.08
	Sample $S_{2.5}$	50	25	12.18	12.2	78.47	125.74
11	Sample $S_{3.1}$	55	5	2.47	1.6	16.8	17.00
	Sample $S_{3.2}$	55	10	5.44	5.1	36.65	45.50
	Sample $S_{3.3}$	55	15	9.58	10.2	64.59	71.64
	Sample $S_{3.4}$	55	20	11.66	11.6	66.47	74.07
	Sample $S_{3.5}$	55	25	9.66	10.9	59.59	102.55
12	Sample $S_{4.1}$	60	5	2.42	2.1	19.28	17.1
	Sample $S_{4.2}$	60	10	3.36	3.8	22.54	33.1
	Sample $S_{4.3}$	60	15	10.79	11.2	66.97	80.7
	Sample $S_{4.4}$	60	20	10.92	12.3	56.19	86.6
	Sample $S_{4.5}$	60	25	14.25	15.3	72.15	97.8

Table C.2: Resulting cutting depth/width data - Sandstone

C.3. FORCE DATA - ARTIFICIAL ROCK

$7-11-B2$ - 45°

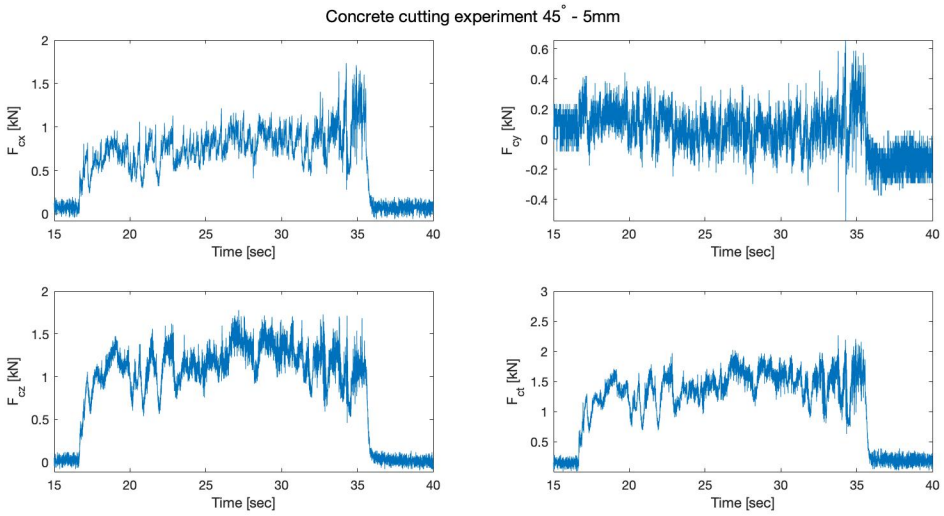

Figure C.1: Force-Time plots $7-11-B_{2.1}$

Experiment	α_c °	$F_{x,max}$ [kN]	$F_{x,mean}$ [kN]	$F_{y,max}$ [kN]	$F_{y,mean}$ [kN]	$F_{z,max}$ [kN]	$F_{z,mean}$ [kN]	$F_{t,max}$ [kN]	$F_{t,mean}$ [kN]
$7-11-B_{2.1}$	45	1.73	0.79	0.66	0.09	1.78	1.14	2.57	1.40

Table C.3: Force-Time plots $7-11-B_{2.1}$

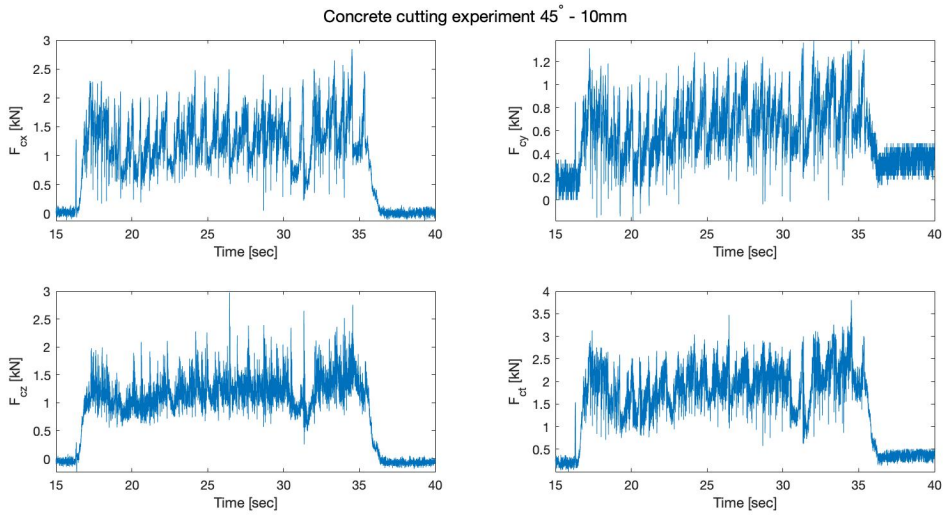

Figure C.2: Force-Time plots $7-11-B_{2.2}$

Experiment	α_c °	$F_{x,max}$ [kN]	$F_{x,mean}$ [kN]	$F_{y,max}$ [kN]	$F_{y,mean}$ [kN]	$F_{z,max}$ [kN]	$F_{z,mean}$ [kN]	$F_{t,max}$ [kN]	$F_{t,mean}$ [kN]
$7-11-B_{2.2}$	45	2.84	1.27	1.39	0.66	2.98	1.19	4.34	1.89

Table C.4: Force-Time plots $7-11-B_{2.2}$

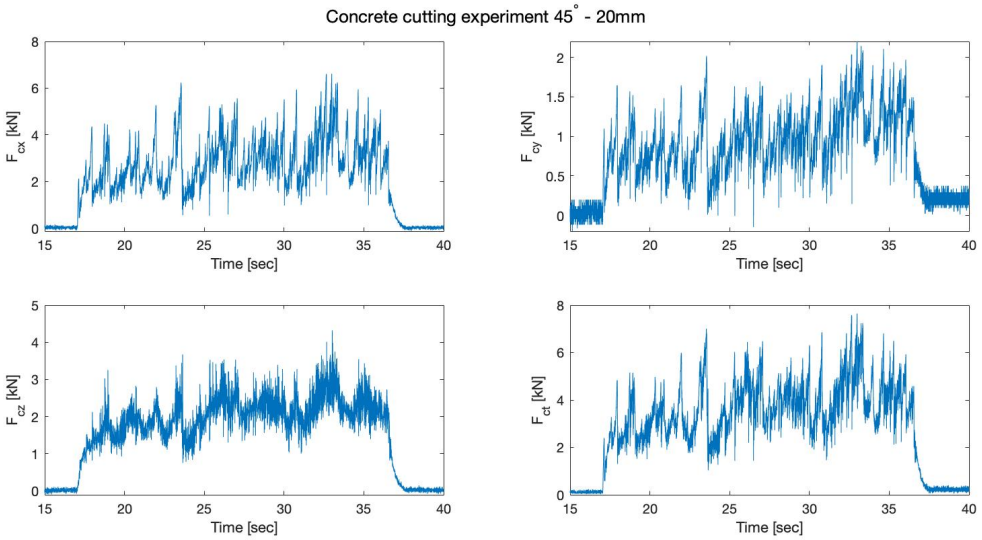

Figure C.3: Force-Time plots $7-11-B_{2.3}$

Experiment	α_c °	$F_{x,max}$ [kN]	$F_{x,mean}$ [kN]	$F_{y,max}$ [kN]	$F_{y,mean}$ [kN]	$F_{z,max}$ [kN]	$F_{z,mean}$ [kN]	$F_{t,max}$ [kN]	$F_{t,mean}$ [kN]
$7-11-B_{2.3}$	45	6.62	2.89	2.20	0.97	4.32	2.04	8.20	3.70

Table C.5: Force-Time plots $7-11-B_{2.3}$

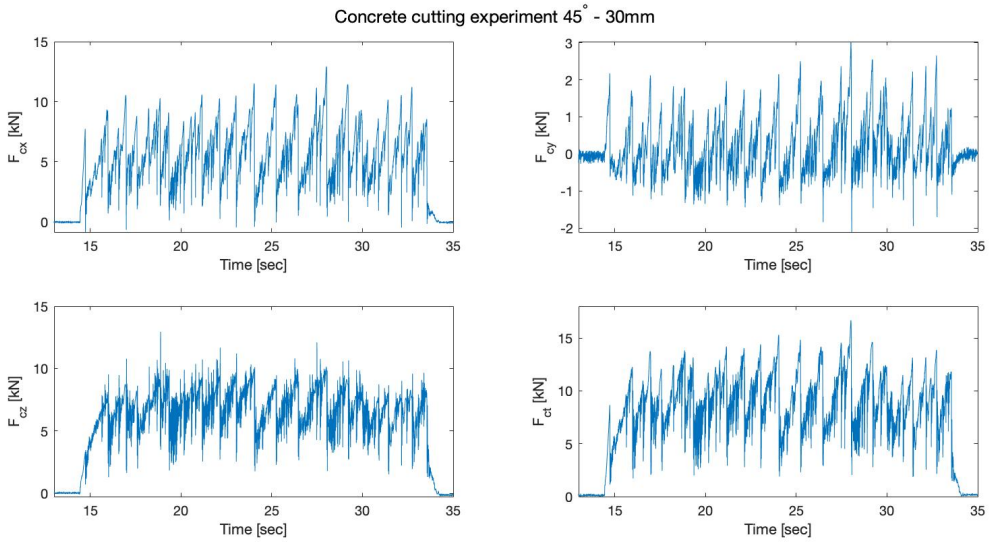

Figure C.4: Force-Time plots $7-11-B_{2.4}$

Experiment	α_c °	$F_{x,max}$ [kN]	$F_{x,mean}$ [kN]	$F_{y,max}$ [kN]	$F_{y,mean}$ [kN]	$F_{z,max}$ [kN]	$F_{z,mean}$ [kN]	$F_{t,max}$ [kN]	$F_{t,mean}$ [kN]
$7-11-B_{2.4}$	45	12.93	5.76	3.03	0.22	12.95	6.71	18.55	8.95

Table C.6: Force-Time plots $7-11-B_{2.4}$

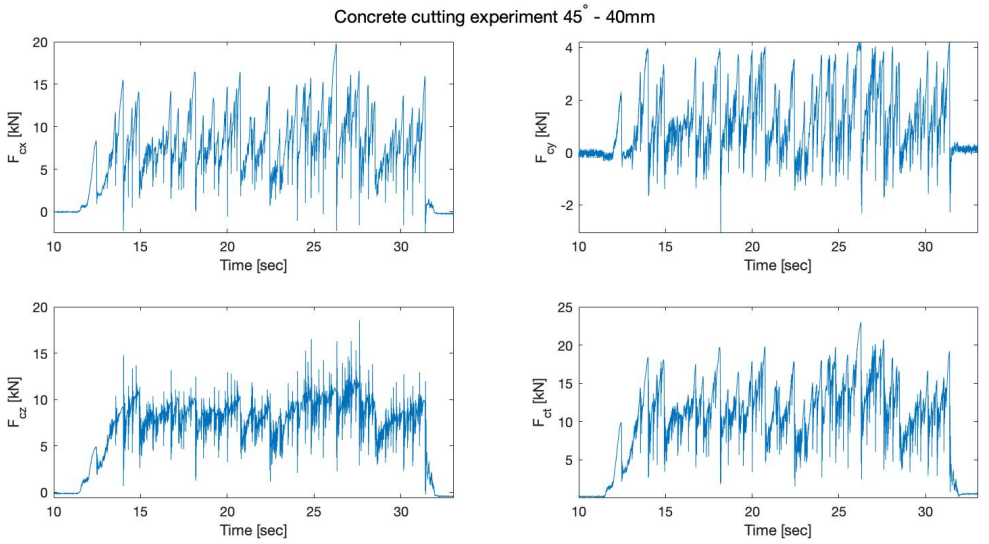

Figure C.5: Force-Time plots $7-11-B_{2.5}$

Experiment	α_c °	$F_{x,max}$ [kN]	$F_{x,mean}$ [kN]	$F_{y,max}$ [kN]	$F_{y,mean}$ [kN]	$F_{z,max}$ [kN]	$F_{z,mean}$ [kN]	$F_{t,max}$ [kN]	$F_{t,mean}$ [kN]
$7-11-B_{2.5}$	45	19.77	8.35	4.22	1.31	18.54	8.09	27.42	11.84

Table C.7: Force-Time plots $7-11-B_{2.5}$

$7-11-B5$ - 50°

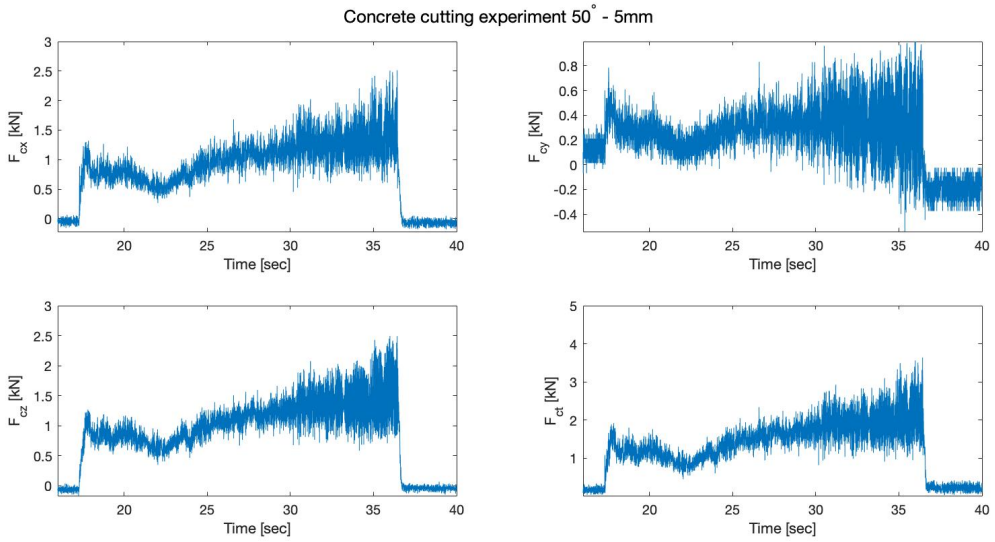

Figure C.6: Force-Time plots $7-11-B_{5.1}$

Experiment	α_c °	$F_{x,max}$ [kN]	$F_{x,mean}$ [kN]	$F_{y,max}$ [kN]	$F_{y,mean}$ [kN]	$F_{z,max}$ [kN]	$F_{z,mean}$ [kN]	$F_{t,max}$ [kN]	$F_{t,mean}$ [kN]
$7-11-B_{5.1}$	50	2.51	1.02	1.00	0.30	2.50	1.10	3.68	1.54

Table C.8: Force-Time plots $7-11-B_{5.1}$

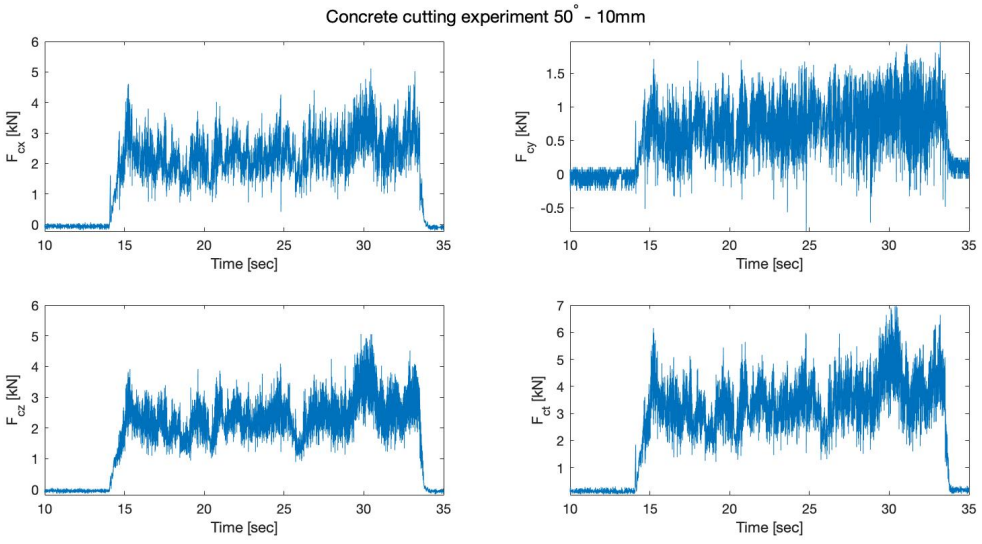

Figure C.7: Force-Time plots $7-11-B_{5.2}$

Experiment	α_c °	$F_{x,max}$ [kN]	$F_{x,mean}$ [kN]	$F_{y,max}$ [kN]	$F_{y,mean}$ [kN]	$F_{z,max}$ [kN]	$F_{z,mean}$ [kN]	$F_{t,max}$ [kN]	$F_{t,mean}$ [kN]
$7-11-B_{5.2}$	50	5.11	2.34	1.97	0.75	5.06	2.34	7.46	3.42

Table C.9: Force-Time plots $7-11-B_{5.2}$

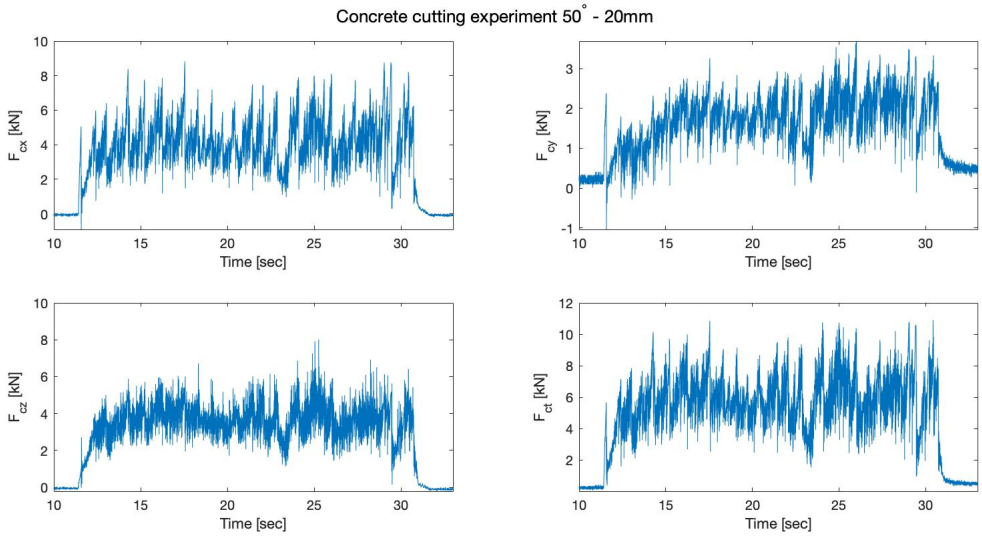

Figure C.8: Force-Time plots $7-11-B_{5.3}$

Experiment	α_c °	$F_{x,max}$ [kN]	$F_{x,mean}$ [kN]	$F_{y,max}$ [kN]	$F_{y,mean}$ [kN]	$F_{z,max}$ [kN]	$F_{z,mean}$ [kN]	$F_{t,max}$ [kN]	$F_{t,mean}$ [kN]
$7-11-B_{5.3}$	50	8.82	4.16	3.69	1.76	8.01	3.55	12.47	5.79

Table C.10: Force-Time plots $7-11-B_{5.3}$

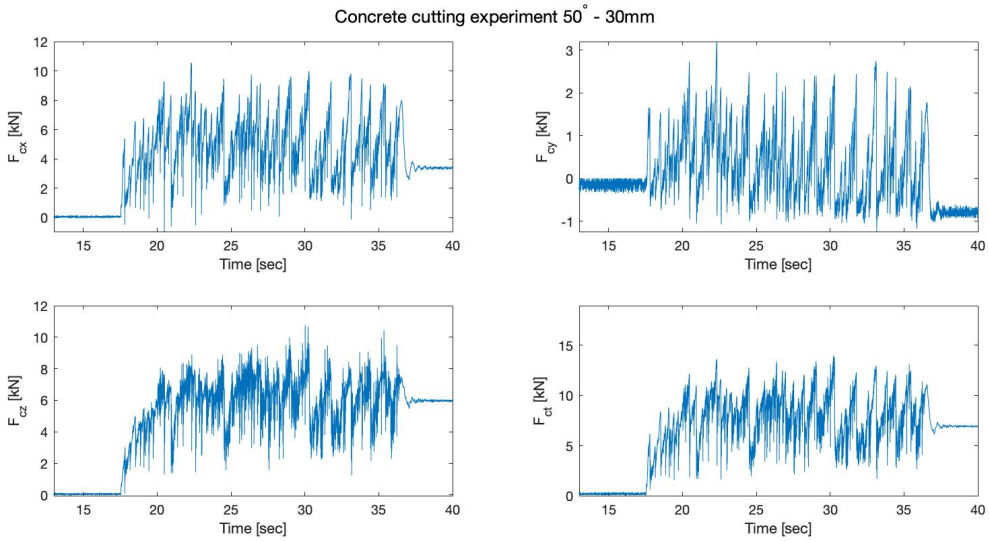

Figure C.9: Force-Time plots $7-11-B_{5.4}$

Experiment	α_c °	$F_{x,max}$ [kN]	$F_{x,mean}$ [kN]	$F_{y,max}$ [kN]	$F_{y,mean}$ [kN]	$F_{z,max}$ [kN]	$F_{z,mean}$ [kN]	$F_{t,max}$ [kN]	$F_{t,mean}$ [kN]
$7-11-B_{5.4}$	50	10.55	5.07	3.20	0.40	10.76	5.88	15.40	7.89

Table C.11: Force-Time plots $7-11-B_{5.4}$

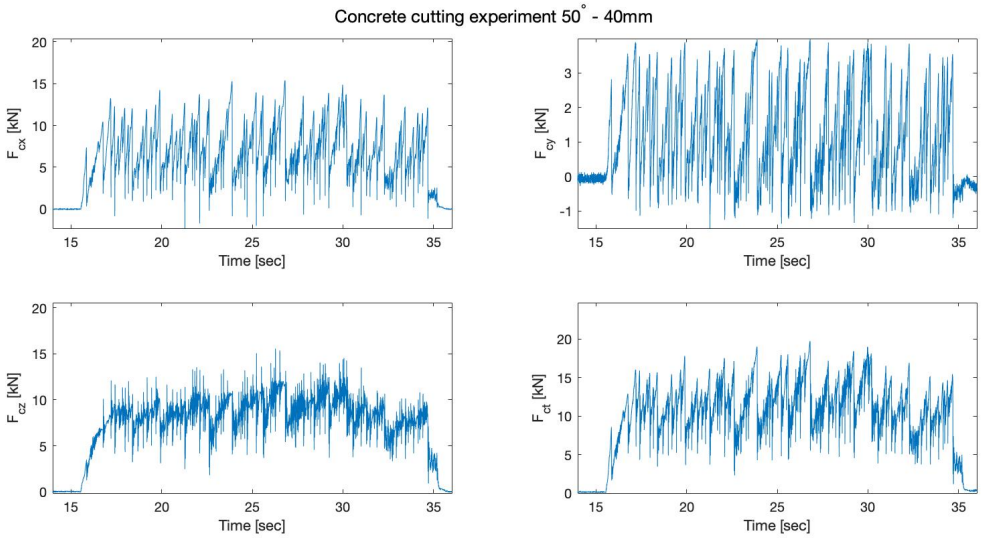

Figure C.10: Force-Time plots $7-11-B_{5.5}$

Experiment	α_c °	$F_{x,max}$ [kN]	$F_{x,mean}$ [kN]	$F_{y,max}$ [kN]	$F_{y,mean}$ [kN]	$F_{z,max}$ [kN]	$F_{z,mean}$ [kN]	$F_{t,max}$ [kN]	$F_{t,mean}$ [kN]
$7-11-B_{5.5}$	50	15.37	7.21	3.99	1.28	15.57	8.43	22.24	11.35

Table C.12: Force-Time plots $7-11-B_{5.5}$

$7-11-B4$ - 55°

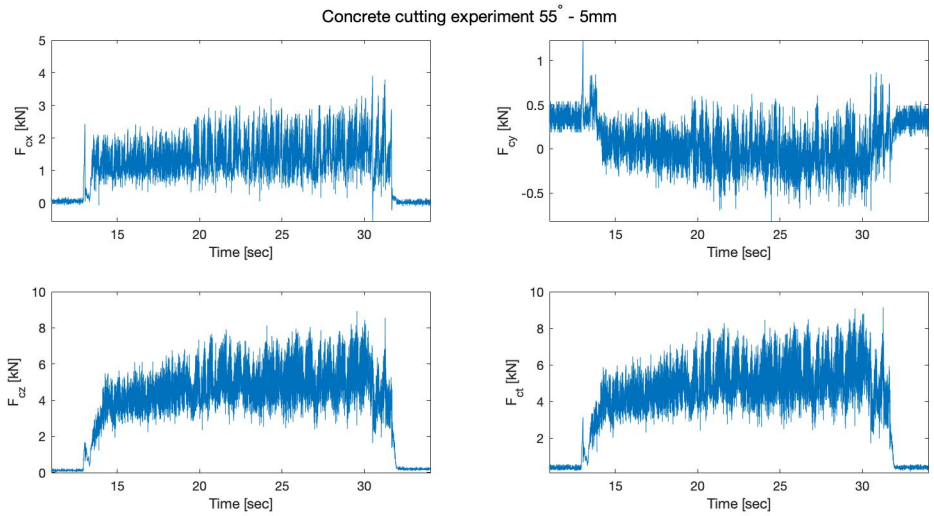

Figure C.11: Force-Time plots $7-11-B_{4.1}$

Experiment	α_c °	$F_{x,max}$ [kN]	$F_{x,mean}$ [kN]	$F_{y,max}$ [kN]	$F_{y,mean}$ [kN]	$F_{z,max}$ [kN]	$F_{z,mean}$ [kN]	$F_{t,max}$ [kN]	$F_{t,mean}$ [kN]
$7-11-B_{4.1}$	55	3.89	1.44	1.23	0.02	8.93	4.52	9.82	4.77

Table C.13: Force-Time plots $7-11-B_{4.1}$

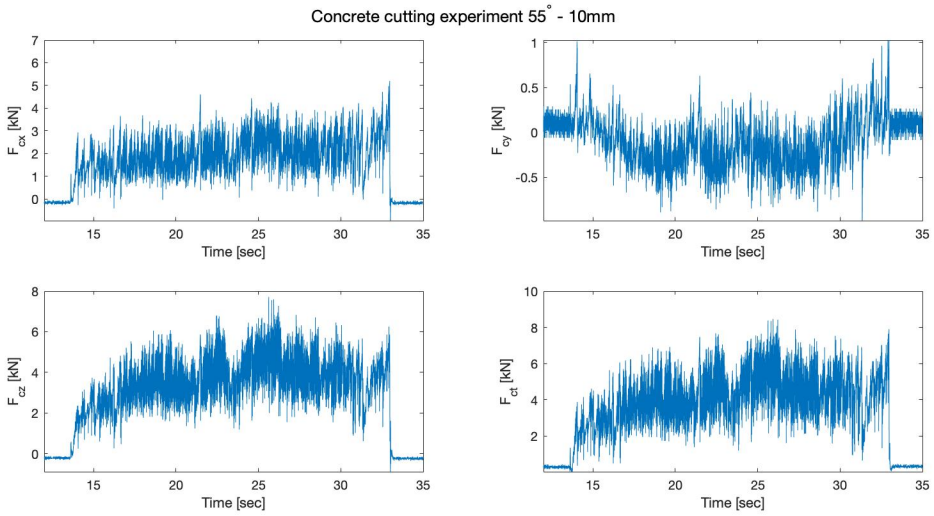

Figure C.12: Force-Time plots $7-11-B_{4.2}$

Experiment	α_c °	$F_{x,max}$ [kN]	$F_{x,mean}$ [kN]	$F_{y,max}$ [kN]	$F_{y,mean}$ [kN]	$F_{z,max}$ [kN]	$F_{z,mean}$ [kN]	$F_{t,max}$ [kN]	$F_{t,mean}$ [kN]
$7-11-B_{4.2}$	55	5.20	2.04	1.03	-0.13	7.71	3.56	9.35	4.13

Table C.14: Force-Time plots $7-11-B_{4.2}$

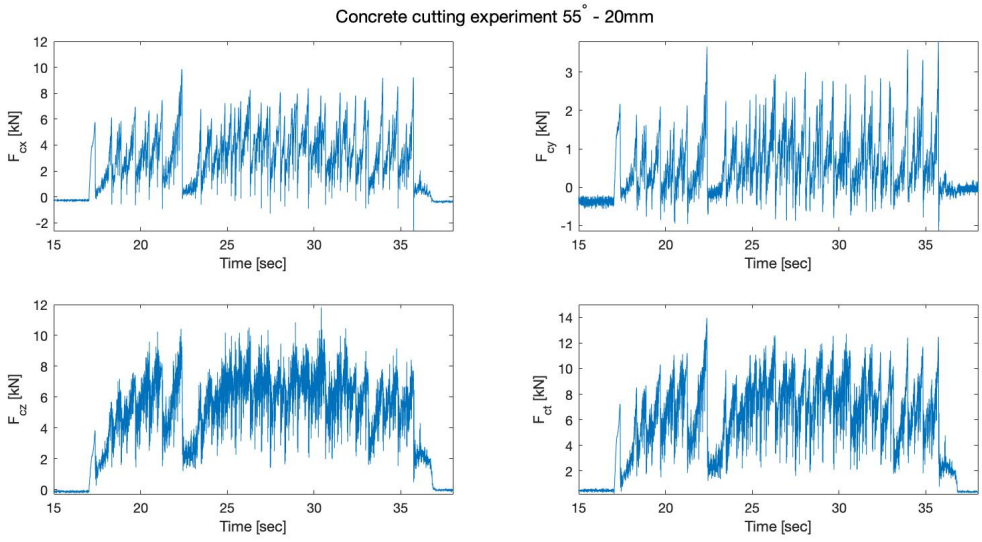

Figure C.13: Force-Time plots $7-11-B_{4.3}$

Experiment	α_c °	$F_{x,max}$ [kN]	$F_{x,mean}$ [kN]	$F_{y,max}$ [kN]	$F_{y,mean}$ [kN]	$F_{z,max}$ [kN]	$F_{z,mean}$ [kN]	$F_{t,max}$ [kN]	$F_{t,mean}$ [kN]
$7-11-B_{4.3}$	55	9.86	3.47	3.80	0.66	11.81	5.56	15.84	6.69

Table C.15: Force-Time plots $7-11-B_{4.3}$

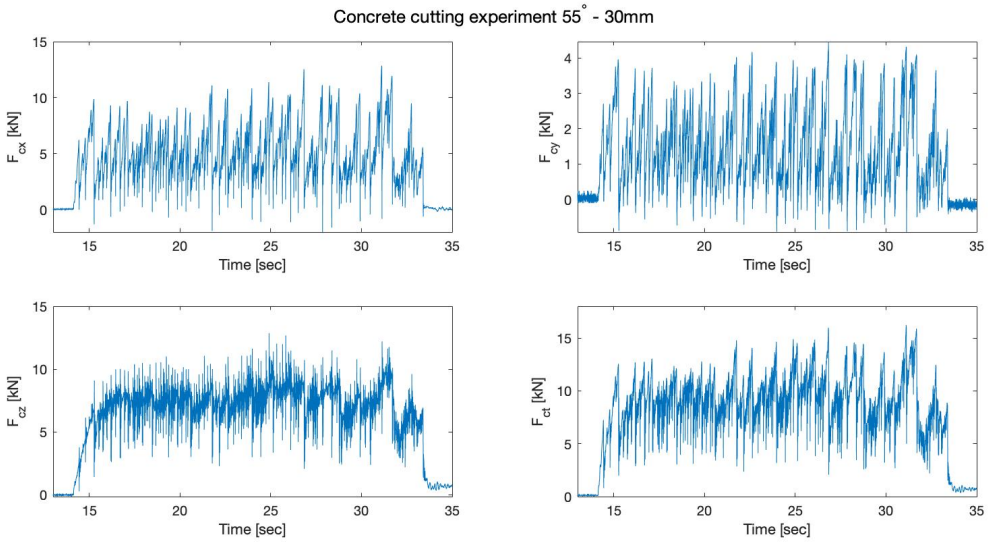

Figure C.14: Force-Time plots $7-11-B_{4.4}$

Experiment	α_c °	$F_{x,max}$ [kN]	$F_{x,mean}$ [kN]	$F_{y,max}$ [kN]	$F_{y,mean}$ [kN]	$F_{z,max}$ [kN]	$F_{z,mean}$ [kN]	$F_{t,max}$ [kN]	$F_{t,mean}$ [kN]
$7-11-B_{4.4}$	55	12.85	5.14	4.46	1.53	12.86	7.11	18.72	9.08

Table C.16: Force-Time plots $7-11-B_{4.4}$

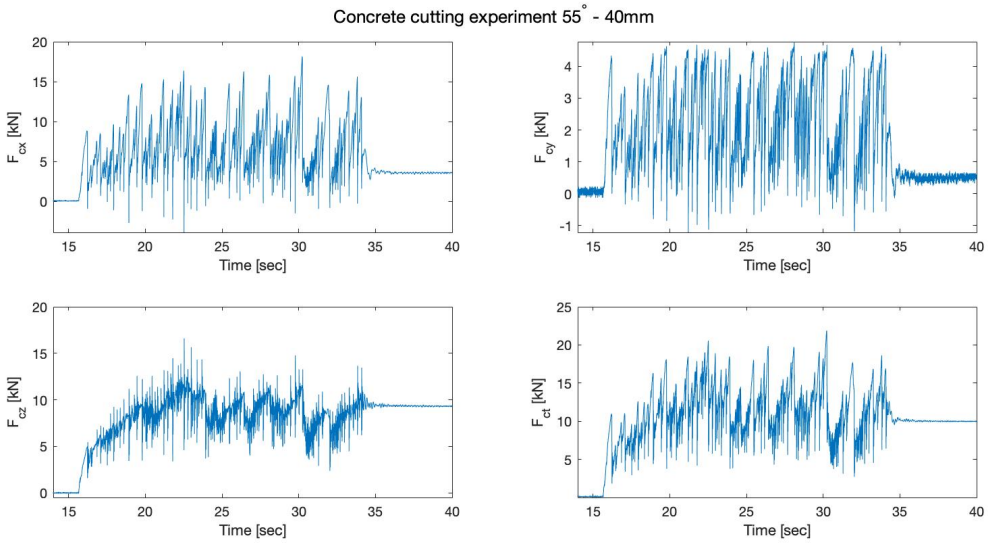

Figure C.15: Force-Time plots $7-11-B_{4.5}$

Experiment	α_c °	$F_{x,max}$ [kN]	$F_{x,mean}$ [kN]	$F_{y,max}$ [kN]	$F_{y,mean}$ [kN]	$F_{z,max}$ [kN]	$F_{z,mean}$ [kN]	$F_{t,max}$ [kN]	$F_{t,mean}$ [kN]
$7-11-B_{4.5}$	55	18.14	7.13	4.77	2.37	16.60	8.33	25.05	11.44

Table C.17: Force-Time plots $7-11-B_{4.5}$

$7-11-B6$ - 60°

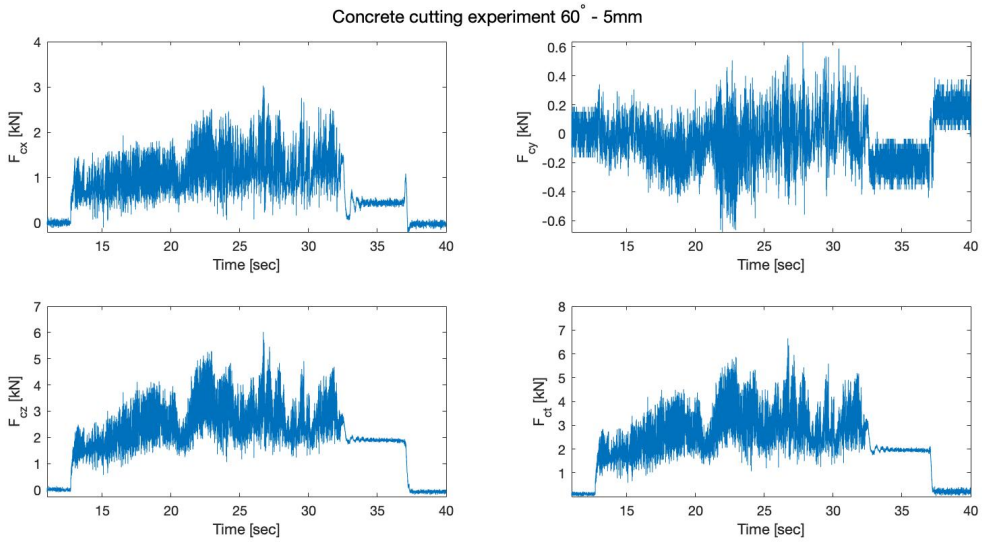

Figure C.16: Force-Time plots $7-11-B_{6.1}$

EExperiment	α_c °	$F_{x,max}$ [kN]	$F_{x,mean}$ [kN]	$F_{y,max}$ [kN]	$F_{y,mean}$ [kN]	$F_{z,max}$ [kN]	$F_{z,mean}$ [kN]	$F_{t,max}$ [kN]	$F_{t,mean}$ [kN]
$7-11-B_{6.1}$	60	3.03	1.17	0.64	-0.03	6.02	2.56	6.77	2.83

Table C.18: Force-Time plots $7-11-B_{6.1}$

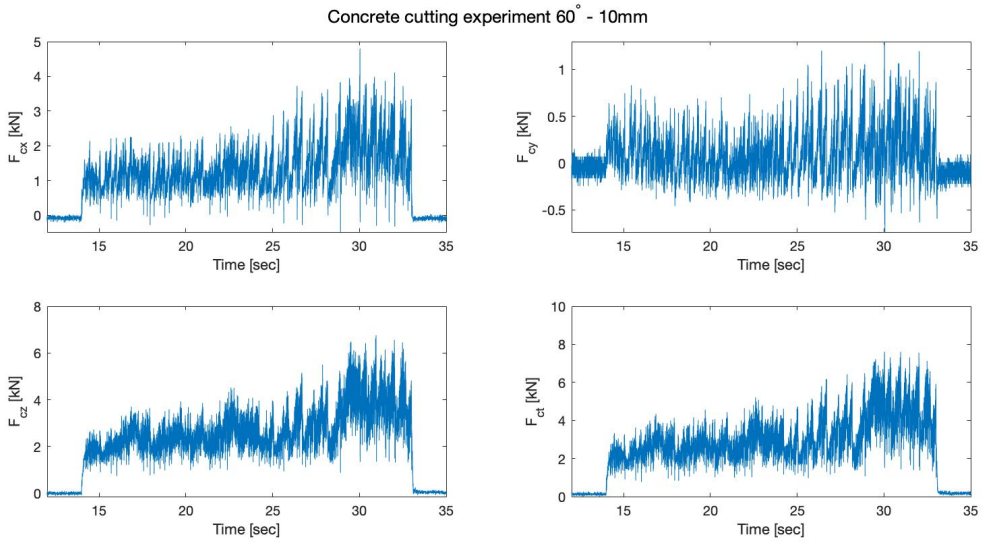

Figure C.17: Force-Time plots $7-11-B_{6.2}$

Experiment	α_c °	$F_{x,max}$ [kN]	$F_{x,mean}$ [kN]	$F_{y,max}$ [kN]	$F_{y,mean}$ [kN]	$F_{z,max}$ [kN]	$F_{z,mean}$ [kN]	$F_{t,max}$ [kN]	$F_{t,mean}$ [kN]
$7-11-B_{6.2}$	60	4.80	1.39	1.30	0.11	6.76	2.68	8.39	3.05

Table C.19: Force-Time plots $7-11-B_{6.2}$

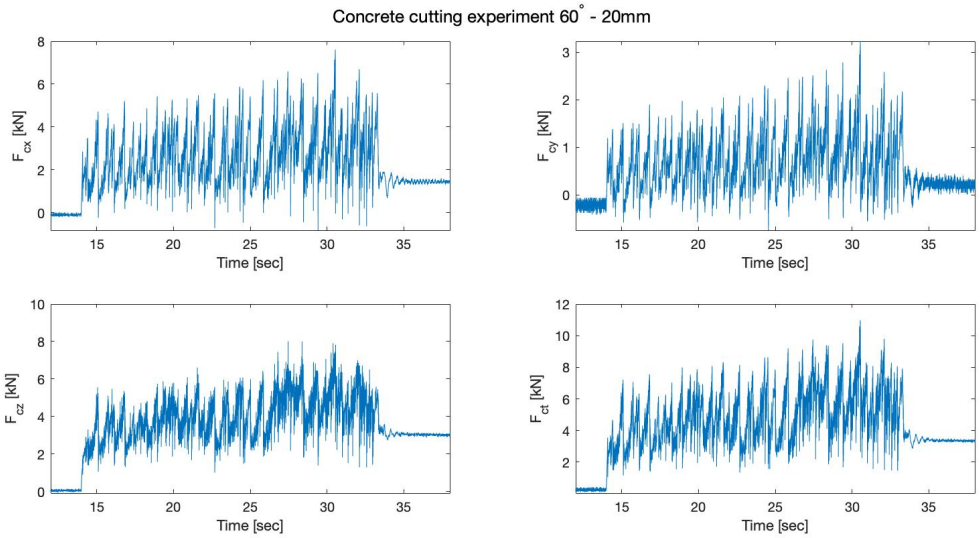

Figure C.18: Force-Time plots $7-11-B_{6.3}$

Experiment	α_c °	$F_{x,max}$ [kN]	$F_{x,mean}$ [kN]	$F_{y,max}$ [kN]	$F_{y,mean}$ [kN]	$F_{z,max}$ [kN]	$F_{z,mean}$ [kN]	$F_{t,max}$ [kN]	$F_{t,mean}$ [kN]
$7-11-B_{6.3}$	60	7.61	2.73	3.23	0.74	8.01	4.03	11.51	4.98

Table C.20: Force-Time plots $7-11-B_{6.3}$

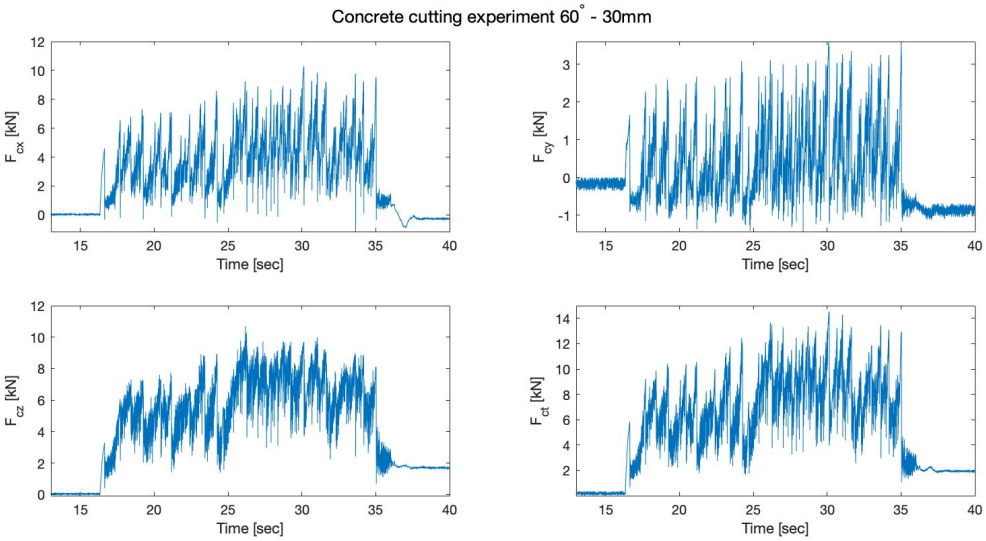

Figure C.19: Force-Time plots $7-11-B_{6.4}$

Experiment	α_c °	$F_{x,max}$ [kN]	$F_{x,mean}$ [kN]	$F_{y,max}$ [kN]	$F_{y,mean}$ [kN]	$F_{z,max}$ [kN]	$F_{z,mean}$ [kN]	$F_{t,max}$ [kN]	$F_{t,mean}$ [kN]
$7-11-B_{6.4}$	60	10.29	4.11	3.60	0.51	10.68	5.87	15.26	7.29

Table C.21: Force-Time plots $7-11-B_{6.4}$

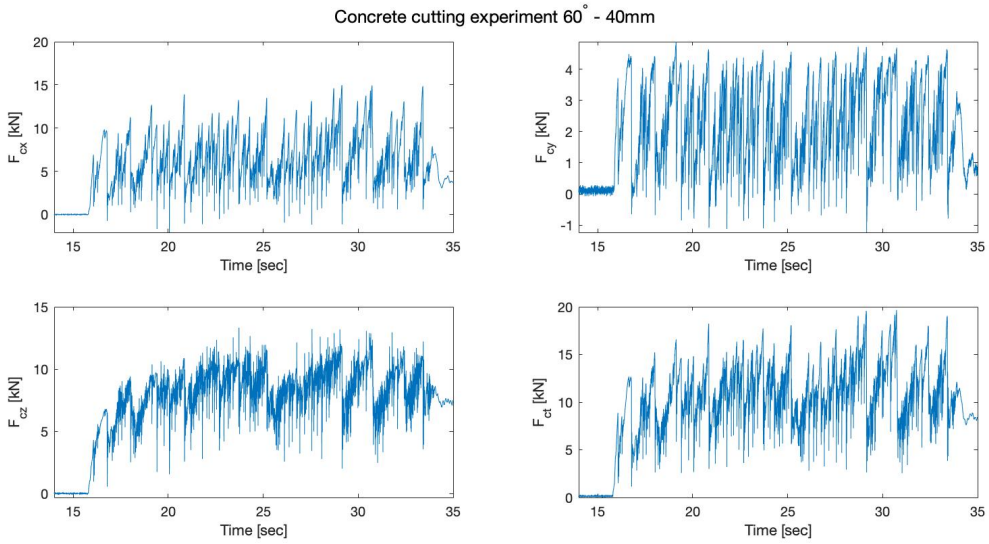

Figure C.20: Force-Time plots $7-11-B_{6.5}$

Experiment	α_c °	$F_{x,max}$ [kN]	$F_{x,mean}$ [kN]	$F_{y,max}$ [kN]	$F_{y,mean}$ [kN]	$F_{z,max}$ [kN]	$F_{z,mean}$ [kN]	$F_{t,max}$ [kN]	$F_{t,mean}$ [kN]
$7-11-B_{6.5}$	60	14.96	6.67	4.88	2.37	13.32	8.16	20.61	10.94

Table C.22: Force-Time plots $7-11-B_{6.5}$

Experiment	α_c °	$F_{x,max}$ [kN]	$F_{x,mean}$ [kN]	$F_{y,max}$ [kN]	$F_{y,mean}$ [kN]	$F_{z,max}$ [kN]	$F_{z,mean}$ [kN]	$F_{t,max}$ [kN]	$F_{t,mean}$ [kN]
$7-11-B_{3.1}$	40	2.74	1.32	1.31	0.35	2.61	1.73	4.00	2.22
$7-11-B_{3.2}$	40	3.58	1.56	1.28	0.40	3.96	1.72	5.49	2.39
$7-11-B_{3.3}$	40	7.97	3.41	2.69	1.24	6.20	2.61	10.45	4.51
$7-11-B_{3.4}$	40	12.68	6.48	2.03	-0.07	16.80	7.66	21.15	10.11
$7-11-B_{3.5}$	40	17.14	8.64	4.17	1.23	16.76	8.57	24.33	12.34
$7-11-B_{2.1}$	45	1.73	0.79	0.66	0.09	1.78	1.14	2.57	1.40
$7-11-B_{2.2}$	45	2.84	1.27	1.39	0.66	2.98	1.19	4.34	1.89
$7-11-B_{2.3}$	45	6.62	2.89	2.20	0.97	4.32	2.04	8.20	3.70
$7-11-B_{2.4}$	45	12.93	5.76	3.03	0.22	12.95	6.71	18.55	8.95
$7-11-B_{2.5}$	45	19.77	8.35	4.22	1.31	18.54	8.09	27.42	11.84
$7-11-B_{5.1}$	50	2.51	1.02	1.00	0.30	2.50	1.10	3.68	1.54
$7-11-B_{5.2}$	50	5.11	2.34	1.97	0.75	5.06	2.34	7.46	3.42
$7-11-B_{5.3}$	50	8.82	4.16	3.69	1.76	8.01	3.55	12.47	5.79
$7-11-B_{5.4}$	50	10.55	5.07	3.20	0.40	10.76	5.88	15.40	7.89
$7-11-B_{5.5}$	50	15.37	7.21	3.99	1.28	15.57	8.43	22.24	11.35
$7-11-B_{4.1}$	55	3.89	1.44	1.23	0.02	8.93	4.52	9.82	4.77
$7-11-B_{4.2}$	55	5.20	2.04	1.03	-0.13	7.71	3.56	9.35	4.13
$7-11-B_{4.3}$	55	9.86	3.47	3.80	0.66	11.81	5.56	15.84	6.69
$7-11-B_{4.4}$	55	12.85	5.14	4.46	1.53	12.86	7.11	18.72	9.08
$7-11-B_{4.5}$	55	18.14	7.13	4.77	2.37	16.60	8.33	25.05	11.44
$7-11-B_{6.1}$	60	3.03	1.17	0.64	-0.03	6.02	2.56	6.77	2.83
$7-11-B_{6.2}$	60	4.80	1.39	1.30	0.11	6.76	2.68	8.39	3.05
$7-11-B_{6.3}$	60	7.61	2.73	3.23	0.74	8.01	4.03	11.51	4.98
$7-11-B_{6.4}$	60	10.29	4.11	3.60	0.51	10.68	5.87	15.26	7.29
$7-11-B_{6.5}$	60	14.96	6.67	4.88	2.37	13.32	8.16	20.61	10.94

Table C.23: Collected force data concrete

C.4. FORCE DATA - SANDSTONE

Sample S1 - 45°

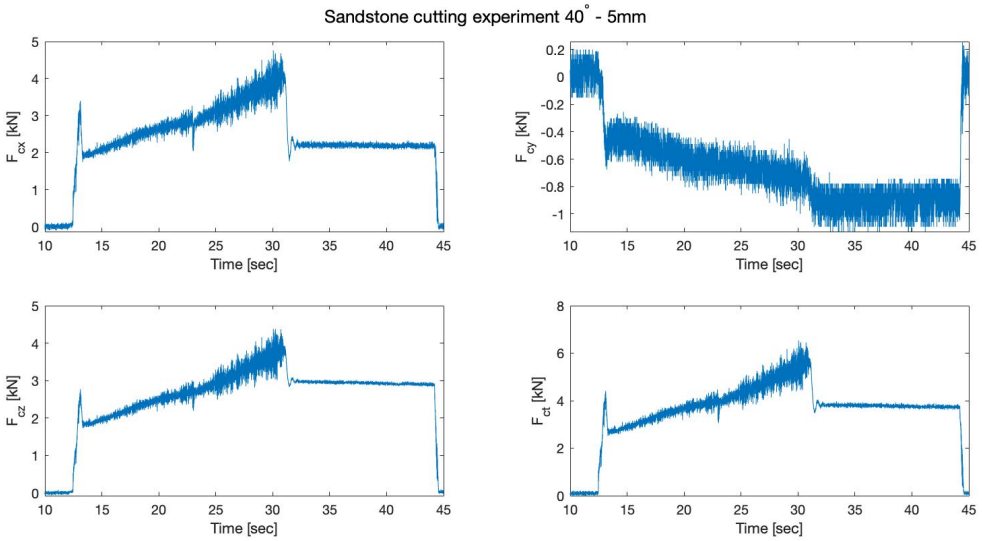

Figure C.21: Force-Time plots $S_{1.1}$

Experiment	α_c °	$F_{x,max}$ [kN]	$F_{x,mean}$ [kN]	$F_{y,max}$ [kN]	$F_{y,mean}$ [kN]	$F_{z,max}$ [kN]	$F_{z,mean}$ [kN]	$F_{t,max}$ [kN]	$F_{t,mean}$ [kN]
$S_{1.1}$	45	4.76	2.85	0.26	-0.59	4.38	2.67	6.48	3.95

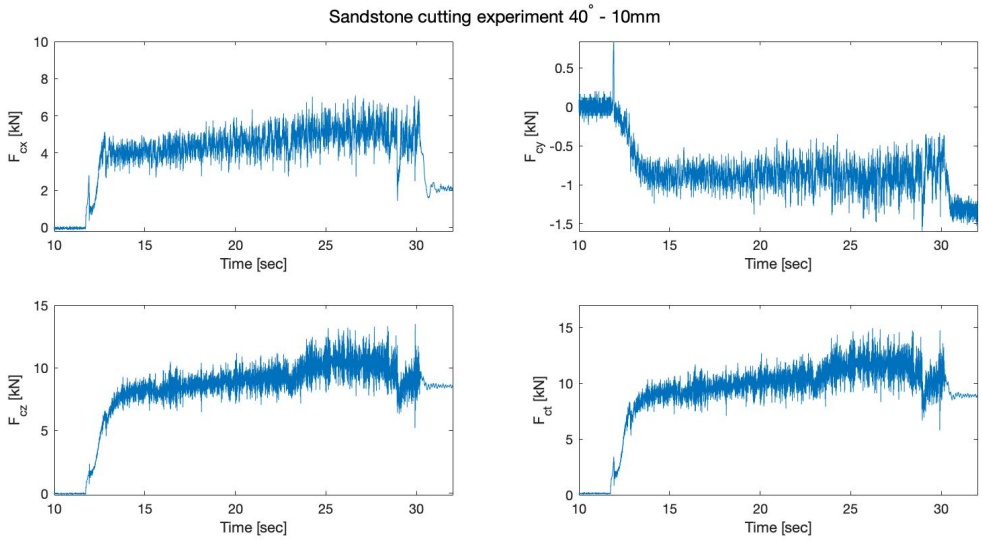

Figure C.22: Force-Time plots $S_{1.2}$

Experiment	α_c °	$F_{x,max}$ [kN]	$F_{x,mean}$ [kN]	$F_{y,max}$ [kN]	$F_{y,mean}$ [kN]	$F_{z,max}$ [kN]	$F_{z,mean}$ [kN]	$F_{t,max}$ [kN]	$F_{t,mean}$ [kN]
$S_{1.2}$	45	7.10	4.48	0.84	-0.82	13.50	8.72	15.27	9.85

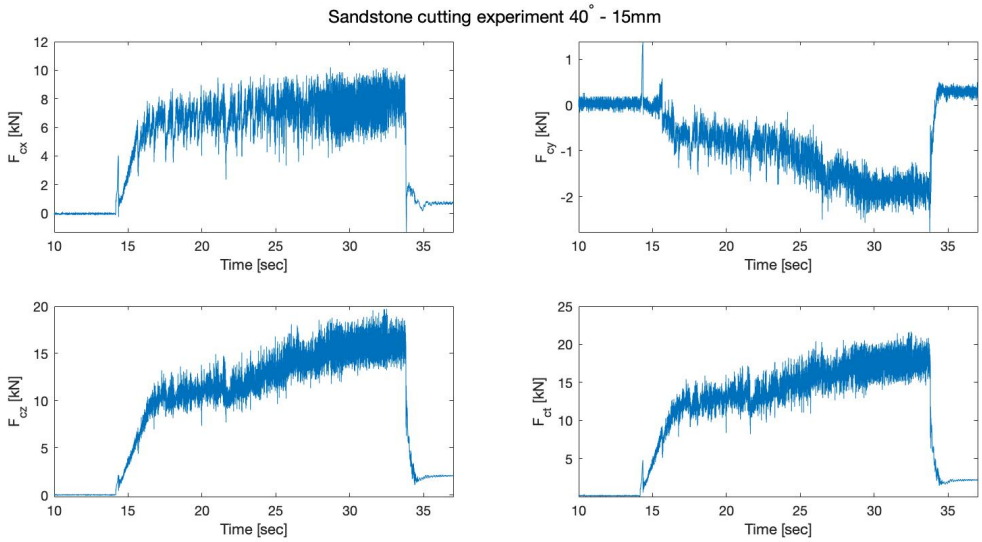

Figure C.23: Force-Time plots $S_{1.3}$

Experiment	α_c °	$F_{x,max}$ [kN]	$F_{x,mean}$ [kN]	$F_{y,max}$ [kN]	$F_{y,mean}$ [kN]	$F_{z,max}$ [kN]	$F_{z,mean}$ [kN]	$F_{t,max}$ [kN]	$F_{t,mean}$ [kN]
$S_{1.3}$	45	10.20	6.68	1.39	-1.08	19.71	12.00	22.24	13.83

Sample S2 - 50°

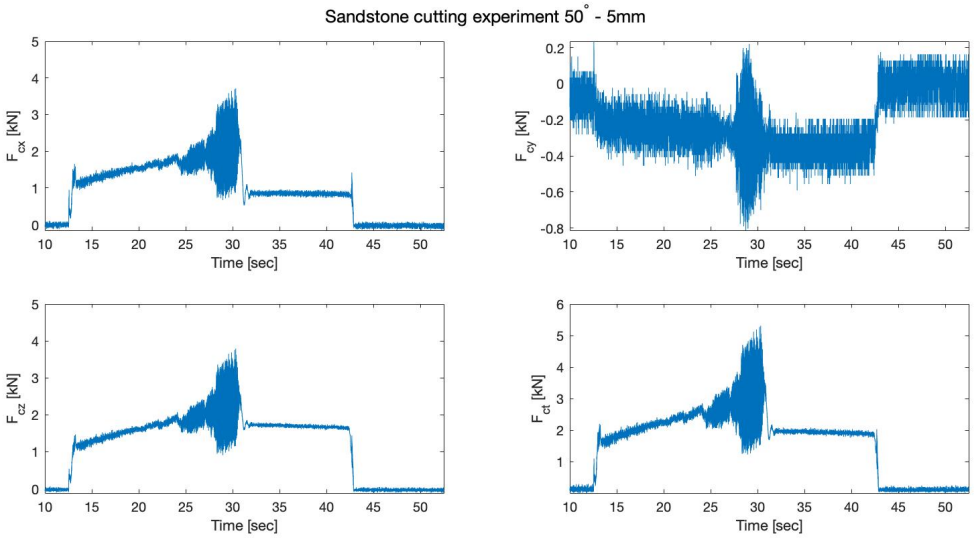

Figure C.24: Force-Time plots $S_{2.1}$

Experiment	α_c °	$F_{x,max}$ [kN]	$F_{x,mean}$ [kN]	$F_{y,max}$ [kN]	$F_{y,mean}$ [kN]	$F_{z,max}$ [kN]	$F_{z,mean}$ [kN]	$F_{t,max}$ [kN]	$F_{t,mean}$ [kN]
$S_{2.1}$	50	3.71	1.61	0.24	-0.26	3.79	1.70	5.31	2.36

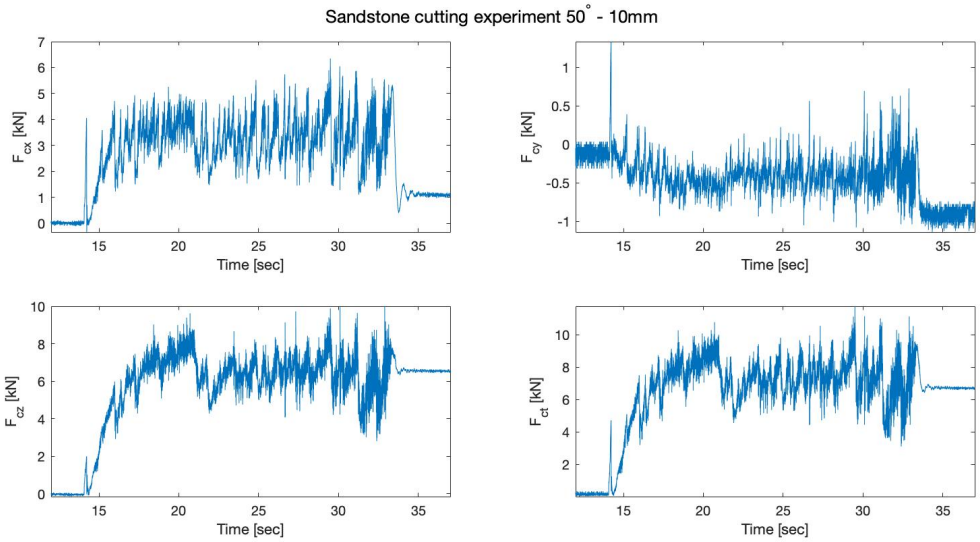

Figure C.25: Force-Time plots $S_{2.2}$

Experiment	α_c °	$F_{x,max}$ [kN]	$F_{x,mean}$ [kN]	$F_{y,max}$ [kN]	$F_{y,mean}$ [kN]	$F_{z,max}$ [kN]	$F_{z,mean}$ [kN]	$F_{t,max}$ [kN]	$F_{t,mean}$ [kN]
$S_{2.2}$	50	6.35	3.21	1.33	-0.39	10.01	6.08	11.92	6.91

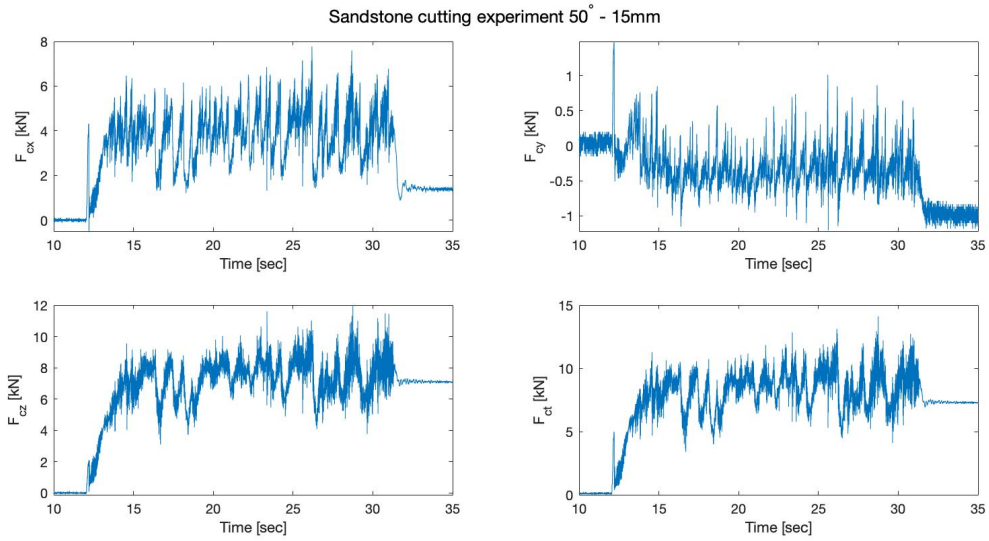

Figure C.26: Force-Time plots $S_{2.3}$

Experiment	α_c °	$F_{x,max}$ [kN]	$F_{x,mean}$ [kN]	$F_{y,max}$ [kN]	$F_{y,mean}$ [kN]	$F_{z,max}$ [kN]	$F_{z,mean}$ [kN]	$F_{t,max}$ [kN]	$F_{t,mean}$ [kN]
$S_{2.3}$	50	7.77	3.78	1.49	-0.29	12.45	7.01	14.75	8.01

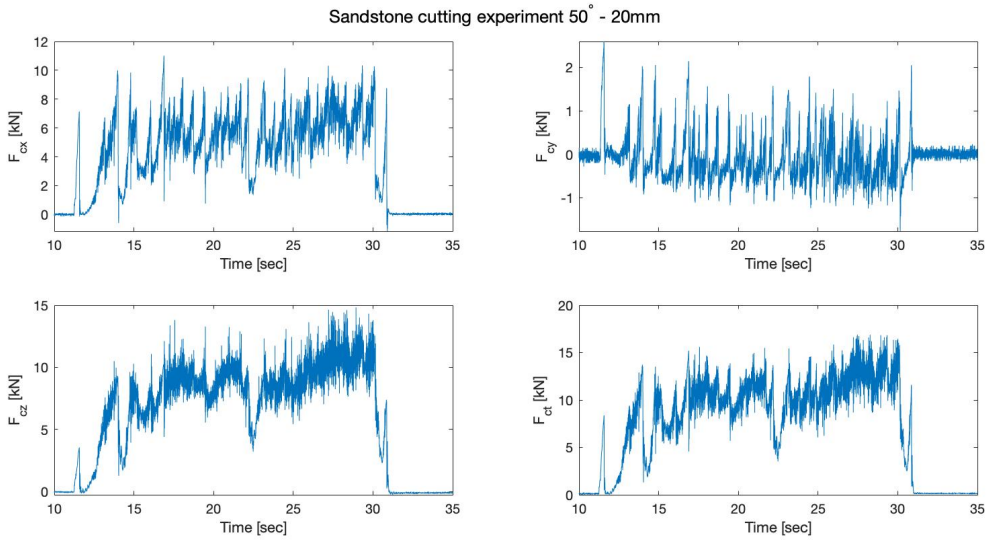

Figure C.27: Force-Time plots $S_{2.4}$

Experiment	α_c °	$F_{x,max}$ [kN]	$F_{x,mean}$ [kN]	$F_{y,max}$ [kN]	$F_{y,mean}$ [kN]	$F_{z,max}$ [kN]	$F_{z,mean}$ [kN]	$F_{t,max}$ [kN]	$F_{t,mean}$ [kN]
$S_{2.4}$	50	11.01	5.12	2.60	-0.09	14.82	7.78	18.64	9.39

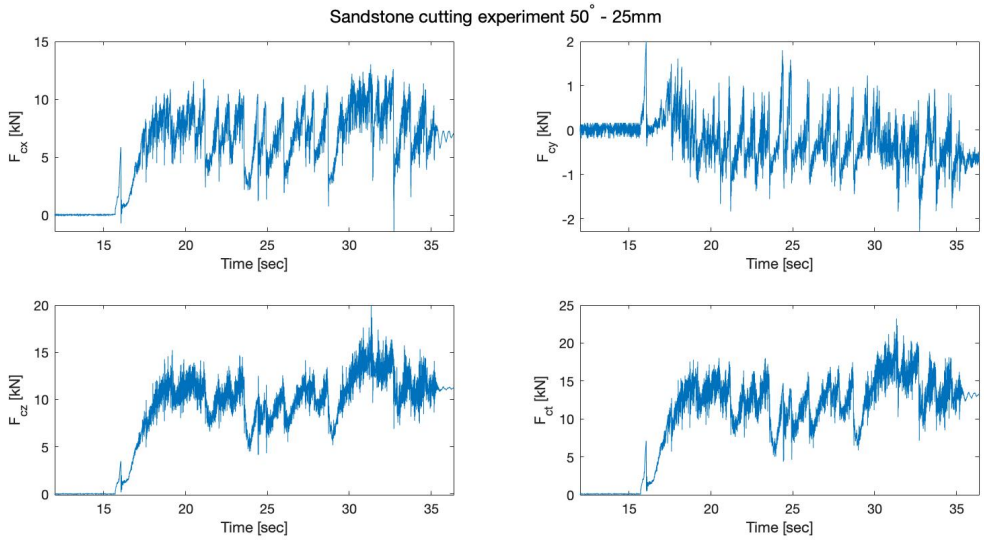

Figure C.28: Force-Time plots $S_{2.5}$

Experiment	α_c °	$F_{x,max}$ [kN]	$F_{x,mean}$ [kN]	$F_{y,max}$ [kN]	$F_{y,mean}$ [kN]	$F_{z,max}$ [kN]	$F_{z,mean}$ [kN]	$F_{t,max}$ [kN]	$F_{t,mean}$ [kN]
$S_{2.5}$	50	13.03	6.89	2.00	-0.26	20.16	9.88	24.09	12.10

Sample S3 - 55°

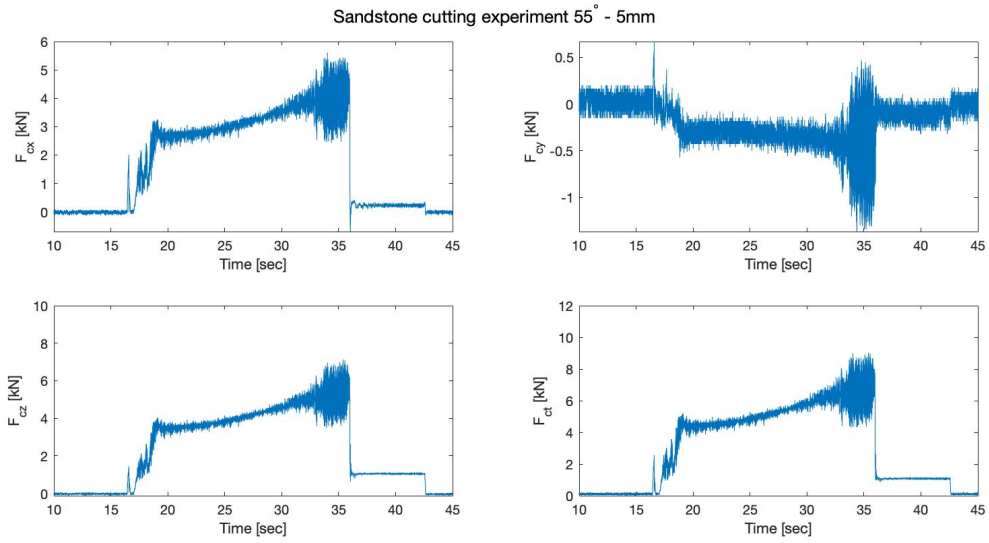

Figure C.29: Force-Time plots $S_{3.1}$

Experiment	α_c °	$F_{x,max}$ [kN]	$F_{x,mean}$ [kN]	$F_{y,max}$ [kN]	$F_{y,mean}$ [kN]	$F_{z,max}$ [kN]	$F_{z,mean}$ [kN]	$F_{t,max}$ [kN]	$F_{t,mean}$ [kN]
$S_{3.1}$	55	5.60	3.03	0.67	-0.31	7.13	3.90	9.09	4.96

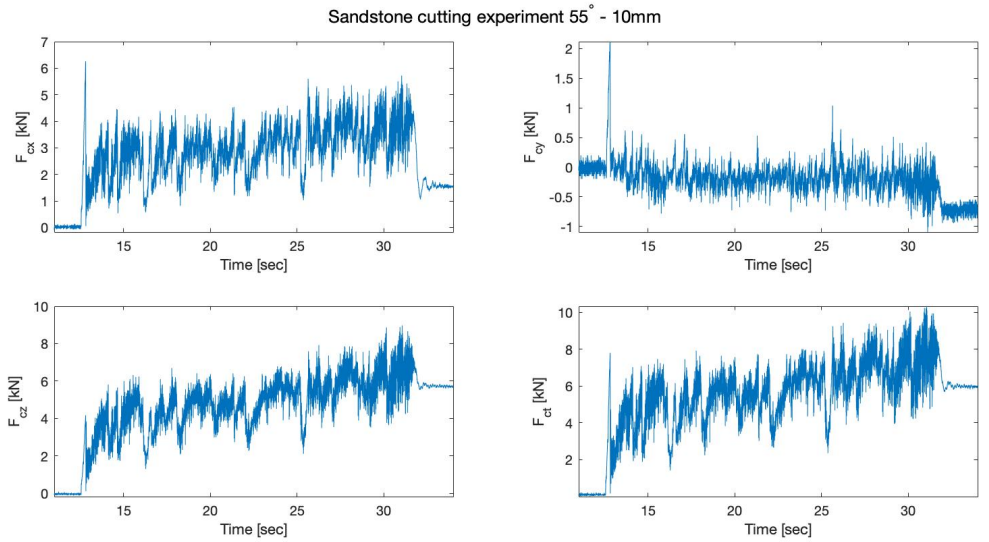

Figure C.30: Force-Time plots $S_{3.2}$

Experiment	α_c °	$F_{x,max}$ [kN]	$F_{x,mean}$ [kN]	$F_{y,max}$ [kN]	$F_{y,mean}$ [kN]	$F_{z,max}$ [kN]	$F_{z,mean}$ [kN]	$F_{t,max}$ [kN]	$F_{t,mean}$ [kN]
$S_{3.2}$	55	6.26	3.03	2.12	-0.16	8.97	4.86	11.14	5.75

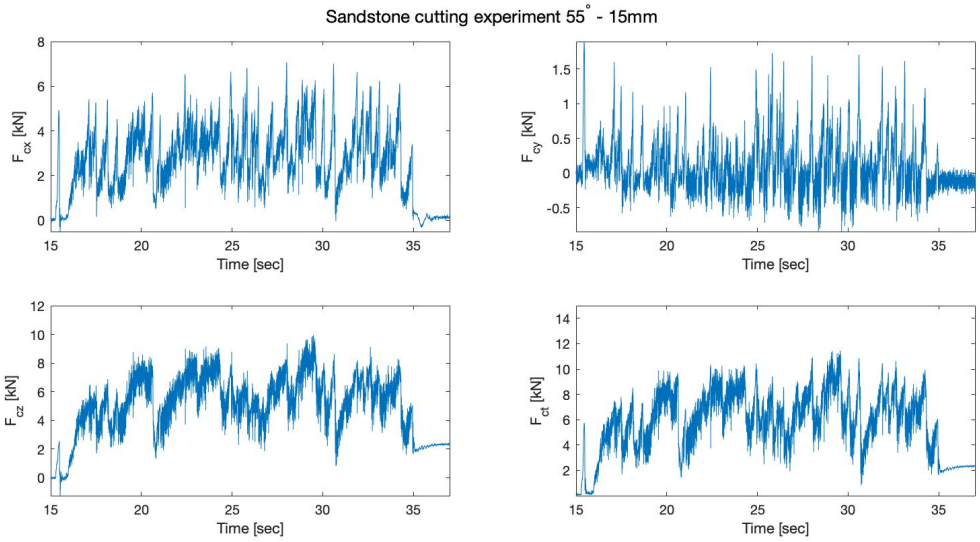

Figure C.31: Force-Time plots $S_{3.3}$

Experiment	α_c °	$F_{x,max}$ [kN]	$F_{x,mean}$ [kN]	$F_{y,max}$ [kN]	$F_{y,mean}$ [kN]	$F_{z,max}$ [kN]	$F_{z,mean}$ [kN]	$F_{t,max}$ [kN]	$F_{t,mean}$ [kN]
$S_{3.3}$	55	7.07	2.95	1.90	0.10	9.95	5.38	12.35	6.19

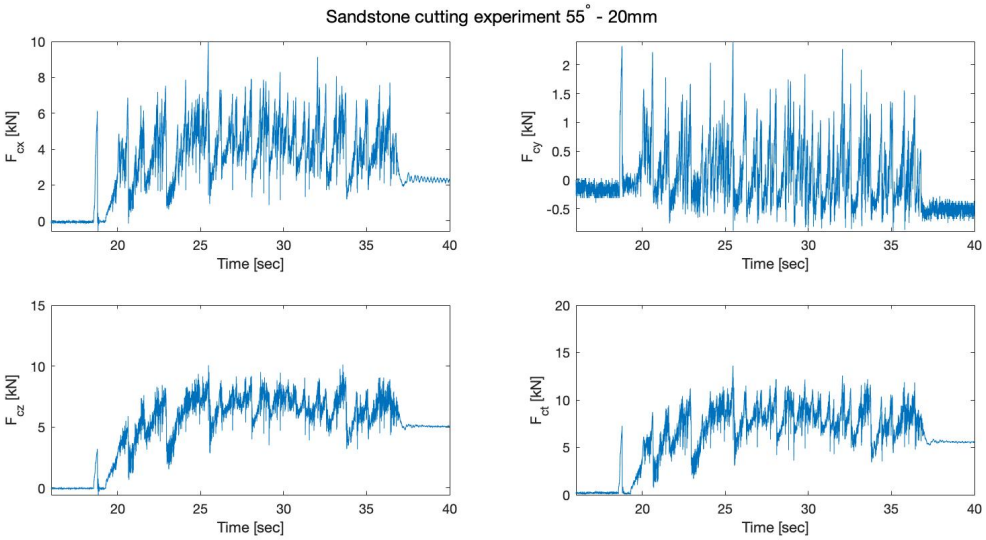

Figure C.32: Force-Time plots $S_{3.4}$

Experiment	α_c °	$F_{x,max}$ [kN]	$F_{x,mean}$ [kN]	$F_{y,max}$ [kN]	$F_{y,mean}$ [kN]	$F_{z,max}$ [kN]	$F_{z,mean}$ [kN]	$F_{t,max}$ [kN]	$F_{t,mean}$ [kN]
$S_{3.4}$	55	9.98	3.98	2.41	0.15	10.12	5.87	14.41	7.16

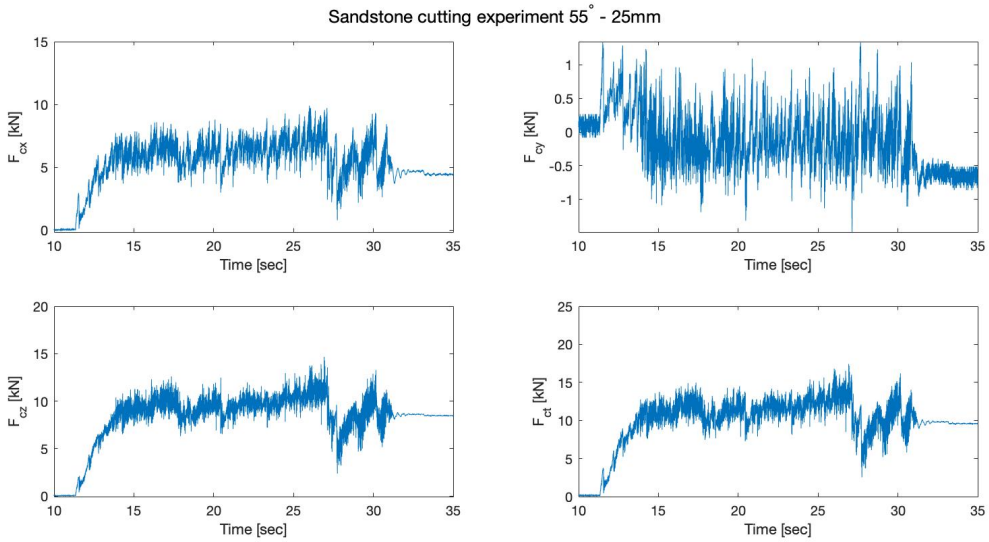

Figure C.33: Force-Time plots $S_{3.5}$

Experiment	α_c °	$F_{x,max}$ [kN]	$F_{x,mean}$ [kN]	$F_{y,max}$ [kN]	$F_{y,mean}$ [kN]	$F_{z,max}$ [kN]	$F_{z,mean}$ [kN]	$F_{t,max}$ [kN]	$F_{t,mean}$ [kN]
$S_{3.5}$	55	9.90	5.84	1.35	-0.06	14.67	8.77	17.75	10.56

Experiment	α_c °	$F_{x,max}$ [kN]	$F_{x,mean}$ [kN]	$F_{y,max}$ [kN]	$F_{y,mean}$ [kN]	$F_{z,max}$ [kN]	$F_{z,mean}$ [kN]	$F_{t,max}$ [kN]	$F_{t,mean}$ [kN]
$S_{1.1}$	45	4.76	2.85	0.26	-0.59	4.38	2.67	6.48	3.95
$S_{1.2}$	45	7.10	4.48	0.84	-0.82	13.50	8.72	15.27	9.85
$S_{1.3}$	45	10.20	6.68	1.39	-1.08	19.71	12.00	22.24	13.83
$S_{2.1}$	50	3.71	1.61	0.24	-0.26	3.79	1.70	5.31	2.36
$S_{2.2}$	50	6.35	3.21	1.33	-0.39	10.01	6.08	11.92	6.91
$S_{2.3}$	50	7.77	3.78	1.49	-0.29	12.45	7.01	14.75	8.01
$S_{2.4}$	50	11.01	5.12	2.60	-0.09	14.82	7.78	18.64	9.39
$S_{2.5}$	50	13.03	6.89	2.00	-0.26	20.16	9.88	24.09	12.10
$S_{3.1}$	55	5.60	3.03	0.67	-0.31	7.13	3.90	9.09	4.96
$S_{3.2}$	55	6.26	3.03	2.12	-0.16	8.97	4.86	11.14	5.75
$S_{3.3}$	55	7.07	2.95	1.90	0.10	9.95	5.38	12.35	6.19
$S_{3.4}$	55	9.98	3.98	2.41	0.15	10.12	5.87	14.41	7.16
$S_{3.5}$	55	9.90	5.84	1.35	-0.06	14.67	8.77	17.75	10.56
$S_{4.1}$	60	4.77	3.12	0.78	-0.47	8.31	5.43	9.61	6.29
$S_{4.2}$	60	6.58	3.91	0.62	-0.40	8.44	5.19	10.72	6.51
$S_{4.3}$	60	6.74	3.22	1.89	0.36	12.05	7.10	13.94	7.85
$S_{4.4}$	60	8.16	4.52	1.98	0.33	13.51	7.62	15.91	8.90
$S_{4.5}$	60	11.79	5.66	3.08	0.69	18.52	10.26	22.17	11.82

Table C.24: Collected force data sandstone experiments

C.5. PRODUCTION DATA - ARTIFICIAL ROCK

#	Sample	α_c	h_c	Production	Chip size distribution/g					
		[°]	[mm]	[g]	<1mm	1-2mm	2-5mm	5-10mm	10-20mm	>20mm
2	7-11-$B_{2.1}$	45	5	149.99	10.86	3.45	11.11	16.40	48.88	53.57
	7-11-$B_{2.2}$	45	10	613.40	51.52	18.49	22.46	26.32	55.55	428.74
	7-11-$B_{2.3}$	45	20	1654.90	114.36	38.62	47.35	60.59	151.45	1218.29
	7-11-$B_{2.4}$	45	30	2682.00	213.04	81.41	69.55	76.72	163.50	2063.00
	7-11-$B_{2.5}$	45	40	4221.00	294.35	124.80	76.61	88.38	200.85	3405.00
3	7-11-$B_{5.1}$	50	5	85.33	18.83	6.10	12.80	7.85	3.18	25.27
	7-11-$B_{5.2}$	50	10	320.06	41.19	13.17	24.49	27.84	99.87	101.72
	7-11-$B_{5.3}$	50	20	896.65	89.33	29.75	49.65	55.49	93.00	597.10
	7-11-$B_{5.4}$	50	30	2161.00	192.51	57.67	59.49	68.79	138.97	1632.00
	7-11-$B_{5.5}$	50	40	3435.00	286.14	82.66	78.64	79.59	192.89	2688.00
4	7-11-$B_{4.1}$	55	5	185.25	32.57	9.24	17.18	22.40	37.85	60.82
	7-11-$B_{4.2}$	55	10	207.72	37.85	12.54	23.96	23.32	78.73	19.64
	7-11-$B_{4.3}$	55	20	1343.34	126.65	44.41	55.55	62.94	92.45	948.24
	7-11-$B_{4.4}$	55	30	2810.00	229.46	75.24	67.43	82.31	156.70	2184.00
	7-11-$B_{4.5}$	55	40	5200.00	320.99	110.11	91.81	115.96	244.12	4288.00
5	7-11-$B_{6.1}$	60	5	104.59	30.10	9.21	13.77	19.64	27.43	0.00
	7-11-$B_{6.2}$	60	10	287.26	58.96	21.18	24.31	27.17	77.42	65.83
	7-11-$B_{6.3}$	60	20	1027.46	150.13	51.61	50.69	58.91	93.21	609.42
	7-11-$B_{6.4}$	60	30	1283.91	95.58	31.22	47.08	53.32	92.55	950.76
	7-11-$B_{6.5}$	60	40	3167.00	191.36	56.78	74.42	94.54	208.49	2527.00

Table C.25: Collection of production data concrete experiments

C.6. CRUSHED VOLUME DEVELOPMENT OVER MEAN CUTTING DEPTH - ARTIFICIAL ROCK

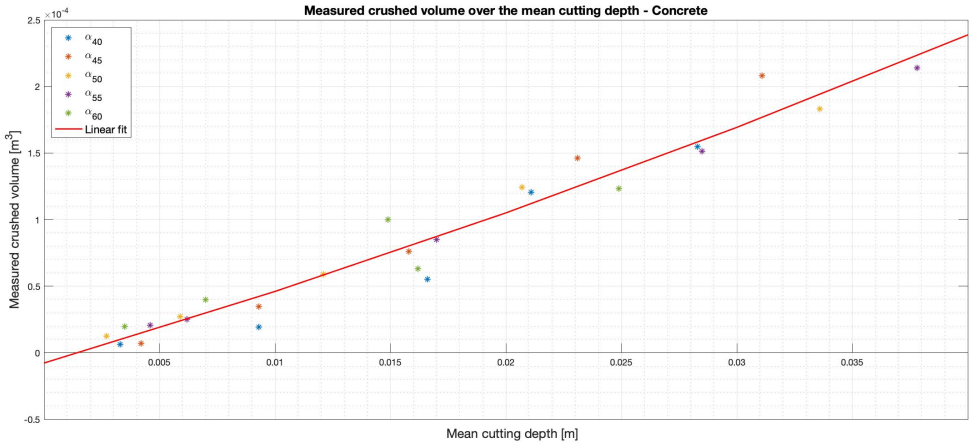

Figure C.34: Crushed volume development over mean cutting depth - Artificial rock

C.7. PRODUCTION DATA - SANDSTONE

#	Sample	α_c [°]	h_c [mm]	Production [g]	Chip size distribution/g <1mm	1-2mm	2-5mm	5-10mm	10-20mm	>20mm
9	$S_{2.1}$	45	5	13.10	2.98	2.12	3.25	2.89	1.86	3.04
	$S_{2.2}$	45	10	191.43	18.33	5.17	17.40	24.31	55.21	71.01
	$S_{2.3}$	45	15	343.54	26.89	7.66	21.41	26.77	51.32	209.49
10	$S_{2.1}$	50	5	15.30	3.55	0.93	2.44	1.20	4.14	3.04
	$S_{2.2}$	50	10	286.54	25.35	4.41	11.52	19.72	61.78	159.96
	$S_{2.3}$	50	15	505.30	33.61	6.33	17.60	18.28	59.97	369.51
	$S_{2.4}$	50	20	1235.63	36.85	8.47	22.02	27.26	37.00	1096.05
	$S_{2.5}$	50	25	1107.70	41.05	8.25	25.16	27.75	37.14	959.56
11	$S_{3.1}$	55	5	17.11	5.44	0.27	1.07	0.00	3.06	2.91
	$S_{3.2}$	55	10	206.69	24.88	5.01	12.70	20.75	68.35	67.61
	$S_{3.3}$	55	15	718.22	40.77	8.92	26.14	26.55	71.14	537.38
	$S_{3.4}$	55	20	872.98	43.29	9.30	30.80	32.71	53.83	696.18
	$S_{3.5}$	55	25	621.25	45.18	9.84	27.44	33.85	63.96	425.12

Table C.26: Collection of production data sandstone experiments

C.8. CRUSHED VOLUME DEVELOPMENT OVER MEAN CUTTING DEPTH - ARTIFICIAL ROCK

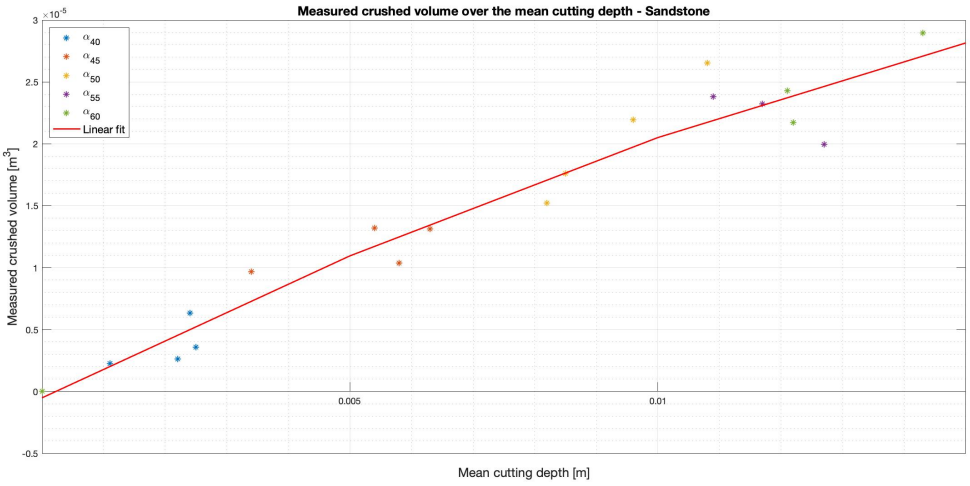

Figure C.35: Crushed volume development over mean cutting depth - Sandstone

C.9. INDIVIDUAL CHIP MEASUREMENTS - ARTIFICIAL ROCK

For the individual chip measurements several dimensions had to be measured. Figure C.36 shows a side view of a typical sandstone chip. It is of interest to approximately determine the shear factor K_s, which is defined as the failure fraction that is subjected to shearing along the complete failure plane. Visual observations have clearly shown that a tensile cracking path is present at the end of the shear failure plane. The point where tensile failure occurs is measured at height h_s. The corresponding horizontal length to this transition point is called l_s. By knowing h_s and l_s, the angle of the shear plane β_s can be determined. This parameter allows us to calculate the imaginary length of the failure plane, since the thickness of the chip h_d is known. Collecting all these measurements, makes it able to determine the shear factor K_s. A collection of chips has been chosen, where three chips were picked from arbitrary production results. Table C.27 and C.28 display the results of the artificial rock and sandstone individual chip measurements, respectively.

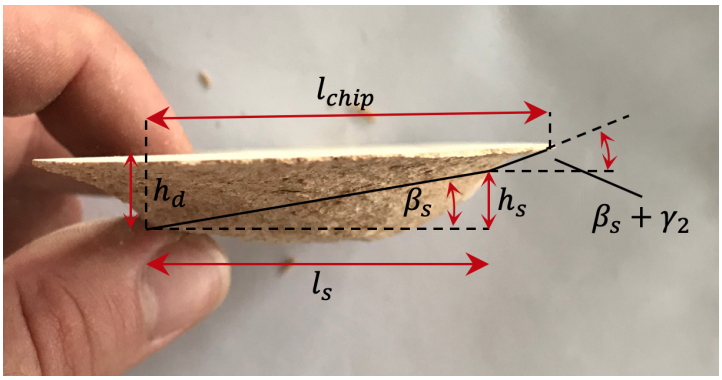

Figure C.36: Side view sandstone chip and parameters for chip measurements

		Concrete 7-11-B2 (45-3.0cm)			**Concrete 7-11-B2 (45-4.0cm)**			**Concrete 7-11-B5 (50-2.0cm)**			**Concrete 7-11-B5 (50-3.0cm)**			**Concrete 7-11-B6 (60-2.0cm)**			**Concrete 7-11-B2 (60-3.0cm)**		
Parameter	Unit	*Chip 1*	*Chip 2*	*Chip 3*	*Chip 1*	*Chip 2*	*Chip 3*	*Chip 1*	*Chip 2*	*Chip 3*	*Chip 1*	*Chip 2*	*Chip 3*	*Chip 1*	*Chip 2*	*Chip 3*	*Chip 1*	*Chip 2*	*Chip 3*
h_{mean}	[m]	0.0231	0.0231	0.0231	0.0311	0.0311	0.0311	0.0121	0.0121	0.0121	0.0207	0.0207	0.0207	0.0149	0.0149	0.0149	0.0162	0.0162	0.0162
l_{chip}	[mm]	61.41	66.81	59.22	71.32	62.19	66.77	56.34	28.09	32.17	57.00	58.27	61.87	42.63	37.91	46.01	37.39	44.21	35.70
h_d	[mm]	14.39	14.1	13.47	16.34	17.88	17.15	11.14	9.97	8.91	17.29	14.08	14.38	9.45	10.98	10.51	9.45	10.97	12.94
h_s	[mm]	9.32	8.43	7.77	5.65	6.89	5.91	9.00	7.88	7.36	12.00	9.78	9.43	8.55	10.22	9.99	8.32	9.15	11.23
h_t	[mm]	5.07	5.67	5.70	10.69	10.99	11.24	2.14	2.09	1.55	5.29	4.30	4.95	0.90	0.76	0.52	1.13	1.82	1.71
l_s	[mm]	20.33	26.10	22.67	20.00	30.00	25.00	48.55	31.40	21.12	22.12	23.12	24.12	25.12	26.12	27.12	28.12	29.12	30.12
$l_{tensile}$	[mm]	41.08	40.71	36.55	51.32	32.19	41.77	7.79	21.40	11.05	34.88	35.15	37.75	17.51	11.79	18.89	9.27	15.09	5.58
β_s	deg	24.63	17.90	18.92	15.77	12.93	13.30	10.50	14.09	19.21	28.48	22.93	21.35	18.80	21.37	20.22	16.48	17.44	20.45
l_{tot}	[mm]	34.53	45.88	41.54	60.10	79.88	74.55	61.12	40.96	27.08	36.26	36.14	39.49	29.33	30.13	30.41	33.31	36.60	37.04
K_s	-	**0.59**	**0.57**	**0.55**	**0.33**	**0.38**	**0.34**	**0.79**	**0.74**	**0.78**	**0.61**	**0.64**	**0.61**	**0.86**	**0.87**	**0.89**	**0.84**	**0.80**	**0.81**

Table C.27: Measured dimensions arbitrary chips and determination shear factor K_s - Artificial rock

C.10. INDIVIDUAL CHIP MEASUREMENTS - SANDSTONE

		Sandstone S_2 (50-1.5cm)			**Sandstone S_2 (50-2.0cm)**			**Sandstone S_2 (50-2.5cm)**			**Sandstone S_4 (60-2.0cm)**			**Sandstone S_4 (60-2.5cm)**		
Parameter	Unit	*Chip 1*	*Chip 2*	*Chip 3*	*Chip 1*	*Chip 2*	*Chip 3*	*Chip 1*	*Chip 2*	*Chip 3*	*Chip 1*	*Chip 2*	*Chip 3*	*Chip 1*	*Chip 2*	*Chip 3*
h_{mean}	[m]	0.00846	0.00846	0.00846	0.01268	0.01268	0.01268	0.01218	0.01218	0.01218	0.01092	0.01092	0.01092	0.01425	0.01425	0.01425
l_{chip}	[mm]	30.00	32.00	22.75	59.31	66.00	60.46	56.31	58.28	49.41	56.00	48.03	46.00	48.00	73.94	60.91
h_d	[mm]	6.15	7.16	7.45	10.77	10.32	9.86	10.14	10.52	10.73	8.60	9.85	7.00	11.98	12.07	12.05
h_s	[mm]	5.80	6.33	6.91	9.20	9.55	8.83	9.45	10.03	9.89	8.21	8.55	6.41	11.23	11.67	11.75
h_t	[mm]	0.35	0.83	0.54	1.57	0.77	1.03	0.69	0.49	0.84	0.39	1.30	0.59	0.75	0.40	0.30
l_s	[mm]	28.55	31.40	21.12	52.51	58.48	54.11	48.30	49.15	42.65	49.09	41.94	39.12	40.77	62.21	52.21
$l_{tensile}$	[mm]	1.45	0.60	1.63	6.80	7.52	6.35	8.01	9.13	6.76	6.91	6.09	6.88	7.23	11.73	8.70
β_s	deg	11.48	11.40	18.12	9.94	9.27	9.27	11.07	11.53	13.06	9.49	11.52	9.31	15.40	10.62	12.68
l_tot	[mm]	30.89	36.23	23.96	62.41	64.03	61.22	52.81	52.61	47.50	52.14	49.31	43.29	45.11	65.46	54.88
K_s	-	**0.92**	**0.87**	**0.88**	**0.84**	**0.91**	**0.88**	**0.91**	**0.93**	**0.90**	**0.94**	**0.85**	**0.90**	**0.90**	**0.95**	**0.95**

Table C.28: Measured dimensions arbitrary chips and determination shear factor K_s - Sandstone

D

NUMERICAL DERIVATIONS

D.1. DERIVATION SHEAR COMPONENT

Before deriving the force balance for the shear component, the an expression for the shear area S_s needs to be found. By keeping figure 6.12 and 6.11a as reference, the total area that is subjected to shear failure can be calculated. Since it is assumed that major shear failure takes place at the boundary of the crushed zone, the crushed zone height h_s and shear angle β_s need to be used to find the length of the shear plane. As known, the failure plane is subjected to a certain fraction of shear failure, which is multiplied by shear factor K_s. The length of the shear plane can be expressed as

$$l_{shear} = K_s \cdot l_{failure} = K_s \cdot \frac{(h_c - h_s)}{sin(\beta_s)} \tag{D.1}$$

Due to the assumed chip shape, as in figure 6.11a, the length of the shear plane l_{shear} is used again as a radius. To determine the shear area due to sideways outbreaking of the chip, integration takes place over θ. The total shear area can be expressed as

$$S_s = \sum_{n=1}^{3} S_{n,s} = \int_{-\frac{\pi}{2}}^{\frac{\pi}{2}} \int_{0}^{K_s \cdot \left(\frac{h_c - h_s}{sin(\beta_s)}\right)} r_s \; dr_s d\theta + \int_{0}^{K_s \cdot \left(\frac{h_c - h_s}{sin(\beta_s)}\right)} w \; dr_s \tag{D.2}$$

$$= \int_{-\frac{\pi}{2}}^{\frac{\pi}{2}} \frac{1}{2} \cdot \left(K_s \cdot \frac{(h_c - h_s)}{sin(\beta_s)} \right)^2 d\theta + w \cdot (K_s \cdot \frac{(h_c - h_s)}{sin(\beta_s)} \tag{D.3}$$

$$= \frac{\pi}{2} \cdot \left(K_s \cdot (\frac{h_c - h_s}{sin(\beta_s)}) \right)^2 + w \cdot K_s \cdot \left(\frac{h_c - h_s}{sin(\beta_s)}\right) \tag{D.4}$$

Now the total shear area S_s is known, a force balance can be constructed in X- and Z-direction, according to figure 6.13

$$\Sigma F_{s,x} = 0 \tag{D.5}$$

$$F_{k1} \cdot sin(\alpha_c + \delta) - F_{k2} \cdot sin(\beta_s + \phi) - c \cdot cos(\beta_s) \cdot \sum_{n=1}^{3} S_{n,s} = 0 \tag{D.6}$$

$$\Sigma F_{s,z} = 0 \tag{D.7}$$

$$F_{k1} \cdot cos(\alpha_c + \delta) + F_{k2} \cdot sin(\beta_s + \phi) - c \cdot sin(\beta_s) \cdot \sum_{n=1}^{3} S_{n,s} = 0 \tag{D.8}$$

Multiplying equation D.6 with $cos(\beta_s + \phi)$ and equation D.8 with $sin(\beta_s + \phi)$ gives

$$-F_{k2}\cdot sin(\beta_s+\phi)\cdot cos(\beta_s+\phi)-c\cdot\sum_{n=1}^{3}S_{n,s}\cdot cos(\beta_s)\cdot cos(\beta_s+\phi)+F_{k1}\cdot sin(\alpha_c+\delta)\cdot cos(\beta_s+\phi)=0 \quad \text{(D.9)}$$

$$F_{k2}\cdot cos(\beta_s+\phi)\cdot sin(\beta_s+\phi)-c\cdot\sum_{n=1}^{3}S_{n,s}\cdot sin(\beta_s)\cdot sin(\beta_s+\phi)+F_{k1}\cdot cos(\alpha_c+\delta)\cdot sin(\beta_s+\phi)=0 \quad \text{(D.10)}$$

Rewriting equation D.10 as an expression of F_{k1} and the cohesive force component, gives

$$F_{k2}=F_{k1}\cdot\frac{cos(\alpha_c+\delta)\cdot sin(\beta_s+\phi)}{sin('beta_s+\phi)\cdot cos(\beta_s+\phi)}-c\cdot\sum_{n=1}^{3}S_{n,s}\cdot\frac{cos(\beta_s)\cdot cos(\beta_s+\phi)}{sin(\beta_s+\phi)\cdot cos(\beta_s+\phi)} \quad \text{(D.11)}$$

Having F_{k2} expressed in terms of F_{k1} and the cohesive force, substitution can be applied to equation 6.23. By equalizing terms and canceling out F_{k2} gives an expression for F_{k1}

$$F_{k1}=-\frac{c\cdot\sum_{n=1}^{3}S_{n,s}\left[cos(\beta_s)\cdot cos(\beta_s+\phi)+sin(\beta_s)\cdot sin(\beta_s+\phi)\right]}{cos(\alpha_c+\phi)\cdot sin(\beta_s+\delta)+sin(\alpha_c+\delta)\cdot cos(\beta_s+\phi)} \quad \text{(D.12)}$$

Equation D.12 can be simplified by applying several goniometric relations. This gives the final expression for F_{k1}

$$F_{k1}=-\frac{c\cdot\sum_{n=1}^{3}S_{n,s}\cdot cos(\phi)}{sin(\alpha_c+\phi+\beta_s+\delta)} \quad \text{(D.13)}$$

Decomposing this expression in horizontal and vertical direction

$$F_{h,k1}=\frac{c\cdot\sum_{n=1}^{3}S_{n,s}\cdot cos(\phi)}{sin(\alpha_c+\phi+\beta_s+\delta)}\cdot sin(\alpha_c+\delta) \quad \text{(D.14)}$$

$$F_{v,k1}=\frac{c\cdot\sum_{n=1}^{3}S_{n,s}\cdot cos(\phi)}{sin(\alpha_c+\phi+\beta_s+\delta)}\cdot cos(\alpha_c+\delta) \quad \text{(D.15)}$$

D.2. DERIVATION TENSILE-DOMINATED FRACTURE MODEL

For the derivation of the tensile-dominated fracture model, it is of importance to determine the force on the rake face of the pickpoint. The pickpoint itself can be divided into three area's, as seen in figure 6.23 in section 6.5. First, the force on section S_1 and S_3 will be calculated, where $S_1 = S_3$.

$$F_{f,1} = \int_0^{\frac{h_c}{sin(\alpha_c)}} \int_0^{\eta} \frac{1}{sin(\alpha_c)} \cdot \frac{(h_c - l_c)}{h_c} \cdot \frac{K_{Ic}}{\sqrt{\pi \cdot l_{crack}}} \cdot l_c \cdot \eta' \; d\eta' \; dl_c \tag{D.16}$$

$$F_{f,1} = \int_0^{\frac{h_c}{sin(\alpha_c)}} \frac{1}{sin(\alpha_c)} \cdot \frac{(h_c - l_c)}{h_c} \cdot \frac{K_{Ic}}{\sqrt{\pi \cdot l_{crack}}} \cdot l_c \cdot \frac{1}{2}\eta^2 \; dl_c \tag{D.17}$$

Above integral form can be written as

$$F_{f,1} = \int_0^{\frac{h_c}{sin(\alpha_c)}} \frac{1}{sin(\alpha_c)} \cdot \frac{(h_c \cdot l_c - l_c^2)}{h_c} \cdot \frac{K_{Ic}}{\sqrt{\pi \cdot l_{crack}}} \cdot \frac{1}{2}\eta^2 \; dl_c \tag{D.18}$$

The integral form can be split into two separate expressions to solve it

$$F_{f,1} = \left[\int_0^{\frac{h_c}{sin(\alpha_c)}} \cdot l_c \; dl_c - \frac{1}{h_c} \int_0^{\frac{h_c}{sin(\alpha_c)}} l_c^2 \; dl_c \right] \cdot \frac{1}{sin(\alpha_c)} \cdot \frac{\eta^2}{2} \cdot \frac{K_{Ic}}{\sqrt{\pi \cdot l_{crack}}} \tag{D.19}$$

Solving both integrals gives

$$F_{f,1} = \left[\frac{1}{2} \cdot l_c^2 \Big|_0^{\frac{h_c}{sin(\alpha_c)}} - \frac{1}{3 \cdot h_c} \cdot l_c^3 \Big|_0^{\frac{h_c}{sin(\alpha_c)}} \right] \cdot \frac{1}{sin(\alpha_c)} \cdot \frac{\eta^2}{2} \cdot \frac{K_{Ic}}{\sqrt{\pi \cdot l_{crack}}} \tag{D.20}$$

$$F_{f,1} = \left[\frac{1}{2} \cdot \left(\frac{h_c}{sin(\alpha_c)} \right)^2 - \frac{1}{3 \cdot h_c} \cdot \left(\frac{h_c}{sin(\alpha_c)} \right)^3 \right] \cdot \frac{1}{sin(\alpha_c)} \cdot \frac{\eta^2}{2} \cdot \frac{K_{Ic}}{\sqrt{\pi \cdot l_{crack}}} \tag{D.21}$$

Since $S_1 = S_3$, it also means that $F_{f,1}$=$F_{f,3}$. To determine the total force on these parts of the pickpoint's rake face, both components need to be added. This gives

$$F_{f,1,3} = \left[\frac{1}{2} \cdot \left(\frac{h_c^2}{sin^3(\alpha_c)} \right) - \frac{1}{3 \cdot h_c} \cdot \left(\frac{h_c^3}{sin^4(\alpha_c)} \right) \right] \cdot \eta^2 \cdot \frac{K_{Ic}}{\sqrt{\pi \cdot l_{crack}}} \tag{D.22}$$

Now the total forces on S_1 and S_3 are known, the force on the remaining surface S_2 can be calculated.

$$F_{f,2} = \int_0^{\frac{h_c}{sin(\alpha_c)}} \frac{(h_c - l_c)}{h_c} \cdot \frac{K_{Ic}}{\sqrt{\pi \cdot l_{crack}}} \cdot w \; dl_c \tag{D.23}$$

$$F_{f,2} = \left[l_c - \frac{l_c}{2 \cdot h_c} \Big|_0^{\frac{h_c}{sin(\alpha_c)}} \right] \cdot \frac{w}{sin(\alpha_c)} \cdot \frac{K_{Ic}}{\sqrt{\pi \cdot l_{crack}}} \tag{D.24}$$

$$F_{f,2} = \left[\frac{h_c}{sin(\alpha_c)} - \frac{(\frac{h_c}{sin(\alpha_c)})^2}{2 \cdot h_c} \right] \cdot \frac{w}{sin(\alpha_c)} \cdot \frac{K_{Ic}}{\sqrt{\pi \cdot l_{crack}}} \tag{D.25}$$

$$F_{f,2} = \left[\frac{h_c}{sin^2(\alpha_c)} - \frac{h_c}{2 \cdot sin^3(\alpha_c)} \right] \cdot w \cdot \frac{K_{Ic}}{\sqrt{\pi \cdot l_{crack}}} \tag{D.26}$$

Now all separately determined force components are known, the total force that is required to initiate a tensile crack, based on the assumptions made, can be written as

$$F_f = \left[\frac{\eta^2}{2} \cdot \left(\frac{h_c^2}{sin^3(\alpha_c)} \right) - \frac{\eta^2}{3 \cdot h_c} \cdot \left(\frac{h_c^3}{sin^4(\alpha_c)} \right) + \left(\frac{h_c}{sin^2(\alpha_c)} - \frac{h_c}{2 \cdot sin^3(\alpha_c)} \right) \cdot w \right] \cdot \frac{K_{Ic}}{\sqrt{\pi \cdot l_{crack}}} \tag{D.27}$$

NOMENCLATURE

Abbreviations

Symbol	Description	Unit
$ASTM$	American Society for Testing and Materials	
BTS	Brazilian Tensile Strength	[MPa]
$CCCC$	China Communication Construction Company	
GSI	Geological Strength Index	
IHI	Indentation Hardness Index	$[\frac{kN}{mm}]$
$ISRM$	International Society of Rock Mechanics	
$NERCD$	National Engineering Research Center of Dredging	
UCS	Uniaxial Compressive Strength	[MPa]

Greek Symbols

Symbol	Description	Unit
α_c	Cutting angle	[°]
β	Shear angle	[°]
δ	External friction angle	[°]
ρ_{csu}	Density concrete sample UCS test	$[\frac{kg}{m^3}]$
ρ_{csb}	Density concrete sample BTS test	$[\frac{kg}{m^3}]$
ρ_{rsu}	Density rock sample UCS test	$[\frac{kg}{m^3}]$
ρ_{rsb}	Density rock sample BTS test	$[\frac{kg}{m^3}]$
γ_2 , γ_3 , γ_4	Generic angles	[°]
ϕ	Internal friction angle	[°]
ψ	External friction angle	[∘]
σ_{bts} , σ_t	Brazilian Tensile Strength	[MPa]
σ_{crit}	Critical stress of crack initiation	[MPa]
σ_{crush}	Crushed zone stress	[MPa]
σ_{ucs}	Uniaxial Compressive Strength	[MPa]
τ_t	Shear stress	[MPa]

Roman Symbols

Symbol	Description	Unit
A_{in}	Indentation area	[mm^2]
$F_{cz,mean}$	Indentation area of spherical cap	[mm^2]
B	Brittleness or Ductility number	[-]
c	Cohesive shear strength	[MPa]
c_{mob}	Mobilized cohesive shear strength	[MPa]
D_s	Diameter rock sample	[m]
d_1 , d_2	Length arm due to moment around O	[mm]
D_{csu}	Diameter concrete sample UCS test	[mm]
D_{csb}	Diameter concrete sample BTS test	[mm]
d	Depth of the cut	[m]
D_{rsu}	Diameter rock sample UCS test	[mm]
D_{rsb}	Diameter rock sample BTS test	[mm]
η	Angle of pickpoint's cutting face	[°]
E_{sp}	Specific energy	[MPa]
U_i	Required energy	[N]
U_i	Internal stored energy	[N]
F_{crush}	Force due to crushing	[kN]
$F_{h,crush,c}$	Horizontal force due to crushing concrete	[kN]
$F_{h,crush,s}$	Horizontal force due to crushing sandstone	[kN]
$F_{v,crush,c}$	Vertical force due to crushing concrete	[kN]
$F_{v,crush,s}$	Vertical force due to crushing sandstone	[kN]
F_f	Cutting forces due to tensile fracturing	[kN]
F_{k1}	Total force component due to shear failure	[kN]
$F_{h,k1}$	Horizontal force component due to shear failure	[kN]
$F_{v,k1}$	Vertical force component due to shear failure	[kN]
F_n	Normal force on rake face of the pickpoint	[kN]
F_{shear}	Cutting forces due to shear failure	[kN]
F_T	Reaction force, acting over external friction angle	[kN]
$F_{tensile}$	Cutting forces due to tensile failure	[kN]
γ , γ_s	Rock surface energy density	[$\frac{J}{m^2}$]
h_i, h_c	Cutting depth	[m]
$h_{\alpha_c,i}$	Crushed zone height	[mm]

h_{ind}	Indentation depth	[mm]
h_{mean}	Mean cutting depth	[m]
h_s	Shear crack initiated height	[mm]
K_{ind}	Indentation coefficient	[-]
K_{nc}	Mode-dependent stress intensity factor	[MPa$\cdot\sqrt{m}$]
K_{eq}	Equivalent length coefficient	[-]
K_s	Empirically-based shear factor	[-]
K_t	Fraction of tensile failure	[-]
l_t	Tip length pickpoint	[mm]
L_{eq}	Equivalent length	[mm]
l_b	Length block	[mm]
l_c	Variable height	[mm]
l_{crack}	Length of the crack	[mm]
M_O	Moment around point O	[mm]
$F_{ct,peak}$	Total peak cutting force	[kN]
$F_{ct,mean}$	Mean total cutting force	[kN]
$F_{cx,peak}$	Peak cutting force x-direction	[kN]
$F_{cx,mean}$	Mean cutting force x-direction	[kN]
$F_{cy,peak}$	Peak cutting force y-direction	[kN]
$F_{cy,mean}$	Mean cutting force y-direction	[kN]
$F_{cz,peak}$	Peak cutting force z-direction	[kN]
$F_{cz,mean}$	Mean cutting force z-direction	[kN]
$K_{sensitivity}$	Sensitivity factor per direction	[-]
S_s	Total shear area where cohesion acts	[mm^2]
S_t	Total area of tensile plane	[mm^2]
t_c	Length of tensile plane	[mm]
t_a , $t_{b,2}$, $t_{b,1}$	Generic length parameters	[kN]
$V_{\alpha_c,i}$	Total volume of crushed material	[m^3]
$E_{measured}$	Measured Voltage	[μV]
E_{total}	Total Voltage	[V]
w_c	Width of the cut	[m]
w	Tip width pickpoint	[mm]
E	Young's Modulus	[MPa]

BIBLIOGRAPHY

[1] I. Evans, *A theory of the cutting force for point-attack picks,* Geotechnical and Geological Engineering **2**, 63 (1984).

[2] Y. Nishimatsu, *The mechanics of rock cutting, International Journal of Rock Mechanics and Mining Sciences & Geomechanics Abstracts*, **9**, 261 (1972).

[3] K. Gehring, *Rock testing procedures at va's geotechnical laboratory in zeltweg,* Tech-nical report, Voest Alpine Zeltweg, Austria, TZU **41** (1987).

[4] C. Fairhurst, *On the validity of the 'brazilian'test for brittle materials, International Journal of Rock Mechanics and Mining Sciences & Geomechanics Abstracts*, **1**, 535 (1964).

[5] W. van Kesteren, *Numerical simulations of crack bifurcation in the chip forming cutting process in rock,* Fracture of Brittle Disordered Materials: Concrete, Rock and Ceramics , 505 (1995).

[6] P. N. Verhoef, *Wear of rock cutting tools: implications for the site investigation of rock dredging projects* (1997).

[7] F. Dagrain and T. Richard, *On the influence of pdc wear and rock type on friction coefficient and cutting efficiency,* EUROROCK 2006: Multiphysics coupling and long term behaviour in rock mechanics (2006).

[8] H. J. R. Deketh, *Wear of rock cutting tools. laboratory experiments on the abrasivity of rock,* in *PhD Thesis, Delft University of Technology.* (1995).

[9] R. Helmons, *Excavation of hard deposits and rocks: On the cutting of saturated rock,* (2017).

[10] T. Richard, F. Dagrain, E. Poyol, and E. Detournay, *Rock strength determination from scratch tests,* Engineering Geology **147**, 91 (2012).

[11] T.Rutten, *Cutting forces in the linear rock cutting process, validating and expanding existing models* (TU Delft, 2019).

[12] S. A. Miedema, *The Delft sand, clay and rock cutting model* (IOS Press, 2014).

[13] R. Goktan and N. Gunes, *A semi-empirical approach to cutting force prediction for point-attack picks,* Journal of the Southern African Institute of Mining and Metallurgy **105**, 257 (2005).

[14] R. Goktan, *A suggested improvement on evans' cutting theory for conical bits,* in *Proceedings of fourth symposium on mine mechanization automation*, Vol. 1 (1997) pp. 57–61.

[15] X. Li, S. Wang, S. Ge, R. Malekian, and Z. Li, *A theoretical model for estimating the peak cutting force of conical picks,* Experimental Mechanics **58**, 709 (2018).

[16] A. Griffith, *Fracture behavior of brittle materials,* Phil. Trans. Roy. Soc. A **221**, 163 (1920).

[17] Z. Bieniawski and M. Bernede, *Suggested methods for determining the uniaxial compressive strength and deformability of rock materials: Part 1. suggested method for determining deformability of rock materials in uniaxial compression,* in *International Journal of Rock Mechanics and Mining Sciences & Geomechanics Abstracts*, Vol. 16 (Elsevier, 1979) pp. 138–140.

[18] Z. Bieniawski and I. Hawkes, *Suggested methods for determining tensile strength of rock materials,* Int J Rock Mech Min Sci Geomech Abstr **15**, 99 (1978).

[19] A. Mwanga, J. Rosenkranz, and P. Lamberg, *Testing of ore comminution behavior in the geometallurgical context—a review,* Minerals **5**, 276 (2015).

[20] T. Szwedzicki, *Draft isrm suggested method for determining the indentation hardness index of rock materials,* in *International Journal of Rock Mechanics and Mining Sciences and Geomechanics Abstracts*, Vol. 6 (1998) pp. 831–835.

[21] S. Yagiz, J. Rostami, *et al.*, *Indentation test for the measurement of rock brittleness,* in *46th US Rock Mechanics/Geomechanics Symposium* (American Rock Mechanics Association, 2012).

[22] Z. Bieniawski and M. Bernede, *Suggested methods for determining the uniaxial compressive strength and deformability of rock materials: Part 1. suggested method for determining deformability of rock materials in uniaxial compression,* in *International Journal of Rock Mechanics and Mining Sciences & Geomechanics Abstracts*, Vol. 16 (Elsevier, 1979) pp. 138–140.

[23] E. Hoek and E. Brown, *Underground excavations in rock, london, instn min. metall.* (1980).

[24] E. Hoek, *Brittle failure of rock. in rock mechanics in engineering practice,* (1968) pp. 99–124.

[25] N. Barton and V. Choubey, *The shear strength of rock joints in theory and practice,* Rock mechanics **10**, 1 (1977).

[26] E. Gaffney, *Measurements of dynamic friction between rock and steel*, Tech. Rep. (SYSTEMS SCIENCE AND SOFTWARE LA JOLLA CA, 1976).

[27] J. Kerkvliet, *Engineering model for rock cutter design,* (2010).

[28] Dr.ir. P.J.G. Schreurs, *Lecture notes fracture mechanics course,* (2012).

[29] Broberg, K Bertram, *Cracks and fracture* (Elsevier, 1999).

[30] Atkinson, B.K., *Fracture mechanics of rock* (Elsevier, 2015).

[31] S. Kahraman and R. Altindag, *A brittleness index to estimate fracture toughness,* International Journal of Rock Mechanics and Mining Sciences **2**, 343 (2004).

[32] H. Guo, N. Aziz, and L. Schmidt, *Rock cutting study using linear elastic fracture mechanics,* Engineering fracture mechanics **41**, 771 (1992).